Patterns and Transport in Axisymmetric Compressible Taylor-Couette flow via Direct Numerical Simulations

A Thesis

Submitted for the Degree of

MASTER OF SCIENCE (ENGINEERING)

by

Tanumoy Dhar

ENGINEERING MECHANICS UNIT
JAWAHARLAL NEHRU CENTRE FOR ADVANCED SCIENTIFIC RESEARCH
(A Deemed University)
Bangalore – 560 064

September 2020

My Family

DECLARATION

I hereby declare that the matter embodied in the thesis entitled "**Patterns and Transport in Axisymmetric Compressible Taylor-Couette flow via Direct Numerical Simulations**" is the result of investigations carried out by me at the Engineering Mechanics Unit, Jawaharlal Nehru Centre for Advanced Scientific Research, Bangalore, India under the supervision of **Prof. Meheboob Alam** and , and that it has not been submitted elsewhere for the award of any degree or diploma.

In keeping with the general practice in reporting scientific observations, due acknowledgment has been made whenever the work described is based on the findings of other investigators.

_____

Tanumoy Dhar

CERTIFICATE

I hereby certify that the matter embodied in this thesis entitled "**Patterns and Transport in Axisymmetric Compressible Taylor-Couette flow via Direct Numerical Simulations**" has been carried out by **Mr.** Tanumoy Dhar at the Engineering Mechanics Unit, Jawaharlal Nehru Centre for Advanced Scientific Research, Bangalore, India under my supervision and that it has not been submitted elsewhere for the award of any degree or diploma.

_____

Prof. Meheboob Alam

(Research Supervisor)

Acknowledgements

Last two and half years seem to have past in the blink of an eye. During this time, I met a lot of amazing people and enjoyed some unforgettable moments. I believe acknowledgements is that part, which tells a story about the person behind the thesis, and, at the same time, the most read by everyone from any background. The completion of this thesis has been possible with the help and support of several people whom I heartily wish to acknowledge, hereby.

I would like to thank Prof. Meheboob Alam for his un-parallel support and encouragement. I do not have enough words to express my gratitude for your guidance. You instilled the vigour of research, in me. Your physical insight and mathematical understanding of a broad spectrum of continuum mechanics have always inspired me. It was a privilege to do science under your guidance and I have learned a lot from you. Whenever I had any question, I could always approach you and discuss with you. I will be forever grateful to you for everything.

I would like to thank Prof. K.R. Sreenivas for being my supervisor when I visited JNCASR for the first time as a summer fellow during the summer undergraduate research program at Engineering Mechanics Unit (EMU), JNCASR. I would like to thank Prof. Ganesh Subramanian, Dr S. V. Diwakar and Prof. Rajesh Ganapathy for their courses. I would like to thank Prof. Subir K. Das for patiently explaining me concepts of Statistical Mechanics, during the course, as I was coming from an engineering background and had no prior knowledge on this subject. I will be always grateful to Prof. Henrik Bruus and Prof. Tomas Bohr in DTU Physics, Copenhagen, Denmark for providing me financial support, to attend the Complex Motion in Fluids, Summer School in Gilleleje, Denmark.

Dear Pratik Aghor, I thank you for generously providing the initial version of your DNS code to me. You taught me numerical methods and dynamics of complex systems, starting from the advice “start from coding 1-d heat equation, if you accomplish something simpler and small, you will have a small sense of pride and will encourage you to get back to the actual code or something bigger”. We have a long way to go !

I would like to thank my other labmates: Reddy, Tsunil, Nandu, Saikat, Ramakrishna, Prashant for the wonderful atmosphere in Prof. Alam’s lab during my first one and a half years. Dear Tsunil, thank you for helping me analyse velocity fields, from the experiments using PIV, and enforcing the importance of Python! Dear Ramakrishna, I thank you for your

quick help on LaTeXand Mathematica software. Dear Saikat da, I will always cherish our fights over petty things, including AC of the lab and many others. Dear Prashant, I thank you for encouraging me to appear in GRE and your practical attitude towards life. I would like to thank my ex-labmates who have always been there to provide valuable suggestions, thanks Achal and Ronak. I would like to express my gratitude to Rafi, Shashank and Vybhav for teaching me experiments during my heat transfer course. I would like to thank Arun, Anand, Pulkit, Laxman and other EMU members.

I would like to heartily thank Akshay, Vinita, Gurshid, Ankit, Prathamesh, Adak and Divya for helping me when I was unwell, I will always be grateful towards you guys, for that. Dear Akshay, thank you for your support from time to time, and high-speed bike rides! I thank Saifuddin and Akanksha for having interesting discussions with me, over lunches and dinners. My dear friends: Surishi, Vinita, Divya, Kajal, Anushka, Ankit, Himani, Swaraj, Rohit, Adak, Swarna, Sachin and Shalu, it was really awesome meeting you guys ! I thank all of you for making my life at JNCASR, full of memories, I am so full of gratitude and joy. In the past two and a half years of Masters, I met many wonderful people with whom I enjoyed various activities like having dinners, outings, morning jogs. I would like to mention their names in no particular order: Abhishek Garg, Himanshu, Sudarshan, Padmalaya, Koyendrila, Robi, Vinayak and Saptarshi. I would also like to thank my other batchmates: Debabrata, Paribesh, Sanchita, Rishov, Sudip, Arunava and others for being around, and keeping the vibe of home, away from home alive, through actively organizing Bijoya Sommiloni and Saraswati Pujo.

I heartily thank JNCASR administration, whose members have been always helpful and prompt. I especially thank Administrative Officer, Joydeep Deb, for his immediate and quick nature for helping students in need. I extend thank you towards admin staff, library staff, hostel staff, security staff, mess workers in NVSH and Students Residence, for their constant help, from time to time. I would like to thank my *Alma Mater*, Mechanical Engineering Department of Jadavpur University, and all the faculty members there, the esteemed alumni, from whom I have learnt everything. I would like to thank all my Teachers and Professors, during different stages of my life.

Finally, I wish to express my deepest gratitude to my parents, who have always been and will be my constant source of love and support.

Abstract

The focus of the present dissertation is to study the spatio-temporal pattern formation and transport in Compressible Taylor-Couette flow. Using the Direct Numerical Simulations (DNS) to study the axisymmetric Taylor-Couette flow (TCF) of an ideal gas with inner cylinder rotating, the solutions are presented as functions of (i) Reynolds number (Re) based on the rotation rate of the inner cylinder, (ii) peripheral Mach number (Ma) of the flow and (iii) the radius ratio $(\eta = r_1/r_2)$, where r_1 and r_2 corresponds to the radii of inner and outer cylinders, respectively. All simulations are carried out with axially periodic boundary conditions, except in Chapter - 6 that deals with axisymmetric counter rotating TCF with end-plates. The primary bifurcation from the pure azimuthal circular Couette flow (CCF) leads to the well-known Taylor Vortex flow (TVF), and the phase diagrams consisting of patterns are identified in the (Re, Ma) and (Re, η) plane. The effect of compressibility (Ma) on TCF and the onset of primary instability which is the transition from purely azimuthal circular Couette flow (CCF) to Taylor vortex flow (TVF) for $\eta = 0.5$ and $\Gamma = h/\delta = \pi/2$, where Γ is the aspect ratio, h is the height of the computational domain and δ $(= r_2 - r_1)$ is the gap width between two cylinders, is analyzed in Chapter 3. It is shown that the compressibility primarily affects the density distribution within the gap between two rotating cylinders by causing an accumulation of mass near the stationary outer cylinder and plays a pivotal role in restraining the onset of instability. A new time-dependent, axially propagating, axisymmetric flow state, called the Travelling wave solution (TWS), is identified in TC cells at higher Re. These are low frequency axially propagating waves, and a comprehensive phase diagram in (Re,Ma) plane is plotted that summarizes the region of TWS. Transport in compressible Taylor vortices is calculated and the analyses of density (ρ) and velocity (u, v, w) fields reveal that the compressibility diminishes the radial (Q_r), azimuthal (Q_θ) and axial (Q_z) transports.

Chapter 4 highlights the effects of radius ratio (η) and compressibility (Ma) on the onset of Taylor vortices from the base state of circular Couette flow (CCF). It is seen that the compressiblity (Ma) effects are less significant in smaller gap-width, TC-cell as the diffusive effects become dominant at $\eta \longrightarrow 1$, which is similar to the linear stability results of Manela & Frankel (2007). The existence of stationary and non-stationary patterns is found and a comprehensive phase diagram in (Re, η) plane is plotted that summarizes these findings. The

scaling of effective-Nusselt number (Nu_ω) with Taylor number (Ta) are presented for different radius ratio (η) for $CCF \longrightarrow TVF$ transition along with the effect of fluid compressibility (Ma) on effective-Nusselt number (Nu_ω) for $\eta = 0.5$ is discussed. Chapter 5 portrays the results on Proper Orthogonal Decomposition (POD) on the flow fields obtained from the DNS data of Taylor-Couette flow. Using the "method of snapshots" on the radial-axial velocity (u,w) spectra combined with density (ρ) and temperature (T) perturbations, scaled with a weight matrix, corresponding to the Mack norm (Mack, 1984), over the (r,z) plane for various Re in the the wide-gap regime ($\eta = 0.5$), it is found that the first three POD modes (for $Re = 210$) and first five POD modes ($Re = 500$) are sufficient to capture more than 95% of the total energy content of the present system.

Chapter 6 presents the results from numerical investigations of Taylor-Couette flow (TCF) of an ideal gas in "finite" cylinders obtained with independently rotating inner-cylinder ($0 < Re_i < 300$) and outer cylinder ($-300 \leq Re_o \leq 300$), where $Re_i = \omega_1 r_1 \delta/\nu$ and $Re_o = \omega_2 r_2 \delta/\nu$ are the Reynolds number of inner and outer cylinder, respectively, and ω_1 and ω_2 are inner and outer cylinder angular velocities, $\delta = r_2 - r_1$ is the gap-width, and ν is the kinematic viscosity at inner cylinder. All these simulations are done by assuming axisymmetric flow. The emergence of localized cellular Taylor vortex state (Abshagen *et al.*, 2010) is found in the counter-rotation regime ($Re_i \in [150, 300]$ and $Re_o \in [-100, -300]$). We also report axisymmetric propagating vortices (previously observed by Hoffmann *et al.* (2013) in incompressible TCF), which travel from end walls towards mid-height, where they get annihilated and the cycle continues. The phase diagram consisting of stationary and travelling patterns is constructed in the (Re_i, Re_o) plane for $Ma = 1$ and $Pr = 1$.

Table of contents

List of figures

List of tables

Chapter 1

Introduction

1.1 Taylor-Couette Flow: Flow between Two Concentric Differentially Rotating Cylinders

The story of flow between two concentric differentially rotating cylinders started its journey during the twilight years of seventeenth century when Sir Isaac Newton *hypothesized* the definition of modern day *Newtonian fluid*. In the Book 2, Section 9, Proposition 51, Corollary 2 of *Principia Mathematica*, Newton states - "If a fluid be contained in a cylindric vessel of an infinite length, and contain another cylinder within, and both the cylinders revolve about one common axis, and the times of their revolutions be as their semidiameters, and every part of the fluid continues in its motion, the periodic times of the several parts will be as the distances from the axis of the cylinders". After a period of one hundred sixty one years, George Gabriel Stokes (1848) solved for the fluid flow velocity between two rotating coaxial cylinders but expressed his concerns about the boundary conditions of the flow (no-slip condition at the wall and free surface).

In the 1880s, Henry Reginald Arnulph Mallock and Maurice Marie Alfred Couette independently determined the viscosity of water in an apparatus consisting of two rotating concentric cylinders. In the year of 1890, the thesis written by Couette illustrated a detailed study of measurement of viscosity of water using a pair of cylinders with the stationary inner cylinder and a rotating outer cylinder. The design of viscometer by Couette (1890) was inspired from the works of Austrian theoretical meteorologist, Max Margules and only the outer cylinder could be rotated. However the apparatus designed by Mallock (1889) operated with more than two different arrangements of the cylinders. This work of Mallock (1889) was communicated by *Lord* Rayleigh on 30th of November 1888, in response to which *Lord* Kelvin wrote a letter to *Lord* Rayleigh, dated 10th July 1895 -

"On Saturday I saw a splendid illustration by Arnulph Mallock of our ideas regarding instability of water between two parallel planes, one kept moving and the other fixed. Coaxial cylinders, nearly enough planes for our illustration[, were used]. The rotation of the outer can was kept very accurately uniform at whatever speed the governor was set for, when left to itself. At one of the speeds he showed me, the water came to a regular regime, *quite smooth*. I dipped a disturbing rod an inch or two down into the water and immediately the torque increased largely. *Smooth* regime would only be reestablished by slowing down and bringing up to speed again, gradually enough. Without the disturbing rod at all, I found that by resisting the outer can by hand somewhat suddenly, but not very much so, the torque increased suddenly and the motion became visibly turbulent at the lower speed and remained so." Later on, *Lord* Rayleigh decided to probe the flow stability in the absence of viscosity. A detailed description of history of the Taylor-Couette flows is excellently summarized in Donnelly (1991).

Around three decades later, *Lord* Rayleigh (1917) derived a criterion for the stability of inviscid rotating flows, which emphasized that the circular Couette flow (CCF) is stable to axisymmetric perturbations only if the square of specific angular momentum of the rotating fluid element increases monotonically outwards from the axis of rotation, or, in other words, the square of the circulation increases outwards. Rayleigh (1917) asserted the above mentioned criterion to be necessary and sufficient. Later Synge (1938) performed linear stability analyses for axisymmetric inviscid perturbations on rotating fluid and concluded that the criterion derived by Rayleigh (1917) was sufficient but not necessary.

The Navier-Stokes equations for purely axisymmetric disturbances are given by:

r- momentum:

$$\frac{Du}{Dt} - \frac{v^2}{r} = -\frac{1}{\rho}\frac{\partial p}{\partial r}, \tag{1.1a}$$

θ-momentum:

$$\frac{Dv}{Dt} + \frac{uv}{r} = 0, \tag{1.1b}$$

z-momentum:

$$\frac{Dw}{Dt} = -\frac{1}{\rho}\frac{\partial p}{\partial z}, \tag{1.1c}$$

where the material derivative can be expressed as

$$\frac{D}{Dt} = \frac{\partial}{\partial t} + u\frac{\partial}{\partial r} + w\frac{\partial}{\partial z}, \tag{1.2}$$

and finally, invoking the equation of continuity,

$$\frac{\partial u}{\partial r} + \frac{u}{r} + \frac{\partial w}{\partial z} = 0, \tag{1.3}$$

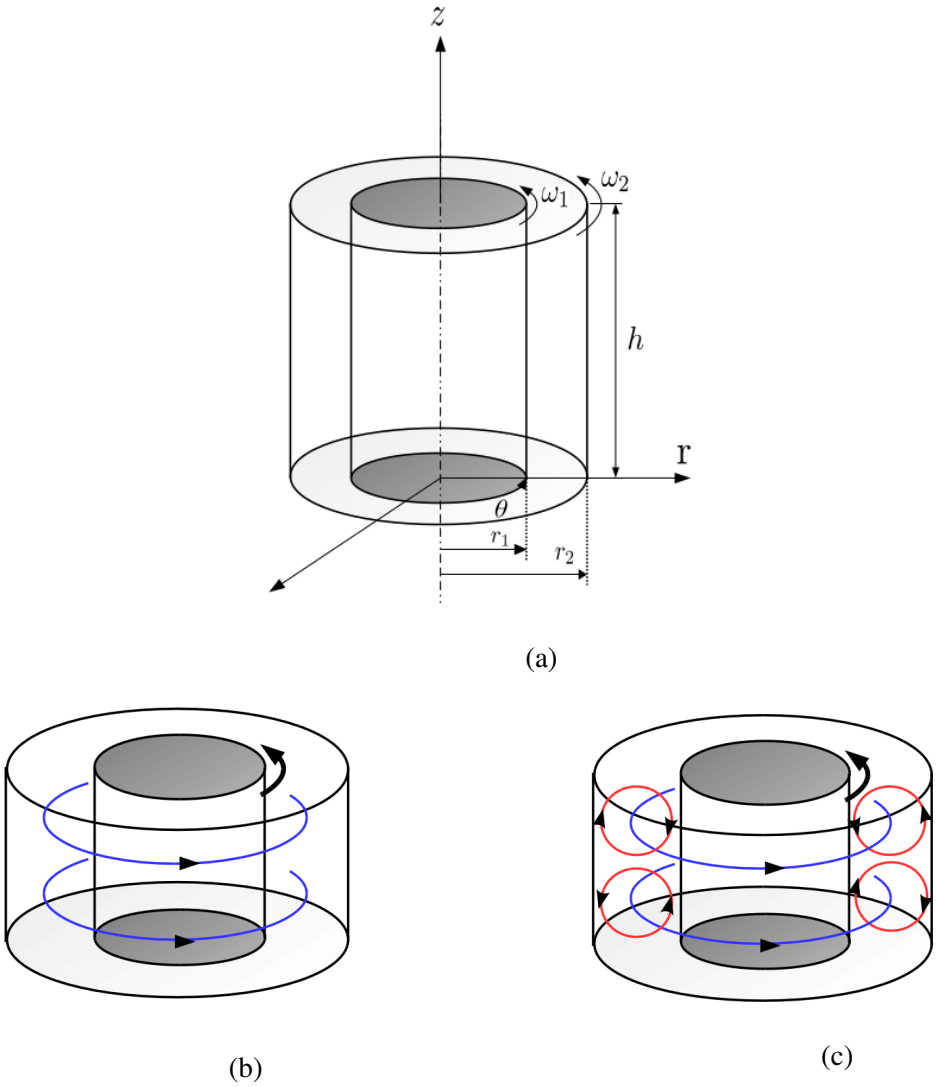

(a)

(b)

(c)

Fig. 1.1 Schematic diagram of (a) Taylor-Couette setup, the inner cylinder $(r = r_1)$ is rotating with angular velocity ω_1 and the outer cylinder $(r = r_2)$ is stationary $(\omega_2 = 0)$. The gap-width between the two cylinders is $\delta = r_2 - r_1$ and the axial extent of cylinder is h; (b) flow pattern showing purely azimuthal CCF (blue lines); (c) flow pattern marked in red circles showing TVF as a primary bifurcation from CCF.

where u,v and w denote radial (r), azimuthal (θ) and axial (z) velocities, respectively; ρ is the mass-density of the fluid and p is the pressure.

Consider the initial flow to be purely azimuthal, i.e.

$$v = r\omega(r), \quad u = 0 = w. \tag{1.4}$$

From the momentum balance in the θ-direction, we have

$$\frac{D(rv)}{Dt} = 0, \tag{1.5}$$

which implies that the quantity $H = rv$, the specific angular momentum of the fluid, is conserved. One can define the kinetic energy per unit volume associated with the azimuthal motion in terms of H as follows:

$$\frac{1}{2}\rho v^2 = \frac{1}{2}\frac{\rho H^2}{r^2}. \tag{1.6}$$

Let us consider two elemental rings of equal volume dV at different radial locations, one at $r = r_1$ and the other at $r = r_2$. Assuming $r_2 > r_1$, total kinetic energy per unit volume is:

$$KE_{12} = \frac{1}{2}\rho\left(\frac{H_1^2}{r_1^2} + \frac{H_2^2}{r_2^2}\right). \tag{1.7}$$

Considering that the fluid in these two elemental volume has swapped positions, the new kinetic energy per unit volume will be:

$$KE_{21} = \frac{1}{2}\rho\left(\frac{H_1^2}{r_2^2} + \frac{H_2^2}{r_1^2}\right), \tag{1.8}$$

and hence the change in kinetic energy is,

$$KE_{21} - KE_{12} = \frac{1}{2}\rho(H_2^2 - H_1^2)\left(\frac{1}{r_1^2} - \frac{1}{r_2^2}\right). \tag{1.9}$$

Note that, for $r_2 > r_1$, $\left(\frac{1}{r_1^2} - \frac{1}{r_2^2}\right) > 0$. If the swap liberates kinetic energy, $KE_{21} - KE_{12} < 0$ or $H_2^2 - H_1^2 < 0$, the base flow will be unstable. This implies that, if H^2 decreases with r, the flow is unstable. Note that, $2\pi H$ is the circulation around a circle, given by $r =$ constant and $z =$constant, see Chandrasekhar (1960). Hence the criterion for stability is given by

$$\frac{dH^2}{dr} > 0. \tag{1.10}$$

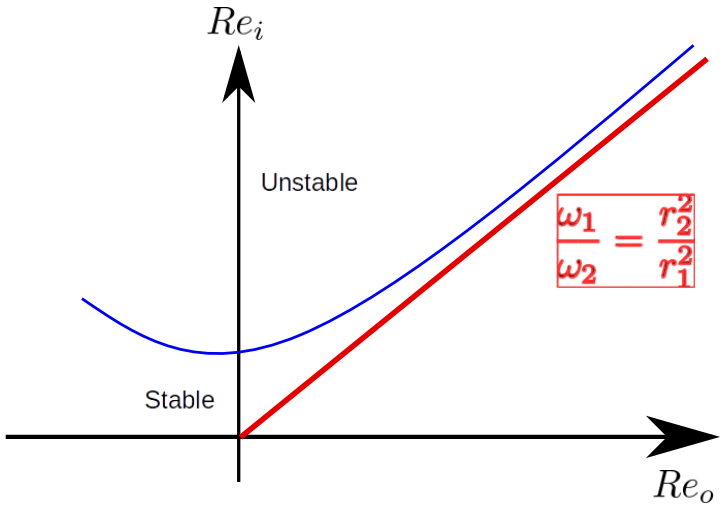

Fig. 1.2 Rayleigh (1917) line (red line) and Taylor (1923) stability line (blue line) in the (Re_o, Re_i) plane.

The above criterion (1.10) is known as Rayleigh's (1917) inviscid stability criterion. Figure 1.2 shows the Rayleigh (1917) line (depicted by the red line) is given by $\omega_1 r_1^2 = \omega_2 r_2^2$ in the (Re_o, Re_i)-plane where ω_1 and ω_2 are the angular velocities of inner and outer cylinders, respectively. The story of the flow between concentric cylinders entered a new phase when, considering the effect of viscosity along with experimental evidence, Taylor (1923) presented a linear stability analysis with narrow-gap approximation which elucidated the occurrence of azimuthally-invariant counter-rotating toroidal vortices, stacked along the axial direction, as a transition to Taylor vortex flow (TVF) from the CCF (see panels (b) CCF and (c) TVF of figure 1.1). This marked as a bridge between theory and experiments proving the NSE (Navier Stokes Equations) to describe the fluid flow and no-slip boundary condition. It took 75 years to demystify the concerns of Stokes (1848) about the boundary conditions in rotating fluid. The apparatus designed by Taylor had the provision for flow visualization which previous experimentalists failed to incorporate. The blue line in figure 1.2 represents a schematic of Taylor's neutral stability curve in (Re_o, Re_i)-plane.

Over a decade later, Taylor (1936*a*) presented torque measurements with (a) inner cylinder rotating and outer cylinder stationary and (b) inner cylinder stationary and outer cylinder rotating. His key finding was that the onset of turbulence happens much earlier in case (a) than in case (b). In a follow up article, Taylor (1936*b*) describes the distribution of fluid velocity between two cylinders with stationary inner and rotating outer cylinder. Chandrasekhar (1958) examined this problem for wider gap scenarios and concluded that viscosity indeed stabilizes the flow. He provided extensive stability analyses on Taylor Couette flow including the effect of magnetic field.

During the past hundred years, the incompressible Taylor-Couette flow (TCF) has emerged as a well-studied problem in fluid mechanics to understand instabilities (Di Prima & Swinney, 1981; Taylor, 1923, 1936*a*), pattern formation (Coles (1965), Andereck *et al.* (1986), Koschmieder (1993), Cross & Greenside (2009), Chossat & Iooss (2012)) and the laminar-turbulent transition (Barcilon *et al.* (1979), Gorman *et al.* (1980), Lathrop *et al.* (1992), Grossmann *et al.* (2016)).

In a seminal work, Coles (1965) discovered, depending on the path to reach a specific Reynolds number Re, more than 70 transitions for a speed range up to about 10 times the first critical speed $(10Re_c)$ which provided conclusive instances of the nonuniqueness of patterns in Taylor-Couette flow. Coles (1965) found that, at large Re, the discrete spectrum obtained from flow pattern changes gradually and reversibly to a continuous one by broadening of the initial sharp spectral lines. He also identified catastrophic transition: when the angular velocity of outer cylinder is larger than the inner one, in which for a given Re different regions in the fluid exists in laminar and turbulent flow states and under certain conditions the flow, the turbulent regions may appear and disappear like intermittency in turbulent bursts and spiral turbulence. Regarding the absence of turbulence in specific regions of the fluid, Coles (1965) stated - "part of the turbulent energy may actually be transferred from the turbulence back to the mean flow rather than merely dissipated as heat." Andereck *et al.* (1986) characterized different flow states and the transition scenarios between them, for a fixed radius ratio of $\eta = r_1/r_2 = 0.883$. The plethora of states included Taylor vortices (TVF), wavy vortices (WVF), modulated wavy vortices (MWV), vortices with wavy outflow boundaries (WOB), vortices with wavy inflow boundaries (WIB), twisted vortices (TWI), spiral vortices (SPI), interpenetrating spirals (IPS), wavy interpenetrating spirals (WIS), spiral turbulence (SPT), turbulent Taylor vortices (TTV), featureless turbulence (TUR), and many more, see figure 1.3. This marked the beginning of tremendous growth and development in the Taylor-Couette flow over the next decades, some of which are reviewed in Grossmann *et al.* (2016).

1.2 Taylor-Couette Flow: Direct Numerical Simulations

The incompressible Taylor-Couette flow, being a paradigmatic model for wall-bounded, shear-driven turbulence, has been probed numerically using direct numerical simulations (DNS) by various groups. Complete access to scalar (temperature and pressure) and vector fields (velocity) can be achieved for every spatial location on the domain of interest at all times in DNS in which the NSE are numerically solved for a given set of initial and boundary conditions without aid from any turbulence model. This translates to the fact that the whole range of spatial

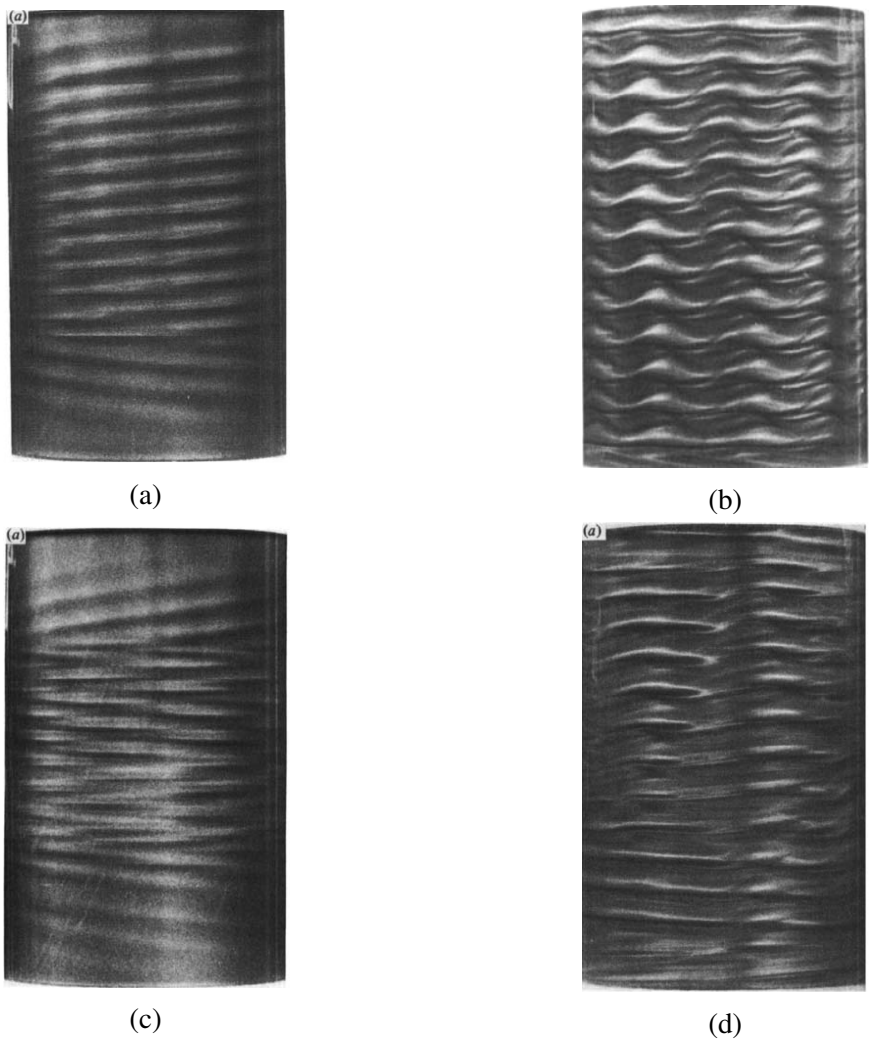

Fig. 1.3 Flow patterns illustrating (a) Spiral vortices (SPI); (b) Modulated Wavy Vortex flow (MWV); (c) Interpenetrating Spirals (IPS) and (d) Wavy Interpenetrating Spirals (WIS) (Andereck *et al.*, 1986)

scales (integral scales to Kolmogorov microscales) are resolved, which, of course, requires high computational costs.

To the author's best of knowledge, the first reported DNS on TCF was done by Meyer (1967), where he solved axisymmetric incompressible NSE using finite difference technique. Later he extended the analysis to fully three dimensional simulations (Meyer, 1969) using a combination of Fourier expansions in azimuthal (θ) direction and finite differencing in radial (r) and axial (z) directions for a radius ratio of $\eta = r_1/r_2 = 0.833$, where r_1 and r_2 are the radii of inner and outer cylinders, respectively. Meyer (1969) performed simulations for three

discrete Reynolds number (of 750, 1000 and 2000), based on inner cylinder radius,

$$Re_{r_1} = \frac{\omega_i r_1^2}{\nu}, \tag{1.11}$$

where ω_i refers to the angular velocity of the inner cylinder and ν refers to the kinematic viscosity of the fluid. Meyer-Spasche & Keller (1980) performed pseudo-arc length continuation to capture bifurcating branches from purely azimuthal CCF to TVF for different gap-widths. Their analysis was restricted to incompressible axisymmetric simulation of NSE with Fourier expansions in z direction and finite difference in r direction.

Jones (1981) performed axisymmetric simulations with inner cylinder rotating and stationary outer cylinder for a wide range of Taylor numbers

$$Ta = \frac{(\omega_i - \omega_o)^2 r_1 (r_2 - r_1)^3}{\nu^2} = \frac{1-\eta}{\eta} Re^2 \tag{1.12}$$

where

$$Re = \frac{(\omega_i - \omega_o) * (r_2 - r_1)}{\nu} \tag{1.13}$$

and ω_o is the angular velocity of the outer cylinder; he computed linearized eigenfunctions which correspond to wavy TVF at a radius ratio of $\eta = 0.875$. Jones (1982) numerically studied the pattern formation scenario in counter-rotating cylinders for small outer cylinder rotation. In a subsequent work, Jones (1985) studied the transition from steady axisymmetric TVF to time dependent WVF. Moser *et al.* (1983) carried out highly resolved simulations using fully spectral method for axisymmetric and three-dimensional simulations in the TVF regime.

Marcus (1984*a*) came up with a robust, fast and highly memory-efficient pseudospectral code in order to compute non-axisymmetric TCF as an initial value problem. He showed the importance of computers to probe the underlying physical mechanisms that govern the dynamics of TCF. In a later work, Marcus (1984*b*) computed wave-speeds, angular-momentum, torque, energy and enstrophy spectra for both TVF and Wavy Vortex flow (WVF) and explained the relevant physics involved.

Fasel & Booz (1984) solved for axisymmetric NSE using a fourth order implicit finite difference method for Re upto 10 times the critical Re corresponding to the transition from the purely azimuthal CCF to TVF. They provided detailed analysis on the evolution of jet-like structures at higher Re, from stream-function, vorticity and velocity data.

1.3 Compressible Taylor-Couette Flow

While the instability mechanism and pattern formation scenario in incompressible TCF is well understood, its compressible counterpart has been relatively less explored. The compressible analog of TCF is relevant in astrophysical fluid dynamics problems such as accretion disk flows (Balbus & Hawley, 1998) and compact astrophysical bodies, like neutron stars (Abney & Epstein, 1996), that admit high Mach number (Ma).

In compressible flows, one has to solve for the continuity, momentum and the energy equations along with the equation of state. In incompressible flows, the pressure Poisson equation imposes the continuity of the flow at the boundaries, whereas in the compressible case, density or pressure has to be explicitly mentioned. In order to mitigate the latter problem, one can use artificial boundary conditions, or, formulate the continuity equation in a manner such that it is not discretized at the boundary, for example, using staggered grid.

The stability of compressible plane Couette flow (PCF), which is a limiting case of the narrow-gap compressible TCF, has been studied by Duck *et al.* (1994), Hu & Zhong (1998), Malik *et al.* (2006) and Malik *et al.* (2008); it has been found at high Re, acoustic instabilities occur for a range of supersonic Ma. These instabilities are caused by the compressibility of the fluid and are referred as *Mack modes* (Mack, 1976). On the other extreme lies the compressible pipe flows in which the Rayleigh's problem (which essentially is a spin up from rest problem) have been extensively studied for the case of infinte cylinders (Park & Hyun, 1989). Rayleigh's problem (Batchelor, 2000) is a canonical problem for incompressible fluid dynamics, in which an infinite flat plate is started to move in a direction parallel to itself through a viscous fluid, and has been considered for compressible fluid by Howarth (1951).

To the author's knowledge, the first experimental study on compressible TCF was done by Kuhlthau (1960) using dry air. The rotor is made up of forged aluminium alloy (2024-T4) 4 inches in diameter and varies from 1 inches to 2.5 inches in length. The rotor is clamped to a flexible steel shaft of 0.1 inches in diameter. The gap between two cylinders is 0.5 inches. The speeds are varied from 400 rev/sec to 1600 rev/sec, corresponding to a range of Mach numbers $0.37 \leq Ma \leq 1.47$ ($Ma = v_f/c_s$ where v_f is the local flow velocity and c_s is the adiabatic sound speed). Torque measurements on the stationary outer cylinder revealed an inception of instability when it started to increase sharply.

Kao & Chow (1992) carried out a temporal stability analysis for the compressible TCF to study the effects of Ma, Re and wall temperatures for a wide-gap Taylor Couette flow ($\eta = r_1/r_2 = 0.5$ is the radius ratio) using Chebychev collocation method. With increasing rotation of the inner cylinder and the stationary outer cylinder, they found that, at all speeds, increasing the temperature ratio ($\chi = T_2/T_1$) stabilises the low-Re flows and destabilises the high-Re flows. As reported by Kao & Chow (1992), at $Re = 100$ and $\chi = 1$, the maximum

growth-rate of the disturbances (ω_i) increases with increasing Ma, indicating the destabilising role of Ma.

Hatay *et al.* (1993) considered two and three dimensional disturbances and analysed the linear stability for a wide range of parameters and found out that increasing Ma stabilizes the flow for narrow gaps ($\eta > 0.8$) and destabilizes for wide gaps. They also found increasing the $\chi = T_2/T_1$ stabilizes the flow irrespective of the gap-width which were in agreement with Kao & Chow (1992). Both Kao & Chow (1992) and Hatay *et al.* (1993) defined the Reynolds number based on the local density of gas.

As reported by Manela & Frankel (2007), the local gas density cannot be *a priori* prescribed since the near-wall gas conditions are likely to change with varying Re and Ma, and it would be more meaningful to use the average density (the ratio of the mass per unit length of fluid between two cylinders to the area of the gap) as a reference density which in turn would respect the mass conservation when the external parameters are varied. Since at high supersonic speeds, the variation between local and average densities can be quite large, which in turn would influence temperature and pressure distribution within the gap, using the critical Re based on the local density is not a good measure when comparing with its incompressible counterpart. Manela & Frankel (2007) carried out a linear stability analysis focusing on narrow-gaps ($\eta \geq 0.893$), and found their results to agree qualitatively with Kuhlthau (1960) in the transonic regime. They concluded that increasing Ma stabilizes the flow and the compressibility effects become more pronounced with decreasing η.

More recently, Welsh *et al.* (2014) performed the linear stability analysis for the compressible TCF for a radius ratio of $\eta = 0.5$. At low Prandtl number ($Pr \leq 1$), they found increasing Ma stabilizes the flow as found previously by Manela & Frankel (2007). Collectively, the works of Manela & Frankel (2007) and Welsh *et al.* (2014) confirmed that the conclusion of Kao & Chow (1992) are incorrect. Interestingly, at high Pr, Welsh *et al.* (2014) found new instability modes in the form of oscillatory axisymmetric modes and steady convective modes along with stationary Taylor-Couette modes. Most notably, they found that the onset of instability can occur even when the angular momentum increases outwards and hence the classical Rayleigh's criterion can be violated in compressible TCF.

1.4 Present Work

The focus of the present thesis is to study the spatio-temporal pattern formation and transport in compressible Taylor-Couette flow of a dilute gas. Using the Direct Numerical Simulations (DNS) to study the axisymmetric Taylor-Couette flow (TCF) of an ideal gas with inner cylinder rotating, the solutions are presented as functions of (i) the Reynolds number (Re) based on the

rotation rate of the inner cylinder, (ii) the peripheral Mach number (Ma) of the flow and (iii) the radius ratio $(\eta = r_1/r_2)$, where r_1 and r_2 corresponds to the radii of inner and outer cylinders, respectively. The phase diagrams consisting of new patterns are drawn in the (Re, Ma) and (Re, η) plane.

1.4.1 Chapter 2

This chapter presents (i) the governing equations, consisting of time-dependent compressible Navier-Stokes equations along with the continuity and energy equations for a monoatomic perfect gas and (ii) the details of the numerical method. We employ no-slip and Dirichlet boundary conditions for velocity fields (u, v, w) and temperature field (T), respectively. Axially periodic boundary conditions are imposed and extensive code validation is presented.

1.4.2 Chapter 3

In this chapter, the effects of compressibility (Ma) on (i) TCF of molecular gases and (ii) the onset of primary instability, which is the transition from purely azimuthal circular Couette flow (CCF) to Taylor vortex flow (TVF), are studied for $\eta = 0.5$ and $\Gamma = h/\delta = \pi/2$; here Γ is the aspect ratio, h is the height of the computational domain and δ $(= r_2 - r_1)$ is gap width between two cylinders. It is shown that the compressibility primarily affects the density distribution within the gap between two rotating cylinders by causing an accumulation of mass near the stationary outer cylinder that, in turn, plays a pivotal role in restraining the onset of instability. Axially propagating waves have been found and a comprehensive phase diagram in the (Re,Ma)-plane is plotted that summarizes the present findings on different patterns. Transport in compressible Taylor vortices has been calculated and the effects of compressibility on the radial (Q_r), azimuthal (Q_θ) and axial (Q_z) transports are discussed.

1.4.3 Chapter 4

This chapter highlights the effects of radius ratio (η) and compressibility (Ma) on the onset of Taylor vortices from the base state of circular Couette flow (CCF). Existence of stationary and non-stationary patterns is found and a comprehensive phase diagram in (Re, η) plane is plotted that summarizes these findings. Qualitative bifurcation diagrams have been constructed for ramp-up and ramp-down protocols. We verify that the periodic boundary conditions in axial direction admits supercritical pitchfork bifurcation at the onset of TVF from CCF, and the order parameter, Δu (radial velocity at the mid-height and mid-gap of the computational domain) shows a square-root scaling $(\Delta u \propto \sqrt{\varepsilon})$, with the driving parameter (ε) being the

distance from the critical point, where $\varepsilon = (Re - Re^{cr})/Re^{cr}$. The axial velocity (w) at mid-height and mid-gap acts as an effective order parameter to quantify the "degree of asymmetry" in asymmetric stationary flow patterns. We also investigate the existence of side by side two rolls concerning short - cylinders with aspect ratios $\Gamma \leq O(1)$ at high Re in the parameter regime of the Travelling wave (TWS) flow state. We calculate the scaling of effective-Nusselt number (Nu_ω) with Taylor number (Ta) for different radius ratio (η).

1.4.4 Chapter 5

This chapter presents the results on Proper Orthogonal Decomposition (POD) on the flow fields obtained from the DNS of Taylor-Couette flow. POD is a technique that takes a set of input data and creates an orthogonal basis constituted by functions which are the solutions of an integral eigenvalue problem. Using the "method of snapshots" on the radial-axial fluctuation velocity (u,w) spectra combined with density (ρ) and temperature (T) perturbations, scaled with a weight matrix, corresponding to the Mack norm (Mack (1984)), obtained from the DNS, over the (r,z) plane for various Re in the the wide-gap regime $(\eta = 0.5)$, we find that the first three POD modes (for $Re = 210$) and first five POD modes $(Re = 500)$ are sufficient to capture more than 95% of the total energy content of the present system. The temporal dynamics is shown by projecting the fields onto the POD basis modes in order to calculate the associated POD coefficients and are plotted in phase diagrams.

1.4.5 Chapter 6

In this chapter, we report results from numerical investigations of Taylor-Couette flow (TCF) of an ideal gas in "finite" cylinders obtained from independently rotating inner-cylinder ($0 < Re_i < 300$) and outer cylinder ($-300 \leq Re_o \leq 300$), where $Re_i = \omega_1 r_1 \delta/\nu$ and $Re_o = \omega_2 r_2 \delta/\nu$ are the Reynolds number of inner and outer cylinder, respectively, and ω_1 and ω_2 are inner and outer cylinder angular velocities, $\delta = r_2 - r_1$ is the gap-width, and ν is the kinematic viscosity at inner cylinder. The Mach number (Ma) of the flow and the Prandtl number (Pr) of the the fluid is set to unity. The geometrical parameters: (a) radius ratio $(\eta = r_1/r_2)$ is 1/2 (wide-gap limit) and (b) the aspect ratio $(\Gamma = h/\delta$, where h is the height of the computational domain). We employ no-slip and Dirichlet boundary condition for velocities (u,v,w) and temperature T, respectively, at the cylinder walls as well as at the top and bottom lids of the domain. The emergence of localized cellular Taylor vortex state (Abshagen *et al.*, 2010) is found in the counter-rotation regime ($Re_i \in [150,300]$ and $Re_o \in [-100,-300]$). We also report axisymmetric propagating vortices (previously observed by Hoffmann *et al.* (2013) in incompressible fluid systems), which travel from mid-height towards end walls, where they get

annihilated and the cycle continues. The phase diagram consisting of stationary and travelling patterns is constructed in the (Re_i, Re_o) plane.

1.4.6 Chapter 7

In this chapter, we summarise the present findings.

Chapter 2

A Finite Difference Code for Compressible Shear Flows in Cylindrical Coordinates

2.1 Introduction

A finite difference code for axisymmetric compressible Taylor-Couette flow (TCF) is presented. We seek solutions of azimuthal invariant [$\partial/\partial\theta(\cdot) = 0$], time-dependent compressible Navier-Stokes equations along with the continuity and energy equations for a monoatomic perfect gas as functions of Reynolds number (Re) based on the rotation rate of inner cylinder, Mach number (Ma), and the radius ratio (η) of two cylinders. This chapter is based on axisymmetric finite difference code originally developed by Aghor (2018), adapted from Harada (1980*a*), Harada (1980*b*) and Hyun & Park (1992), and later modified, extended and optimized in the present thesis.

2.2 Axisymmetric Compressible TCF and Boundary Conditions

The compressible flow of a perfect gas driven by the rotation of inner cylinder of radius r_1 and stationary outer cylinder of radius r_2, as shown in schematically in figure 2.1, is the focus of the current study. The inner cylinder is rotated at an angular velocity $(\omega_1 > 0)$ and the outer cylinder is at rest $(\omega_2 = 0)$. The problem is formulated in cylindrical coordinates, (r, θ, z), that refer to the radial (wall-normal), azimuthal (flow) and spanwise (axis of the cylinders) directions, respectively. The flow velocity is denoted by $\mathbf{u} = (\tilde{u}, \tilde{v}, \tilde{w})$, where $\tilde{u}$, $\tilde{v}$ and $\tilde{w}$ are

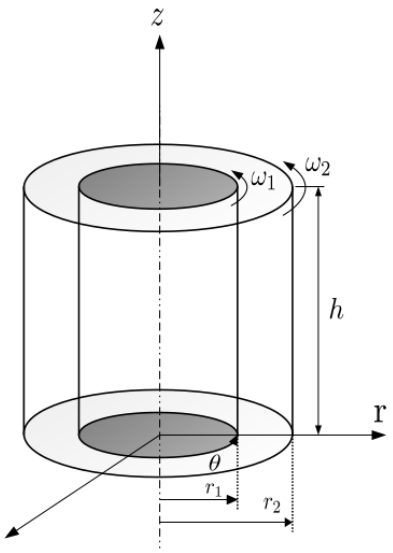

Fig. 2.1 Schematic diagram of Taylor-Couette setup. The inner cylinder is rotating with angular velocity ω_1 and the outer cylinder is stationary ($\omega_2 = 0$). The gap between the two cylinders is $\tilde{\delta}_r = \tilde{r_2} - \tilde{r_1}$ and the height of cylinders is $\tilde{h}$.

its components along r, θ and z directions, respectively. The fluid considered in the present study is a dilute mono-atomic compressible gas of density $\tilde{\rho}$, pressure $\tilde{p}$ and temperature $\tilde{T}$. The shear viscosity ($\tilde{\mu}$), the thermal conductivity ($\tilde{\kappa}$), the specific heat at constant pressure ($\tilde{c_p}$) and specific heat at constant volume ($\tilde{c_v}$) are assumed to be constants and independent of temperature. We consider the heat capacity ratio of the gas ($\gamma = \tilde{c_p}/\tilde{c_v}$) to be 5/3. We assume the bulk viscosity to be zero (i.e. $\tilde{\zeta} = 0$) such that the Stokes (2009) assumption, can be invoked ($\tilde{\lambda} = \tilde{\zeta} - \frac{2}{3}\tilde{\mu} = 0 - \frac{2}{3}\tilde{\mu}$). The temperature of the inner ($\tilde{T_1}$) and outer ($\tilde{T_2}$) cylinders are kept constant.

2.2.1 Dimensionless governing equations: axisymmetric TCF

Let us choose a reference length scale of the problem, $\tilde{\delta}_r$, where $\tilde{\delta}_r = \tilde{r_2} - \tilde{r_1}$ is the gap between two cylindrical walls, a reference time scale, $\tilde{t_r}$, where $\tilde{t_r} = \tilde{\delta}_r{}^2/\tilde{\nu}_r$ is the viscous time scale and a reference velocity scale, $\tilde{u_r}$ where $\tilde{u_r} = \tilde{\delta}_r/\tilde{t_r}$, and $\tilde{\nu}_r = \tilde{\mu_r}/\tilde{\rho}_r$ is the kinematic viscosity of the gas. Hence the non-dimensional variables are as follows -

$$(r,z) = (\tilde{r},\tilde{z})/\tilde{\delta}_r, \qquad t = \frac{\tilde{t}}{(\tilde{\delta}_r{}^2/\tilde{\nu}_r)}, \qquad (u,v,w) = (\tilde{u},\tilde{v},\tilde{w})/\tilde{u_r}. \tag{2.1}$$

The tilde over any physical quantity denotes the dimensional quantity and its unclad equivalent is dimensionless. Note that, δ represents the dimensionless length scale instead of δ_r, chosen

to avoid confusion with δ_r representing the derivative in finite difference formulation (section 2.3). The reference scale for viscosity ($\tilde{\mu}_r$), thermal conductivity ($\tilde{\kappa}_r$) and temperature ($\tilde{T}_r$) are based on their values at the inner cylinder. As per Welsh *et al.* (2014), let us consider $\tilde{m}_w$ be the mass of the gas per unit length between the two cylinders; the reference average gas density is

$$\tilde{\rho}_r = \tilde{m}_w / \pi(\tilde{r_2}^2 - \tilde{r_1}^2) \tag{2.2}$$

and the reference scale for pressure ($\tilde{p}_r$) is taken to be $(\tilde{c_p} - \tilde{c_v})\tilde{\rho}_r\tilde{T}_r$, where $\tilde{c_p}$ and $\tilde{c_v}$ are specific heats at constant pressure and volume, respectively. The dimensionless density and pressure are defined as follows:

$$\rho = \tilde{\rho}/\tilde{\rho}_r, \qquad p = \tilde{p}/\tilde{p}_r. \tag{2.3}$$

Using (2.1) and (2.3), we define the Reynolds number at the inner cylinder to be

$$Re = \omega_1 r_1 \delta / \nu_r. \tag{2.4}$$

The peripheral Mach number (Ma) is defined as

$$Ma = Re/c_{is}, \tag{2.5}$$

where c_{is} is the isothermal sound speed defined via

$$c_{is}^2 = \frac{(c_p - c_v)T_r\delta^2}{\nu_r^2}$$

and the subscript "*is*" denotes the quantity being evaluated at isothermal conditions.
The final parameter is the Prandtl number of the gas (Pr), which is the ratio of molecular diffusivity of momentum and molecular diffusivity of heat. For most simulations reported in this thesis, we take $Pr = 1$ which is close to that of air. The effect of varying Pr will be considered for some specific cases.

Following Harada (1980*a*), the governing equations are written in terms of a new variable $\bar{\rho}$

$$\bar{\rho} = \rho r, \tag{2.6}$$

The governing equations in terms of $\bar{\rho}$ and casted for azimuthally-invariant $[\partial/\partial\theta(\cdot) = 0]$ flows are as follows:

$$\frac{\partial \bar{\rho}}{\partial t}+\frac{\partial}{\partial r}(\bar{\rho}u)+\frac{\partial}{\partial z}(\bar{\rho}w)=0, \tag{2.7}$$

$$\begin{aligned}
&\frac{\partial(\bar{\rho}u)}{\partial t}+\frac{\partial}{\partial r}[u(\bar{\rho}u)]+\frac{\partial}{\partial z}[w(\bar{\rho}u)]-\frac{\bar{\rho}v^2}{r}\\
&=r\Bigg[-\frac{Re^2}{Ma^2}\left(\frac{\partial p}{\partial r}\right)+\mu\left(\frac{\partial^2 u}{\partial r^2}+\frac{\partial^2 u}{\partial z^2}+\frac{\partial}{\partial r}\left(\frac{u}{r}\right)\right.\\
&\left.+\frac{1}{3}\frac{\partial}{\partial r}\left(\frac{1}{r}\frac{\partial(ru)}{\partial r}+\frac{\partial w}{\partial z}\right)\right)-\frac{2}{3}\left(\frac{1}{r}\frac{\partial(ru)}{\partial r}+\frac{\partial w}{\partial z}\right)\left(\frac{\partial \mu}{\partial r}\right)\\
&+\left(\frac{\partial \mu}{\partial r}\frac{\partial u}{\partial r}+\frac{\partial \mu}{\partial z}\frac{\partial u}{\partial z}\right)+\left(\frac{\partial \mu}{\partial r}\frac{\partial u}{\partial r}+\frac{\partial \mu}{\partial z}\frac{\partial w}{\partial r}\right)\Bigg],
\end{aligned} \tag{2.8}$$

$$\begin{aligned}
&\frac{\partial(\bar{\rho}v)}{\partial t}+\frac{\partial}{\partial r}[u(\bar{\rho}v)]+\frac{\partial}{\partial z}[w(\bar{\rho}v)]+\frac{\bar{\rho}uv}{r}\\
&=r\left[\mu\left(\frac{\partial^2 v}{\partial r^2}+\frac{\partial^2 v}{\partial z^2}+\frac{\partial}{\partial r}\left(\frac{v}{r}\right)\right)+\left(\frac{\partial \mu}{\partial r}\frac{\partial v}{\partial r}+\frac{\partial \mu}{\partial z}\frac{\partial v}{\partial z}\right)-\frac{v}{r}\frac{\partial \mu}{\partial r}\right],
\end{aligned} \tag{2.9}$$

$$\begin{aligned}
&\frac{\partial(\bar{\rho}w)}{\partial t}+\frac{\partial}{\partial r}[u(\bar{\rho}w)]+\frac{\partial}{\partial z}[w(\bar{\rho}w)]\\
&=r\Bigg[-\frac{Re^2}{Ma^2}\left(\frac{\partial p}{\partial z}\right)+\mu\Bigg(\left(\frac{\partial^2 w}{\partial r^2}+\frac{\partial^2 w}{\partial z^2}+\frac{1}{r}\frac{\partial w}{\partial r}\right)\\
&+\frac{1}{3}\frac{\partial}{\partial z}\left(\frac{1}{r}\frac{\partial(ru)}{\partial r}+\frac{\partial w}{\partial z}\right)\Bigg)-\frac{2}{3}\left(\frac{1}{r}\frac{\partial(ru)}{\partial r}+\frac{\partial w}{\partial z}\right)\frac{\partial \mu}{\partial z}\\
&+\left(\frac{\partial \mu}{\partial r}\frac{\partial w}{\partial r}+\frac{\partial \mu}{\partial z}\frac{\partial w}{\partial z}\right)+\left(\frac{\partial \mu}{\partial r}\frac{\partial u}{\partial z}+\frac{\partial \mu}{\partial z}\frac{\partial w}{\partial z}\right)\Bigg],
\end{aligned} \tag{2.10}$$

$$\begin{aligned}
&\frac{\partial(\bar{\rho}T)}{\partial t}+\frac{\partial}{\partial r}[(\bar{\rho}u)T]+\frac{\partial}{\partial z}[(\bar{\rho}w)T]\\
&=-(\gamma-1)pr\left(\frac{1}{r}\frac{\partial(ru)}{\partial r}+\frac{\partial w}{\partial z}\right)+r\gamma\Bigg[\kappa\left(\frac{1}{r}\frac{\partial}{\partial r}\left(r\frac{\partial T}{\partial r}\right)+\frac{\partial^2 T}{\partial z^2}\right)\\
&+\left(\frac{\partial T}{\partial r}\frac{\partial \kappa}{\partial r}+\frac{\partial T}{\partial z}\frac{\partial \kappa}{\partial z}\right)\Bigg]+r(\gamma-1)\frac{Ma^2}{Re^2}\Phi,
\end{aligned} \tag{2.11}$$

where

$$\begin{aligned}\Phi &= \mu\left[2e_{ij}e_{ij} - \frac{2}{3}(\nabla\cdot u)^2\right] \\ &= \mu\left[\left\{2\left(\frac{\partial u}{\partial r}\right)^2 + 2\left(\frac{u}{r}\right)^2 + 2\left(\frac{\partial w}{\partial z}\right)^2 + \left(\frac{\partial v}{\partial r} - \frac{v}{r}\right)^2 + \left(\frac{\partial u}{\partial z} + \frac{\partial w}{\partial r}\right)^2 + \left(\frac{\partial v}{\partial z}\right)^2\right\}\right. \\ &\left. - \frac{2}{3}\left\{\frac{1}{r^2}\left(\frac{\partial (ru)}{\partial r}\right)^2 + \left(\frac{\partial w}{\partial z}\right)^2 + \frac{2}{r}\frac{\partial (ru)}{\partial r}\frac{\partial w}{\partial z}\right\}\right].\end{aligned} \tag{2.12}$$

is the viscous dissipation.
The equation of state is

$$p = \frac{\bar{\rho}T}{r} \tag{2.13}$$

2.2.2 Dimensionless initial and boundary conditions

Computations were initialised from the rest state $(u = v = w = 0)$, unit density and temperature $(\rho, T = 1)$ for all reported runs. The boundary conditions for velocities, (u, v, w), is no-slip at the walls of the cylinder and the temperature, T, admits Dirichlet boundary conditions. The inner and outer cylinders are placed at the dimensionless radial location of $r_1 = \frac{\eta}{(1-\eta)}$ and $r_2 = \frac{1}{(1-\eta)}$, respectively, where

$$\eta = \frac{r_1}{r_2} \tag{2.14}$$

is the radius ratio. The dimensionless boundary conditions can be written as follows -

$$u = 0, \quad w = 0 \quad \text{at} \quad r_1 = \frac{\eta}{(1-\eta)} \quad \text{and} \quad r_2 = \frac{1}{(1-\eta)} \tag{2.15}$$

$$v = Re \quad \text{at} \quad r_1 = \frac{\eta}{(1-\eta)}; \qquad v = 0 \quad \text{at} \quad r_2 = \frac{1}{(1-\eta)} \tag{2.16}$$

$$T = 1 \quad \text{at} \quad r_1 = \frac{\eta}{(1-\eta)}; \qquad T = \frac{T_2}{T_1} = \chi \quad \text{at} \quad r_2 = \frac{1}{(1-\eta)} \tag{2.17}$$

Note that, while varying the gap-width (δ), we change the radial location of outer cylinder, $(r = r_2)$, but keep the inner cylinder fixed at $r = r_1 = 1$. Effectively, the inner and outer cylinders are placed radially at $r_1 = 1$ and $r_2 = 1/\eta$. One has to account for the fact that changing $\eta = 0.3$ to 0.8 at a constant cylinder height amounts to change in aspect ratio $(\Gamma = h/\delta)$ from $\Gamma(\eta = 0.3) = 0.673$ to $\Gamma(\eta = 0.8) = 6.283$. This protocol, however, changes the length-scale of the problem, initially being the gap-width between two cylinders (δ), later being the radius of the inner cylinder (r_1). This change is accounted for in the Reynolds number (Re), in Eqn.(3.1) and has been discussed in detail in the section 4.1.

2.3 Numerical Method

A variant of the finite difference method used by Harada (1980*a*) is adapted. The details of the numerical implementation are described in Aghor (2018). We discretize the spatial derivatives with central-difference scheme of second order accuracy and a donor-cell technique is used for the convective derivatives which provides numerical stability. An explicit scheme of Dufort-Frankel leapfrog type of second order accuracy is used for both the time derivatives and diffusive terms. A staggered grid is used in which the scalar variables are defined at the center of each cell; the axial and radial components of velocity(mass-flux), $w(\bar{\rho}w)$ and $u(\bar{\rho}u)$ are defined at the midpoints of the axial and radial cell edges, respectively. The azimuthal component of velocity(mass-flux) $v(\bar{\rho}v)$ is defined at the same point as $u(\bar{\rho}u)$. continuity

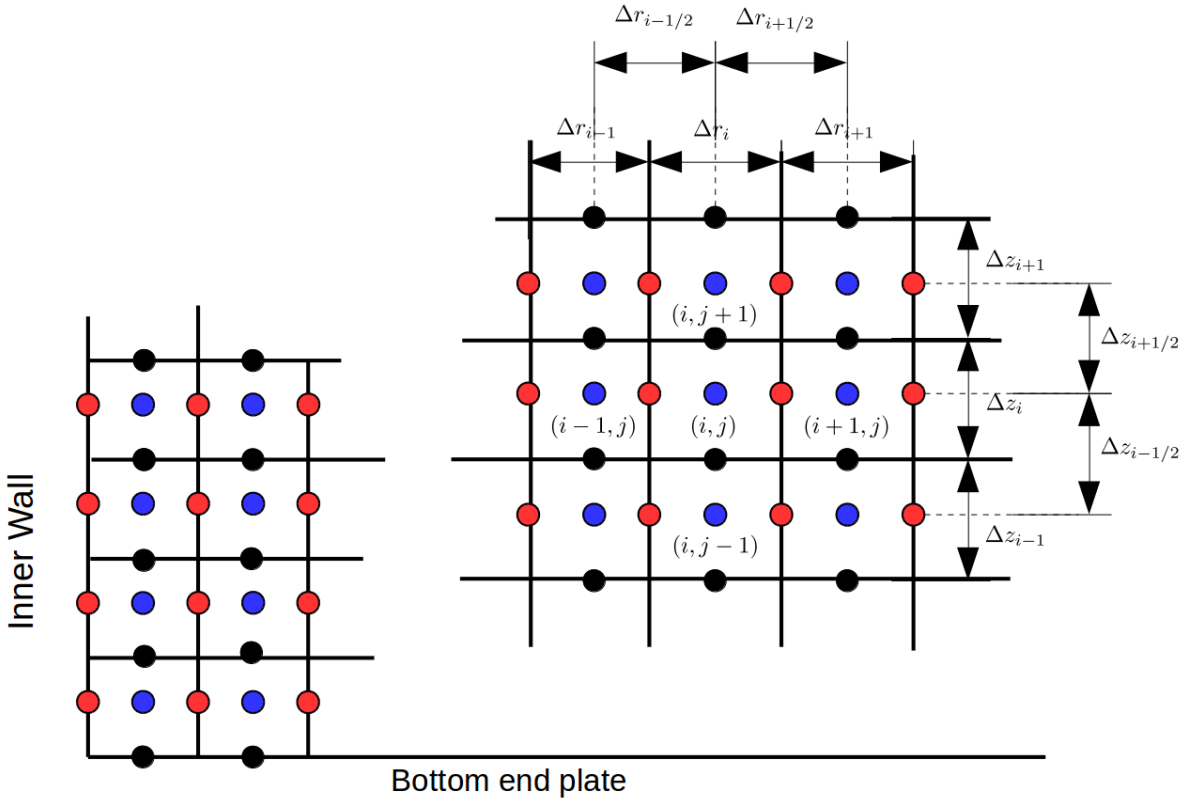

Fig. 2.2 Schematic diagram of grid points; $\bar{\rho}$ and T are defined at the center of the cell at the blue filled circles, u or $\bar{\rho}u$ and v or $\bar{\rho}v$ at the side faces at the red filled circles and w or $\bar{\rho}w$ at the top and bottom of the cell at the black filled circles, This arrangement of grids have been adapted from Harada (1980*a*) and Hyun & Park (1992).

equation:

$$\frac{\bar{\rho}^{n+1} - \bar{\rho}^{n-1}}{2\Delta t} = -[\delta_r(\bar{\rho}u)^{n+1} + \delta_z(\bar{\rho}w)^{n+1}], \tag{2.18}$$

r - momentum equation:

$$\begin{aligned}\frac{(\bar{\rho}u)^{n+1}-(\bar{\rho}u)^{n-1}}{2\Delta t} &= -[\delta_r(\bar{\rho}uu)+\delta_z(\bar{\rho}uw)]^n+\left(\frac{\bar{\rho}v^2}{r}\right)^n \\ &+\Bigg[-\frac{Re^2}{Ma^2}\delta_r p^n+\mu^n\Bigg(\delta_r\delta_r u^{\bar{n}}+\delta_z\delta_z u^{\bar{n}}+\delta_r\left(\frac{u}{r}\right)^n \\ &+\frac{1}{3}\delta_r\Bigg(\delta_r u^{\bar{n}}+\left(\frac{u}{r}\right)^n+\delta_z w^n\Bigg)\Bigg)-\frac{2}{3}\Bigg(\delta_r u^n+\left(\frac{u}{r}\right)^n \\ &+\delta_z w^n\Bigg)\delta_r\mu^n+2\delta_r\mu^n\delta_r u^n+\delta_z\mu^n(\delta_z u^n+\delta_r w^n)\Bigg], \qquad (2.19)\end{aligned}$$

θ - momentum Balance:

$$\begin{aligned}\frac{(\bar{\rho}v)^{n+1}-(\bar{\rho}v)^{n-1}}{2\Delta t} &= -[\delta_r(\bar{\rho}uv)+\delta_z(\bar{\rho}vw)]^n-\left(\frac{\bar{\rho}uv}{r}\right)^n \\ &+r\Bigg[\mu^n\Bigg(\delta_r\delta_r v^{\bar{n}}+\delta_z\delta_z v^{\bar{n}}+\delta_r\left(\frac{v}{r}\right)^n\Bigg)+\delta_r\mu^n.\delta_r v^n \\ &+\delta_z\mu^n.\delta_z v^n-\left(\frac{v}{r}\right)^n\delta_r\mu^n\Bigg], \qquad (2.20)\end{aligned}$$

z - momentum Balance:

$$\begin{aligned}\frac{(\bar{\rho}w)^{n+1}-(\bar{\rho}w)^{n-1}}{2\Delta t} &= -[\delta_r(\bar{\rho}uw)+\delta_z(\bar{\rho}ww)]^n+\Bigg[-\frac{Re^2}{Ma^2}\delta_z p^n+\mu^n\Bigg(\delta_r\delta_r w^{\bar{n}} \\ &+\delta_z\delta_z w^{\bar{n}}+\frac{1}{r}.\delta_r w^n+\frac{1}{3}\delta_z\Bigg(\delta_r u^n+\left(\frac{u}{r}\right)^n+\delta_z w^{\bar{n}}\Bigg)\Bigg) \\ &-\frac{2}{3}\Bigg(\left(\frac{u}{r}\right)^n+\delta_r u^n+\delta_z w^n\Bigg).\delta_z\mu^n+\delta_r\mu^n.\Bigg(\delta_r w^n+\delta_z u^n\Bigg) \\ &+2\delta_z\mu^n\delta_z w^n\Bigg], \qquad (2.21)\end{aligned}$$

energy equation:

$$\begin{aligned}\frac{(\bar{\rho}T)^{n+1}-(\bar{\rho}T)^{n-1}}{2\Delta t} &= -[\delta_r(\bar{\rho}u)^{n+1}T^n+\delta_z(\bar{\rho}w)^{n+1}T^n]+r(\gamma-1)\Bigg(-p^{n+1}\Bigg(\delta_r u^n+\left(\frac{u}{r}\right)^n \\ &+\delta_z w^n\Bigg)+r\gamma\Bigg[\kappa\Bigg(\delta_r\delta_r T^{\bar{n}}+\frac{1}{r}\delta_r T^n+\delta_z\delta_z T^{\bar{n}}\Bigg)+\delta_r T^n.\delta_r\kappa^n+\delta_z T^n\delta_z\kappa^n\Bigg] \\ &+r(\gamma-1)\frac{Ma^2}{Re^2}\Phi, \qquad (2.22)\end{aligned}$$

where,

$$\Phi^n = \mu^n \left[2e_{ij}e_{ij} - \frac{2}{3}(\nabla \cdot u)^2 \right]^n$$
$$= \mu^n \left[\left\{ 2\left(\frac{\partial u^n}{\partial r}\right)^2 + 2\left(\frac{u^n}{r}\right)^2 + 2\left(\frac{\partial w^n}{\partial z}\right)^2 + \left(\frac{\partial v^n}{\partial r} - \frac{v^n}{r}\right)^2 + \left(\frac{\partial u^n}{\partial z} + \frac{\partial w^n}{\partial r}\right)^2 \right. \right. \quad (2.23)$$
$$\left. \left. + \left(\frac{\partial v^n}{\partial z}\right)^2 \right\} - \frac{2}{3}\left\{ \frac{1}{r^2}\left(\frac{\partial (ru^n)}{\partial r}\right)^2 + \left(\frac{\partial w^n}{\partial z}\right)^2 + \frac{2}{r}\frac{\partial (ru^n)}{\partial r}\frac{\partial w^n}{\partial z} \right\} \right].$$

$$p^{n+1} = \frac{(\bar{\rho}T)^{n+1}}{r}. \quad (2.24)$$

For any arbitrary physical quantity Θ,

$$\delta_r \Theta_i = \frac{\Theta_{i+\frac{1}{2}} - \Theta_{i-\frac{1}{2}}}{\Delta r_i} \quad (2.25)$$

where δ_r is used to represent δ_r and δ_z and Δr_i denotes the grid spacing between two consecutive grid points, which can be either Δr_i or Δz_i, portraying the grid spacing in radial and axial directions, respectively.

$$\delta_r \delta_r \Theta^{\bar{n}} = \frac{1}{\Delta r_i}\left[\frac{(\Theta_{i+1} - \bar{\Theta}_i)}{\Delta r_{i+1/2}} - \frac{(\bar{\Theta}_i - \Theta_{i-1})}{\Delta x_{i-1/2}} \right]^n \quad (2.26)$$

$$\bar{\Theta}^n = \frac{(\Theta_i^{n+1} - \Theta_i^{n-1})}{2}, \quad (2.27)$$

$$\Delta r_{i+1/2} = \frac{(\Delta r_i + \Delta r_{i+1})}{2}, \quad (2.28)$$

and

$$\Delta r_i = \frac{(\Delta r_{i+1/2} + \Delta x_{i-1/2})}{2}, \quad (2.29)$$

where Θ can be anything between u, v, w, $\bar{\rho}$, $\bar{\rho}u, \bar{\rho}v, \bar{\rho}w$, T, p, μ and κ. In the current investigations $\Delta r_i = \Delta x_{i-1/2} = \Delta r_{i+1/2}$, as a result of uniform grid.

The solution procedure after finite difference formulation is as follows Harada (1980*a*), Hyun & Park (1992) and Aghor (2018)-

1. We substitute $\Theta^1 = \Theta^0$ as the computational initial condition and Θ can be $u, v, w, \bar{\rho}, T, p$
2. Mass velocities $(\bar{\rho}u)^{n+1}$, $(\bar{\rho}v)^{n+1}$, $(\bar{\rho}w)^{n+1}$ to be computed from momentum equations (2.8)-(2.10).

3. Volume fraction $\bar{\rho}^{n+1}$ is computed from the continuity equation (2.7).

4. The pressure, p^{n+1} (2.13) is computed from the energy equation (3.3).

5. The values of u^{n+1}, v^{n+1}, w^{n+1}, T^{n+1} are computed by dividing $(\bar{\rho}u)^{n+1}$, $(\bar{\rho}v)^{n+1}$, $(\bar{\rho}w)^{n+1}$, $(\bar{\rho}T)^{n+1}$ by $\bar{\rho}^{n+1}$.

6. To avoid computational splitting caused by leapfrog scheme, as described in Harada (1980*a*), filter after every m time steps is used according to the following equation-

$$\Theta^{n\pm1/2} = \frac{(\Theta^{n} + \Theta^{n\pm1})}{2}$$

   In the present simulations, $m = 11$, and results are invariant for $m = 21$ and $m = 31$; fig 2.3 illustrates the comparison of radial-axial velocity (u,w) spectra at the mid-height mid-gap of the Taylor-Couette cell using different values of the computational filter, m = 11,21 and 31 for different Reynolds number. (a) $Re = 300$, (b) $Re = 410$ and (c) $Re = 500$.

7. The steps $(ii) - (vii)$ are repeated with time marching until the kinetic energy of the system saturates to some constant value.

In order to analyse the steady state of the system, we use the average quantities, defined as volume integral over $(r-z)$ section of the cylindrical annulus (Harada, 1980*a*) by

$$\langle \phi \rangle = 2\pi \sum_{1}^{\frac{1}{\eta}} \sum_{0}^{\frac{2\pi}{k}} \Theta r \Delta r \Delta z, \tag{2.30}$$

where N_r and N_z denotes the number of grids in radial (r) and axial (z) directions. Δr and Δz are respective grid spacing in r and z directions. The average grid-independent kinetic energies are calculated -

$$KE_u = \langle \frac{1}{2}\rho u^2 \rangle \quad \text{and} \quad KE_v = \langle \frac{1}{2}\rho v^2 \rangle \quad \text{and} \quad KE_w = \langle \frac{1}{2}\rho w^2 \rangle \tag{2.31a,b,c}$$

and the total kinetic energy of the system is given by,

$$KE_{total} = KE_u + KE_v + KE_w. \tag{2.32}$$

The dimensionless height of computational domain is chosen to be $h = 2\pi/k$, where $k = 2\pi/\lambda_f$ and λ_f is the wavelength of fastest growing mode obtained from the linear stability

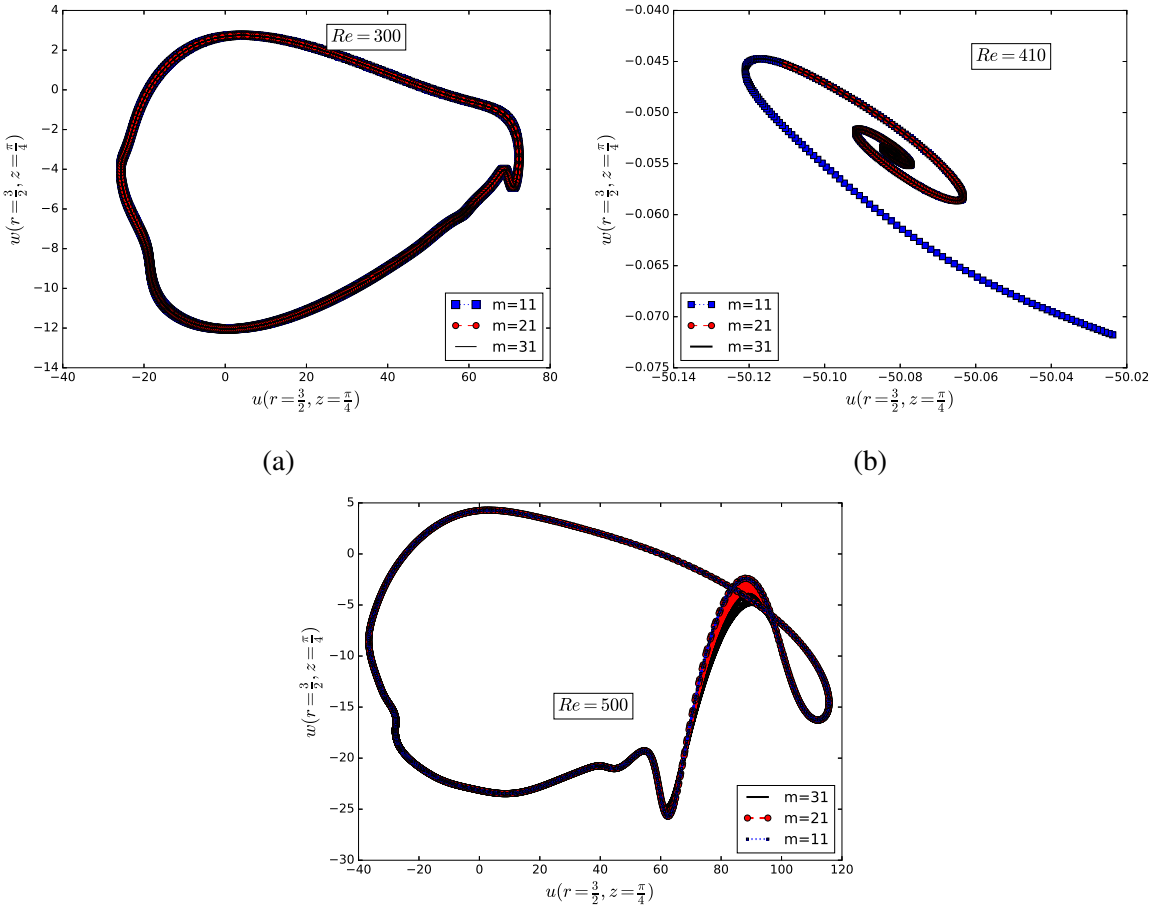

Fig. 2.3 Comparison of radial-axial velocity (u,w) spectra at the mid-height mid-gap using different values of computational filter, $m = 11, 21$ and 31 for various Re; (a) $Re = 300$, (b) $Re = 410$ and (c) $Re = 500$

of compressible TCF (Welsh *et al.*, 2014). For all simulations, we set $k = 4$, resulting in the dimensionless length of computational domain to be $\pi/2$. The aspect ratio (Γ) can be written as a function of the radius ratio η as

$$\Gamma = \frac{\pi\eta}{2(1-\eta)}. \tag{2.33}$$

2.4 Validation of the Code

2.4.1 Base state validation of compressible TCF

For time-independent and fully developed circular Couette flow (*CCF*), the base state velocity, density and temperature are given by

$$u = (u^0, v^0, w^0), \quad \rho^0 \quad \text{and} \quad T^0. \tag{2.34}$$

The analytical solution of the base state of compressible TCF has been derived by Welsh *et al.* (2014). In order to find the base state from (2.7)-(2.13) with appropriate boundary conditions, we look for a solution with $u^0 = w^0 = 0$ and $v^0 = v^0(r)$. The azimuthal velocity is taken as (Chandrasekhar, 1960),

$$v^0(r) = C_1 r + \frac{C_2}{r}, \tag{2.35}$$

where

$$C_1 = Re\frac{\Omega - \eta^2}{\eta(1+\eta)} \qquad \text{and} \qquad C_2 = Re\frac{\eta(1-\Omega)}{(1-\eta)(1-\eta^2)}. \tag{4.2a,b}$$

where the rotation-ratio is $\Omega = \omega_2/\omega_1$. The base state temperature profile is obtained by solving the following equation (Welsh *et al.*, 2014)

$$\frac{1}{r}\frac{d}{dr}\left(r\frac{dT^0}{dr}\right) + \frac{\gamma-1}{\gamma}\frac{PrMa^2}{Re^2}\left[r\frac{d}{dr}\left(\frac{v^0}{r}\right)\right]^2 = 0, \tag{2.37}$$

which yields

$$T^0 = \chi + \frac{\gamma-1}{\gamma}\frac{PrMa^2}{Re_1^2}C_2^2\left(C_3\ln r - \frac{1}{r^2} + C_4\right) + (1-\chi)\frac{\ln[r(1-\eta)]}{\ln\eta}, \tag{2.38}$$

with

$$C_3 = \frac{(1-\eta^2)(1-\eta)^2}{\eta^2\ln\eta} \qquad \text{and} \qquad C_4 = (1-\eta^2)\left[1 + \frac{1-\eta^2}{\eta^2}\frac{\ln(1-\eta)}{\ln\eta}\right]. \tag{4.5a,b}$$

being integration constants and $\chi = T_2/T_1$. Following Welsh *et al.* (2014), in order to compute for the base state density profile, we need to form a governing equation for density in terms of

a boundary value problem. We define local density as

$$\rho^0(r) = \frac{1}{2\pi r}\frac{dm(r)}{dr}, \tag{2.40}$$

where

$$m(r) = 2\pi \sum_{1}^{r} r\rho^0(r)\Delta r. \tag{2.41}$$

For the base state (2.34), the r - momentum equation (Eqn. 2.8) reduces to

$$\frac{Ma^2}{Re^2}\left(\frac{(v^0)^2}{rT^0}\right) = \frac{1}{T^0}\frac{\partial T^0}{\partial r} + \frac{1}{\rho^0}\frac{\partial \rho^0}{\partial r}. \tag{2.42}$$

Substitution of Eqn. (2.40) into Eqn. (2.42) yields the second order boundary value problem,

$$\frac{d^2m}{dr^2} + \left[\frac{1}{T^0}\frac{dT^0}{dr} - \frac{Ma^2}{Re^2}\left(\frac{(v^0)^2}{rT^0}\right) - \frac{1}{r}\right]\frac{dm}{dr} = 0, \tag{2.43}$$

subjected to the following boundary conditions,

$$m(r_1 = \eta/(1-\eta)) = 0 \qquad \text{and} \qquad m(r_2 = 1/(1-\eta)) = \pi\left[(1/(1-\eta))^2 - (\eta/(1-\eta))^2\right]. \tag{3.12a,b}$$

Equations (2.43 - 2.44) have been solved numerically, and the base state density is determined from (2.40).

Figure 2.4 shows the base state validation of compressible TCF against the work by Welsh *et al.* (2014) for $Pr = 1$. Figures $(a), (b)$ and (c) shows variation of the base state profiles of velocity (v^0), density (ρ^0) and temperature (T^0) with $Ma \in [0.01, 3]$ for different values of critical Reynolds number (Re^{cr}) for the purely azimuthal CCF to TVF, respectively. The incompressible limit for code validation has been taken as $Ma = 0.01$ since it is practically not feasible to run simulations below this value of Ma. However, for the incompressible limit simulations for higher Re (well beyond CCF), we admit $Ma = 0.1$. The height (h) of the computational domain used is $2\pi/k$, and we choose to employ the axial wavenumber (k), $k = 4$, for all the simulations reported in this current dissertation. This particular value of k was chosen in order to ensure that we get the base state values unambiguously and can match with the linear stability results of Welsh *et al.* (2014). In the $Ma = 0.01$, the constant temperature (T^0) and density (ρ^0) profiles are found and match well with the incompressible Re for CCF to TVF

transition. With increasing Ma, the primary effect is observed in the radial density profiles (see panel (b) of figure 2.4 between the two walls. Notice that, density near the inner cylinder is less compared to the density at the outer wall. This attributed to the fact that the centrifugal forces are very high near the inner cylinder compared to the outer cylinder, as a result of which asymmetry in radial density profile is manifested. The panel (c) of figure 2.4 shows the temperature variations along the radial direction. Note that, a hump in the temperature profile is developed with increasing Ma. Since, we employ isothermal walls (which acts as a thermostat), viscous dissipation takes place which is manifested in the temperature profiles. This viscous dissipation in the energy equation is enhanced with increasing Ma, see the base state energy equation:

$$\frac{\gamma}{Pr}\left(\frac{1}{r}\frac{\partial}{\partial r}\left(r\frac{\partial T}{\partial r}\right)\right)+(\gamma-1)\frac{Ma^2}{Re^2}\left(\frac{\partial v}{\partial r}-\frac{v}{r}\right)^2=0. \tag{2.45}$$

Hence, the radial gradient in the temperature field increases with increasing Ma, and is evident from the solid lines (red and black) in the panel (c) of figure 2.4.

Panels $(a),(b)$ and (c) of figure 2.5 portrays base state profiles of velocity (v^0), density (ρ^0) and temperature (T^0) for $Ma=1$, variation with $Pr\in[1,15]$, respectively. It is noted from Fig 2.5, (c) the gradients in temperature increase with increasing Pr for a given Ma number, which can be explained from the equation (2.45), and the $\nabla T\propto Pr$. Because of high temperature gradients, the fluid expands locally and causes a depletion in the local density, see Fig 2.5 (b).

2.4.2 Validation of effective-Nusselt number: incompressible Taylor-Couette flow

The second code validation was done to compare effective-Nusselt number (Nu_ω) obtained from the torque measurements in incompressible TCF via DNS studies of Pirro & Quadrio (2008), Fasel & Booz (1984) and Ostilla *et al.* (2013). In *CCF* regime, the radial $(u=0)$ and axial velocities $(w=0)$ over the domain is zero and the base flow is purely azimuthal, resulting in only molecular transport of angular momentum $(\mathscr{L})$. With the onset of Taylor vortices, both radial $(u>0)$ and axial velocities $(w>0)$ become non-zero giving rise to large scale circulation in the (r,z) plane which increases with increasing Re. The convective transport of angular momentum comes into motion and with increasing Re, the convection effects become more pronounced. In analogous to the heat current in thermally driven Rayleigh Benard flow (RBF), Eckhardt *et al.* (2007) defined local angular momentum current(J^ω), which relates the sum of Reynolds stress $(<u,\omega>_{A(r),t})$ (convective transport) and the product of kinematic viscosity (ν) with the radial derivative of $<\omega>_{A(r),t}$ profile (molecular transport) as described

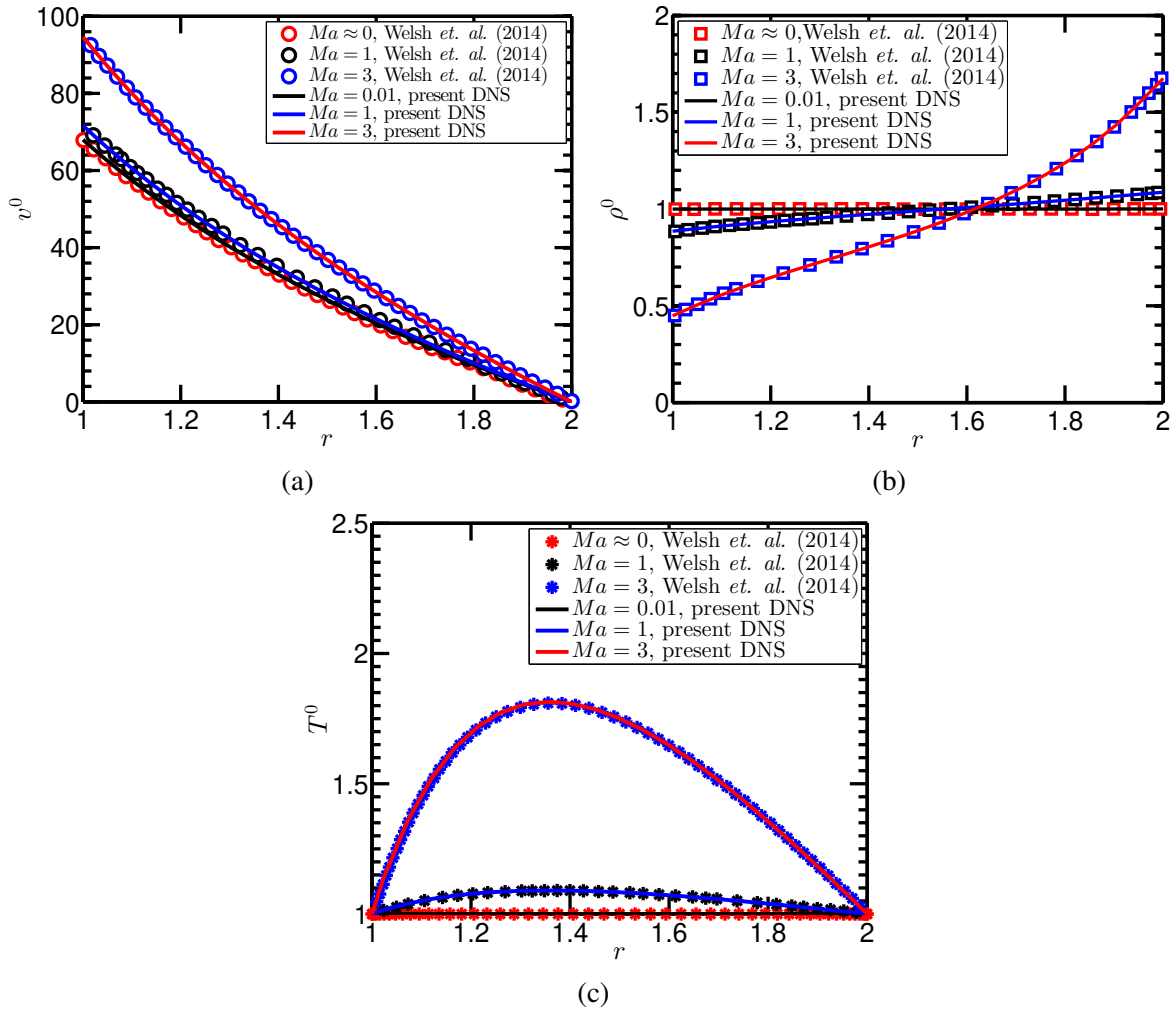

Fig. 2.4 Comparison of base state profiles of (a) velocity, (b) density and (c) temperature with variation in Ma for $Pr = 1$ respectively, with the results obtained by Welsh *et al.* (2014). The Re of the inner cylinder is close to its the critical value for their respective Ma and Pr $(Re \sim Re^{cr})$ and the outer cylinder is at rest $(\omega_2 = 0)$.

below -

$$J^{\omega} = r^3(\langle u\omega \rangle_{A(r),t} - \nu \frac{\partial}{\partial r}\langle \omega \rangle_{A(r),t}) \tag{2.46}$$

where, $\langle ... \rangle_{A(r),t}$ denotes a spatial average of cylindrical surface coaxial with the bounding cylinders of radius r, $(r_1 \leq r \leq r_2)$ and the temporal average. The first term in (2.46) denotes Reynolds stress and the second term is transverse derivative of averaged angular momentum $(\mathscr{L} = \rho v r)$, and is related to the dimensionless torque (Σ) , $\Sigma = 2\pi h \rho \nu^2 G$, where $G = \frac{J^{\omega}}{\nu^2}$. In the current problem, equation (2.46) reduces to -

$$J^{\omega} = r^3(\langle u\omega \rangle_t - \nu \frac{\partial}{\partial r}\langle \omega \rangle_t) \tag{2.47}$$

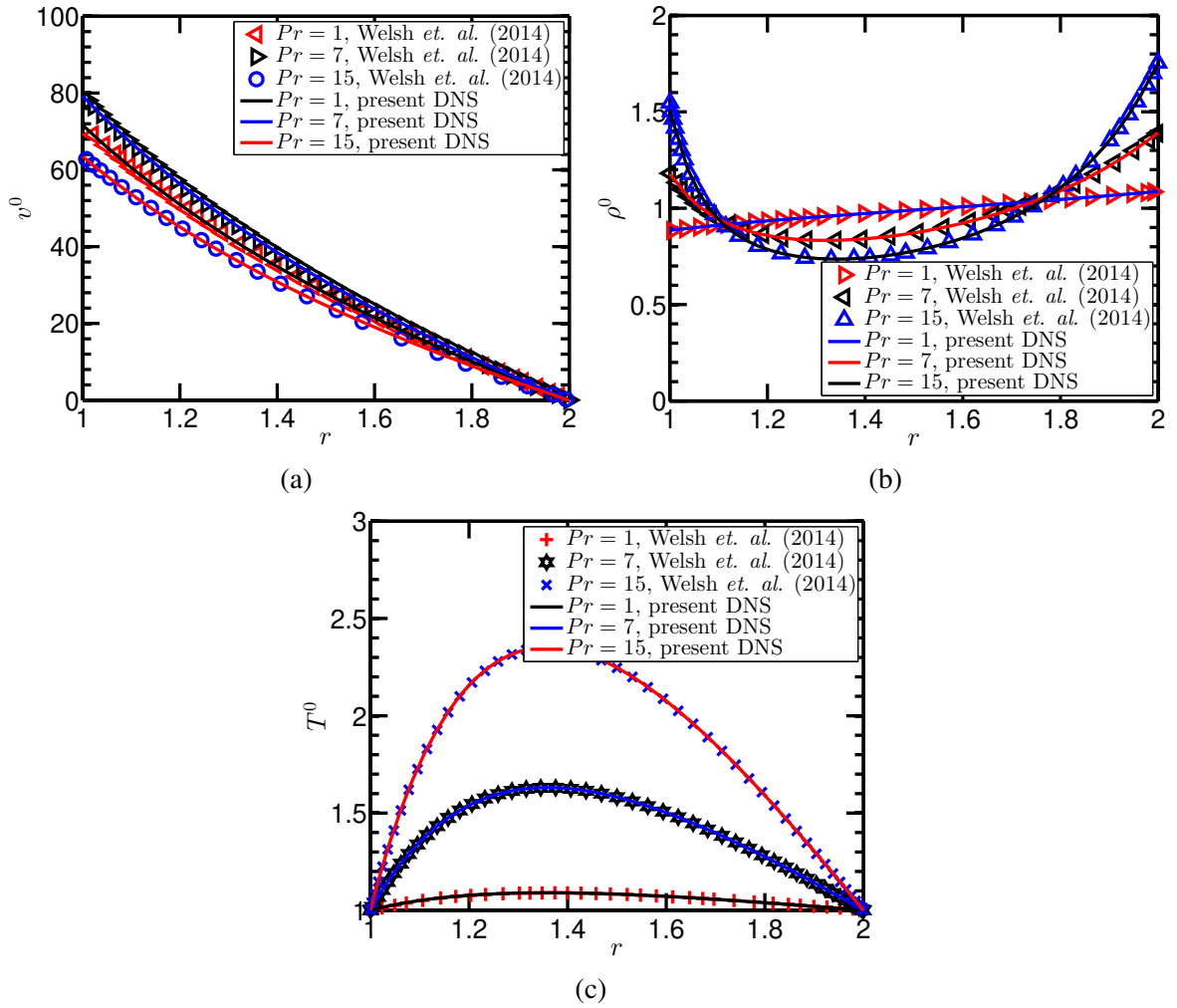

Fig. 2.5 Comparison of base state profiles of (a) velocity, (b) density and (c) temperature with variation in Pr for $Ma = 1$, respectively, with the results obtained by Welsh *et al.* (2014). The Re of the inner cylinder is close to its the critical value for their respective Ma and Pr $(Re \sim Re^{cr})$ and the outer cylinder is at rest $(\omega_2 = 0)$.

owing to the axisymmetric nature of the problem. In terms of azimuthal velocity (v),

$$J^{\omega} = r^3\left(\langle\frac{uv}{r}\rangle_t - \nu\frac{\partial}{\partial r}\langle\frac{v}{r}\rangle_t\right) = r^3\left(\langle\frac{uv}{r}\rangle_t - \nu\frac{\partial}{\partial r}\frac{\langle v\rangle_t}{r}\right)$$

Hence,

$$J^{\omega} = r^3\left(\langle\frac{uv}{r}\rangle_t - \nu\frac{1}{r}\frac{\partial\langle v\rangle_t}{\partial r} + \frac{\nu\langle v\rangle_t}{r^2}\right) \tag{2.48}$$

Re	Nu_ω (current work) $Ma = 0.1$	Nu_ω (Ostilla *et al.* (2013)) $Ma = 0.0$	Nu_ω (PQ08)	Nu_ω (FB84)	% deviation from Ostilla *et al.* (2013)
60	0.9919	1.0005	1.0000	1.0000	-0.859
68	0.9920	1.0006	1.0000	1.0000	-0.869
70	1.0218	1.0235	1.0238	1.0237	-0.17
75	1.0857	1.0835	1.0834	1.0833	+0.22
80	1.1415	1.1375	1.1372	1.1371	+0.4

Table 2.1 Comparison of Nu_ω for $\Gamma = 2$, $\eta = 0.5$ and $Re_o = 0$ and $Ma = 0.1$ with their incompressible counterpart provided by Ostilla *et al.* (2013), PQ08 (Pirro & Quadrio, 2008) and FB84 (Fasel & Booz, 1984).

The laminar value of local angular momentum current (J_l^ω), is given by

$$J_l^\omega = 2\nu\omega_1 \frac{r_1^2 r_2^2}{r_2^2 - r_1^2} = \frac{2\nu v_1 r_1}{1-\eta^2} \tag{2.49}$$

The effective-Nusselt number (Nu_ω) is given by

$$Nu_\omega = J^\omega / J_l^\omega \tag{2.50}$$

The comparison of Nu_ω near inner cylinder has been done in a range identical to Ostilla *et al.* (2013) (between $60 \leq Re \leq 80$) and provided in the Table 2.1. The geometry of setup for the code validation was chose to be $\Gamma = 2$ and $\eta = 0.5$ which was different from $\Gamma = \pi/2$ for $\eta = 0.5$ used in rest of the simulations in the present study. The number of grids ($N_z \times N_r$) was 61×61 whereas in the DNS studies of Ostilla *et al.* (2013), Pirro & Quadrio (2008) and Fasel & Booz (1984), the number of grids chosen was 64×64. In the CCF, for $Re = 60$ and 68, we observe the Nu_ω predicted by our code is less than Ostilla *et al.* (2013) by 0.86 % and for $Re = 75$ it is more by 0.2 %. Since the variations of Nu_ω with Ostilla *et al.* (2013) are well within 1%, we successfully validate our code. Henceforth, $Ma = 0.1$ serves as good test case for incompressible Taylor-Couette.

2.4.3 Code validation at low and high Prandtl limit

Most of the geophysical examples admit Prandtl number ($Pr = \nu/\alpha$, where ν is the kinematic viscosity and α is the thermal diffusivity) of $\mathcal{O}(1)$ for gases, $\mathcal{O}(10)$ for water, and $\mathcal{O}(10^4)$ for magma in volcanic flows. However, the in the limit of $Pr << 1$ is found the liquid metals ($Pr \sim$

$\mathscr{O}(10^{-3}-10^{-1})$) and astrophysical fluid flows like stellar interiors where $Pr \sim \mathscr{O}(10^{-9}-10^{-5})$ (see Garaud (2018)).

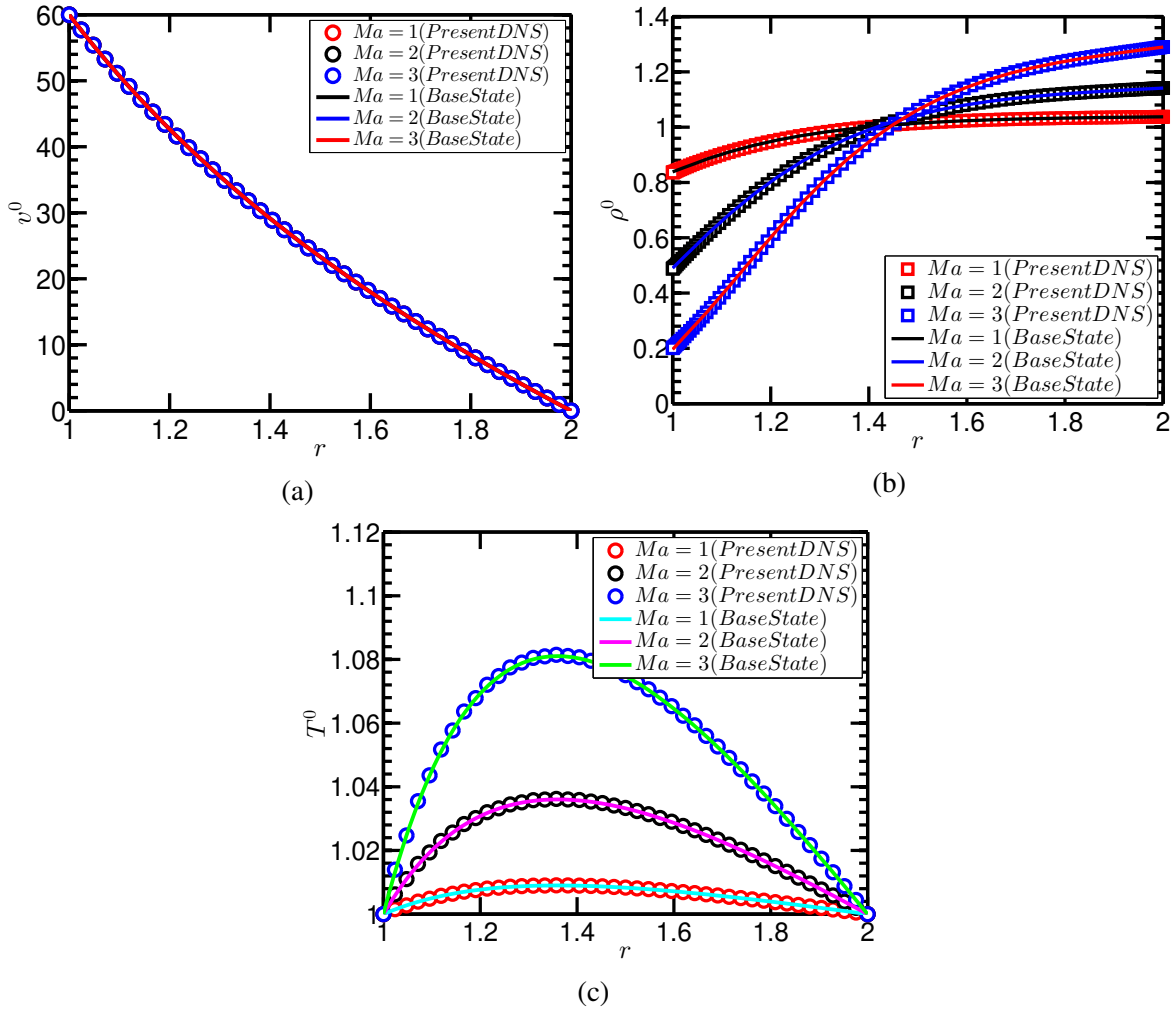

Fig. 2.6 Comparison of the base state profiles of (a) velocity, (b) density and (c) temperature with variation in Ma for $Pr = 0.1$, respectively, with the results obtained by the present DNS code. The Re of the inner cylinder is $Re = 60$ and the outer cylinder is at rest $(\omega_2 = 0)$.

Figure 2.6 illustrates comparison of the base state profiles of (a) velocity, (b) density and (c) temperature with variation in Ma for $Pr = 0.1$, respectively, with the results obtained by the present DNS code. The Re of the inner cylinder is $Re = 60$ and the outer cylinder is at rest $(\omega_2 = 0)$. From the base state energy equation, we find, that the heat conduction is balanced by the viscous dissipation. At low Pr, the conduction of the fluid in the gap between two cylinders dominate as a result of which increase in Ma enhances the viscous dissipation.

Figure 2.7 shows the comparison of the base state profiles of (a) velocity, (b) density and (c) temperature with variation in Ma for $Pr = 10$, respectively, with the results obtained by the

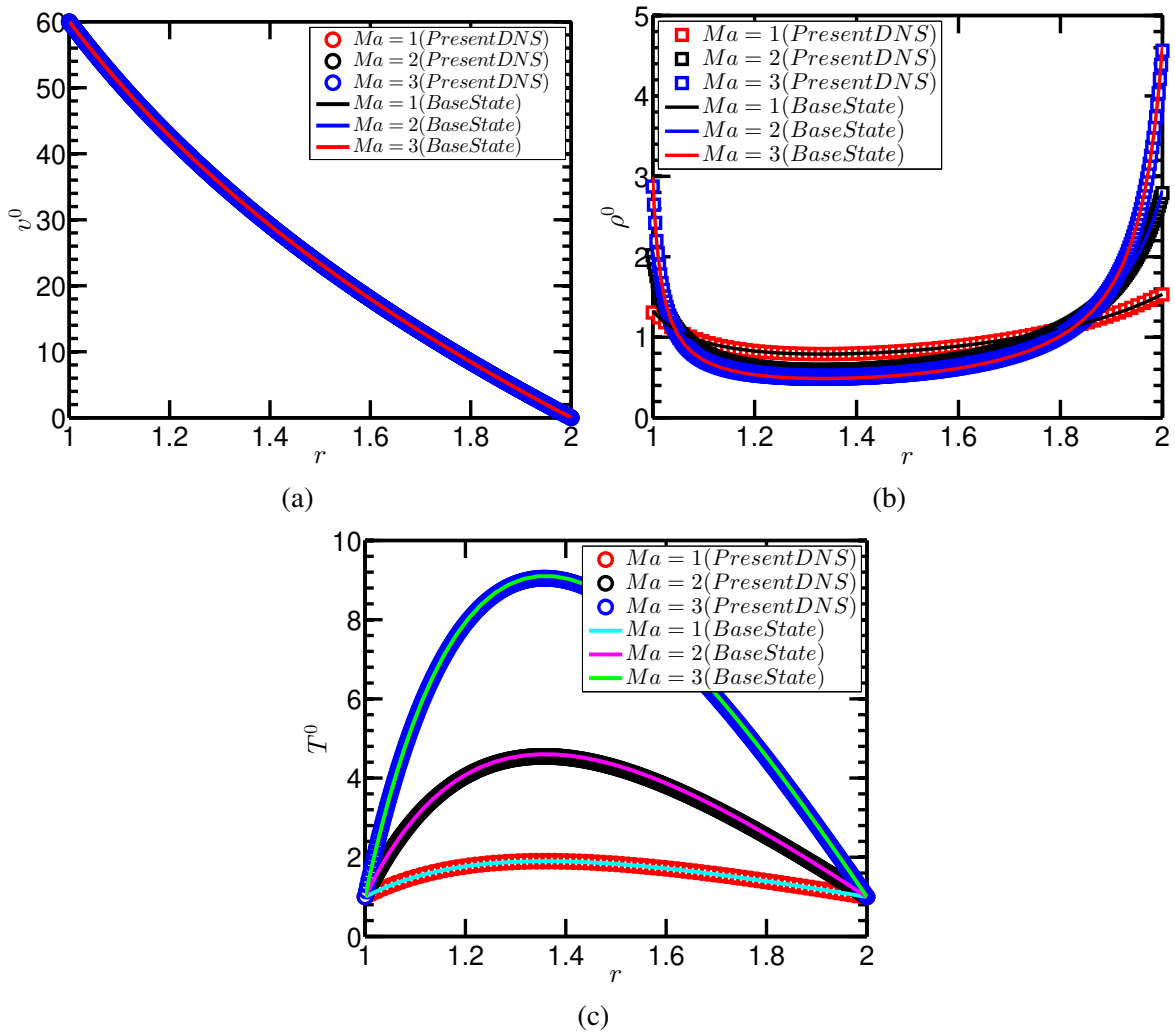

Fig. 2.7 Comparison of the base state profiles of (a) velocity, (b) density and (c) temperature with variation in Ma for $Pr = 10$, respectively, with the results obtained by the present DNS code. The Re of the inner cylinder is $Re = 60$ and the outer cylinder is at rest $(\omega_2 = 0)$.

present DNS code. The Re of the inner cylinder is 60 and the outer cylinder is at rest $(\omega_2 = 0)$. We use 201 grid points in the radial direction and 51 grid points in the axial direction and the completion time is 168 CPU hours. The necessity of using a large number of grid points in the radial direction is to resolve very thin thermal boundary layer compared to velocity boundary layer ($\alpha << \nu$, where $\alpha = \kappa/(\rho c_p)$ is the thermal diffusivity and ν is kinematic viscosity).

$$\frac{\gamma}{Pr}\left(\frac{1}{r}\frac{\partial}{\partial r}\left(r\frac{\partial T}{\partial r}\right)\right) + (\gamma - 1)\frac{Ma^2}{Re^2}\left(\frac{\partial v}{\partial r} - \frac{v}{r}\right)^2 = 0, \tag{2.51}$$

Figure 2.7 (b) shows the radial density variation at large Pr for a $Re = 60$. Following equation (2.51), we see large temperature gradients at higher Pr for a given Ma and Re, which results from the hot fluid near the mid-gap as compared to the boundaries, causing local thermal expansion and depletion of material. Invoking the equation of continuity, the fluid accumulates near the cylinder walls (both inner and outer wall) and causing the formation of negative density gradient near the inner cylinder. As pointed by Welsh *et al.* (2014), in the presence of the centrifugal forces acting on the fluid system in shear driven flow, this acts as an effective gravity from inner cylinder to outer cylinder. This configuration has the potential to setup Rayleigh–Taylor (RT) instabilities, where a heavy fluid layer sits on top of a lighter fluid layer and gravity acts downwards. Close to the outer cylinder wall, the radial density gradient is positive ($\frac{\partial \rho}{\partial r} > 0$), forming a stable stratification which can give rise to waves analogous to gravity waves.

2.5 Summary

In this Chapter, we have presented (i) the governing equations, consisting of time-dependent compressible Navier-Stokes equations along with the continuity and energy equations for a monoatomic perfect gas and (ii) the details of the numerical method. We employed no-slip and Dirichlet boundary conditions for velocity fields (u, v, w) and temperature field (T), respectively. Axially periodic boundary conditions are imposed and extensive code validation was presented considering (i) the base state of CCF and (ii) the effective Nusselt-number scaling in the TVF regime.

Chapter 3

Axisymmetric Compressible TCF: Effect of Mach Number on Patterns and Transport

3.1 Introduction

The genesis of Taylor vortices arising from the centrifugal instability in a fluid rotating between two coaxial cylinders is a paradigmatic problem in the hydrodynamic stability theory (Chandrasekhar, 1961; Drazin & Reid, 2004; Taylor, 1923). While the instability mechanism and pattern formation scenario in incompressible TCF is well understood, its compressible counterpart has been relatively less explored. The compressible analog of TCF is relevant in accretion disk flows (Balbus & Hawley, 1998) that admit high Mach number (Ma). Only a few studies have addressed the compressible TCF problem (Kuhlthau (1960), Kao & Chow (1992), Hatay *et al.* (1993), Manela & Frankel (2007), Welsh *et al.* (2014)) from linear stability analyses.

In this chapter, we seek to address the following questions: (i) How does the variation in Mach number (Ma), a measure of the compressibility of the fluid, affect the critical Reynolds number (Re^{cr}) for the onset of primary $(CCF \longrightarrow TVF)$ instability? (ii) Are there new patterns? (iii) What are the flow patterns at high Re? (iv) How does the frequencies of the travelling wave vary with Re and Ma? For all results, we set the radius ratio to $\eta = r_1/r_2 = 1/2$ and the Prandtl number is $Pr = 1$. The role of radius ratio on pattern transitions is considered in Chapter 4.

We define the Reynolds number (Re) at the inner cylinder to be :

$$Re = \frac{\omega_1 r_1 \delta}{\nu_r}, \tag{3.1}$$

where $\omega_1 r_1$ is the speed of the inner cylinder and $\delta = r_2 - r_1$ is the gap-width and ν_r is the kinematic viscosity of the gas. The peripheral Mach number (Ma) is defined as

$$Ma = \frac{Re}{c_{is}}, \tag{3.2}$$

where c_{is} is the isothermal sound speed defined via

$$c_{is}^2 = \frac{(c_p - c_v) T_r \delta^2}{\nu_r^2}$$

and the subscript "is" denotes the quantity being evaluated at isothermal conditions. T_r denotes the reference scale for temperature, c_p and c_v are specific heats at constant pressure and volume, respectively.

3.2 Numerical Method and Resolution Tests

The numerical method has been described in Chapter 2 of the current thesis. We employ axially periodic boundary conditions along with no-slip and Dirichlet boundary condition for velocities (u, v, w) and temperature T, respectively, at the inner and outer cylinders.

The results presented here consist of two different grids chosen as per requirement of the spatial resolution. As discussed by Curry *et al.* (1984), a lower number of grid points than the optimum may induce chaos in computational solution which ceases to exist with adequate resolution. He showed that high Pr Rayleigh-Benard convection (RBC) exhibits such fictitious chaos when subjected to poor resolution. This phenomenon has been previously reported by Orszag & Kells (1980) and Treve & Manley (1982). For the present system, a detailed grid independence study has been made in order to choose optimum grid resolution based on the Reynolds number of the flow.

Figure 3.1 presents grid independence study for Reynolds number of (a) $Re = 210$ (u, w) phase portrait; (b) $Re = 210$, single-sided axial velocity (w) fluctuation power spectra; (c) $Re = 500$ (u, w) phase portrait; (d) $Re = 500$, single-sided axial velocity fluctuation (w) power spectra corresponding to $\eta = 0.5$, $Ma = 1.0$ and $Pr = 1.0$. We carry out numerical simulations using the following grid-points along axial and radial directions $(N_z \times N_r)$: 41×41, 61×61, 81×81 and 101×101 for $210 < Re < 500$. From figure 3.1, one can conclude that the flow

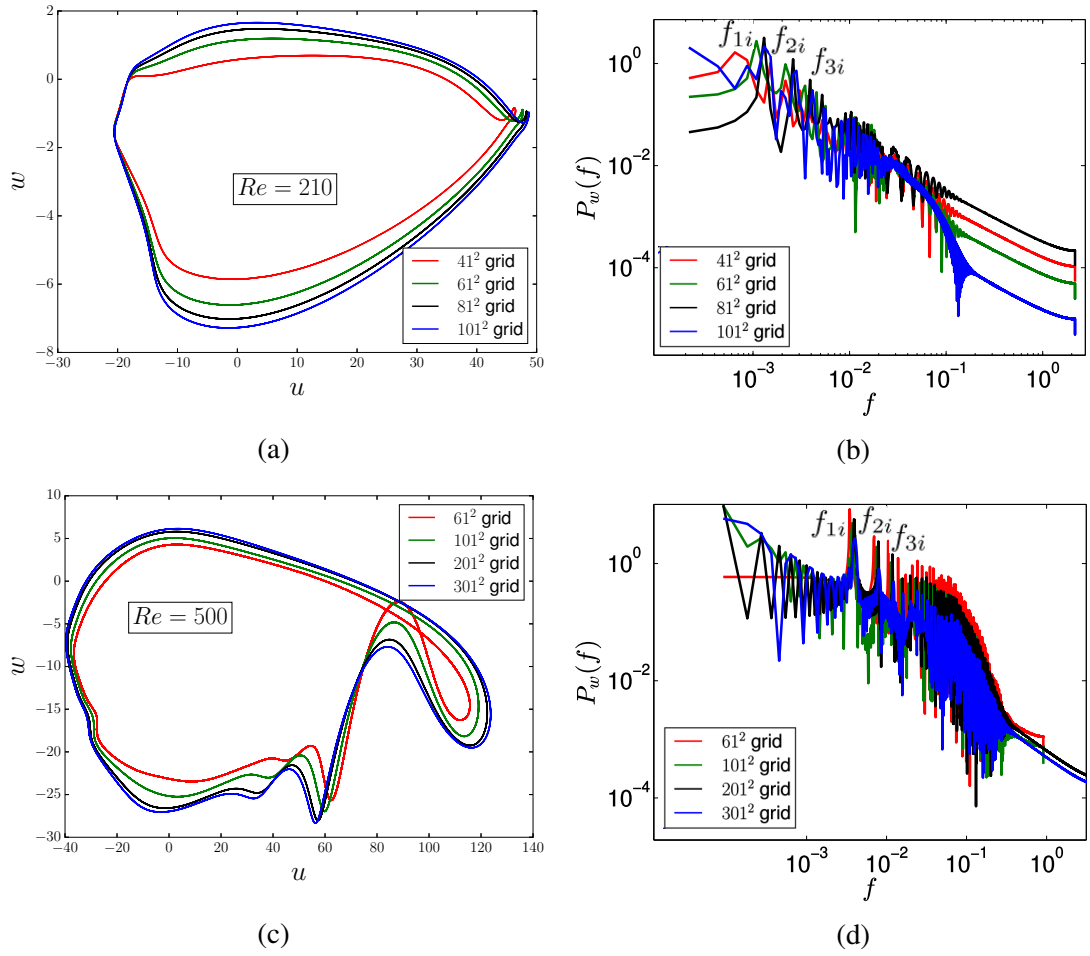

Fig. 3.1 Grid independence study for Reynolds number (a) $Re = 210$ (u,w) phase portrait; (b) $Re = 210$, single-sided axial velocity (w) fluctuation power spectra; (c) $Re = 500$ (u,w) phase portrait; (d) $Re = 500$, single-sided axial velocity fluctuation (w) power spectra corresponding to $\eta = 0.5$, $Ma = 1.0$ and $Pr = 1.0$.

features become more resolved with increased grid points and the difference between two successive phase plot ($u(r = 3/2, z = \pi/4)$, $w(r = 3/2, z = \pi/4)$) decreases with increase of grid resolution (see panel (a) of figure 3.1). Hence for the regime considered ($210 \leq Re < 500$), we choose a grid size of 61×61. For higher Reynolds number regime ($Re \geq 500$), we observe a grid size of 61×61 is unable to accurately reproduce the topology of (u,w) phase portrait (see panel (c) of figure 3.1), hence 101×101 and higher grids can be used to study the flow features at $Re \geq 500$.

Panels (b) and (d) of figure 3.1 correspond to single-sided axial velocity (w) fluctuation power spectra, based on different grid sizes, for (b) $Re = 210$ and (d) $Re = 500$, respectively. Table 3.1 shows dominant and sub-dominant frequencies for different grid sizes; the columns

illustrate the inner cylinder Reynolds number (Re), number of grid-points along axial and radial directions ($N_z \times N_r$), first dominant frequency f_{1i}, second dominant frequency f_{2i} and third dominant frequency f_{3i} where subscript i denotes the frequency based on inertial time scale $(1/\omega_1)$.

Re	$N_z \times N_r$	f_{1i}	f_{2i}	f_{3i}
210	41×41	0.0006494	1.296×10^{-3}	1.96×10^{-3}
	61×61	0.00112	2.24×10^{-3}	3.37×10^{-3}
	81×81	0.001299	2.597×10^{-3}	3.896×10^{-3}
	101×101	0.001299	2.814×10^{-3}	4.113×10^{-3}
500	61×61	0.003455	0.007	0.01045
	101×101	0.003727	0.007455	0.01118
	201×201	0.003909	0.007909	0.01182
	301×301	0.004	0.008	0.01227

Table 3.1 Dominant and sub-dominant frequencies for different grid sizes. The columns illustrate the inner cylinder Reynolds number (Re), number of grid-points along axial and radial directions ($N_z \times N_r$), first dominant frequency f_{1i}, second dominant frequency f_{2i} and third dominant frequency f_{3i} where subscript i denotes the frequency based on inertial time scale.

The main panel of figure 3.2 illustrates the evolution of the radial (KE_u) and axial (KE_w) kinetic energy with time (t), shown by the blue and red lines, respectively. The temporal invariance of the radial (KE_u) and axial (KE_w) kinetic energy is taken as the steady state of the flow, see the main panel in figure 3.2. The inset in figure 3.2 displays a steady state snapshot of Taylor rolls, the radial-axial (u,w) velocity vectors are superimposed on the azimuthal velocity (v) field in the meridional (r,z) plane. The control parameters are $\eta = 0.5$, $\Gamma = \pi/2$, $Re = 100$, $Ma = 1$ and $Pr = 1$. It is observed that there is a radially outward jet at the mid-height of the domain and two radially inward jets near the top and bottom of the periodic box - this pattern is known as Taylor-vortex flow (TVF) after Taylor (1923).

Figure 3.3 displays steady state snapshot of Taylor rolls at different values of Mach number. The radial-axial (u,w) velocity vectors are superimposed on the density (ρ) field. The control parameters are $\eta = 0.5$, $\Gamma = \pi/2$, $Re = 100$, $Pr = 1$ with (a) $Ma = 0.1$, (b) $Ma = 1$ and (c) $Ma = 3$. Refering to figure 3.3 (a), at $Ma = 0.1$, i.e. the incompressible limit, the density is nearly evenly distributed throughout the gap between two cylinders. We observe, with increasing Ma (see panels (b) and (c) of figure 3.3), the region near the inner cylinder becomes more rarefied compared to the region near the outer cylinder, i.e., more mass of the gas moves from the inner cylinder towards the outer cylinder, making the region near the outer cylinder denser.

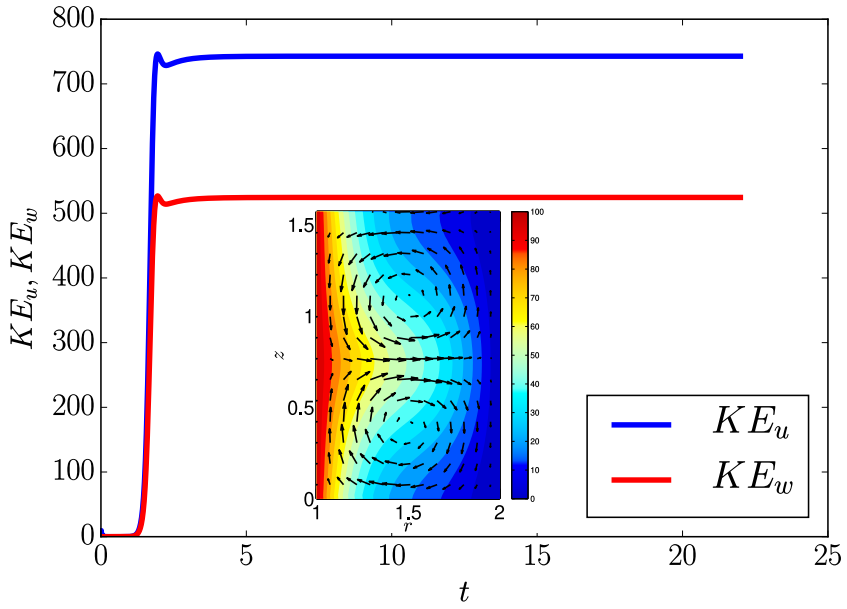

Fig. 3.2 Main panel: Temporal evolution of the radial (KE_u) and axial (KE_w) kinetic energy, showed in the blue and red lines, respectively. Inset: Steady state snapshot of Taylor rolls; the radial-axial (u,w) velocity vectors are superimposed on the azimuthal velocity (v) field. The control parameters are $\eta = 0.5$, $\Gamma = \pi/2$, $Re = 100$, $Ma = 1$ and $Pr = 1$. Note that time has been non-dimensionalized by viscous time-scale.

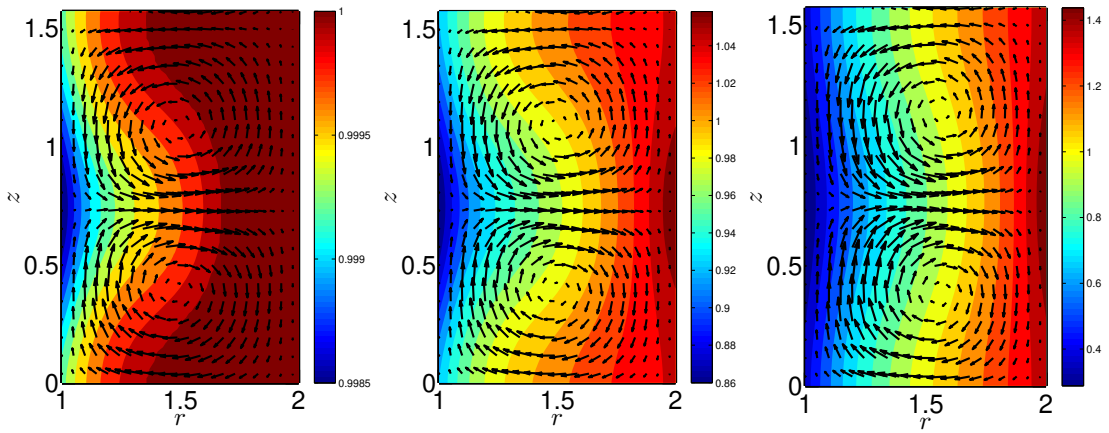

Fig. 3.3 Steady state snapshot of Taylor rolls; the radial-axial (u,w) velocity vectors are superimposed on the density (ρ) field. The control parameters are $\eta = 0.5$, $\Gamma = \pi/2$, $Re = 100$, $Pr = 1$ for (a) $Ma = 0.1$, (b) $Ma = 1$ and (c) $Ma = 3$.

3.3 Phase-diagram of Patterns

The main panel of figure 3.4 summarises all patterns for a range of Mach number $Ma \in [0.1, 3]$ and Reynolds number $Re \in [50, 600]$ that have been obtained from the numerical integration of compressible Navier-Stokes equations, with the energy equation and ideal gas equation of state. These patterns enumerated on the phase diagram of (Re, Ma) are obtained by varying the Reynolds number (Re) of the inner cylinder, $Re = \omega_1 r_1 \delta/\nu \in [50, 600]$ for a given $Ma \in [1, 3]$. The purely azimuthal circular Couette flow (CCF) are shown by red filled circles and the Taylor rolls are marked by blue colored plus symbols at different Ma. Apart from these two stationary patterns, we report existence of a travelling wave (described in section 3.4) and are represented by black ∞ symbols. The axial extent of the periodic domain was set at $h = 2\pi/k = \pi/2$, based on the value of axial wavenumber $k = 4$. The choice of this k was motivated by the linear stability data provided in Welsh *et al.* (2014), where the value of critical wavenumber is $k_c \in [3.1729, 3.2459]$ for $Ma \in [1, 5]$. The initial conditions of the flow is chosen to be "starting from rest" for all the simulations in figure 3.4. After covering the initial transients, the Taylor rolls develop. However, while presenting the data for $Ma < 1$ in figure 3.4, we used a different protocol for $Re \geq 100$; once the flow settles at a given Re for $Ma = 1$, we use that solution as as initial condition and march in Ma towards $Ma = 0.1$ (incompressible limit), with $dMa/dt \sim 0.1$. At each time step the flow was allowed to become steady before further decreasing Ma. The choice of this particular setting is two fold. Firstly, the coefficient (Re^2/Ma^2) of radial and axial pressure gradient terms in momentum equation becomes excessively large with decrease in Ma number ($Ma = 0$ being the singular limit). Secondly, the coefficient (Ma^2/Re^2) of viscous dissipation terms in energy equation becomes too small ($Ma = 0$ makes the code inviscid) resulting in the destabilization of the code.

3.3.1 Role of fluid compressibility on Taylor-rolls

The role of fluid compressibility on the onset of Taylor vortices from the base state of circular Couette flow (CCF) has been addressed by various groups, from linear stability analysis. Some argued that compressibility can be stabilizing as well as destabilizing based on geometrical parameters (Kao & Chow(1992)), strictly destabilizing (Hatay *et. al.* (1993), Riechelmann & Nanbu (1993)) and stabilizing (Stefanov & Cercignani (1993), Yoshida & Aoki (2006), Manela & Frankel (2007), Welsh *et. al.* (2014)). We will illustrate the role of fluid compressibility on the onset of Taylor vortices from the base state of circular Couette flow (CCF) using DNS of

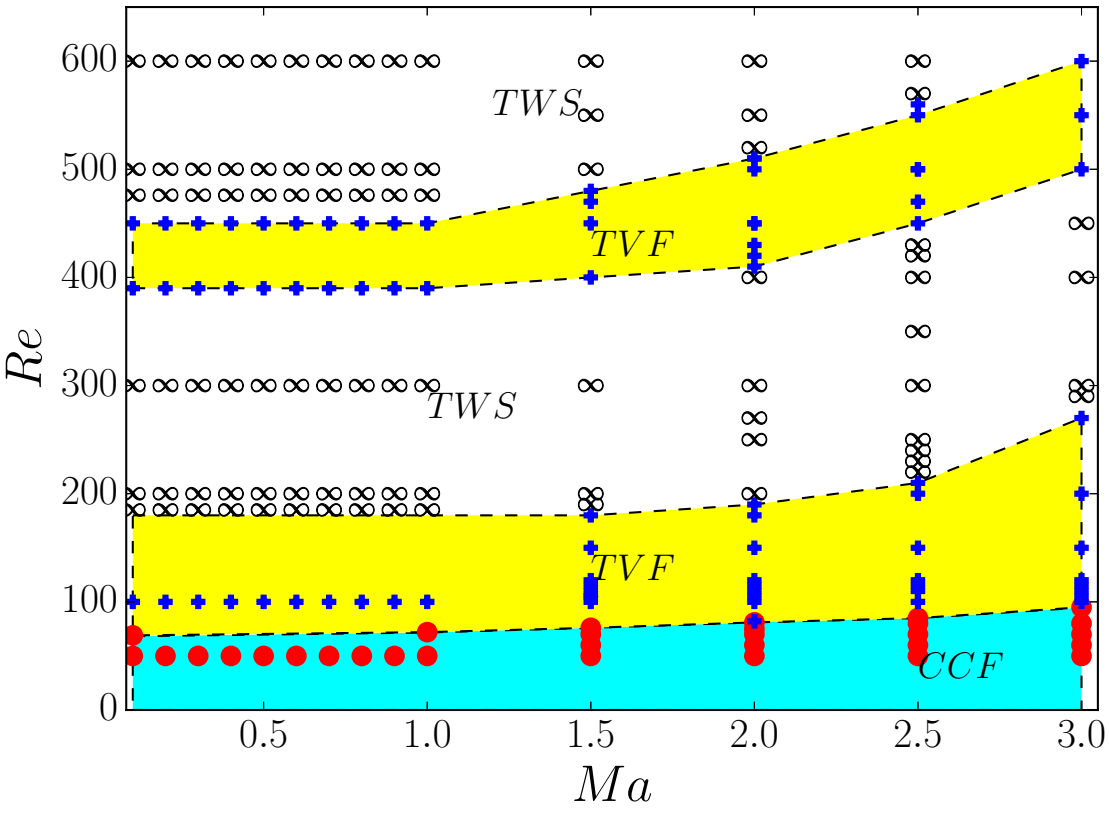

Fig. 3.4 Phase diagram of patterns in (Re, Ma)-plane for a radius ratio of $\eta = 1/2$ and aspect ratio of $\Gamma = \pi/2$. All states have been identified by starting simulations from the rest state; red circle denotes the *CCF* (circular Couette flow), plus denotes the *TVF* (Taylor vortex flow) and ∞ denote the *TWS* (Travelling Wave solution).

compressible TCF. The energy equation is given as follows:

$$\begin{aligned}
&\frac{\partial(\bar{\rho}T)}{\partial t} + \frac{\partial}{\partial r}[(\bar{\rho}u)T] + \frac{\partial}{\partial z}[(\bar{\rho}w)T] \\
&= -(\gamma-1)pr\left(\frac{1}{r}\frac{\partial(ru)}{\partial r} + \frac{\partial w}{\partial z}\right) + r\gamma\left[\kappa\left(\frac{1}{r}\frac{\partial}{\partial r}\left(r\frac{\partial T}{\partial r}\right) + \frac{\partial^2 T}{\partial z^2}\right)\right. \\
&\left. + \left(\frac{\partial T}{\partial r}\frac{\partial \kappa}{\partial r} + \frac{\partial T}{\partial z}\frac{\partial \kappa}{\partial z}\right)\right] + r(\gamma-1)\frac{Ma^2}{Re^2}\Phi,
\end{aligned} \tag{3.3}$$

where viscous dissipation Φ is given by

$$\begin{aligned}\Phi &= \mu\left[2e_{ij}e_{ij} - \frac{2}{3}(\nabla\cdot u)^2\right] \\ &= \mu\left[\left\{2\left(\frac{\partial u}{\partial r}\right)^2 + 2\left(\frac{u}{r}\right)^2 + 2\left(\frac{\partial w}{\partial z}\right)^2 + \left(\frac{\partial v}{\partial r} - \frac{v}{r}\right)^2 + \left(\frac{\partial u}{\partial z} + \frac{\partial w}{\partial r}\right)^2 + \left(\frac{\partial v}{\partial z}\right)^2\right\}\right. \\ &\left. - \frac{2}{3}\left\{\frac{1}{r^2}\left(\frac{\partial (ru)}{\partial r}\right)^2 + \left(\frac{\partial w}{\partial z}\right)^2 + \frac{2}{r}\frac{\partial (ru)}{\partial r}\frac{\partial w}{\partial z}\right\}\right].\end{aligned} \tag{3.4}$$

is substantial near the inner wall of TC cell due to increase in Ma at a given Re and is reflected in a form of hump in the radial temperature profile (see Chapter 2). This elevated fluid temperature is a characteristic property of wall-bounded compressible shear flows and has been addressed by Manela & Frankel (2007), Manela & Zhang (2012) and recently by Welsh *et al.* (2014). Similar phenomenon has been addressed by Park & Hyun (1989) where they observe the location of peak temperature moving radially inwards in the transient simulation of compressible gas contained in infinite cylinder. We also find, that for small Mach numbers (Ma), the temperature profile shows no radial variation; pertaining to the fact that the effect of viscous dissipation is completely negligible in the incompressible Taylor-Couette flow (TCF).

Figure 3.4 illustrates the explicit dependence of the critical Re on Ma for $\eta = 0.5$. In the case of $1 \leq Ma \leq 3$, we observe compressibility, in general, stabilizes the flow since the critical Re for transition from one flow state to other increases. The region where the TWS returns back to TVF, continues to exist with increase in Ma, however shifts vertically upward in (Re, Ma)-plane. As it is evident from figure 3.4, for $Ma < 1$, the region of reappearance of TVF exists, but there is no distinct shift of critical Reynolds number (Re^{cr}) due to compressibility. Note that, in purely incompressible TCF, existing literature has not reported any oscillations analogous to TWS in the parameter regime under study.

The observed flow transitions ($CCF \longrightarrow TVF \longrightarrow TWS \longrightarrow TVF \longrightarrow TWS$) enlisted in figure 3.4 are found to be new in the case of compressible Taylor-Couette flow of an ideal gas. The nature of bifurcation $TVF \longrightarrow TWS$ is analysed in detail in Section 3.4.1.

3.3.2 Rayleigh inviscid stability and angular momentum

The base state of Taylor-Couette flow is CCF for which the flow is purely azimuthal (i.e. $v = v(r), u = w = 0$) if the system is of infinite length. As discussed in Chapter 1, the inviscid stability argument of Rayleigh (1917) asserts that the radial variation of the specific angular momentum $(\mathscr{L})$, where

$$\mathscr{L} = \rho v r, \tag{3.5}$$

should increase towards the outer cylinder, i.e. $d\mathscr{L}/dr > 0$, for the flow to remain in CCF. In other words, for any finite inner cylinder rotation rate (with stationary outer cylinder), the CCF is unstable to axisymmetric perturbations, yielding the critical Re for the transition from CCF to TVF regime, $Re^{cr} = 0$. Taylor (1923) demonstrated with a linear stability analysis that viscosity stabilizes the flow, admitting a finite $Re^{cr} > 0$ for CCF to TVF transition. Recently, Welsh *et al.* (2014) analyzed the Rayleigh inviscid stability argument in the light of compressible TCF and they found the primary instability can occur much below the Rayleigh line at moderate and high Prandtl numbers (Pr), violating the canonical Rayleigh criterion.

The effect of compressibility is depicted in Figs. 3.5 and 3.6 for the radial variations of density (ρ), azimuthal velocity (v) and specific angular momentum ($\mathscr{L}$) profiles. The leftmost panels of figure 3.5 (a,d,g,j) and figure 3.6 (a,d) show a strong radial stratification in density (ρ) with increasing Ma. The radial density stratification is a hallmark of the spin-up process in rotating compressible flows and has been previously studied by Harada (1980*a*,*b*), Park & Hyun (1989), Hyun & Park (1992) and recently observed by Welsh *et al.* (2014) in the base state of compressible TCF. The variation of density (ρ) profiles with r, for a given Ma remains identical in the CCF regime (see panels (a) and (d) in figure 3.5). Interestingly, at higher Re (panels (a) and (d) of the figure 3.6), the density profile changes and develops an inflection point. This results in horizontally displaced radial location of crossover of the density profiles which has strong implications on the radial $\mathscr{L}$ profiles.

The central panels in figure 3.5 and figure 3.6 show the variation of azimuthal velocity (v) along the radial extent between the two cylinders. It is seen from the panels $(b)(Re = 50)$ and $(e)(Re = 60)$ in figure 3.5, that the azimuthal velocity profiles for different Ma are identical. However, there exists a slight deviation in the azimuthal velocity profiles in the TVF, which increases with Re [see panels $(h)(Re = 80)$ and $(k)(Re = 100)$ in figure 3.5]. This deviation in the radial profiles of azimuthal velocity (v) can be clearly observed towards the outer cylinder. Interestingly, this deviation occurring near outer cylinder shifts towards the inner cylinder with increasing Re [see $(b)(Re = 120)$ and $(e)(Re = 150)$ in figure 3.6].

Figure 3.5 $((c),(f),(i)$ and $(l))$ and figure 3.6 $((c)$ and $(f))$ show non-monotonic behaviour of specific angular momentum $(\mathscr{L})$ with increase in r. With increasing Ma, locally causing $d\mathscr{L}/dr > 0$ near the inner cylinder (see unfilled circles, green triangles, unfilled magenta squares and black stars for $Ma = 1.5, 2, 2.5, 3.0$ in the rightmost panels $((c),(f),(i),(l))$ of figure 3.5). This suggests that this part of variation of specific angular momentum $\mathscr{L}$ with r is stable to inviscid axisymmetric perturbation whereas the remaining part is unstable ($d\mathscr{L}/dr < 0$). For super-critical Reynolds number of $Re = 120$ and $Re = 150$, the behaviour of specific angular momentum $(\mathscr{L})$ becomes increasingly complex. We observe distinct plateau regions, where $d\mathscr{L}/dr \sim 0$ (see panel (c) and (f) (green triangles, unfilled magenta squares and black

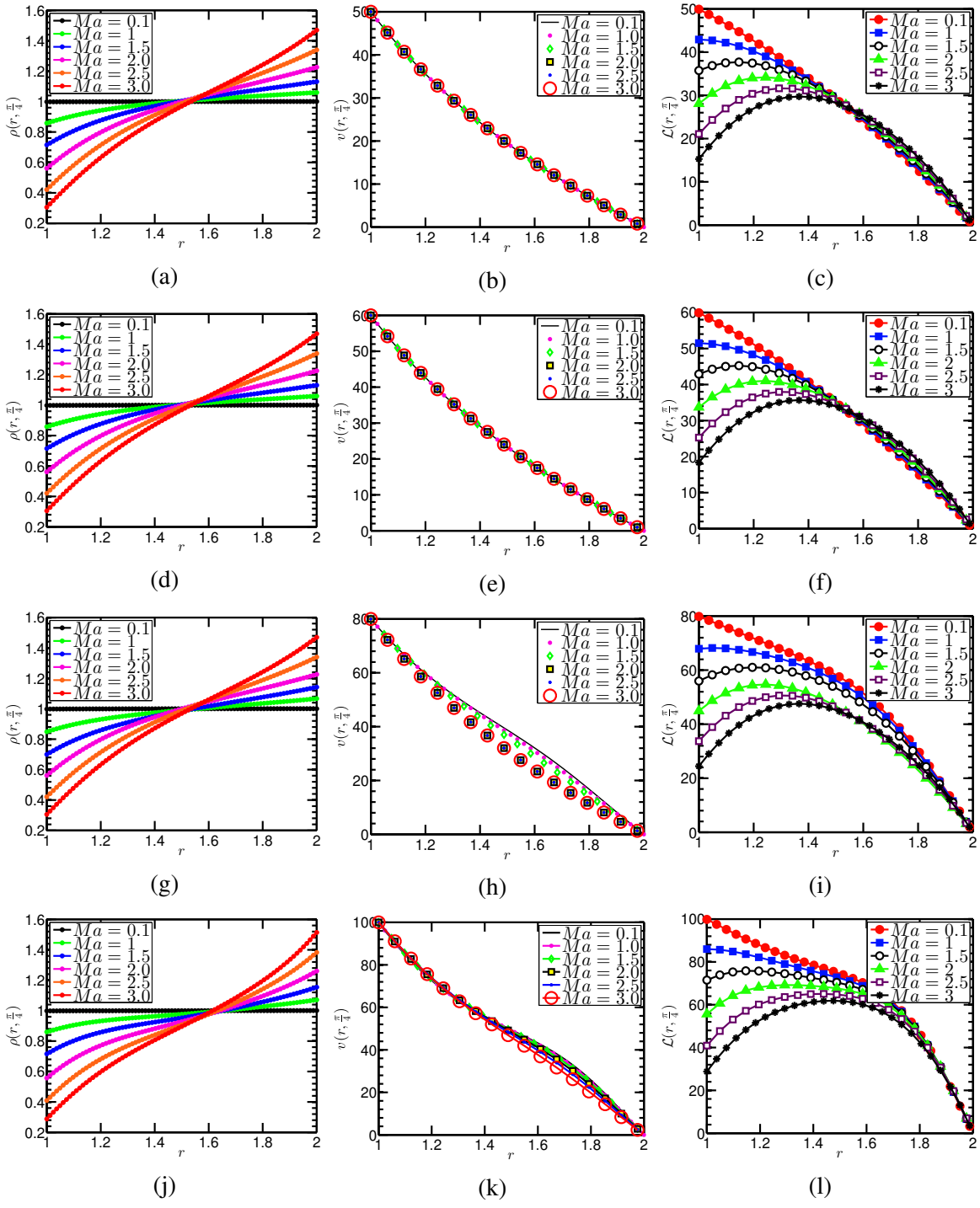

Fig. 3.5 The effect of compressibility on mid-height radial profiles of (a,d,g,j) density (ρ), (b,e,h,k) azimuthal velocity (v) and (c,f,i,l) angular momentum $(\mathscr{L})$ profiles for $(a-c)$ $Re = 50$ (CCF); $(d-f)$ $Re = 60$ (CCF); $(g-i)$ $Re = 80$ $(CCF : Ma = 2, 2.5, 3)$ and $(TVF : Ma = 1, 1.5)$; $(j-l)$ $Re = 100$ (TVF); $\omega_2 = 0$ and $Pr = 1$.

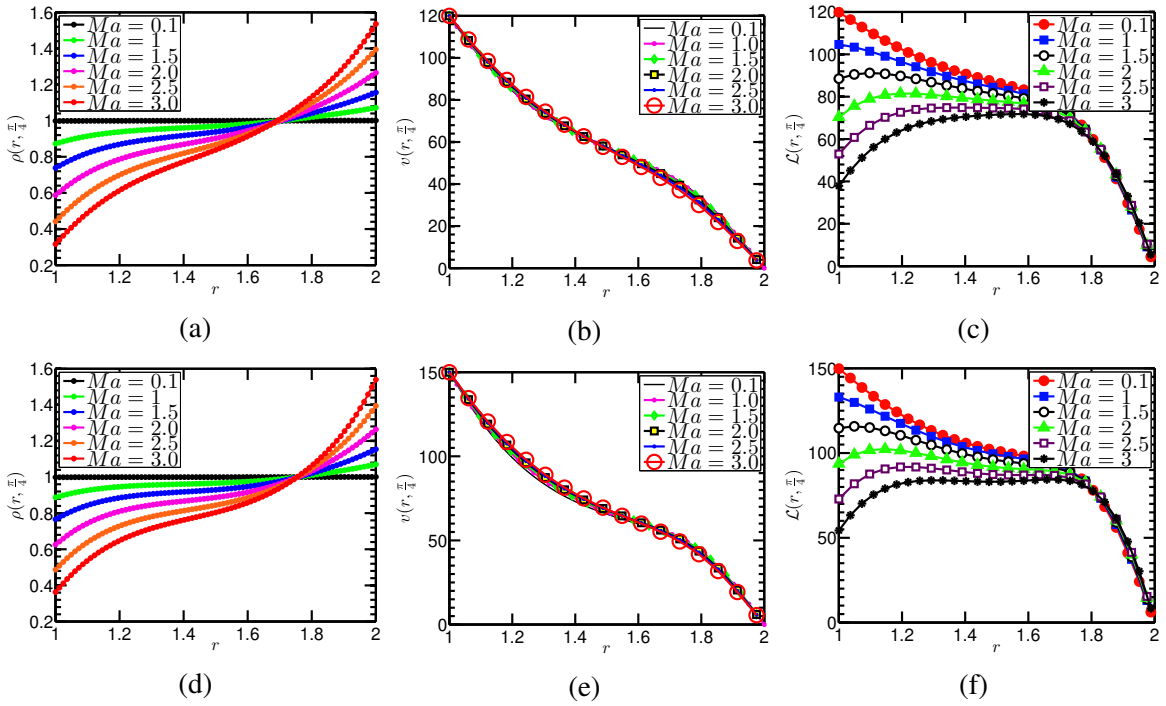

Fig. 3.6 The effect of compressibility on mid-height radial profiles of (a,d) density (ρ), (b,e) azimuthal velocity (v) and (c,f) angular momentum $(\mathscr{L})$ profiles for $(a-c)$ $Re = 120$ (TVF); $(d-f)$ $Re = 150$ (TVF); $\omega_2 = 0$ and the Pr being unity.

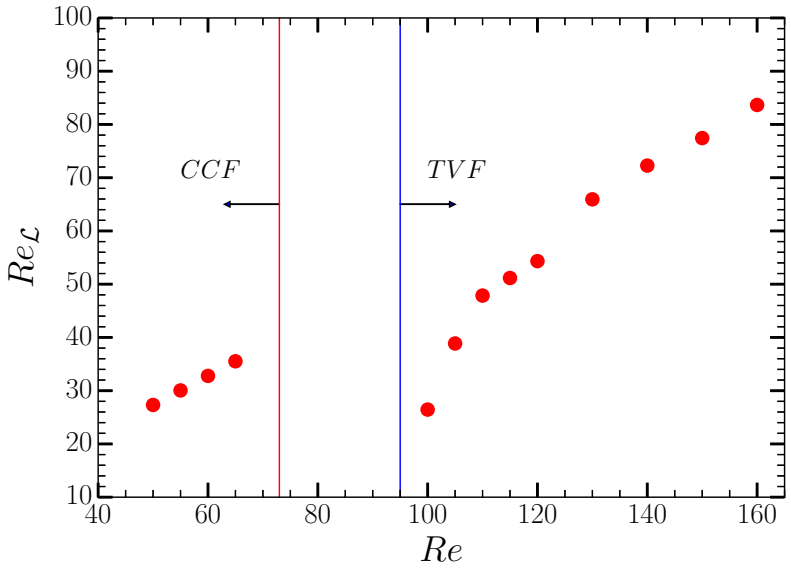

Fig. 3.7 Variation of $Re_{\mathscr{L}}$ with Re at $\eta = 0.5$; the vertical red line indicates the boundary below which the flow is CCF for $Ma \in [0.1,3]$; the blue line indicates the boundary above which the flow is TVF for $Ma \in [0.1,3]$.

stars) in figure 3.6). With increase in $Re(\geq 150)$, at $Ma \geq 2.5$, the radial profiles of $\mathscr{L}$ shows a bimodal distribution. The origin of the non-monotonic specific angular momentum $(\mathscr{L})$ profiles can be linked to the underlying density (ρ) stratification. We have found strong radial variation of density, with the density crossover (corresponding to different Ma) shifting towards the outer cylinder with increasing Re. This is attributed to the fact that more fluid is thrown outward due to increasing centrifugal force (increasing Re). The azimuthal velocity (v) profiles are always decreasing towards the stationary outer cylinder. As a result, a part of the $\mathscr{L}$ profiles (irrespective of Ma) decreases monotonically towards the outer cylinder representing "Rayleigh-unstable" regime and a "Rayleigh-stable" (see Fig. 1.1 in Chapter 1) part being located near the inner cylinder.

Based on figure 3.5 and 3.6, we can define a Reynolds number, $(Re_{\mathscr{L}})$, based on the length scale chosen to be the radial location $(r_{\mathscr{L}})$ from inner cylinder at the crossover point of $\mathscr{L}$ curves, which is independent of Ma for a given Re. The density $(\rho_{\mathscr{L}})$ and reference velocity $(v_{\mathscr{L}})$ used are evaluated at $r_{\mathscr{L}}$.

$$Re_{\mathscr{L}} = \frac{\rho_{\mathscr{L}} v_{\mathscr{L}} r_{\mathscr{L}}}{\mu}$$

Variation of $Re_{\mathscr{L}}$ with Re is displayed in figure 3.7. For the flow in purely CCF regime (for all Ma), we observe $Re_{\mathscr{L}} \propto Re^{\alpha}$, where $\alpha = 1$ and the exponent α significantly deviates from unity in TVF regime.

3.3.3 Effect of Compressibility on Taylor Vortices and Transport

In this section, we uncover how the stratification in the hydrodynamic fields associated with Taylor vortices affect the transport in the present fluid system. Figure 3.8 shows the axial variation of density (ρ) (see panels (a) and (b)) and radial velocity (u) (see panels (c) and (d)) at the mid-gap along the mid-height for different Re. For a given Reynolds number (Re), in the TVF regime, we find the radially outward jet at the mid-height and two radially inward jets manifested at the top and the bottom of the computational domain. However, for a periodic system, either of the possibilities (radially outward jet or radially inward jet at the mid-height) are stable, and corresponds to stable branches in the CCF to TVF regime. For a given Re, the radially outward jet at the mid-height is accompanied by lower density and the radially inward jets are accompanied by higher density (see panel (a) and (c) of figure 3.8). With increase in Re, the degree of axial stratification

$$\Delta\rho\left(\frac{\delta}{2},z\right) = \rho\left(\frac{\delta}{2},z\right)_{max} - \rho\left(\frac{\delta}{2},z\right)_{min} \tag{3.6}$$

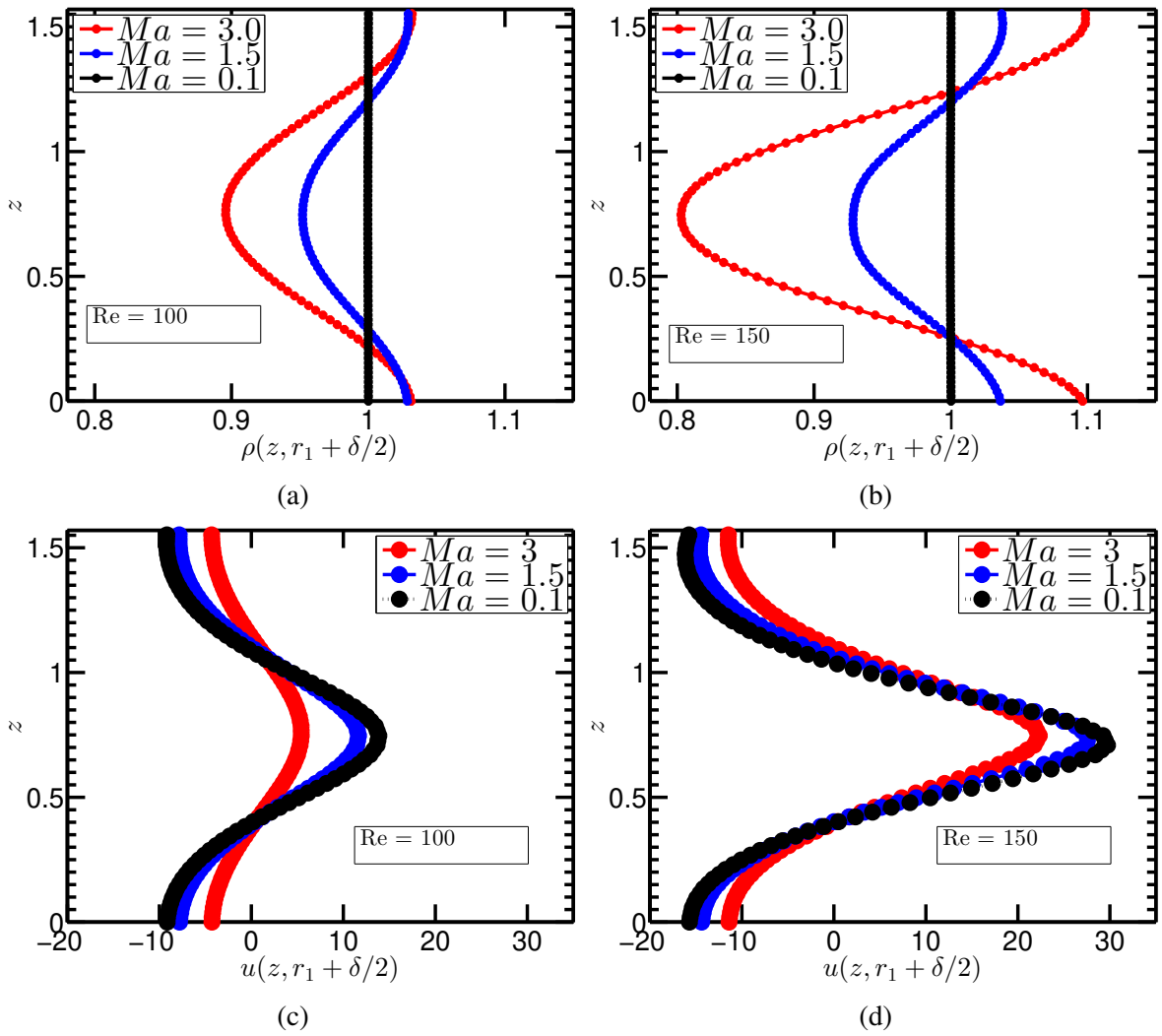

Fig. 3.8 Upper row: axial variation of density (ρ) due to change in Ma for different Re, (a) $Re = 100$, (b) $Re = 150$; Lower row: radial velocity (u) variation along the height of the computational domain with Ma for different Re, (c) $Re = 100$, (d) $Re = 150$.

increases and this is more pronounced at higher Ma (see the red curves in the panels (a) and (b) in the figure 3.8). This leads to the formation of the alternate regions of rarified and dense regimes along the axial direction and remarkably different from its incompressible counterpart. Note that, the increase in the axial stratification in radial velocity (u) with increase in Re is as expected.

Figure 3.9 shows the radial variation of density (ρ) (see panels (a) and (b)) and axial velocity (u) (see panels (c) and (d)) at the mid-height along the mid-gap for different Re. With the increase in Ma, for a given Re, the radial stratification of density (ρ) becomes increasingly asymmetric (see panels (a) and (b) of figure 3.9). The radial location of crossover of different

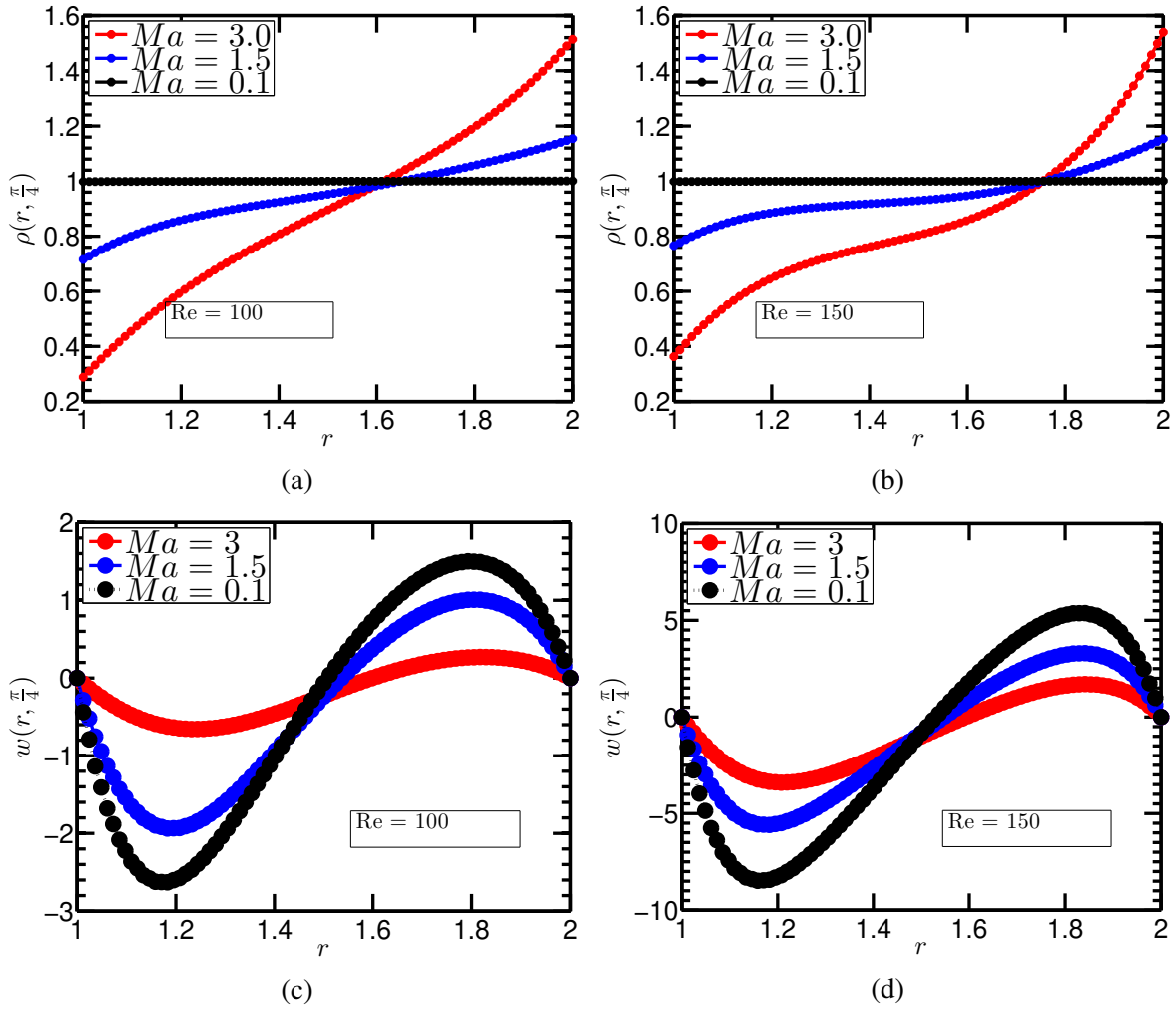

Fig. 3.9 Upper row: radial variation of density (ρ) due to change in Ma for different Re, (a) $Re = 100$, (b) $Re = 150$; Lower row: radial variation of axial velocity (w) with Ma for different Re, (c) $Re = 100$, (d) $Re = 150$.

density profiles along the radial direction shifts towards the outer cylinder with increase in Re. Note that, in the CCF regime, this crossover location of radial density profiles are invariant with increase in Re (see panels (a) and (d) of figure 3.5). This is attributed to the fact that the flow in CCF regime is purely azimuthal and there is no radial component $(u = 0)$. In the TVF regime, the hydrodynamic fields are coupled and with increase in Re, the radial velocity (u) increases, as a result the strength of outward jet at the mid-height increases, pushing the crossover point towards the outer cylinder. Panels (c) and (d) of figure 3.9 shows the radial variation in axial velocity (w), which portrays that the extent of radial variation

$$\Delta w\left(r, \frac{\pi}{4}\right) = w\left(r, \frac{\pi}{4}\right)_{max} - w\left(r, \frac{\pi}{4}\right)_{min} \tag{3.7}$$

increases with decreasing Ma.

We study the effect of compressibility is studied on the radial $(\tilde{Q}_r)$, axial $(\tilde{Q}_z)$ and azimuthal $(\tilde{Q}_\theta)$ transport obtained using the formulation described in Abcha *et al.* (2013) and Hoffmann *et al.* (2004). Compressible TCF shows significant variation of density across the radial extent between the cylinders and hence, we use the following definitions of $(\tilde{Q}_r)$, $(\tilde{Q}_z)$ and $(\tilde{Q}_\theta)$:

$$\tilde{Q}_r(\tilde{r_1}+\tilde{\delta}/2,\tilde{z}) = \tilde{r}\int_0^{2\pi}\int_0^{\tilde{h}} \tilde{\rho}(\tilde{r},\tilde{z})\tilde{u}(\tilde{r},\tilde{z})d\tilde{z}d\theta \tag{3.8}$$

$$\tilde{Q}_z(\tilde{r},\tilde{h}/2) = \int_0^{2\pi}\int_{\tilde{r_1}}^{\tilde{r_2}} \tilde{\rho}(\tilde{r},\tilde{z})\tilde{w}(\tilde{r},\tilde{z})\tilde{r}d\tilde{r}d\theta \tag{3.9}$$

$$\tilde{Q}_\theta(\tilde{r},\tilde{z}) = \int_0^{2\pi}\int_{\tilde{r_1}}^{\tilde{r_2}}\int_0^{\tilde{h}} \tilde{\rho}(\tilde{r},\tilde{z})\tilde{v}(\tilde{r},\tilde{z})d\tilde{r}d\tilde{z}d\theta \tag{3.10}$$

The unclad equivalent of dimensional quantities represent the corresponding dimensionless analog. Using the gap between two cylindrical walls $\tilde{\delta}_r = \tilde{r_2} - \tilde{r_1}$ as the length scale, a diffusion time scale, $\tilde{t_r} = \tilde{\delta}_r^{\,2}/\tilde{\nu}_r$, the corresponding velocity scale $\tilde{u_r} = \tilde{\delta}_r/\tilde{t_r}$, along with reference scale for density being defined at the wall of inner cylinder, the dimensionless radial (Q_r), axial (Q_z) and azimuthal (Q_θ) transport are -

$$Q_r\left(1+\frac{\varsigma_r}{2},z\right) = 2\pi(1+\frac{\varsigma_r}{2})\int_0^{\frac{\pi}{2}} \rho(r,z)u(r,z)dz \tag{3.11}$$

$$Q_z\left(r,\pi/4\right) = 2\pi\int_{\frac{\eta}{(1-\eta)}}^{1/(1-\eta)} \rho(r,z)w(r,z)rdr \tag{3.12}$$

$$Q_\theta\left(r,z\right) = 2\pi\int_{\frac{\eta}{(1-\eta)}}^{1/(1-\eta)}\int_0^{\frac{\pi}{2}} \rho(r,z)v(r,z)drdz \tag{3.13}$$

where $\varsigma_r = \delta/2$ and the factor 2π denotes the imposed axisymmetry in evaluated dimensional quantities. It is clear that the Q_r, Q_θ and Q_z in compressible TCF is strongly reduced in comparison to its incompressible analog $(Ma = 0.1)$. The trend shows with increasing Ma, Q_r, Q_θ and Q_z reduces and Q_r and Q_z become less negative in magnitude. This is attributed to the fact that in a periodic domain, far from the critical Re of CCF to TVF transition, the Taylor rolls can axially shift resulting in small negative value of Q_r and Q_z.

Figure 3.10(a) shows the variation Q_r with Ma (refer to relation 3.11). Figure 3.8 shows the axial variation of density (ρ) $((a),(b))$ and the axial variation of radial velocity (u) $((c),(d))$ profiles along the mid-height at the mid-gap, for different Re. We would like to point out that, for $Ma = 0.1$ and 1.5, with the change in Re, the axial variation of ρ profiles is not pronounced, whereas in the case of $Ma = 3$, the axial variation of density (ρ) profiles increases with increase

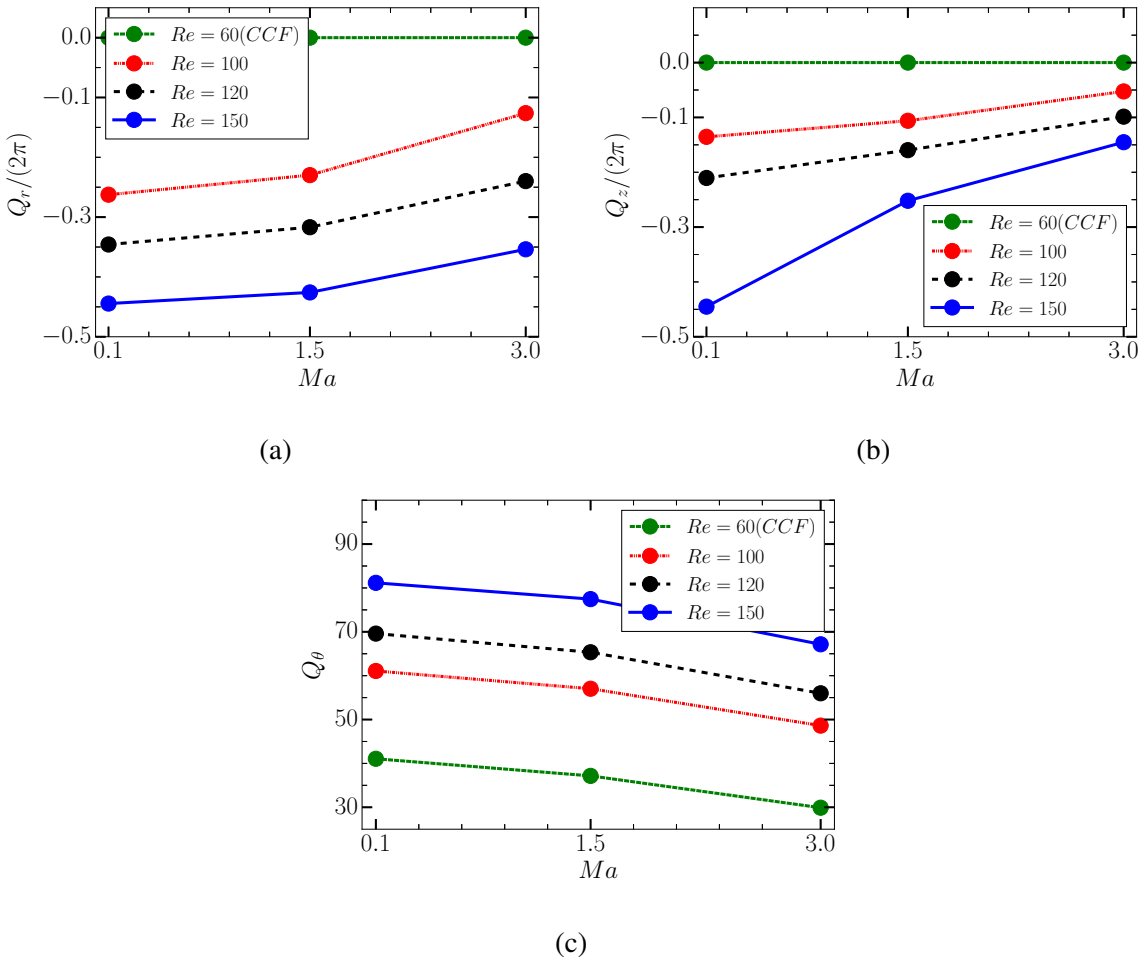

Fig. 3.10 Variation of Ma with non-dimensional (a) radial flow-rate Q_r; (b) axial flow-rate Q_z and (a) azimuthal flow-rate Q_θ for different $Re = 60, 100, 120, 150$.

in Re (see panels $(a), (b)$ in the figure 3.8). It is also noted the same argument does not holds for axial variation of radial velocity (u) profiles at mid-way between two cylinders, with increase in Re the variation from the mean u increases irrespective of Ma (see panels (c) and (d) in the figure 3.8). In the plot of Q_r with Ma, a reference has given with respect to purely azimuthal CCF at $Re = 60$, where no radial-transport (Q_r) is observed irrespective of Ma.

Similarly, figure 3.10(b) shows the variation Q_z with Ma. Figure 3.9 shows the radial variation of density (ρ) profiles along the mid-gap at the mid-height, and the radial variation of axial velocity (w), for different Re. It is noted that the crossover point for different Ma of ρ curves at constant Re, displaces towards the outer cylinder with increase in Re (see panels $(a), (b)$ and (c) in the figure 3.9). Although, the radial ρ variation does not change significantly for a given Ma at different Re. Analysis of the axial velocity profiles at the mid-height (see figures 3.9 (d),(e) and (f)) we come to the conclusion that vortex centers remain at the same

location independent of Ma at a given Re. However one can say, the strength of Taylor-rolls (radial variation of w from the mean value) decrease with increase in Ma at a given Re. We can safely conclude from figure 3.10(b), the axial transport decreases (in other words, become less negative) with increase in Ma.

Figure 3.10 (c) illustrates the variation of azimuthal flow-rate (Q_θ) with Ma for the four different Re studied previously. This involves the azimuthal velocity (v) and density (ρ) field integrated over the (r,z) section for different Re and Ma (see equation 3.13). The same trend continues as observed in the case of 3.10(a) and 3.10(b), with increasing Ma, Q_θ decreases. Considering the fact that the base flow is purely azimuthal, the relative magnitude of Q_θ is $O(10^2)$ larger than that of Q_r and Q_z. We may conclude from the above section that enhanced compressibility (manifested in terms of higher peripheral Ma) diminishes the radial $(\tilde{Q}_r)$, axial $(\tilde{Q}_z)$ and azimuthal $(\tilde{Q}_\theta)$ transports observed in TVF regime.

3.4 Flow Patterns at High Reynolds Number

In the standard Taylor-Couette experiments, it is a well known fact that the axisymmetric TVF bifurcates to non-axisymmetric Wavy vortex flow (WVF). In the WVF, waves develop on top of the Taylor vortices in the azimuthal (θ) direction and the whole structure starts rotating in the θ-direction at some speed. However, the symmetry group $SO_2 \times O_2$ remains intact and no broken symmetry in axial direction is observed. O_2 refers to general orthogonal group which includes both rotation and reflection which forms in the axial direction due to periodic boundary conditions. The symmetry group SO_2 refers to purely rotational symmetry in azimuthal (θ) direction. We report a new time-dependent, axially propagating, axisymmetric flow state, dubbed Travelling Wave solution (TWS), identified in the present fluid system at higher Reynolds number (Re). Figure 3.11 illustrates the time dependence of axial velocity (w) at mid-height and mid-plane of the computational domain for $Re = 500$, $Ma = 1$ and $Pr = 1$, where, the right panel is an enlargement of the left figure showing a single wave. Velocity vectors on (r,z) plane superimposed on dimensional temperature contour plots are displayed in top and right panels, the red colour in temperature contour plot shows hotter region and blue shows the temperature magnitude of unity. Note that the two cylinder walls are isothermal and have dimensionless temperature unity. Figure 3.12 is same as figure 3.11 but for $Re = 410$ and $Ma = 3$. In these oscillations, the Taylor rolls start propagating axially downwards. However, at higher Re (≥ 500), the distance between the vortex center changes and their alignment is broken compared to case of TVF regime. Since our system is axisymmetric $[\partial/\partial\theta(\cdot) = 0]$, the reported TWS is not an analog of WVF observed in incompressible TCF. Secondly, as described in DiPrima & Swinney (1981), the critical Re for transition from TVF to WVF in

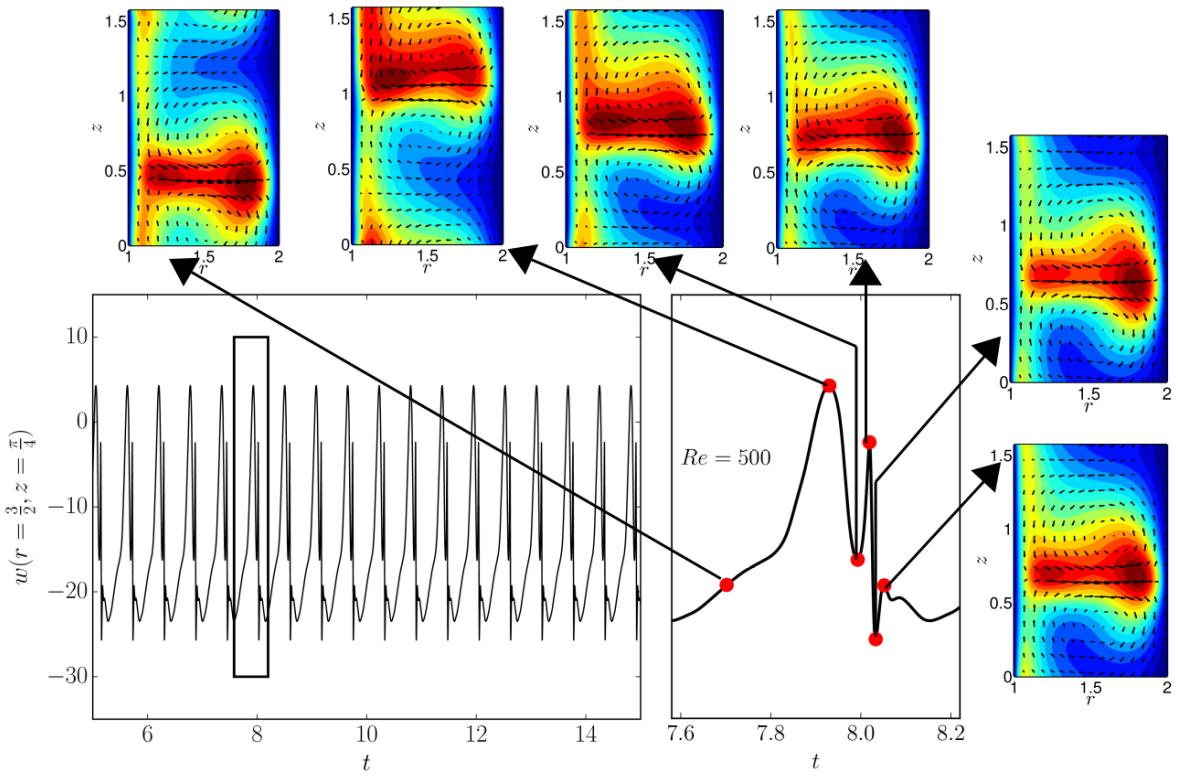

Fig. 3.11 Time dependence of axial velocity (w) at mid-height and mid-plane of the computational domain; the right panel is an enlargement of the left figure showing a single wave. Velocity vectors on (r,z) plane superimposed on temperature contour plots are displayed in top and right panels for $Re = 500$, $\eta = 0.5$, $Ma = 1$ and $Pr = 1$.

wide-gap ($\eta = 0.5$) TC cells is around $Re = 681.9$, for incompressible TCF. We observe the oscillations in the fields at Re much below above mentioned onset in incompressible TCF. In the incompressible Taylor Couette systems, axially propagating waves along with azimuthally travelling waves are observed in counter-rotation (Spirals) (Andereck *et al.*, 1986) which are inherently non-axisymmetric. These oscillations are characterized using the axial-velocity (w) and radial-velocity (u) vs t plots at the mid-height and mid-plane of the computational domain. These results are presented from figure A.2 to figure A.4 for $Ma = 1$ and $\eta = 0.5$ (see Appendix A). The single-sided amplitude spectrum is plotted in the frequency domain and it has been found that the sub dominant frequencies are present as integral multiples of the dominant frequency.

In order to gain qualitative insight about these oscillations, we plot the dominant as well as other sub-dominant frequencies obtained from the power spectrum of radial or axial velocity at the mid-point and mid-height of the domain. We also convert the dimensionless frequencies from viscous time-scale, (δ^2/ν), to the inertial time scale, $(1/\omega_1)$, in order to obtain qualitative

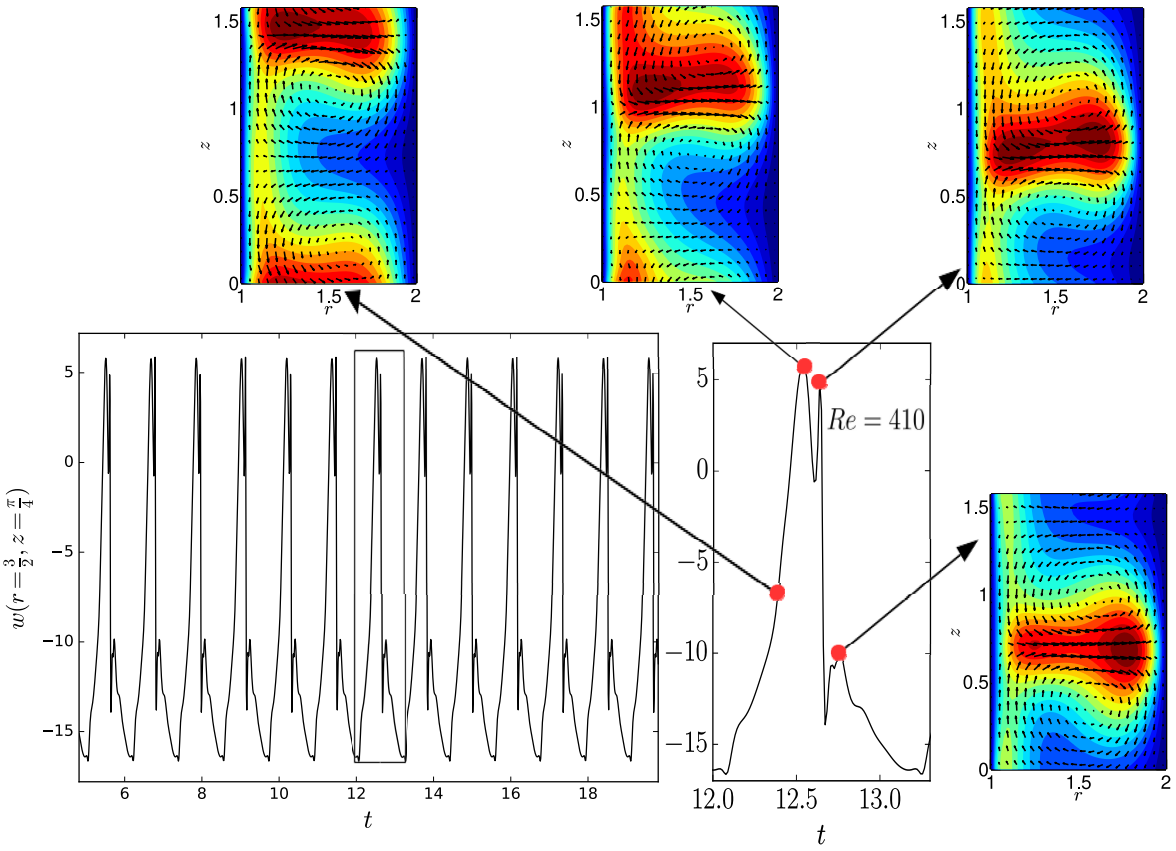

Fig. 3.12 Same as figure 3.11 but for $Re = 410$ and $Ma = 3$.

information about their variation with the rotation of the inner cylinder. We denote the dimensional frequency $\tilde{f}$, dimensionless frequency on the viscous time-scale as f_v and the dimensionless frequency on the inertial time-scale as f_i and they are related as follows -

$$f_i = \frac{f_v}{Re} \frac{\eta}{(1-\eta)} \tag{3.14}$$

Figure 3.13 illustrates variation of dimensionless frequency (f) of oscillations scaled with (a) viscous time-scale (f_v) and (b) inertial time scale (f_i) with Re for different Ma for $\eta = 0.5$, $Pr = 1$; dimensionless time period (c) $\tau_v = 1/f_v$ and (d) $\tau_i = 1/f_i$. It is noted that the curves of f_i versus Re follow the same trend as that of f_v versus Re. Also it is observed at a constant Re, both f_i and f_v decreases with increase in Ma. However, the order of magnitude of these frequencies are very less compared to the frequencies of oscillatory eigenfunctions reported by Welsh *et al.* (2014) at high Pr (see Table 3.2).

Re	k	Ma	Pr	f_v	f_i
143.6191	3.1549	1.0	3.0	7.8603	0.0547
94.4030	3.1094	1.0	5.0	4.6189	0.0489
79.2450	3.1243	1.0	7.0	3.0374	0.038
(190-600)	4.0	1.0	1.0	(0.17-2.41)	(0.0009291-0.004)

Table 3.2 Comparison of dimensionless frequencies of oscillatory eigenfunctions reported by Welsh *et al.* (2014) with the travelling wave solution (TWS) for $\Gamma = 2\pi/k$, $\eta = 0.5$ and $Re_o = 0$. The last row (coloured red) denotes the current simulations reported for $Re = 190$ to $Re = 600$ for $k = 4$, $Ma = 1$ and $Pr = 1$, the dimensionless frequency based on viscous time scale $f_v \in [0.17, 2.41]$

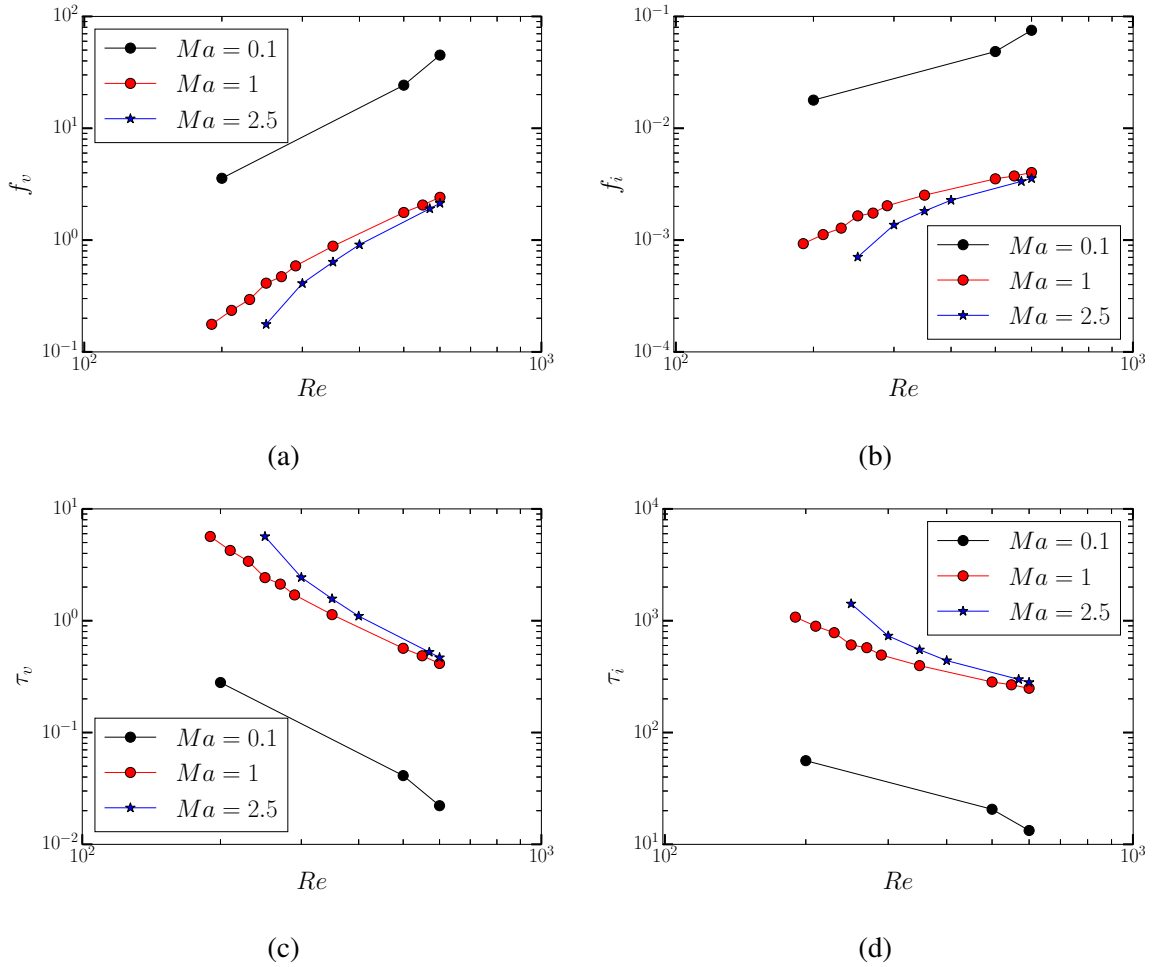

Fig. 3.13 Variation of dimensionless frequency (f) of oscillations scaled with (a) viscous time-scale (f_v) and (b) inertial time scale (f_i) with Re for different Ma for $\eta = 0.5$, $Pr = 1$; dimensionless time period (c) $\tau_v = 1/f_v$ and (d) $\tau_i = 1/f_i$.

3.4.1 Effect of ramp up and ramp down: subcritical bifurcation

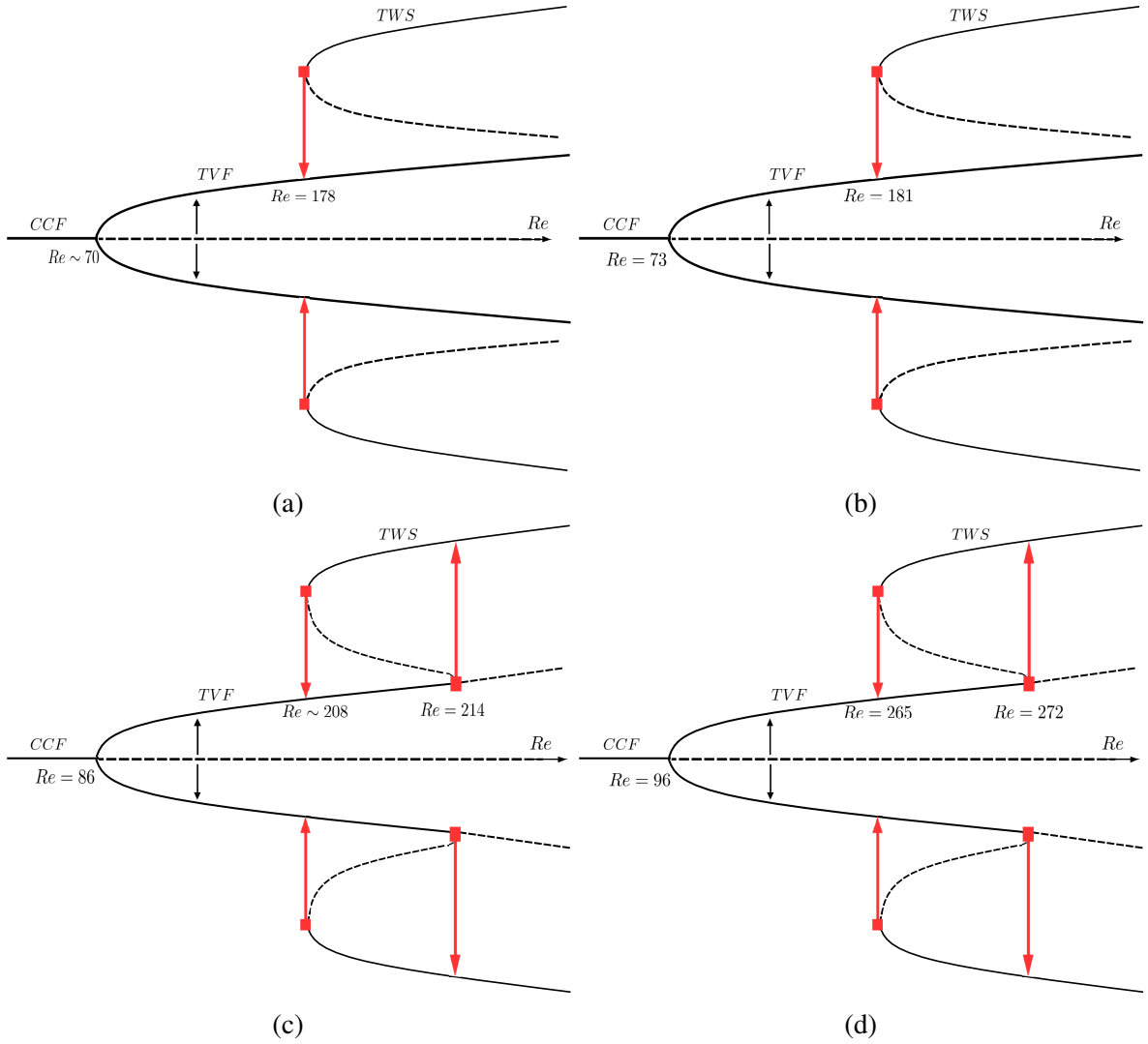

Fig. 3.14 Schematic of bifurcation diagram at (a) $Ma = 0.5$; (b) $Ma = 1$; (a) $Ma = 2.5$; and (d) $Ma = 3$ for $\eta = 1/2$; Ramp-rate of upsweep and downsweep runs are $dRe/dt \sim 0.45$, where t is the dimensionless time based on visous time scale.

In this section, we study the effect of quasi-static change in the Reynolds number (Re). It is a kind of continuation routine, implemented using the current finite-difference code. Figure 3.14 illustrates the schematic of bifurcation diagram at (a) $Ma = 1$; (b) $Ma = 3$ for $\eta = 1/2$; Re was changed in steps of $\Delta Re = 1$ after every 20000 time-steps, corresponding to a ramp-rate of $dRe/dt = 1/(5 \times 10^{-6} \times 20000 \times 22) \sim 0.45$, where t is the dimensionless time based on visous time scale. Figure 3.14 (a) shows that while performing upsweep protocol (slowly increasing the Re at the $dRe/dt \sim 0.45$), we do not encounter Travelling wave state

(TWS), and the flow remains as Taylor-vortex flow (TVF), over Re range we have reported for simulations starting from rest (see Figure 3.4). Interestingly, we encounter TVF while performing downsweep protocol (slowly decreasing the Re at the $dRe/dt \sim 0.45$) from the TWS state. This jump to TVF from TWS happens at $Re = 181$ for $Ma = 1$.

In order to study this typical behaviour further, we carried out simulations using the present DNS code for $Ma = 3$. (see figure 3.14 (b)) keeping all other parameters same. Figure 3.14 (b) shows that while performing upsweep protocol (slowly increasing the Re at the $dRe/dt \sim 0.45$), we encounter Travelling wave state (TWS) at $Re = 272$, following which the stationary TVF branch becomes unstable (see dotted black line in figure 3.14 (b)). On the other hand, we encounter TVF while performing downsweep protocol (slowly decreasing the Re at the $dRe/dt \sim 0.45$) from the TWS state. This jump to TVF from TWS happens at $Re = 265$, forming a finite hysteris loop, between $Re = 265$ and $Re = 272$ (see the region between two red lines in figure 3.14 (b)).

Uniqueness: For a higher ramping rate of $dRe/dt \sim 10$, performing the upsweep protocol at $Ma = 1$, we encounter the transition from TVF to TWS regime. This can be attributed to the fact that more energy is required to pump into the system using shear work, in order to switch from TVF to TWS branch. However, while performing the downsweep run, irrespective of ramp rate ($dRe/dt \sim 10$ or $dRe/dt \sim 0.45$), the system relaxes to the stationary TVF state. It also explains the reason why we have observed Travelling Wave solution (TWS) when the system was started from rest. Interestingly, the system starting from rest and reaching a particular state in the phase space (such as in Fig. 3.4) in the very next time step corresponds to a large magnitude of ramping rate ($dRe/dt = 1/(5 \times 10^{-6} \times 1 \times 22) \sim 9000$).

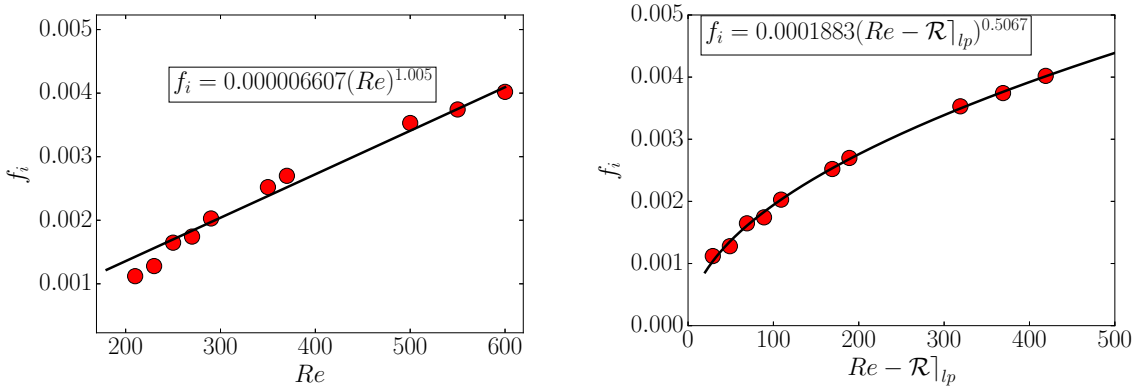

(a) (b)

Fig. 3.15 Scaling of frequency of Travelling Wave solution (TWS) based on inertial time scale $(1/\omega_1)$, (a) with the Reynolds number (Re), (b) with the distance from the limit point $(Re - \mathscr{R}]_{lp})$. The control parameters are $\eta = 1/2$, $\Gamma = \pi/2$, $Ma = 1$ and $Pr = 1$.

Figure 3.15 shows the scaling of frequency of Travelling Wave solution (TWS) based on inertial time scale $(1/\omega_1)$ with the (a) Reynolds number (Re), and (b) distance from the limit point $(Re-\mathscr{R}]_{lp})$. The control parameters are $\eta = 1/2$, $\Gamma = \pi/2$, $Ma = 1$ and $Pr = 1$. For $Ma = 1$, we define the limit point (lp) as the Re corresponding to $TWS \longrightarrow TVF$ transition while performing the downsweep runs. For $Ma = 1$, based on panel (a) of figure 3.15; the Reynolds number at the limit point is:

$$\mathscr{R}]_{lp} = 181 \tag{3.15}$$

$$f_i = \alpha(Re)^{\beta} \tag{3.16}$$

and, the found as scaling of the inertial frequency with the distance from the limit point $(Re-\mathscr{R}]_{lp})$ is:

$$f_i = \alpha(Re-\mathscr{R}]_{lp})^{\beta} \tag{3.17}$$

The coefficients α and β are determined by least-square fitting all data of f_i vs (Re) using Eqn. (3.16), with $\alpha \approx 0.000006607$ and $\beta \approx 1.005$, in the 95% confidence bound for $\alpha \in [5.07\times10^{-7}, 1.27\times10^{-5}]$ and $\beta \in [0.8528, 1.156]$. The coefficients α and β are determined by least-square fitting all data of f_i vs $(Re-Re_{lp})$ using Eqn. (3.17), with $\alpha \approx 0.0001883$ and $\beta \approx 0.5067$, in the 95% confidence bound for $\alpha \in [0.0001642, 0.0002123]$ and $\beta \in [0.4835, 0.5298]$, utilising the MATLAB software.

3.5 Summary

We have studied compressible Taylor-Couette flow of an ideal gas and investigated the effect of Mach number (Ma) on the onset of axisymmetric instabilities for a radius ratio of $\eta = 0.5$ and an aspect ratio of $\Gamma = \pi/2$, with periodic boundary conditions along the axial direction. For the pure driving of the inner cylinder $(Re_i > 0)$ and stationary outer cylinder $(Re_o = 0)$, we find compressibility stabilises. Emergence of alternate regions of rarified and dense layers are identified from the axial density density (ρ) profile and the extent of axial stratification is found to increase with Re at larger Ma. For a given Re, the radially outward jet at the mid-height is accompanied by lower density and the radially inward jets are accompanied by higher density. We also find that compressibility diminishes the axial (Q_z), radial (Q_r) and azimuthal (Q_θ) transport for the current fluid system. Beyond Taylor vortex flow (TVF), low frequency axially propagating waves have been found and a comprehensive phase diagram in (Re, Ma)-plane is plotted that summarized these findings.

We find that the frequency, based on the inertial time scale f_i, of Travelling Wave solution (TWS) scales with the distance from the limit point $(Re - \mathscr{R}\rceil_{lp})$ as $f_i \propto (Re - \mathscr{R}\rceil_{lp})^{0.5}$, for $\eta = 1/2$, $\Gamma = \pi/2$, $Ma = 1$ and $Pr = 1$. It is noted for slow ramp-up $(dRe/dt < 1)$, the Travelling Wave solution (TWS) is not encountered, it remains as a disconnected branch. This previously has not been found in incompressible TCF and our conjecture is that this branch is disconnected in strictly incompressible limit $(Ma = 0)$ and connected for any finite value of Mach number $(Ma > 0)$. Further analysis is required to shed light on these issues, which will constitute a considerable extension of the present work.

Chapter 4

Axisymmetric Compressible TCF: Effect of Radius Ratio on Flow Patterns

4.1 Introduction

Previous chapter deals with the pattern-formation scenario in axisymmetric compressible Taylor-Couette flow (TCF) of an ideal gas, with rotating inner cylinder ($Re_i > 0$) and stationary outer cylinder ($Re_o = 0$) with axially periodic boundary conditions. We study the effects of variation of the radius ratio ($\eta = r_1/r_2$) on pattern transition and compressibility (Ma) for a fixed height of the computational box ($h = \pi/2$) on the observed patterns in compressible TCF. Numerical simulations starting from resting initial conditions are performed upto $Re = 800$ for six different radius ratios ($0.3 \leq \eta \leq 0.8$). It is shown that the compressibility primarily affects the density distribution within the gap between two rotating cylinders by causing an accumulation of mass near the stationary outer cylinder and plays a pivotal role in restraining the onset of instability. Axially propagating waves have been found and a comprehensive phase diagram in (Re, Ma)-plane is plotted that summarizes these findings.

Figure 4.1 shows the stability boundary obtained by Esser & Grossmann (1996) that holds for axially periodic incompressible Taylor-Couette flow. The critical Reynolds number (Re^{cr}) is evaluated using the expression (Esser & Grossmann, 1996) for case of stationary outer cylinder ($Re_o = 0$),

$$Re^{cr} = \frac{1}{\sigma^2} \frac{(1+\eta)^2}{2\eta\sqrt{(1-\eta)(3+\eta)}}, \tag{4.1}$$

where, σ is a constant factor,

$$\sigma = 0.1556. \tag{4.2}$$

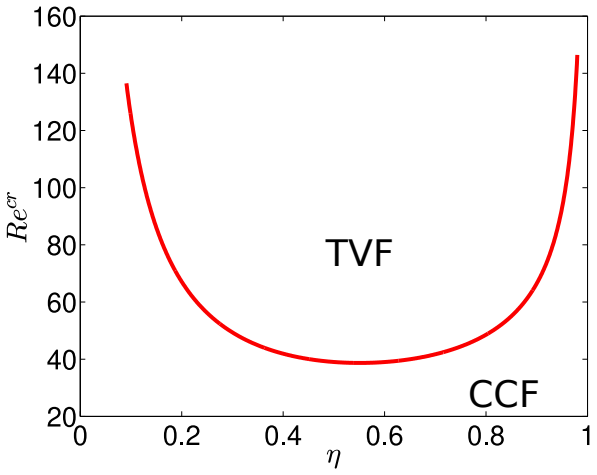

Fig. 4.1 Stability boundary obtained by Esser & Grossmann (1996) that holds for axially periodic incompressible TCF. CCF (circular Couette flow) and TVF (Taylor vortex flow).

In this chapter, we seek answers to two questions: (i) how does the radius ratio (η) and the Mach number (Ma) affect the critical Reynolds number $Re^{cr}(Ma,\eta)$ for the onset of flow patterns from base state of circular Couette flow (CCF) in contrast to the situation in the incompressible fluid systems, for a fixed Prandtl number $(Pr = 1)$ and axial wavenumber $(k = 4)$? (ii) What are the secondary bifurcation scenarios associated with different radius ratio (η) for $Ma = 1$?

4.2 Numerical Procedure

All simulations are carried out with axially periodic boundary conditions along with no-slip and Dirichlet boundary condition for velocities (u,v,w) and temperature T, respectively, at the inner and outer cylinder. The length of computational domain used is $\pi/2$ and the radius ratio (η) is changed by varying the radial location of the outer cylinder (r_2) keeping the radius of the inner cylinder (r_1) at unity $(r_1 = 1$ and $r_2 = 1/\eta)$. This in turn changes the aspect ratio $(\Gamma = h/(r_2 - r_1))$ from $\Gamma(\eta = 0.3) = 3\pi/14$ to $\Gamma(\eta = 0.8) = 2\pi$ (see the upper horizontal axis in figure 4.2). Phase diagrams of patterns are portrayed in the (Re,η) plane for unit Mach number (Ma) and Prandtl number (Pr). In this process of keeping the radius of the inner cylinder constant and changing the outer cylinder radius, the length scale of the current problem changes. Instead of the length scale being the gap-width $(\delta = r_2 - r_1)$ between two cylinders, the inner cylinder radius (r_1) is taken as the reference length scale. Accordingly, we define the Reynolds number, Re_{r_1}, based on inner cylinder radius as follows:

$$Re_{r_1} = \frac{\omega_1 r_1^2}{\nu_r}. \tag{4.3}$$

We use the above definition of Re_{r_1} (to be followed hereafter till the end of this section). Recall that changing the length scale does not change the physics of the flow, henceforth an one to one correspondence can be obtained between the Re_{r_1} and Re (see equation 4.4). While performing the simulations, we varied Re_{r_1} at different η and later scaled Re_{r_1} back to Re using the relation described below:

$$Re = \frac{\omega_1 r_1^2}{\nu_r} = \left(\frac{\omega_1 r_1^2}{\nu}\right)\left(\frac{\delta}{r_1}\right) = \left(\frac{1}{\eta} - 1\right) Re_{r_1}. \tag{4.4}$$

We present detailed phase diagrams of patterns in the (Re, η) plane for $Ma = 1$ and $Pr = 1$. The resolution tests for various radius ratio $\eta = 0.5$ to $\eta = 0.8$ are described in Table B.3 to Table B.6 of Appendix B.

4.3 Phase Diagram of Flow Patterns: Stationary and Non-Stationary States

Figure 4.2 summarizes all patterns for a range of radius ratio $\eta = r_1/r_2 \in$ (0.3,0.8) that have been obtained from the simulations starting from the resting initial conditions by changing Re $\in$ (50,800). The Taylor vortices having different number of rolls are marked by the following symbols - plus (blue) for 2 rolls, square (black) for 4 rolls, square (half-filled black) for 4 rolls, hexagon (green) for 6 rolls, octagon (pink) for 8 rolls. The non-stationary patterns are marked using red star (localized vortex oscillations) and ∞ symbol (travelling wave solutions). In comparison to the results presented in Chapter 3, a new non-stationary state, called LVO, has been identified at $\eta \sim 0.6$.

Figure 4.3 shows the magnified region in the (Re, η) plane, focussing on the transition from the base state of circular Couette flow (CCF) to Taylor Vortex flow (TVF) across different radius ratios ranging from wide gap $(\eta = 0.3)$ to narrow gap $(\eta = 0.8)$. The filled yellow coloured circular markers joined using the dash-dotted line shows the critical isoline marking the transition from $CCF \longrightarrow TVF$ for the incompressible case; we use $Ma = 0.1$ in order to characterize the transition in case of incompressible Taylor-Couette for the identical geometrical parameters. The filled red coloured markers joined by dashed line characterize the transition scenario for the case of $Ma = 1$. The critical Reynolds number for $CCF \longrightarrow TVF$ transition varies non-monotonically within, with a minimal at $\eta \approx 0.5$. This is similar to the incompressible TCF, Esser & Grossmann (1996).

We define a quantity ΔRe, where

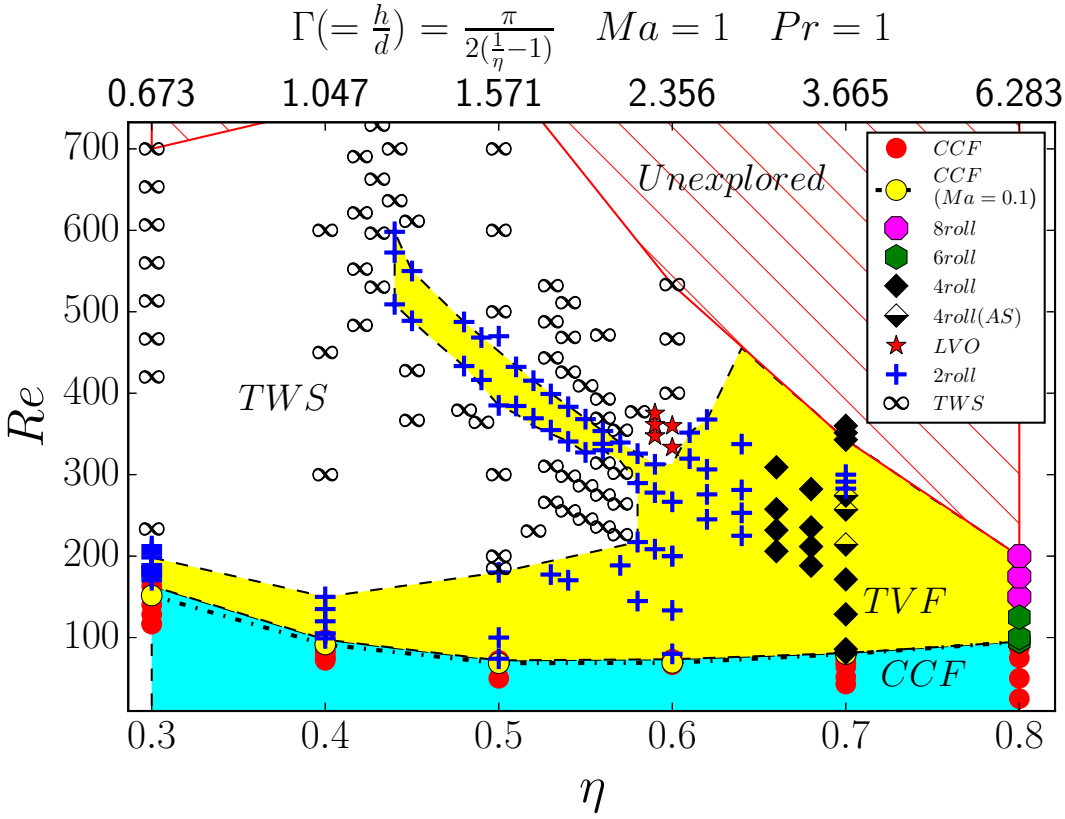

Fig. 4.2 Phase diagram of patterns illustrating the dependence of critical Reynolds numbers on radius ratio, η, for $Ma = 1$ and $Pr = 1$; the dotted line with yellow markers corresponds to $Ma = 0.1$. All states have been identified by starting simulations from the rest state. *CCF* (circular Couette Flow); *TVF* (Taylor Vortex Flow); *TWS* (Travelling Wave Solution); LVO (Localized Vortex Oscillations).

$$\Delta Re = Re^{cr}(Ma = 1) - Re^{cr}(Ma = 0.1) \tag{4.5}$$

is the difference between the critical Re between the compressible $(Ma = 1)$ and incompressible $(Ma = 0.1)$ TCF. Figure 4.4 shows the plot of ΔRe versus η. It is seen that the magnitude of ΔRe decreases with increasing η which implies that compressiblity (Ma) effects are less significant in smaller gap-width, TC-cell as the diffusive effects become dominant at $\eta \longrightarrow 1$. This later observation is similar to the linear stability results of Manela & Frankel (2007).

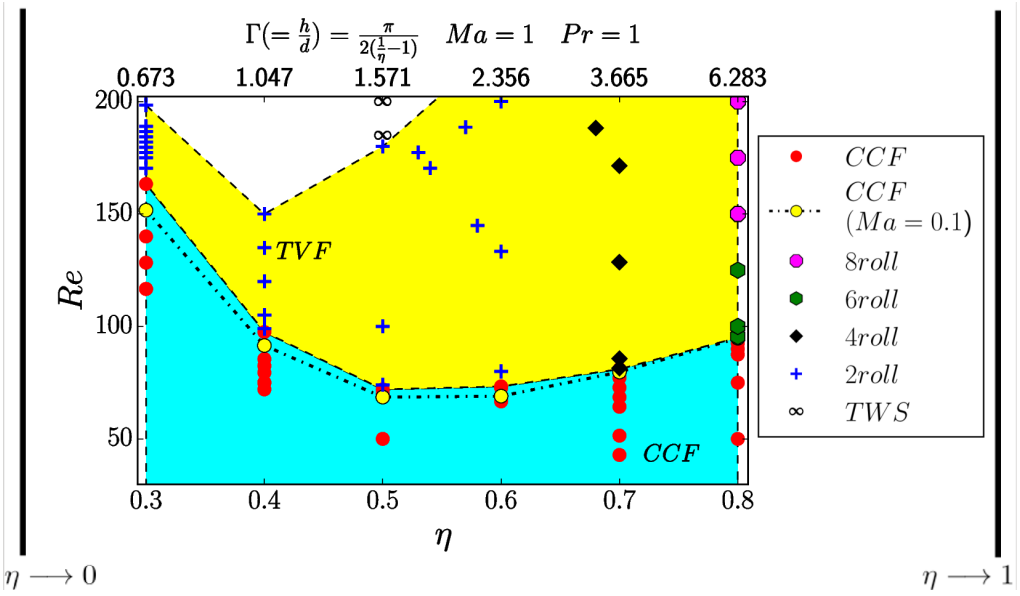

Fig. 4.3 Magnified phase diagram illustrating the dependence of Reynolds number on radius ratio; plotted as a function of Reynolds number of the inner cylinder rotation (Re) versus the radius ratio (η); The dashed line shows transition from $CCF \longrightarrow TVF$ with variation of η for $Ma = 1$; dash-dotted line with yellow circular markers shows the transition from $CCF \longrightarrow TVF$ for $Ma = 0.1$

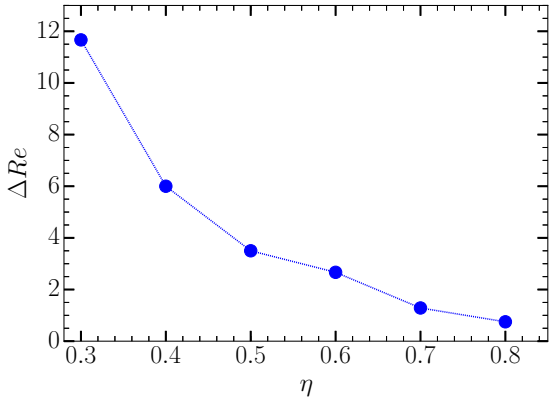

Fig. 4.4 Plot of ΔRe versus η, where $\Delta Re = Re^{cr}(Ma = 1) - Re^{cr}(Ma = 0.1)$, Eqn. (4.5), is the magnitude of difference between the critical Re as a function of radius ratio (η) between the compressible $(Ma = 1)$ and incompressible $(Ma = 0.1)$ TCF. The magnitude of ΔRe decreases with increasing η.

4.3.1 Flow Patterns at moderate to narrow gap

Occurrence of localized oscillations

In figure 4.2, we found the occurrence of localized oscillations in the present fluid system for a range of Reynolds number $Re \in [333, 375]$ for radius ratios of $\eta \in [0.59, 0.6]$. Figures 4.5 (a) and 4.5 (b) show the time evolution of (a) radial kinetic energy KE_u and (b) axial kinetic energy KE_w, (see equation 2.31 in Chapter 2), the grid-points along axial and radial directions $(N_z \times N_r)$ are taken to be 101×101. Figure 4.5(c) shows the space-time plot of radial velocity (u) at the mid-gap along the mid-height $(r = r_1 + \delta/2)$ of localized oscillations for $Re = 333$, $\eta = 0.6$, $Ma = 1$ and $Pr = 1$. The red color in the plot shows the location of radially outward jet which is no longer at the mid-height of the computational domain.

The time period (τ) of these localized oscillation is $\tau = 0.043$ and the corresponding dimensionless frequency, based on viscous time scale, is $f_v = 23.31$.

Figure 4.5(d) shows the velocity vectors on (r, z) plane superimposed on temperature contour plots over one cycle of oscillation.

Existence of perfect pitchfork bifurcation $CCF \longrightarrow TVF$

In an infinite cylinder, or, a periodic system in computations of TCF, the onset of Taylor vortex flow (TVF) from circular Couette flow (CCF), admits a perfect pitchfork bifurcation (Andereck *et al.* (1986)). The amplitude equation for such bifurcatio, up-to cubic order in amplitude $\mathscr{A}$, can be written as (Golubitsky *et al.* (2012), Strogatz (2001)):

$$\frac{d\mathscr{A}}{dt} = \alpha_1 \mathscr{A} + \alpha_2 \mathscr{A}^3, \tag{4.6}$$

where $\mathscr{A}$ is the order parameter and α_1 and α_2 are functions of Re, etc. The equilibrium amplitude $(d\mathscr{A}/dt = 0)$ is given by:

$$\mathscr{A}_{eq} = \pm\sqrt{\frac{-\alpha_1}{\alpha_2}} \sim \sqrt{Re - Re^{cr}} \tag{4.7}$$

For the present system, the order parameter $\mathscr{A}$ could be taken as the radial velocity (u) at the mid-gap and mid-height of the computational domain. The positive and negative signs of $\mathscr{A}$ correspond to the existence of Taylor-rolls with radially outward and radially inward jet at the mid-height of the computational domain, respectively. Equation (4.7) suggests that the equilibrium amplitude can be measured as a function of the distance from bifurcation point.

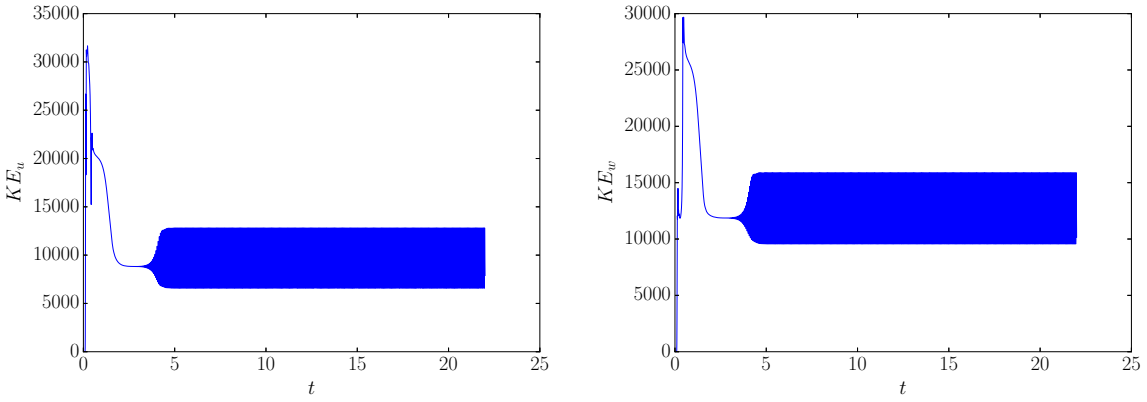

(a) (b)

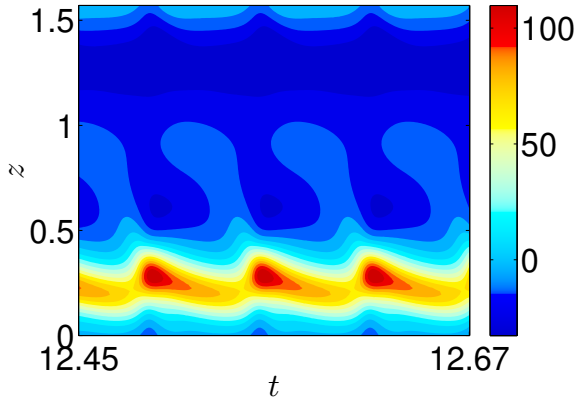

(c)

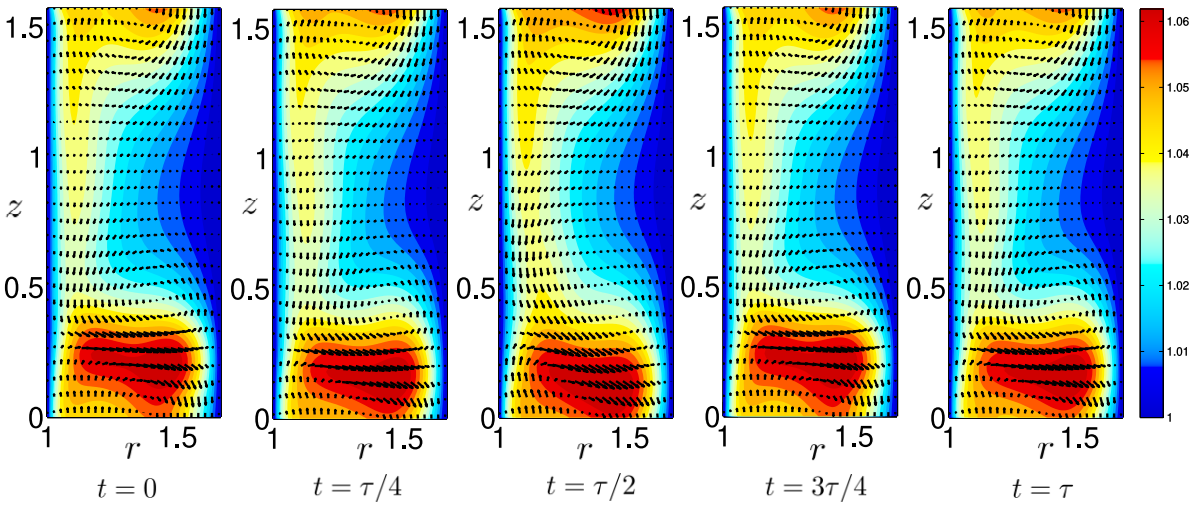

(d)

Fig. 4.5 Time evolution for (a) radial kinetic energy KE_u; (b) axial kinetic energy KE_w, (see equation 2.31 in Chapter 2), the grid-points along axial and radial directions $(N_z \times N_r)$ are 101×101. (c) Space-time plot of radial velocity (u) at the mid-gap along the mid-height $(r = r_1 + \delta/2)$ of localized oscillations. (d) Velocity vectors on (r,z) plane are superimposed on temperature contour plots over one cycle of oscillation for $Re = 333$, $\eta = 0.6$, $Ma = 1$ and $Pr = 1$.

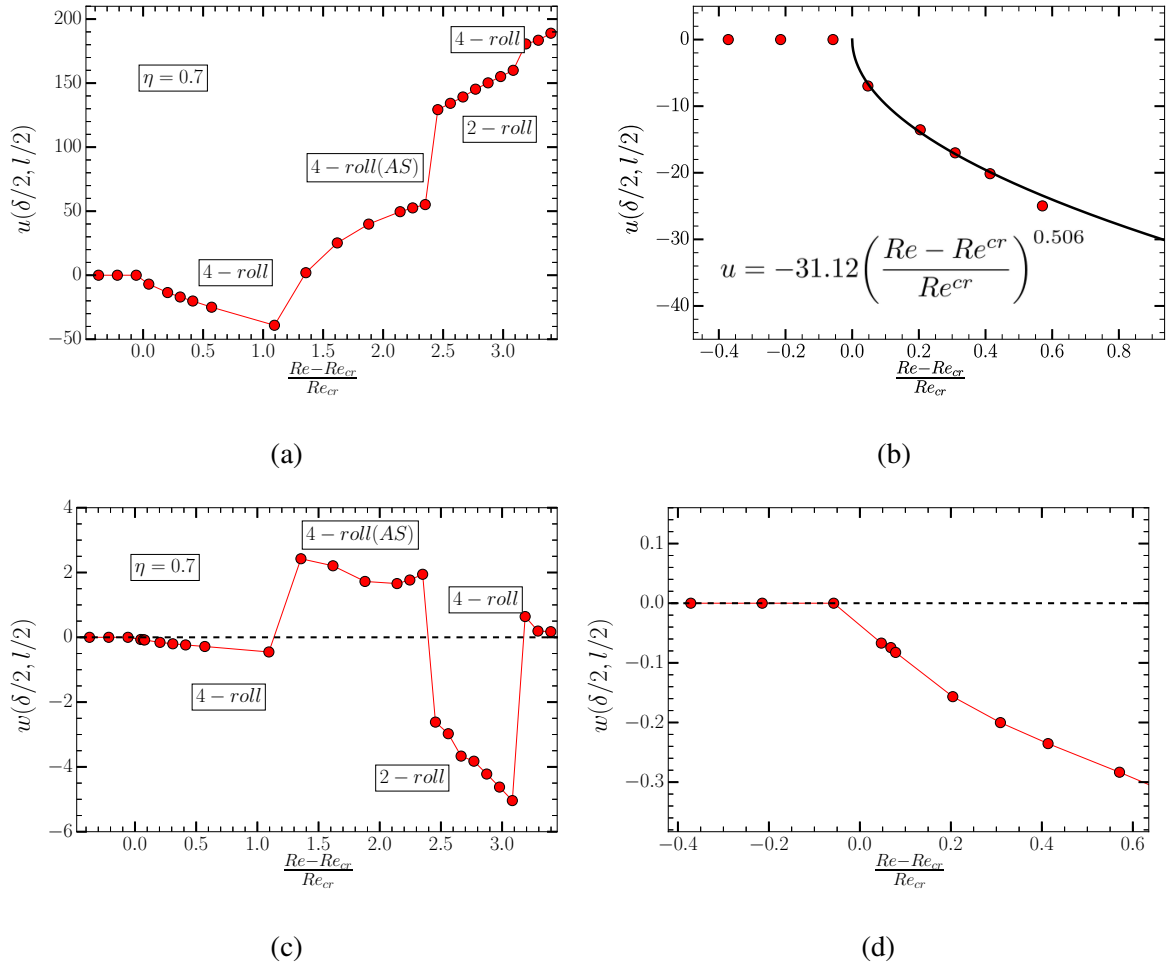

Fig. 4.6 Variations of (a) the radial velocity at mid-height and mid-plane with Re, (b) its magnified view near primary bifurcation. The exponent α, where u $\propto \left(\frac{Re-Re_{cr}}{Re_{cr}}\right)^{\alpha}$, comes out to be 0.506 close to the $CCF \longrightarrow TVF$ bifurcation with 95% confidence bounds $\alpha \in [0.4753, 0.5366]$; (c) Axial velocity (w) at the mid-height and mid-plane with Re, and its (d) the magnified part showing $CCF \longrightarrow TVF$ transition; the black dotted line shows the zero axial velocity (w) line for perfectly symmetric Taylor vortices about the mid-height.

Figures 4.6 (a,b) and 4.7 (a,b) show the variation of radial velocity (u) at the mid-gap and mid-height of the domain with the normalized distance from the bifurcation point,

$$\varepsilon = \frac{Re - Re^{cr}}{Re^{cr}} \tag{4.8}$$

for radius ratios of $\eta = 0.7$ and $\eta = 0.8$, respectively. Figure 4.6(b) and figure 4.7(b) are magnified portion of figure 4.6(a) and figure 4.7(a), respectively, showing the onset of Taylor-vortices from CCF. It is noted that, the exponent β, where

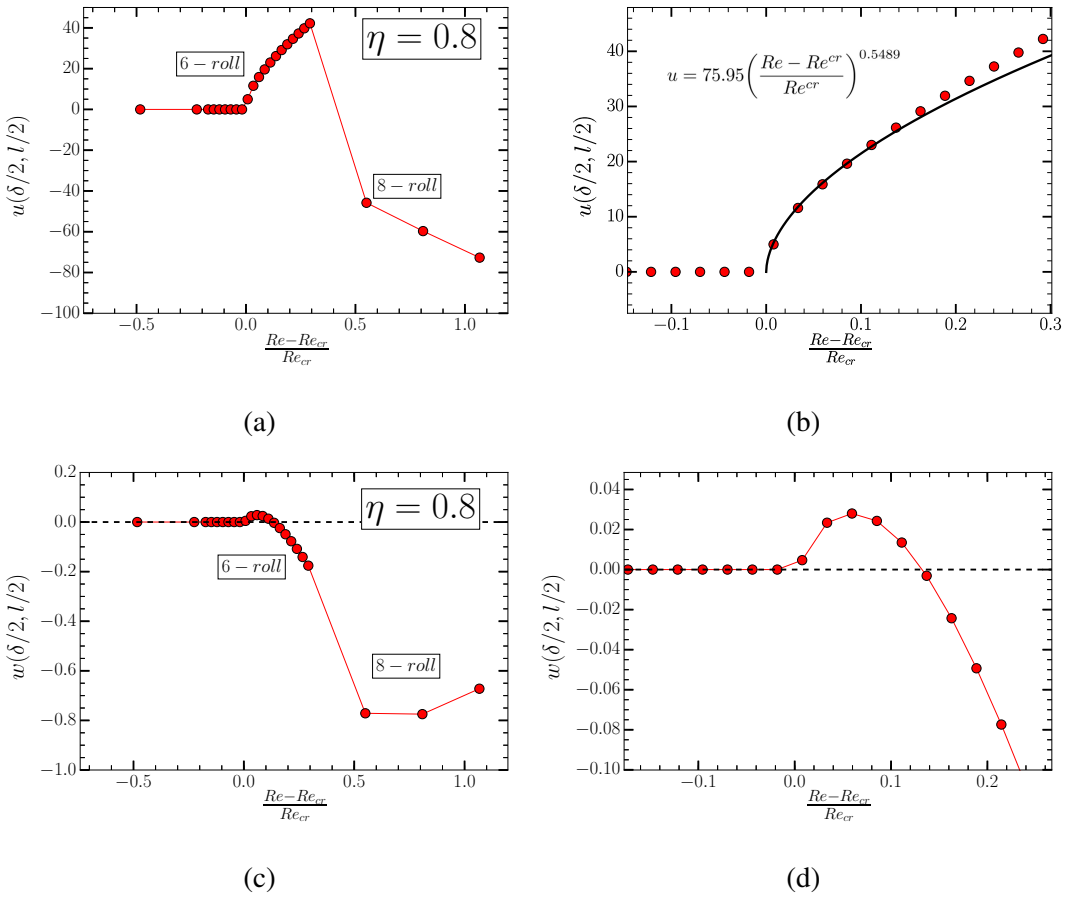

Fig. 4.7 Same as figure 4.6, but for $\eta = 0.8$. The exponent α, where u $\propto \left(\frac{Re-Re_{cr}}{Re_{cr}}\right)^{\alpha}$, comes out to be 0.5489 close to the $CCF \longrightarrow TVF$ bifurcation with 95% confidence bounds $\alpha \in [0.4801, 0.6176]$.

$$u = \alpha\left(\frac{Re - Re_{cr}}{Re_{cr}}\right)^{\beta}, \tag{4.9}$$

is determined using least-square fitting. From figure 4.6(b) $\alpha \approx -31.12$ and $\beta \approx 0.506$, in the 95% confidence bound for $\alpha \in [-32.65, -29.59]$ and $\beta \in [0.4753, 0.5366]$, utilising the MATLAB software. Similarly, from figure 4.7(b) $\alpha \approx 75.95$ and $\beta \approx 0.5489$, in the 95% confidence bound for $\alpha \in [62.07, 89.82]$ and $\beta \in [0.4801, 0.6176]$.

The exponent close to the bifurcation from $CCF \longrightarrow TVF$ comes out to 0.5, which shows that the present system follows the amplitude scaling of cubic-Landau equation (4.6).

Asymmetric Taylor Vortices

In the phase diagram in figure 4.2, we found the existence of asymmetric 4-roll state at $\eta = 0.7$. Figure 4.8 shows flow structures illustrating density (ρ) contours with the arrows showing the flow in meridional $(r-z)$ plane with magnitude of $\sqrt{u^2+w^2}$ denoted in the length of arrow: (a) $Re = 86$ (4 roll) with radially inward jet at the mid-height; (b) $Re = 214$ (assymetric 4 roll); (c) $Re = 300$ (2 roll) and (d) $Re = 343$ (4 roll) with radially outward jet at the mid-height. The blue colour denotes lower density and the red colour denotes higher density. Streamline plots have been created using the surface LIC module of the *paraview* Software (Ahrens *et al.*, 2005). Figure 4.8 (b) shows Taylor rolls with different vortex sizes stacked along the axial extent of the periodic domain - this is called asymmetric 4-roll state.

In order to quantify the asymmetry of vortices far from the bifurcation point $(Re - Re^{cr})/Re^{cr}$, we plot the variation of axial velocity (w) at mid-height and mid-plane with Re (see panel (c) and (d) of figure 4.6). For asymmetric four roll structure, we see the axial velocity (w) at mid-height and mid-plane to be positive in magnitude, also evident from the panel (b) of figure 4.8, because of axially downward shift in Taylor vortices. This flow structure is robust and has been checked with different grid sizes (see Appendix B for detailed simulations). This asymmetry can be attributed to the choice of domain length as described in Meyer (1967). Meyer (1967) carried out numerical simulations for axisymmetric incompressible TCF for Reynolds number based on inner cylinder, $Re_{r_1} = \omega_i r_1^2/\nu = 2000$, $\eta = 0.833$ and stationary outer cylinder, for two different domain lengths and concluded that there is insufficient freedom in a restricted domain pertaining to the genesis of asymmetries, which provides evidence for preferred length.

Following the asymmetric four roll state, we encounter a pair of symmetric vortices about the mid-height of the computational domain, see figure 4.8 (c) for $Re = 300$. However figure 4.6 (c) shows a large negative magnitude of axial velocity (w) at mid-height and mid-plane, and this is attributed to the structure of Taylor rolls. The centers of Taylor rolls do not lie along the mid-gap, and are placed towards the outer cylinder, along with a small axial shift; consequently, the magnitude of axial velocity (w) at mid-height and mid-plane turns out to be negative.

For a radius ratio of $\eta = 0.8$, we find three symmetric pairs of rolls as the primary roll state from purely azimuthal circular Couette flow. Figure 4.7 shows the variations of (c) axial velocity (w) at the mid-height and mid-plane with Re, and its (d) the magnified part showing $CCF \longrightarrow TVF$ transition; the black dotted line shows the zero axial velocity (w) line for perfectly symmetric Taylor vortices about the mid-height. The axial velocity (w) at mid-height and mid-plane initially turns out to be positive and later negative with increasing Re, purely because of axial displacement in Taylor rolls. Figure 4.9 portays the flow structures illustrating ρ contours with the arrows showing the flow in meridional $(r-z)$ plane with magnitude of

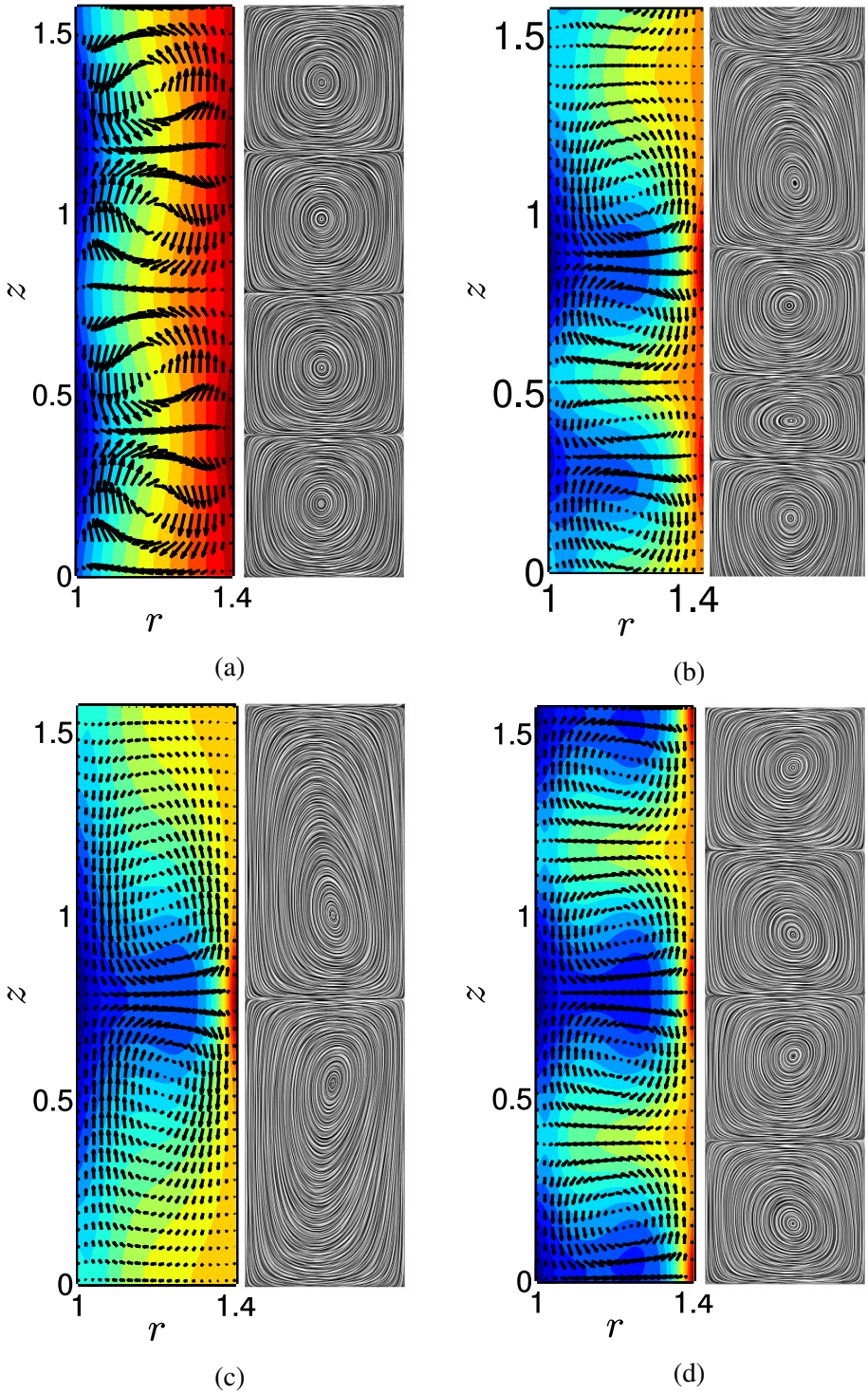

Fig. 4.8 Flow structures illustrating density (ρ) contours with the arrows showing the flow in meridional $(r-z)$ plane with magnitude of $\sqrt{u^2+w^2}$ denoted by the length of arrow; (a) $Re = 86$ (4 roll) with radially inward jet at the mid-height; (b) $Re = 214$ (assymetric 4 roll); (c) $Re = 300$ (2 roll) and (d) $Re = 343$ (4 roll) with radially outward jet at the mid-height. The blue colour denotes lower density and the red colour denotes higher density. Streamline plots have been created using the surface LIC module of software *paraview* (Ahrens *et al.*, 2005).

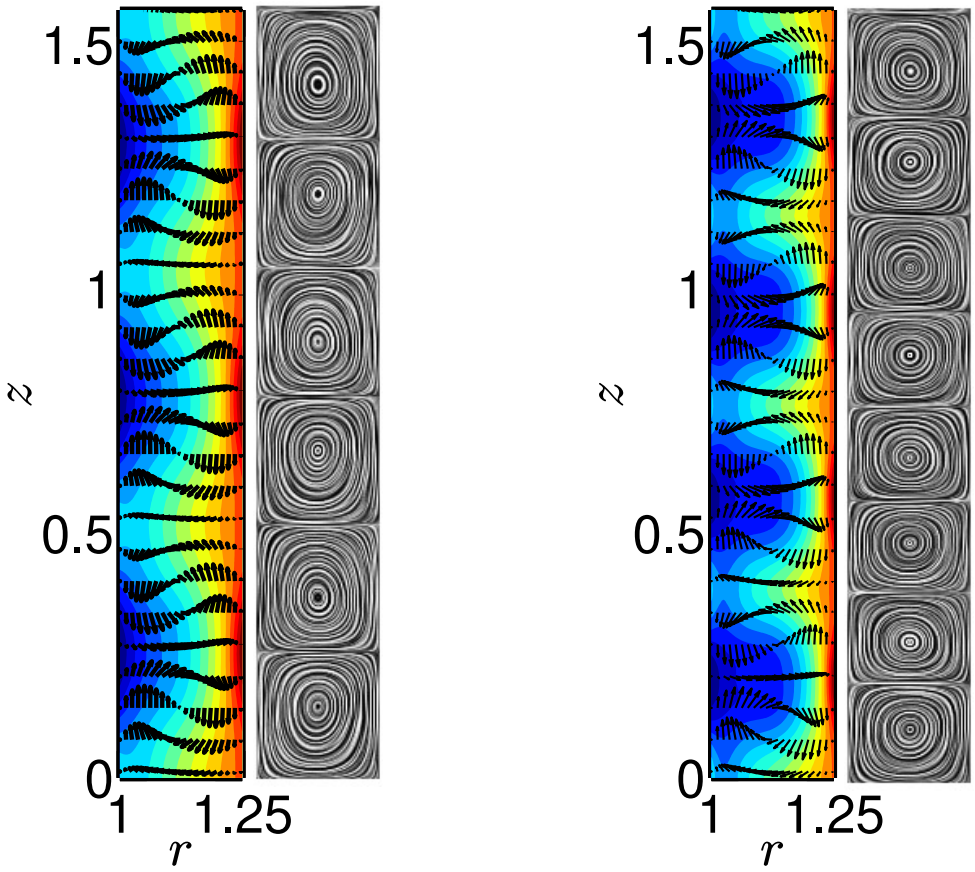

(a) (b)

Fig. 4.9 Flow structures illustrating ρ contours with the arrows showing the flow in meridional $(r-z)$ plane with magnitude of $\sqrt{u^2+w^2}$ denoted by the length of arrow; (a) $Re = 125$ (6 roll) and (b) $Re = 200$ (8 roll). The blue colour denotes lower density and the red colour denotes higher density. Adjacent panels on the right hand side of contour plots show the streamline plot created using surface LIC module of paraview software (Ahrens *et al.*, 2005).

$\sqrt{u^2+w^2}$ denoted by the length of arrow; (a) $Re = 125$ (6 roll) and (b) $Re = 200$ (8 roll). The blue colour denotes lower density and the red colour denotes higher density. Adjacent panels on the right hand side of contour plots show the streamline plot created using surface LIC module of paraview software (Ahrens *et al.*, 2005).

4.3.2 Flow patterns in short-cylinders

Here we discuss results corresponding to short-cylinders with aspect ratios of $\Gamma \leq O(1)$, which corresponds to $\eta = 0.3$ and $\eta = 0.4$. Figure 4.10 presents the flow structures illustrating the LIC streamline plots. Different points numbered on each panel refer to various instants over one cycle of oscillation (see the central panel). The control parameters are $\eta = 0.3$, $\Gamma = 0.673$

and $Re = 700$. The 2-roll vortex state breaks into a 4-roll state over the period of one cycle of oscillation and rejoins into a 2 roll state. Figure 4.11 shows the corresponding density colormaps with the arrows showing the flow in meridional (r,z) plane. The red colour shows higher density and blue colour shows lower density. The velocity vector plots reveal that the rolls near the inner cylinder are much stronger in comparison to the rolls formed near the outer cylinder ($O(10)$ larger in magnitude).

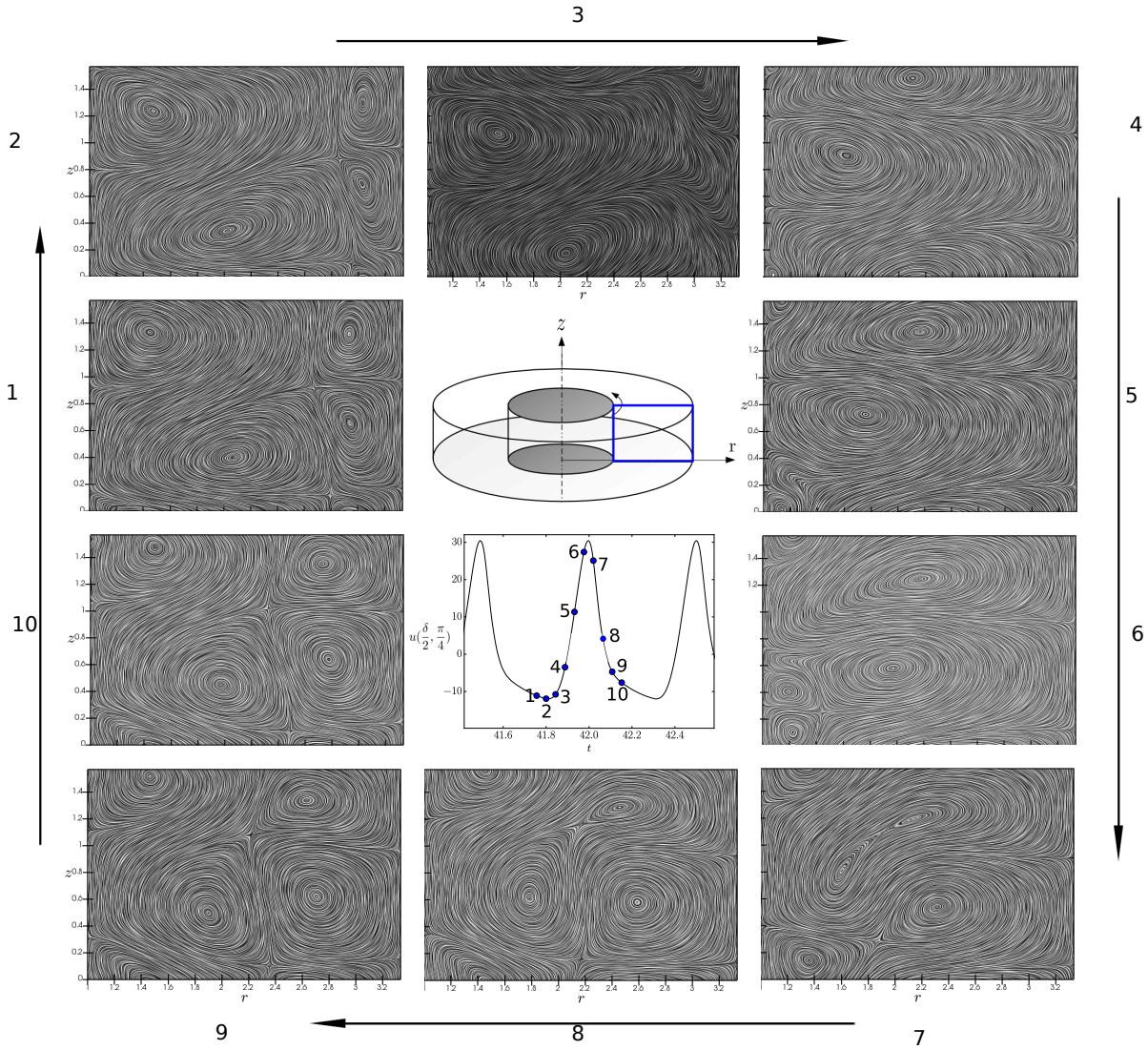

Fig. 4.10 Flow structures illustrating the streamline plot created using surface LIC module of paraview software (Ahrens *et al.*, 2005); different points numbered on the figure shows various instants over one cycle of oscillation (see the central panel); The control parameters are $\eta = 0.3$, $\Gamma = 0.673$ and $Re = 700$.

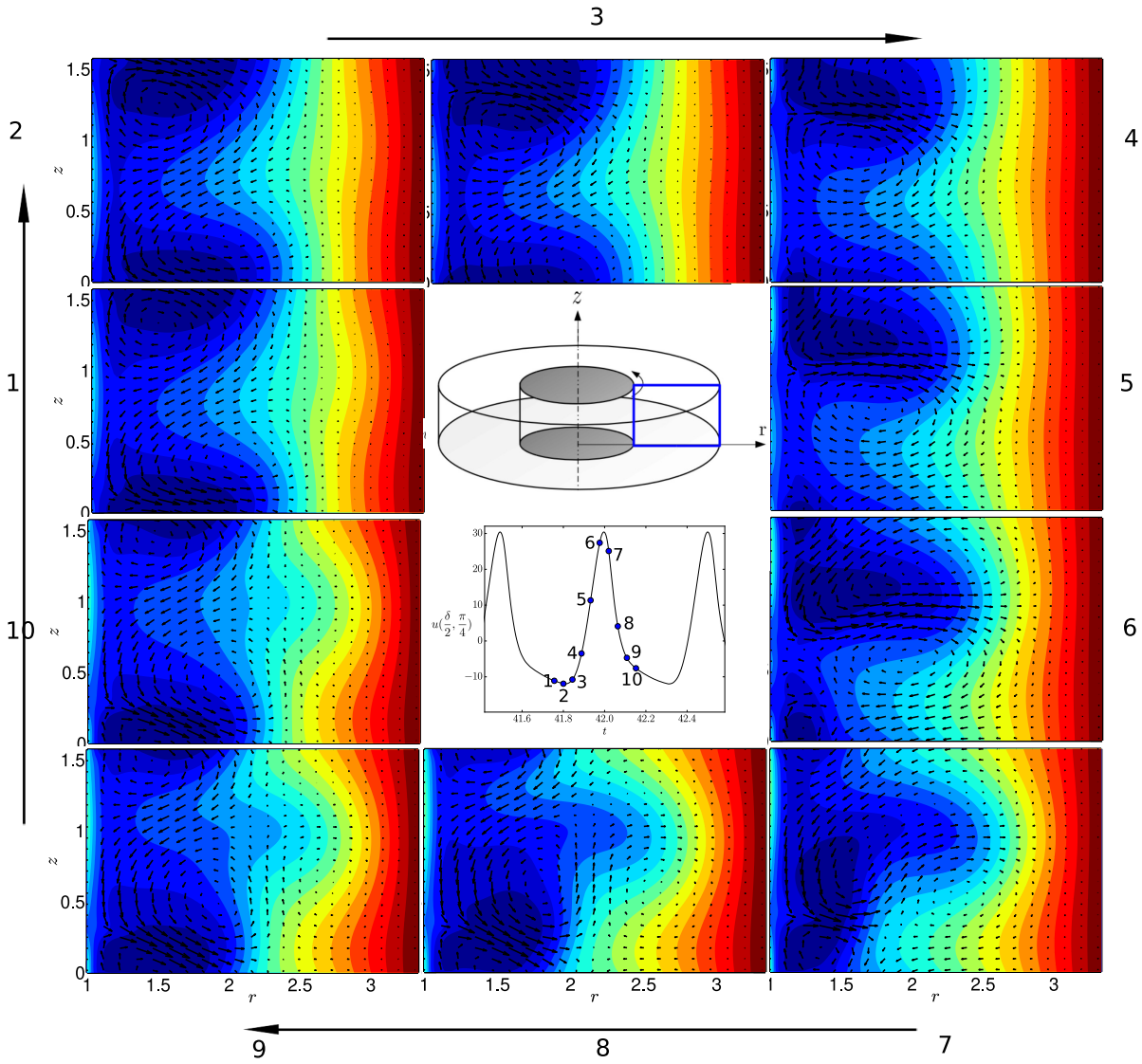

Fig. 4.11 Same as figure 4.10, but illustrates the density ρ contours with the velocity-vector maps showing the flow in meridional $(r-z)$ plane.

4.4 Torque scaling

A complimentary way to characterize the onset of Taylor rolls $CCF \longrightarrow TVF$ is look at the variation of the effective-nusselt (Nu_ω) number with the Reynolds number (Re). As described in the previous section, along with monitoring the radial velocity (u) at mid-height and mid-plane, we have computed the effective-nusselt (Nu_ω) near the inner cylinder. In this section, we present the dimensionless torque (Nu_ω) near the inner cylinder, as a function of Re for different radius ratios $(\eta = 0.5, 0.6, 0.7, 0.8)$. At higher Re (after the occurrence of Taylor vortices from CCF regime), the transport of angular momentum $(\mathscr{L} = \rho v r)$ is governed by simultaneous

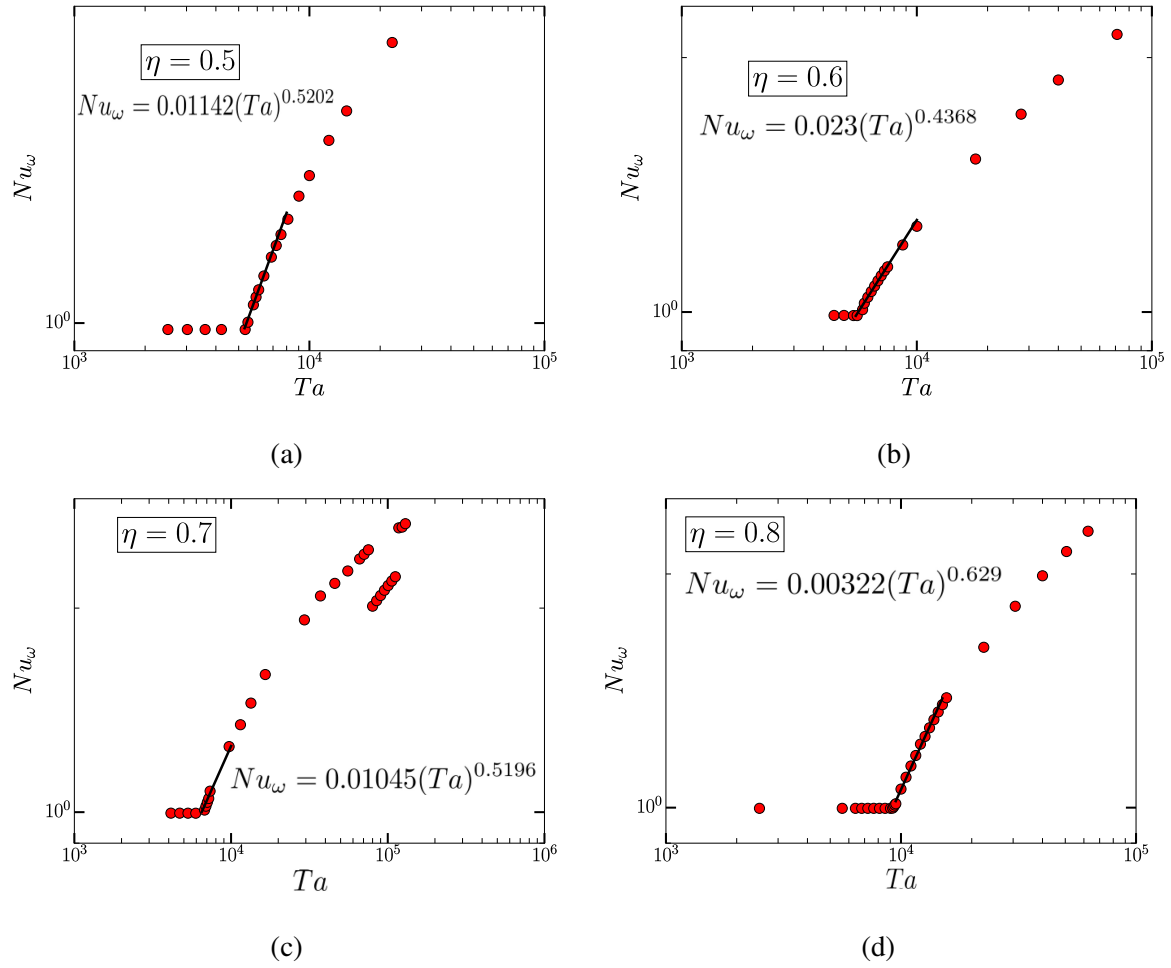

Fig. 4.12 Variation of effective-nusselt (Nu_ω) number as described in Eckhardt *et al.* (2007), with Ta corresponding to (a) $\eta = 0.5$, (b) $\eta = 0.6$, (c) $\eta = 0.7$ and (d) $\eta = 0.8$. The black line shows fitting $Nu_\omega = \alpha Ta^\beta$ close to the $CCF \longrightarrow TVF$ transition.

molecular and convective effects. In *CCF* regime, the radial $(u = 0)$ and axial velocities $(w = 0)$ over the domain is zero and the base flow is purely azimuthal $(v > 0)$ resulting in purely molecular transport of angular momentum $(\mathscr{L})$. With the onset of Taylor vortices, both radial $(u > 0)$ and axial velocities $(w > 0)$ become non-zero giving rise to large scale circulation in the (r,z) plane which increases with increasing Re. The convective transport of angular momentum comes into motion and with increasing Re, the convection effects become more pronounced. In analogous to the heat current in thermally driven Rayleigh Benard flow (RBF), Eckhardt *et al.* (2007) defined local angular momentum current(J^ω), which relates the sum of Reynolds stress $(< u, \omega >_{A(r),t})$ (convective transport) and the product of kinematic viscosity $(\nu = \mu/\rho)$ with the radial derivative of $< \omega >_{A(r),t}$ profile (molecular transport) as described below:

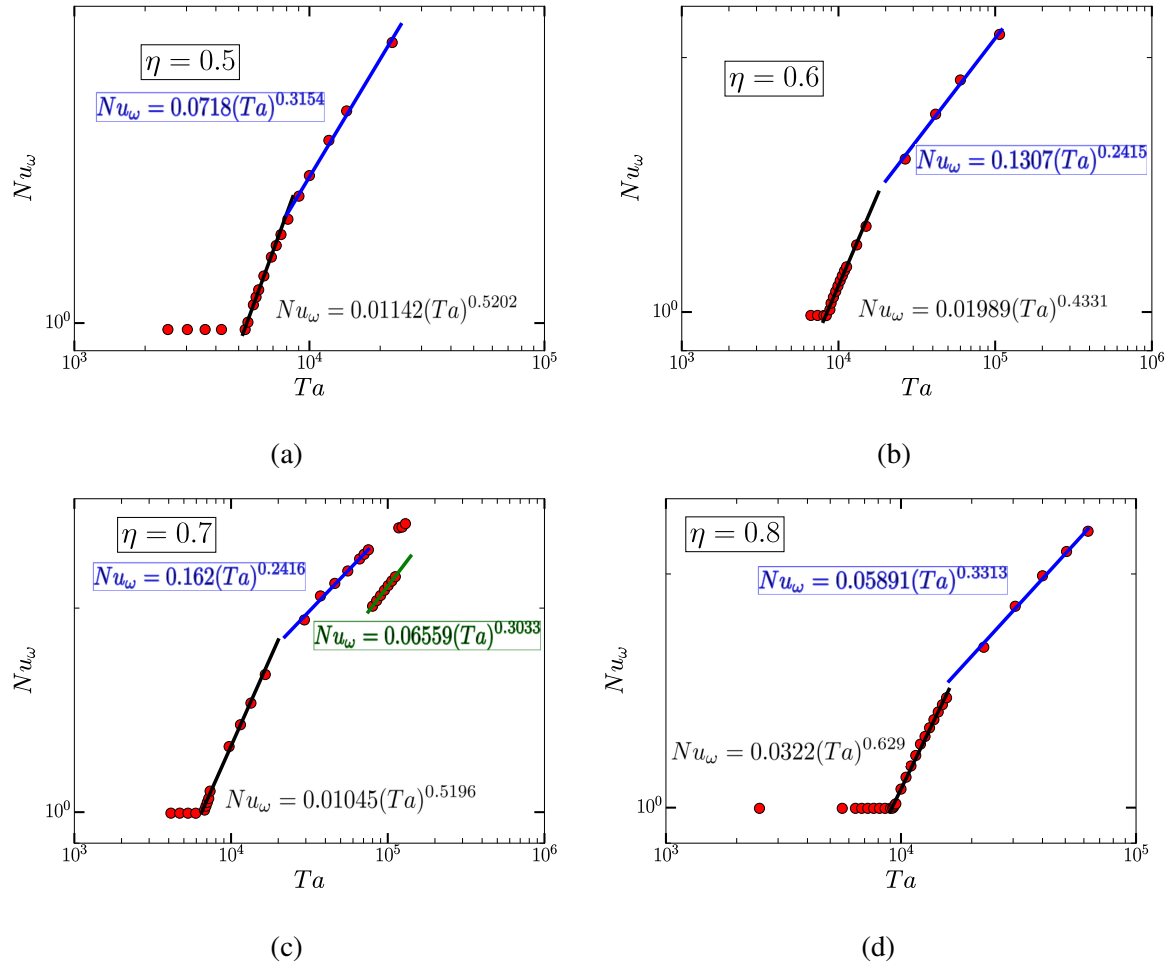

Fig. 4.13 Variation of effective-nusselt (Nu_ω) number as described in Eckhardt *et al.* (2007), with Ta corresponding to (a) $\eta = 0.5$, (b) $\eta = 0.6$, (c) $\eta = 0.7$ and (d) $\eta = 0.8$. The blue line shows fitting $Nu_\omega = \alpha Ta^\beta$ beyond the onset of TVF from CCF. The green line in panel (c) shows the scaling for 2 vortex state, which appears after 4-roll asymmetric state in $\eta = 0.7$.

$$J^\omega = r^3(\langle u\omega\rangle_{A(r),t} - \frac{\mu}{\rho}\frac{\partial}{\partial r}\langle\omega\rangle_{A(r),t}), \tag{4.10}$$

where, $\langle\ldots\rangle_{A(r),t}$ denotes a spatial average of cylindrical surface coaxial with the bounding cylinders of radius r, $(r_1 \leq r \leq r_2)$ and the temporal average. The first term in Eqn. (4.10) denotes Reynolds stress and the second term is transverse derivative of averaged angular momentum ($\mathscr{L} = \rho v r$), and is related to the dimensionless torque (Σ) , $\Sigma = 2\pi h\mu^2 G/\rho$, where $G = \frac{J^\omega \rho^2}{\mu^2}$. For the current problem, Eqn. (4.10) reduces to:

$$J^\omega = r^3(\langle u\omega\rangle_t - \frac{\mu}{\rho}\frac{\partial}{\partial r}\langle\omega\rangle_t), \tag{4.11}$$

owing to the axisymmetric nature of the problem. In terms of azimuthal velocity (v),

$$J^{\omega} = r^3\left(\langle\frac{uv}{r}\rangle_t - \frac{\mu}{\rho}\frac{\partial}{\partial r}\langle\frac{v}{r}\rangle_t\right) = r^3\left(\langle\frac{uv}{r}\rangle_t - \frac{\mu}{\rho}\frac{\partial}{\partial r}\frac{\langle v\rangle_t}{r}\right),$$

and hence,

$$J^{\omega} = r^3\left(\langle\frac{uv}{r}\rangle_t - \frac{\mu}{\rho}\frac{1}{r}\frac{\partial\langle v\rangle_t}{\partial r} + \frac{\frac{\mu}{\rho}\langle v\rangle_t}{r^2}\right). \tag{4.12}$$

The laminar value of local angular momentum current (J_l^{ω}), is given by

$$J_l^{\omega} = 2\frac{\mu}{\rho}\omega_1\frac{r_1^2 r_2^2}{r_2^2 - r_1^2} = \frac{2\frac{\mu}{\rho}v_1 r_1}{1-\eta^2}, \tag{4.13}$$

The effective-Nusselt number (Nu_{ω}) is given by

$$Nu_{\omega} = J^{\omega}/J_l^{\omega}. \tag{4.14}$$

Following Eckhardt *et al.* (2007),for the inner cylinder rotating $(\omega_1 > 0)$, and stationary outer cylinder $(\omega_2 = 0)$, the Taylor number is defined as:

$$Ta = \frac{(1+\eta)^6}{64\eta^4}Re^2. \tag{4.15}$$

We choose the following function to describe the dependence of effective - Nusselt number (Nu_{ω}) with Taylor number (Ta):

$$Nu_{\omega} = \alpha(Ta)^{\beta} \tag{4.16}$$

Figure 4.12 shows the variation of effective-nusselt (Nu_{ω}) number as described in Eckhardt *et al.* (2007), with Ta corresponding to (a) $\eta = 0.5$, (b) $\eta = 0.6$, (c) $\eta = 0.7$ and (d) $\eta = 0.8$. The black line shows fitting $Nu_{\omega} = \alpha Ta^{\beta}$ close to the $CCF \longrightarrow TVF$ transition. The coefficients α and β are determined by least-square fitting all data of Nu_{ω} vs Ta, using equation (4.16). The coefficients corresponding to figure 4.12 (a) $\alpha \approx 0.01142$ and $\beta \approx 0.5202$, in the 95% confidence bound for $\alpha \in [0.007634, 0.01522]$ and $\beta \in [0.4822, 0.5582]$; (b) $\alpha \approx 0.023$ and $\beta \approx 0.4368$, in the 95% confidence bound for $\alpha \in [0.0197, 0.02629]$ and $\beta \in [0.4205, 0.453]$; (c) $\alpha \approx 0.01045$ and $\beta \approx 0.5196$, in the 95% confidence bound for $\alpha \in [0.006259, 0.014]$ and $\beta \in [0.476, 0.5633]$ and (d) $\alpha \approx 0.00322$ and $\beta \approx 0.629$, in the 95% confidence bound for $\alpha \in [0.002345, 0.0042]$ and $\beta \in [0.6014, 0.6566]$ utilising the MATLAB software.

Figure 4.13 shows the variation of effective-nusselt (Nu_{ω}) number, with Ta corresponding to (a) $\eta = 0.5$, (b) $\eta = 0.6$, (c) $\eta = 0.7$ and (d) $\eta = 0.8$. The blue line shows fitting $Nu_{\omega} = \alpha Ta^{\beta}$ beyond the onset of TVF from CCF. The coefficients α and β are determined by least-square

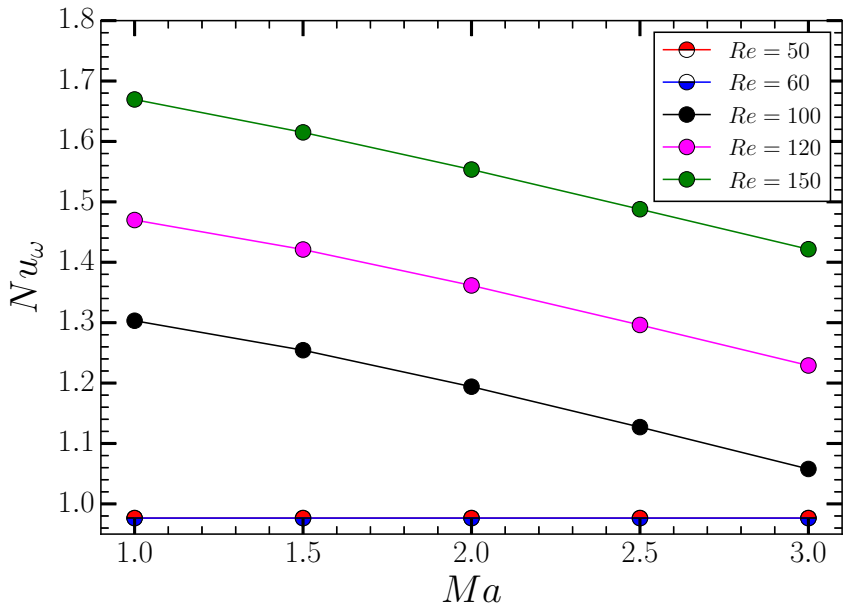

Fig. 4.14 Variation of effective-nusselt (Nu_ω) number as described in Eckhardt *et al.* (2007) with Ma for $\eta = 0.5$

fitting all data of Nu_ω vs Ta, using equation (4.16). The coefficients corresponding to figure 4.13 (a) $\alpha \approx 0.0718$ and $\beta \approx 0.3154$, in the 95% confidence bound for $\alpha \in [0.05345, 0.09015]$ and $\beta \in [0.2884, 0.3423]$; (b) $\alpha \approx 0.1307$ and $\beta \approx 0.2415$, in the 95% confidence bound for $\alpha \in [0.06685, 0.1945]$ and $\beta \in [0.1971, 0.286]$; (c) $\alpha \approx 0.162$ and $\beta \approx 0.2416$, in the 95% confidence bound for $\alpha \in [0.1223, 0.2017]$ and $\beta \in [0.2191, 0.2641]$ and (d) $\alpha \approx 0.05891$ and $\beta \approx 0.3313$, in the 95% confidence bound for $\alpha \in [0.0333, 0.08452]$ and $\beta \in [0.2905, 0.3721]$ utilising the MATLAB software. The blue line in figure 4.13 (a,b) shows that at a larger Ta (beyond the onset of TVF), the scaling of effective-nusselt (Nu_ω) number with Ta changes, even though, the number of vortices in the periodic box remains constant. This is attributed to fact that at higher Ta, the rolls are not symmetric about the mid-height and are axially displaced. Figure 4.13 (c) shows different scaling of Nu_ω with Ta (see the black and the blue line) and is attributed to the fact that the Taylor rolls become increasingly asymmetric (in terms of size of vortices, see figure 4.8 (a,b)). The green line in figure 4.13(c) shows the scaling for 2 vortex state, which appears after 4-roll asymmetric state in $\eta = 0.7$ and the coefficients corresponding to $\alpha \approx 0.06559$ and $\beta \approx 0.3033$, in the 95% confidence bound for $\alpha \in [0.060, 0.071]$ and $\beta \in [0.2961, 0.3106]$. It is noted from the figure 4.13 (c), that the transport decreases as the number of Taylor rolls in the domain drops from four to two. Following this decrease in transport, it again increases as the four roll state re-appears at larger Ta. Figure 4.13 (d) shows

different scalings, in the black and blue lines, corresponding to 6-rolls and 8-rolls, flow state, respectively.

Figure 4.14 shows the variation of effective-nusselt (Nu_ω) number with Ma for $\eta = 0.5$ for different Re. In the CCF regime, we find the Nu_ω is $\mathcal{O}(1)$ irrespective of Ma. The magnitude of Nu_ω decreases with increase in Ma, as shown in the curves corresponding to $Re = 100$, $Re = 120$ and $Re = 150$, in the TVF regime. This can be explained from the equation (4.12), where the first term corresponding to Reynolds stress slightly decreases when Ma is increased for a given Re. However, the second term in the equation (4.12) becomes more negative since the kinematic viscosity near the inner cylinder increases ($\nu = \mu/\rho$, where μ is constant but due to the radial stratification of density, ρ near inner cylinder decreases with increase in Ma). The third term is not affected in the Re range we envisage. The independent contribution from these terms causes the effective-nusselt (Nu_ω) to decrease with increasing Ma.

4.5 Summary

The existence of stationary and non-stationary patterns was found and a comprehensive phase diagram in (Re, η) plane was plotted that summarized these findings. It was seen that the compressiblity (Ma) effects are less significant in smaller gap-width, TC-cell as the diffusive effects become dominant at $\eta \longrightarrow 1$. This later observation was similar to the linear stability results of Manela & Frankel (2007). We found a new state called Localized Vortex Oscillations (LVO) in the Taylor vortex pair for $\eta \sim 0.6$ for $300 \leq Re \leq 400$. We verified that the periodic boundary conditions in axial direction admits supercritical pitchfork bifurcation at the onset of TVF from CCF, and the order parameter, Δu (radial velocity at the mid-height and mid-gap of the computational domain) showed a square-root scaling ($\Delta u \propto \sqrt{\varepsilon}$), with the driving parameter (ε) being the distance from the critical point, where $\varepsilon = (Re - Re^{cr})/Re^{cr}$. The axial velocity (w) at mid-height and mid-gap acts as an effective order parameter to quantify the "degree of asymmetry" in asymmetric stationary flow patterns. We also found the existence of side by side two rolls in short - cylinders with aspect ratios $\Gamma \leq O(1)$ at high Re in the parameter regime of the Travelling wave (TWS) flow state. The Taylor rolls near the inner cylinder are stronger compared to the rolls formed near the outer cylinder, which is ascertained from the velocity vector maps over the meridional plane in the present system.

The scaling $u = \alpha \left(\frac{Re - Re_{cr}}{Re_{cr}} \right)^{\beta}$ close to the bifurcation from $CCF \longrightarrow TVF$ comes out to be $\beta \sim 0.5$, which shows that the present system follows the amplitude scaling of cubic-Landau equation. The scaling of effective-Nusselt number (Nu_ω) with Taylor number (Ta) are presented for different radius ratio (η) for $CCF \longrightarrow TVF$ transition. Increase in fluid

compressibility decreases the effective-Nusselt number (Nu_ω) near the inner cylinder, at a given Re for $\eta = 0.5$.

Chapter 5

Proper Orthogonal Decomposition of the Flow Field in Compressible TCF

5.1 Introduction

The concept of Proper Orthogonal Decomposition (POD) was used for different purposes independently by Kosambi (1943), Karhunen (1946) and Loeve (1955). This is also known as Kosambi-Karhunen–Loève decomposition, or, principal component analysis (Jolliffe, 1986) or singular value decomposition (Golub & Van Loan, 1990). The proper orthogonal decomposition (POD) was introduced in the context of atmospheric turbulence by Lumley (1967). A complete description on POD can be found in Holmes *et al.* (2012) and is excellently reviewed in Tropea & Yarin (2007). The POD has been used to compute low-dimensional models that are able to describe Coherent Structures of turbulence. Reduced-order modelling is based on projecting the governing equations of motion onto subspaces spanned by the POD basis functions (also referred to as Galerkin projection) resulting in a set of nonlinear ordinary differential equations (ODEs).

The earliest work on POD dates back to Bakewell Jr & Lumley (1967) where they have measured two-point correlations of streamwise velocity component near the wall region of a fully developed turbulent pipe flow of glycerine. They have reconstructed the two-point correlation tensor using incompressibility and closure assumption. By using the numerical simulation data on channel flow results from Kim *et al.* (1987), Moin & Moser (1989) carried out extensive POD analysis to identify coherent structures. In the context of free shear flows, Glauser *et al.* (1987) carried out POD of axisymmetric turbulent jet and demonstrated the effectiveness of POD in determining the shape of eigenfunctions. In the context of Rayleigh Benard convection (RBC), Sirovich & Park (1990) and Park & Sirovich (1990) carried out POD on the numerical

data obtained from solving the Boussinesq equations for a fully inhomogeneous turbulent flow. They calculated three dimensional empirical eigenfunctions. Rodriguez & Sirovich (1990) extended POD to the Ginzburg-Landau (GL) equation and generated optimal basis and used Galerkin projection to reconstruct the dynamical system. Kirby & Armbruster (1992) used a conditional POD and a "moving" POD in order to the study of bifurcation scenarios in the Kuramoto-Sivashinsky equation. Extensive details on POD can be found in Berkooz *et al.* (1993).

In the context of Taylor-Couette flows (TCF), Imomoh *et al.* (2010) used spectral analysis and POD to identify flow transitions and structural characteristics of the flow states preceding turbulence. Gul *et al.* (2018) used Particle Image Velocimetry (PIV) together with the POD to measure torque and the instantaneous flow fields to understand the hysteresis in the measured torque in a Taylor–Couette system with a radius ratio (η) of 0.917 and aspect ratios (Γ) between 22 to 88.

In this chapter, we carry out Proper Orthogonal Decomposition (POD) on the computed flow fields obtained from the DNS of compressible Taylor-Couette flow. The primary goal is to identify structure of first few modes that contain about 95% of the fluctuating energy.

5.2 Method of Proper Orthogonal Decomposition

Proper orthogonal decomposition (see Berkooz *et al.* (1993)) is used to find an optimal basis set of spatial modes $\Phi_n(X)$ for a vector field $U(X,t)$ with respect to its total energy content $\int\langle\Phi_n(X)^2\rangle dX$, where $\langle\cdot\rangle$ denotes the temporal average. The spatial modes are identified such that they maximize the projection of $U(X,t)$ which leads to the following eigenvalue problem:

$$\int_\Omega \sum_{k=1}^{M} \langle U^m(X,t)U^k(X',t)\rangle \Phi_n^k(X')dX' = \lambda_n \Phi_n^m(X), \tag{5.1}$$

where M is the dimension of the vector field and the spatial domain $\Omega\,(x=(x,y,z)\in\Omega)$. The POD modes span an orthonormal basis allowing the decomposition of the vector field $\mathbf{U}(\mathbf{X},\mathbf{t})$:

$$U(X,t) = \sum_{n=1}^{\infty} a_n \Phi_n(X) \tag{5.2}$$

The projection coefficients a_n are equal to the eigenvalues λ_n via

$$\langle a^n(t)a^m(t)\rangle = \delta_{nm}\lambda_n \tag{5.3}$$

where δ_{nm} is the Kronecker symbol. The eigenvalue (λ_n) associated with a POD mode is a measure of its energy content and the principal objective of this method is to restrict the decomposition (5.2) to a few modes so that the flow dynamics can be analysed in a low-order subspace which is able to capture the most of the energy content of the flow field $\mathbf{U}(\mathbf{X},\mathbf{t})$. By projecting the POD modes on the velocity field, corresponding velocity vectors (eigen-modes) for the POD modes are determined. Since the eigenvalues are ordered in a descending manner, the first mode represents the highest energy. For more details, the reader is referred to the book by Holmes *et al.* (2012).

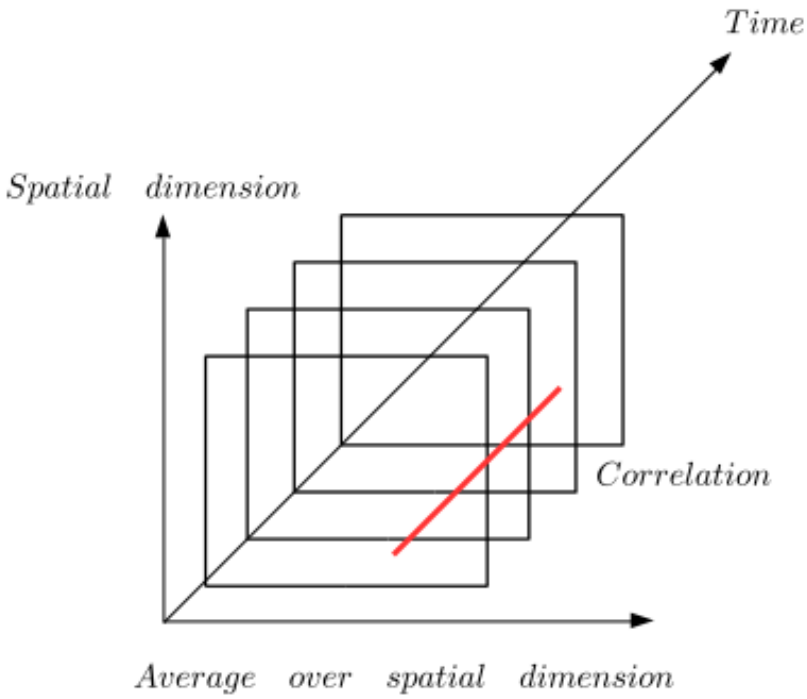

Fig. 5.1 Schematic diagram of snapshot POD, originally proposed by Sirovich & Park (1990); This diagram has been adapted from Tropea & Yarin (2007).

Let $\mathbf{U}(\mathbf{X})$, with $\mathbf{X} = (\mathbf{x}, t_n) \in D = \mathbb{R}^3 \times \mathbb{R}^+$, denote a set of snapshots obtained at N different time steps (t_n) over a spatial domain $\Omega\,(X = (x,y,z) \in \Omega)$. These snapshots can be experimental or numerical data of velocity fields, temperatures, density, etc. taken at different time steps. Following Lumley (1967), a coherent structure is defined as the deterministic function which is best correlated on average with the realizations $\mathbf{U}(\mathbf{X})$. In other words, we construct a function Φ (to be an element of $\mathscr{L}^2\ (\mathscr{D})$, the collection of square-integrable functions defined on the flow region $\mathscr{D}$) that has the largest mean square projection on to the observations $|(\mathbf{U}(\mathbf{X}), \Phi)|^2$. Figure 5.1 shows the schematic diagram of snapshot POD, originally proposed by Sirovich &

Park (1990), this diagram has been adapted from Tropea & Yarin (2007). The red line over the sequence of snapshots denotes the correlation over them. The velocity vectors from N time steps are arranged to form a velocity matrix, such that each row contains all the velocities at a single time-step. An auto-covariance matrix (C) where $C(\mathbf{X},\mathbf{X}') = \mathbf{U}(\mathbf{X}) \otimes \mathbf{U}(\mathbf{X}')$, (where the superscript $'$ denotes the complex conjugate and $\otimes$ is the dyadic product) using the velocity matrix U is formed while performing this operation

which can be written as a Fredholm integral eigenvalue problem

$$\int_{\mathscr{D}} C(\mathbf{X},\mathbf{X}')\Phi(\mathbf{X}')d\mathbf{X}' = \lambda\Phi(X), \tag{5.4}$$

in other words,

$$C\Phi_i = \lambda_i\Phi_i \tag{5.5}$$

is solved. The eigenvectors Φ_i are combined with the velocity matrix U to obtain the POD modes, in the following way:

$$\Phi_i = \frac{U_i\Phi_i}{||U_i\Phi_i||}. \tag{5.6}$$

These POD modes (Φ_i) are arranged according to the eigenvalues λ in the descending order such that the first few POD modes carry the maximum energy of the fluid system. Since the modes are ordered according to their magnitude of energy content $(\lambda_1 > \lambda_2 ... \lambda_{N-1} > 0)$, the most energetic POD mode is the first mode, which is related to the dominant coherent structure, if any, existing in the flow. In this chapter, we use "The Method Of Snapshots" proposed by Sirovich (1987). It is a numerical procedure which is computationally less-intensive.

5.2.1 Applications of POD in compressible flows

The key idea of performing Proper Orthogonal Decomposition (POD) is to determine a nested family of subspaces, of increasing but finite dimensions, that optimally span the data, and the error in the projection onto each subspace spanned by these modes, are minimized. Most of the POD tools have been applied to study incompressible flows. In an incompressible flow, we employ POD to the velocity fields only. The pressure enforces the incompressibility constraint in the pressure poison equation, and may in fact be eliminated completely from the equations of motion. As Rowley *et al.* (2004) points out that in the compressible flows, the thermodynamic variables (ρ, T) are also dynamically important. This poses the question, whether to treat the thermodynamic variables (ρ, T) separately from the velocity fields (u, v, w), or perform POD on a mixed vector-valued variable $(U = [u, v, w, \rho, T])$. To compute POD modes, we first need

to define an appropriate inner product.

$$\langle U_1, U_2 \rangle = \int (u_1 u_2 + v_1 v_2 + w_1 w_2 + \rho_1 \rho_2 + T_1 T_2) \tag{5.7}$$

As Rowley *et al.* (2004) reports, the above formulation presents a problem, since one cannot add velocity (u, v, w) and density (ρ) and temperature (T), in which scenario, one could simply non-dimensionalize the flow variables, but the appropriate choice of non-dimensionalization is critical. Rowley *et al.* (2004) presents a energy norm based on the integrated stagnation enthalpy. For a 2D configuration, Rowley *et al.* (2004) introduced a vector-valued variable $q = (u, v, a)$, where u and v are the velocities and a is the local sound speed, and defined a family of inner product as follows -

$$\langle q_1, q_2 \rangle = \int \left(u_1 u_2 + v_1 v_2 + \frac{2\xi}{\gamma(\gamma-1)} a_1 a_2 \right) \tag{5.8}$$

where γ is the ratio of specific heats and ξ is a parameter; If $\xi = \gamma$ then the induced energy norm gives $q^2 = 2h_0$, twice the total enthalpy of the flow, and for $\xi = 1$ then the induced norm gives twice the total energy of the flow. For more details, one is encouraged to read Rowley *et al.* (2004) and Rowley & Williams (2006).

Similar to the equation (5.8), Mack (1984) presented a norm in the context of compressible boundary layer flow as:

$$\langle p_1, p_2 \rangle = \int_0^\infty (p_1' \mathscr{M} p_2) dy \tag{5.9}$$

where, $p = [u, v, w, \rho, T]^{tr}$; "$tr$" stands for the transpose. As presented in Mack (1984), $\mathscr{M}$ is a diagonal positive definite matrix, as follows

$$\mathscr{M} = \text{diag}[\rho^0, \rho^0, \rho^0, T^0/\rho^0 \gamma Ma^2, \rho^0/\gamma(\gamma-1)T^0 Ma^2] \tag{5.10}$$

where the superscript denotes the base state profiles of velocity (v^0), density (ρ^0) and temperature (T^0) for a given combination of Reynolds number (Re) and Mack number (Ma).

In the present study, we use $(\mathscr{M})$ as scaling matrix, which corresponds to the mack norm (Mack, 1984) and has been extensively used in many transient growth studies in compressible flows (Hanifi *et al.* (1996), Malik *et al.* (2006)). As described in Malik *et al.* (2006), the definition of energy is free from any contribution due to pressure work or pressure related terms in the governing equations. Since pressure work is conservative, its contribution to the total fluctuation energy should vanish. In the present context of POD of compressible Taylor Couette

flows, we use the following scaling matrix -

$$\mathscr{M} = \text{diag}[\rho^0, \rho^0, T^0/\rho^0\gamma Ma^2, \rho^0/\gamma(\gamma-1)T^0Ma^2] \tag{5.11}$$

as a result, we have the composite covariance matrix (U),

$$U = \left[\sqrt{\rho^0}u, \sqrt{\rho^0}w, \sqrt{\frac{T^0}{\rho^0\gamma Ma^2}}\rho, \sqrt{\frac{\rho^0}{\gamma(\gamma-1)T^0Ma^2}}T\right] \tag{5.12}$$

with appropriate scaling factors. Recall that, the base state profiles of velocity (v^0), density (ρ^0) and temperature (T^0) are axially invariant and hence can be treated as vectors in the meridional (r,z) plane.

Snapshots of the fluctuation velocity fields (u,w), temperature (T) and density fields (ρ) are extracted from the DNS of compressible TCF with a constant sampling period of 0.01 in non-dimensional time units (as per viscous time scale), making a statistical dataset of 1000 samples. The mean of the scalar fields density (ρ) and temperature (T) was subtracted from the ensemble before applying the snapshot POD. The same has been checked with a statistical dataset of 2000 samples and the eigenmodes with associated eigenspectra found out to be invariant.

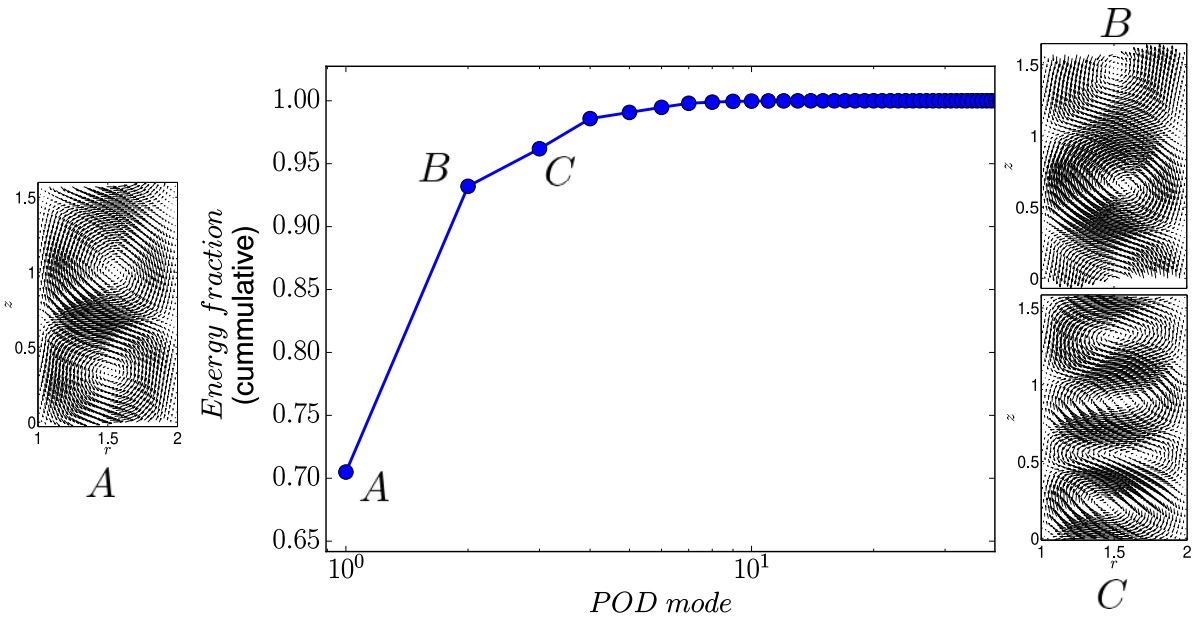

Fig. 5.2 The POD eigenspectrum (cumulative) for $Re = 210(TVF)$, $Ma = 1$, $Pr = 1$, $\eta = 0.5$, $\Gamma = \pi/2$; The vector visualisations corresponding to points A, B and C shows the flow in the meridional plane (r,z) for first three POD modes.

5.3 Results: POD Spectra and Associated Modes in Compressible TCF

5.3.1 The POD spectra and the associated modes

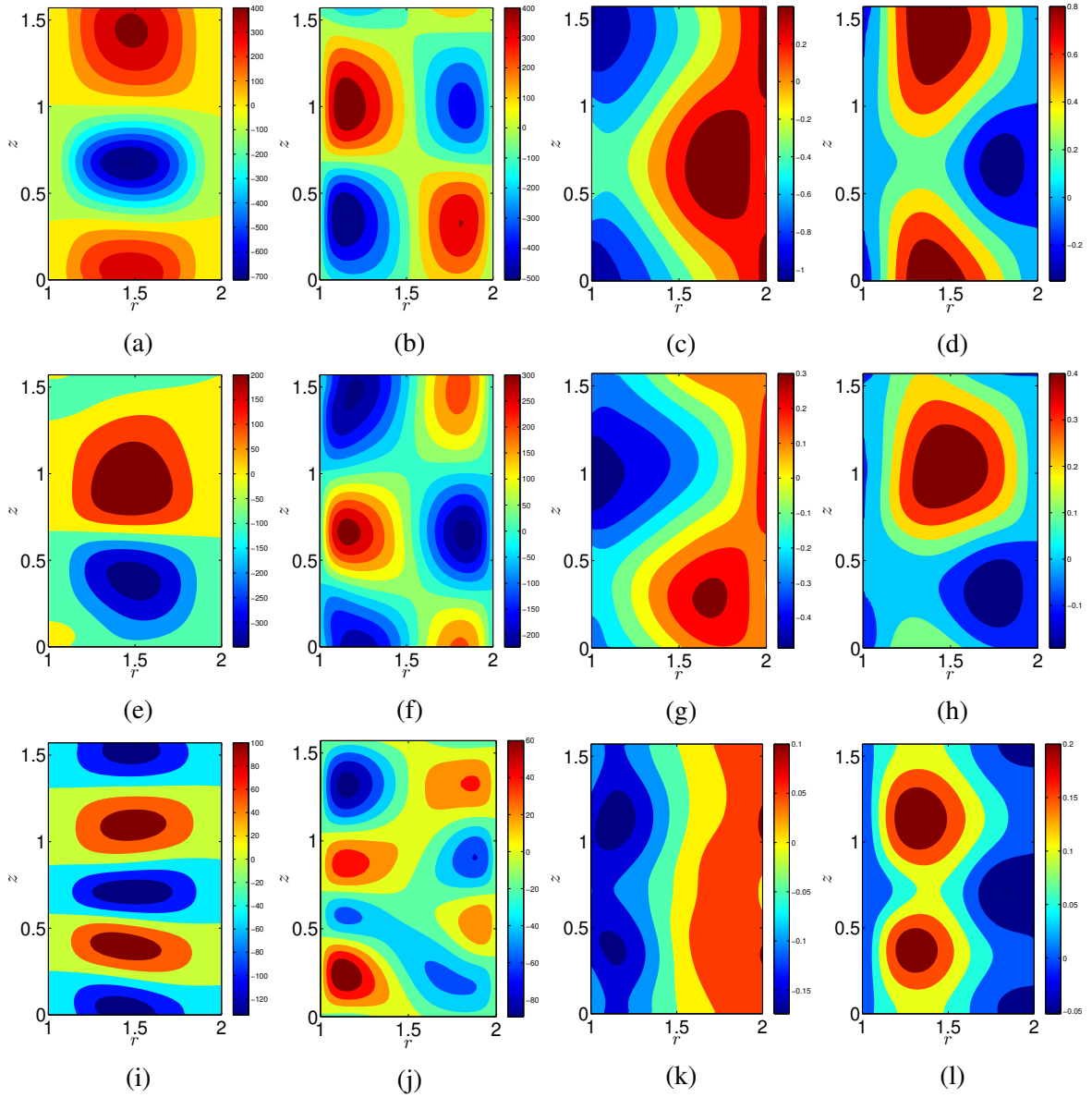

Fig. 5.3 Eigenfunctions of POD modes $(a-d)$ 1st mode, $(e-h)$ 2nd mode and $(i-l)$ 3rd mode for $Re = 210(TVF)$, $Ma = 1$, $Pr = 1$, $\eta = 0.5$, $\Gamma = \pi/2$; (a,e,i) radial velocity (u), (b,f,j) axial velocity (w), (c,g,k) density (ρ) and (d,h,l) temperature (T).

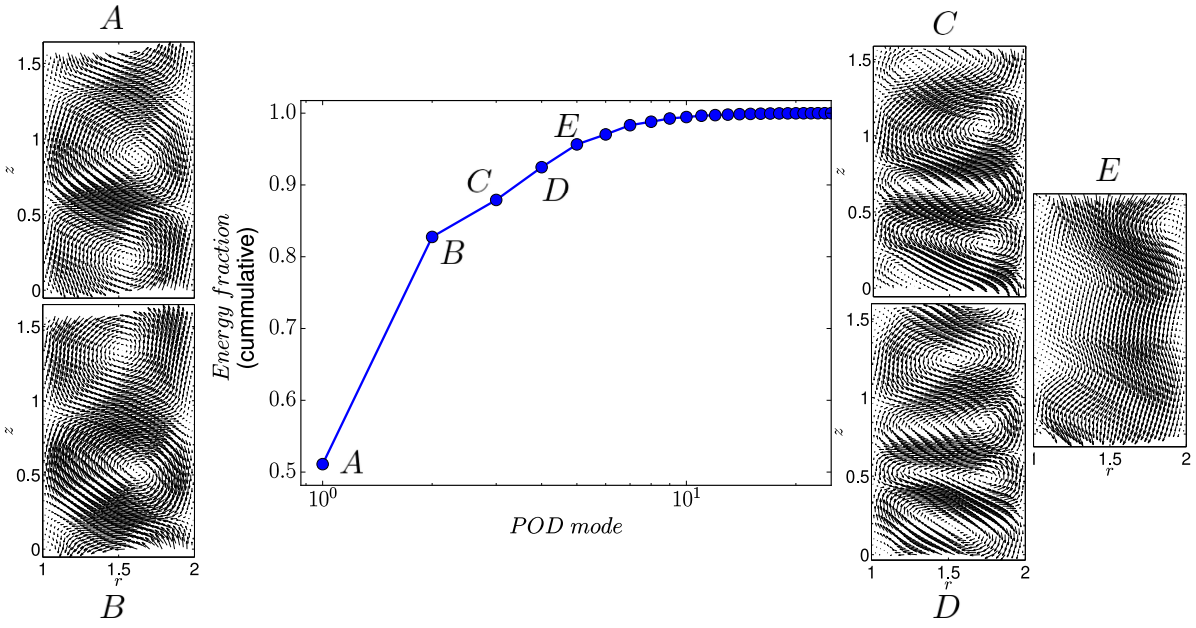

Fig. 5.4 The POD eigenspectrum (cumulative) for $Re = 500(TVF)$, $Ma = 1$, $Pr = 1$, $\eta = 0.5$, $\Gamma = \pi/2$; The vector visualisations corresponding to points A, B and C shows the flow in the meridional plane (r,z) for first three POD modes.

In this section, we present the results on POD analysis of the flow fields for the radius ratio, $\eta = r_1/r_2 = 1/2$. The Mach number (Ma) and the Prandtl number (Pr) of the system is unity. The aspect ratio (Γ) of the present system turns out to be $\pi/2$. The eigenvalues obtained from POD of radial-axial velocity fields represent the energy carried by the modes, respectively. Figure 5.2 illustrates the POD eigenspectrum (cumulative) for $Re = 210(TVF)$, the vector visualisations corresponding to points A, B and C shows the flow in the meridional plane (r,z) for first three POD modes, where the first three modes are sufficient to capture more than 95% of the total energy norm of the system. It is noted that the vector visualisation corresponding to the first POD mode (see panel A of figure 5.2) admits a radially inward jet at the meridional plane at the mid-height (slight axial displacement is attributed to periodic boundary conditions). Higher modes have Taylor rolls with considerable axial displacement (see panel B) and existence of multiple rolls (see panel C of figure 5.2).

Figure 5.3 shows the eigenfunctions of POD modes where the 1st mode $(a-d)$, 2nd mode $(e-h)$ and 3rd mode $(i-l)$ are portrayed with different panels (a,e,i) showing radial velocity (u), (b,f,j) axial velocity (w), (c,g,k) density (ρ) and (d,h,l) temperature (T). Analyzing the density (ρ) (c,g,k) and temperature (T) (d,h,l) modes, one comes to the conclusion that the perturbation temperature is lower near the outer cylinder, consequently the perturbation density to be higher at the location. This can be explained from the base state equations (see chapter 2), where a temperature maxima at the mid gap asymmetrically towards the inner

cylinder. As the Reynolds number (Re) of the flow is increased (for given Ma and Pr), the viscous dissipation increases resulting in larger hump in the temperature profile and the radial location of the temperature maxima shifts closer to the inner cylinder in comparison to the base state distribution, resulting in negative temperature perturbation near the outer cylinder.

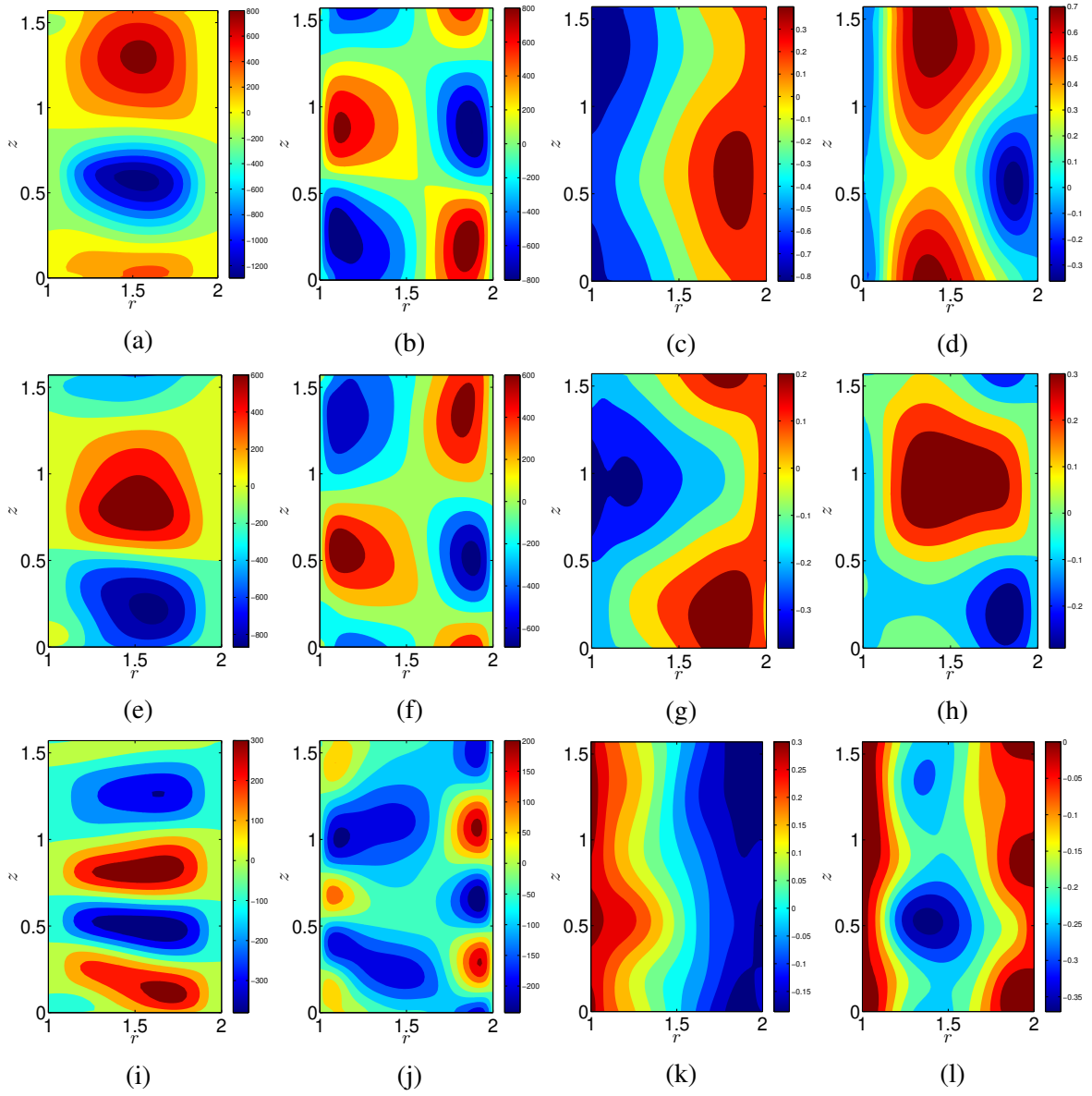

Fig. 5.5 Eigenfunctions of POD modes $(a-d)$ 1st mode, $(e-h)$ 2nd mode and $(i-l)$ 3rd mode for $Re = 500(TWS)$, $Ma = 1$, $Pr = 1$, $\eta = 0.5$, $\Gamma = \pi/2$; (a,e,i) radial velocity (u), (b,f,j) axial velocity (w), (c,g,k) density (ρ) and (d,h,l) temperature (T).

Similarly, figure 5.4 illustrates the POD eigenspectrum (cumulative) for $Re = 500(TVF)$, the vector visualisations corresponding to points A, B, C, D and E shows the flow in the

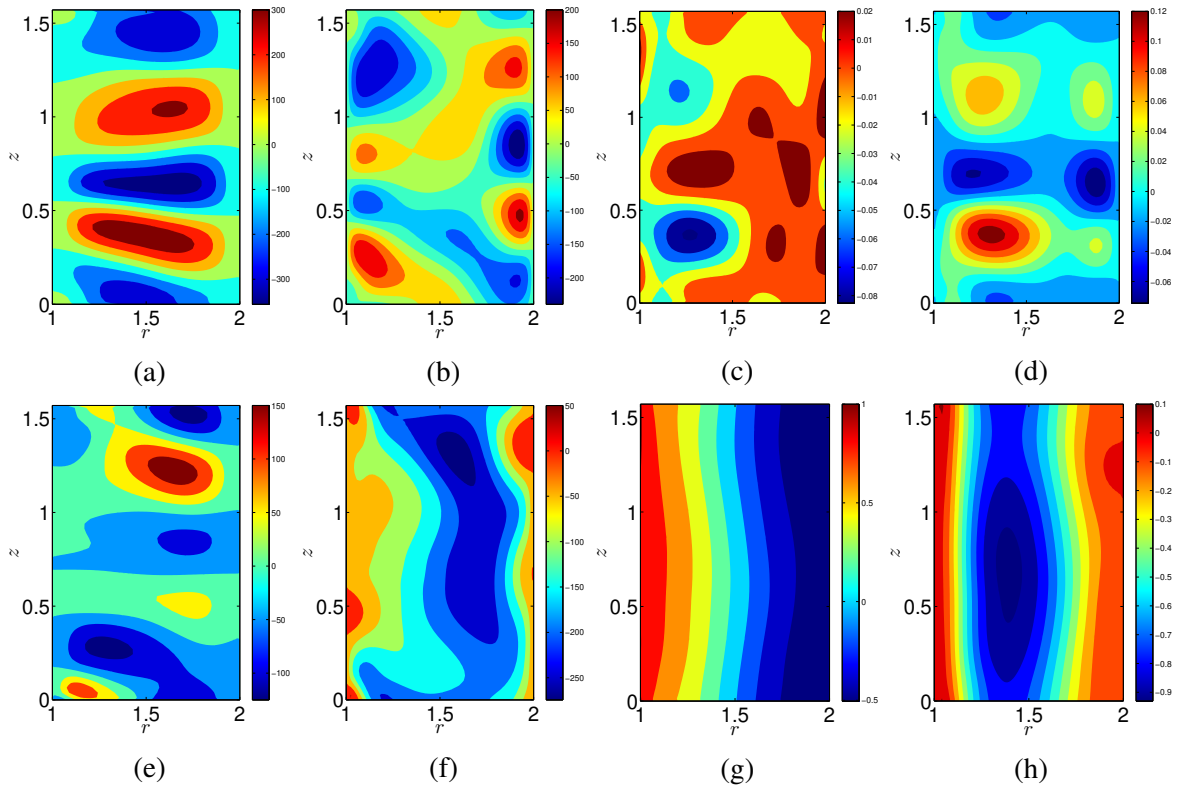

Fig. 5.6 Eigenfunctions of POD modes $(a-d)$ 4th mode and $(e-h)$ 5th mode for $Re = 500(TWS)$, $Ma = 1$, $Pr = 1$, $\eta = 0.5$, $\Gamma = \pi/2$; (a,e,i) radial velocity (u), (b,f,j) axial velocity (w), (c,g,k) density (ρ) and (d,h,l) temperature (T).

meridional plane (r,z) for first five POD modes, where the first five modes are sufficient to capture more than 95% of the total energy norm of the system.

Figure 5.5 shows the eigenfunctions of POD modes where the 1st mode $(a-d)$, 2nd mode $(e-h)$ and 3rd mode $(i-l)$ are portrayed with different panels (a,e,i) showing radial velocity (u), (b,f,j) axial velocity (w), (c,g,k) density (ρ) and (d,h,l) temperature (T). Similarly, figure 5.6 shows eigenfunctions of POD modes 4th mode $(a-d)$ and 5th mode $(e-h)$ are shown in different panels (a,e,i) radial velocity (u), (b,f,j) axial velocity (w), (c,g,k) density (ρ) and (d,h,l) temperature (T). The dominant density (ρ) and temperature (T) modes shows similar nature in comparison to the $Re = 210$ case.

5.3.2 Temporal dynamics

The snapshot dataset in the meridional plane (r,z) has been projected onto the POD basis modes in order to calculate the associated POD coefficients:

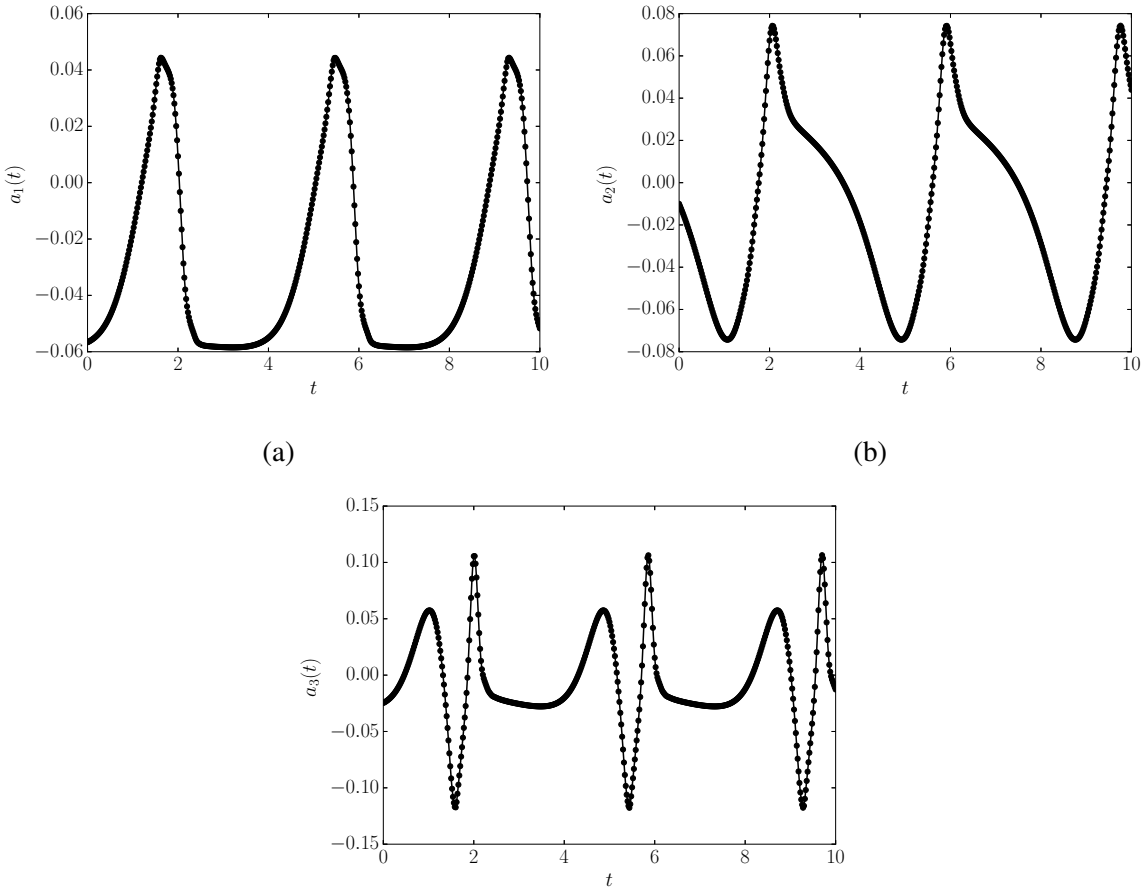

Fig. 5.7 Time dependence of the first three POD coefficients for $Re = 210$ (TWS), $Ma = 1$, $Pr = 1$, $\eta = 0.5$, $\Gamma = \pi/2$; (a) $a_1(t)$, (b) $a_2(t)$ and (c) $a_3(t)$.

$$a_n(t) = \int U(X,t) \cdot \Phi_n(X) dX \tag{5.13}$$

The time series of the amplitudes for $Re = 210(TWS)$ are shown in figure 5.7 and for $Re = 500(TWS)$ in figure 5.8. Panels (a), (b) and (c) of figure 5.7 shows the time dependence of amplitudes $a_1(t)$, $a_2(t)$ and $a_3(t)$, respectively. Panels (a), (b), (c), (d), (e) and (f) of figure 5.8 shows the time dependence of amplitudes $a_1(t)$, $a_2(t)$, $a_3(t)$, $a_4(t)$ and $a_5(t)$, respectively.

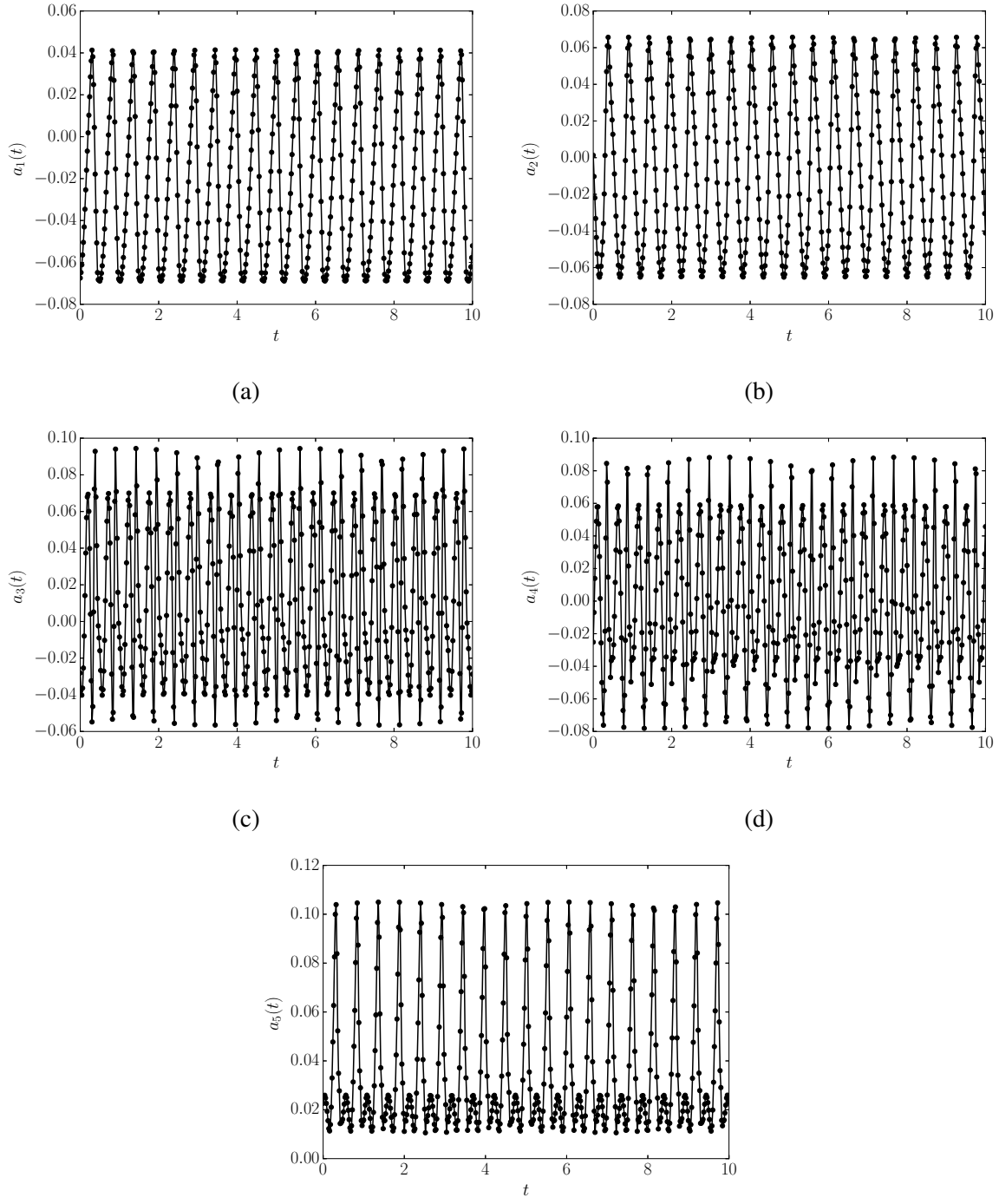

Fig. 5.8 Time dependence of first five POD coefficients for $Re = 500$ (TWS), $Ma = 1$, $Pr = 1$, $\eta = 0.5$, $\Gamma = \pi/2$; (a) $a_1(t)$; (b) $a_2(t)$; (c) $a_3(t)$; (d) $a_4(t)$ and (e) $a_5(t)$.

5.4 Summary

This chapter presents the results on Proper Orthogonal Decomposition (POD) applied to the radial-axial (u,w) velocity fields, density (ρ) and temperature (T) fields obtained from DNS of compressible Taylor-Couette flow. Using the "method of snapshots" on the radial-axial fluctuation velocity (u,w) spectra combined with density (ρ) and temperature (T) perturbations, scaled with Mack norm, obtained from the DNS, over the (r,z) plane for various Re in the the wide-gap regime $(\eta = 0.5)$, we find that the first three POD modes (at $Re = 210$) and the first five POD modes (at $Re = 500$) are sufficient to capture more than 95% of the total energy content of the present system. The temporal dynamics is shown by projecting the fields onto the POD basis modes.

The tools of POD based analysis and Galerkin projection provide a statistical method to derive reduced-order models from data (both DNS and experiments). The implications of POD eigenmodes and corresponding eigenfunctions have not been investigated; this can be done by using the POD based decomposition and applying Galerkin projection on the compressible Navier-Stokes equations (NSE) to derive a set of coupled non-linear ordinary differential equations (ODE's) and would be an interesting work to carry forward. Further analysis is required to shed light on these issues.

Chapter 6

Cellular States and Propagating vortices in Axisymmetric Compressible TCF : Independently Rotating Cylinders

6.1 Introduction

The last five chapters focussed on the effect of compressibility (Ma) and radius ratio $(\eta = r_1/r_2)$ on the pattern formation scenario of the Taylor-Couette flow of an ideal gas with periodic boundary conditions at the top and the bottom end-walls. The present study focusses on the genesis of novel cellular states (Heise *et al.*, 2008) in the finite cylinders. In contrast to the assumption of infinite cylinders manifested by periodic boundary conditions, the stationary end-walls at the top and the bottom of the domain are simulated using no-slip boundary condition which decreases the azimuthal velocity (v) from some finite value from the bulk to zero, generating a boundary layer circulation near these walls. This flow gives rise to so called Ekman vortices (Coles, 1965) which are directed radially inwards at the stationary end-walls. Experiments in Taylor–Couette flow (TCF) are done with stationary lids at the top and bottom, breaking the axial translational invariance and the endwalls induce Ekman vortices at any finite rotation rate. These end walls are responsible for breaking the perfect pitchfork bifurcation for transition from purely azimuthal circular Couette flow (CCF) (that holds for infinite cylinders) to Taylor vortex flow (TVF) (Benjamin (1978), Benjamin & Mullin (1981), Jones (1982), Czarny *et al.* (2003), Heise *et al.* (2008), Abshagen *et al.* (2010), Hoffmann *et al.* (2013)).

In this chapter, we report results from numerical investigations of Taylor-Couette flow (TCF) of an ideal gas in finite cylinders obtained from independently rotating inner-cylinder

$(0 < Re_i < 300)$ and outer cylinder $(-300 \leq Re_o \leq 300)$, where

$$Re_i = \omega_1 r_1 \delta / \nu \tag{6.1}$$

and,

$$Re_o = \omega_2 r_2 \delta / \nu \tag{6.2}$$

are the Reynolds number of inner and outer cylinder, respectively, and ω_1 and ω_2 are inner and outer cylinder angular velocities, $\delta = r_2 - r_1$ is the gap-width, and ν is the kinematic viscosity at inner cylinder. The Mach number (Ma) of the flow and the Prandtl number (Pr) of the fluid are set to unity. The geometrical parameters: (a) radius ratio $(\eta = r_1/r_2)$ is 1/2 (wide-gap limit) and (b) the aspect ratio $(\Gamma = h/\delta$, where h is the height of the computational domain) is four. The emergence of localized cellular Taylor vortex state (Abshagen *et al.*, 2010) is found in the counter-rotation regime ($Re_i \in [150, 300]$ and $Re_o \in [-100, -300]$). We also report axisymmetric propagating vortices, previously observed by Hoffmann *et al.* (2013) in incompressible TCF, which travel from mid-height towards end walls, where they get annihilated and the cycle continues. The phase diagram consisting of stationary and travelling patterns is constructed in the (Re_i, Re_o) plane.

6.2 Numerical method and boundary conditions

The details of the numerical method are described in Chapter 2 of the current thesis. Computations were initialised from the rest state $(u = v = w = 0)$ with unit density and temperature $(\rho, T = 1)$ for all reported runs. The inner and outer cylinders are placed at the dimensionless radial locations of $r_1 = \frac{\eta}{(1-\eta)}$ and $r_2 = \frac{1}{(1-\eta)}$, and the top and bottom endwalls are placed at $z_1 = h$ and $z_2 = 0$, respectively. We employ no-slip and Dirichlet boundary condition for velocities (u, v, w) and temperature T, respectively, at the cylinder walls as well as at the top and bottom lids of the domain. The dimensionless boundary conditions can be written as follows -

$$u = 0, \quad w = 0 \quad \text{at} \quad r_1 = \frac{\eta}{(1-\eta)} \quad \text{and} \quad r_2 = \frac{1}{(1-\eta)} \tag{6.3}$$

$$u = 0, \quad w = 0 \quad \text{at} \quad z_1 = 0 \quad \text{and} \quad z_2 = h \tag{6.4}$$

$$v = Re_i \quad \text{at} \quad r_1 = \frac{\eta}{(1-\eta)}; \qquad v = Re_o \quad \text{at} \quad r_2 = \frac{1}{(1-\eta)} \tag{6.5}$$

$$v = 0 \quad \text{at} \quad z_1 = 0 \quad \text{and} \quad z_2 = h \tag{6.6}$$

$$T = 1 \quad \text{at} \quad r_1 = \frac{\eta}{(1-\eta)}; \qquad T = \frac{T_2}{T_1} = \chi \quad \text{at} \quad r_2 = \frac{1}{(1-\eta)} \tag{6.7}$$

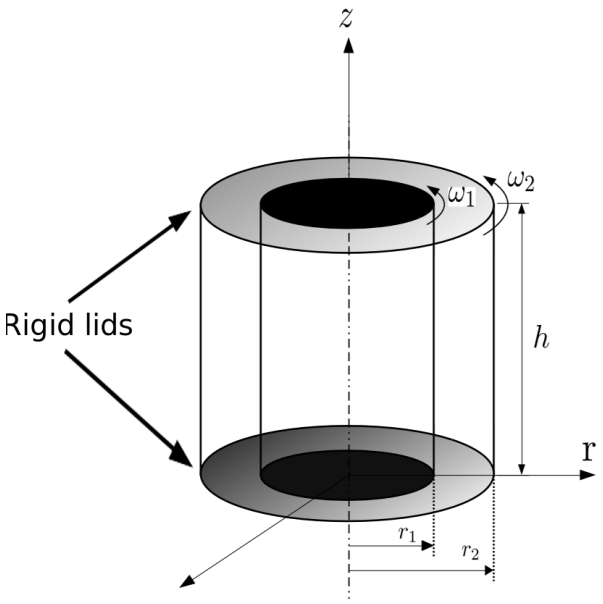

Fig. 6.1 Schematic diagram of (a) Taylor-Couette setup, the inner cylinder $(r = r_1)$ is rotating with angular velocity ω_1 and the outer cylinder $(r = r_2)$ is rotating with ω_2. The gap-width between the two cylinders is $\delta = r_2 - r_1$ and the axial extent of cylinder is h; $z = 0$ corresponds to the bottom plate and $z = h$ corresponds to top plate. The four walls (the inner and outer cylinder and two stationary endwalls) are kept at isothermal boundary condition.

$$T = 1 \quad \text{at} \quad z_1 = 0 \quad \text{and} \quad z_2 = h \tag{6.8}$$

6.3 Code Validation For Independently Rotating Cylinders

6.3.1 Localized cellular state: incompressible Taylor-Couette flow

The code has been found to validate the streamline plot of cellular state (see Fig. 6.2) for moderate aspect ratio ($\Gamma = 4$) and $Re_i = 150$ and $Re_o = -300$ where Re_i and Re_o are the Reynolds number of the inner and outer cylinders, presented in Abshagen *et al.* (2010). A symmetric pair of small vortices always formed closer to the inner cylinder and a pair of large vortices near the outer cylinders. Note that, we employed finite lids at the top and the bottom of the cylinder instead to periodic boundary conditions.

6.3.2 Grid Independence Test

In order to check the grid dependency of present computations, a set of runs are performed for two different grid-sizes at $Re_i = 100$ and $Re_o = -100$ with $Ma = 1$, $Pr = 1$, $\eta = 0.5$ and $\Gamma = 4$. The temporal evolution of global kinetic energies based on (i) radial kinetic energy

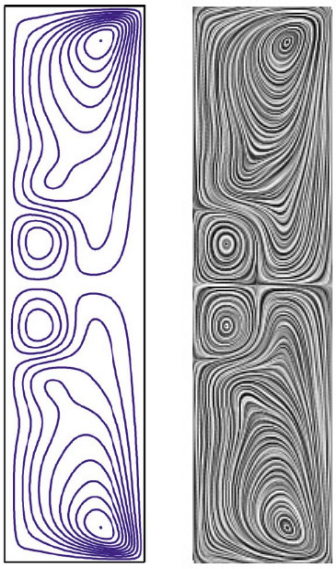

Fig. 6.2 Comparison of streamline plot of cellular state for an aspect ratio of $\Gamma = 4$ and $Re_i = 150$ and $Re_o = -300$. The left panel shows the plot taken from Abshagen *et al.* (2010); the right panel shows the surface LIC contour for $Ma = 0.1$ (current code).

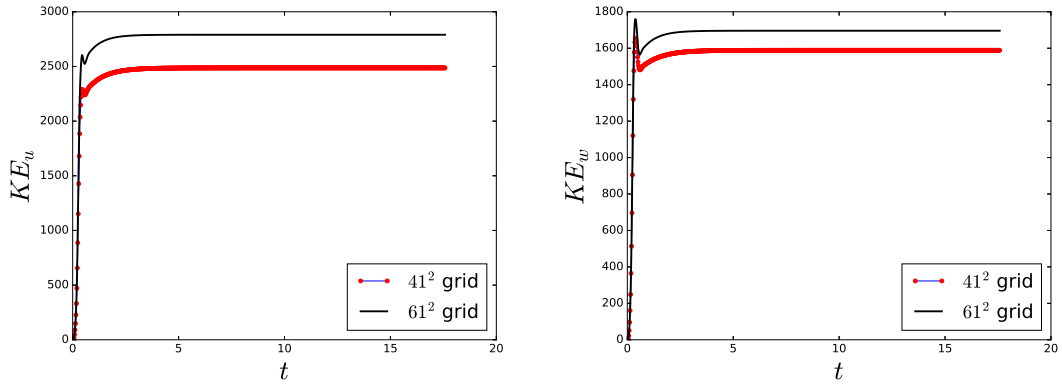

(a) (b)

Fig. 6.3 Time evolution for (a) KE_u, Eq. (6.9), and (b) KE_w, Eq. (6.10) $Re_i = 150$ and $Re_o = -100$; grid-points along axial and radial directions ($N_z \times N_r$) are as follows:41×41 (red) and 61×61 (black).

(KE_u) (ii) axial kinetic energy (KE_w) are given by:

$$KE_u = \left\langle \frac{1}{2}\rho u^2 \right\rangle = 2\pi \sum_{\eta/(1-\eta)}^{1/(1-\eta)} \sum_{0}^{\frac{2\pi}{k}} \left(\frac{1}{2}\rho u^2 \right) r\Delta r\Delta z, \tag{6.9}$$

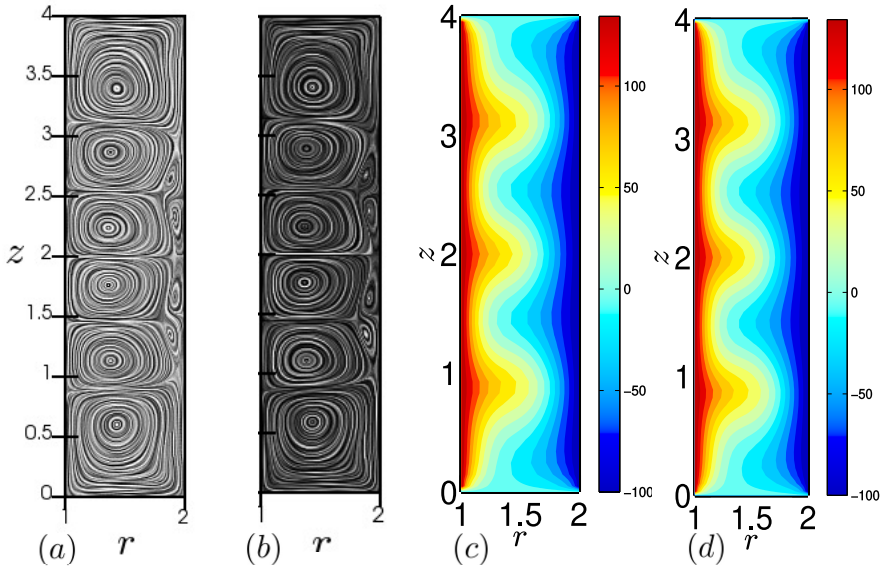

Fig. 6.4 Grid independence study for $Re_i = 150$ and $Re_o = -100$; surface LIC plots in (r,z) plane (a) 41×41 grid (b) 61×61 grid; contour-maps of azimuthal (v) velocity with (c) 41×41 grid (d) 61×61 grid. Six vortex state consists of two Ekman rolls and two pair of small vortices near mid-height close to the inner wall.

$$KE_w = \left\langle \frac{1}{2}\rho w^2 \right\rangle = 2\pi \sum_{\eta/(1-\eta)}^{1/(1-\eta)} \sum_{0}^{\frac{2\pi}{k}} \left(\frac{1}{2}\rho w^2\right) r\Delta r\Delta z, \tag{6.10}$$

Panel (a) and (b) of figure 6.3 shows the variation of KE_u and KE_w with time, respectively. All the simulations are started from rest. Figure 6.4 presents grid independence study for $Re_i = 150$ and $Re_o = -100$ and the surface LIC plots in (r,z) plane (a) 41×41 grid (b) 61×61 grid. The contour-maps of azimuthal (v) velocity with (c) 41×41 grid (d) 61×61 grid are also shown. The six vortex state consists of two Ekman rolls and two pair of vortices symmetrically placed at the mid-height. The flow patterns look strikingly similar even with a coarser grid of 41×41 and robust.

Panels (a) and (b) of figure 6.5 shows upsweep/downseep protocol. During each run the Reynolds number of the inner cylinder (Re_i) is increased from 100 to 150 from $t = 0$ to $t = 110$ and then decreased back to 100 from $t = 110$ to $t = 220$; Re_i was changed in steps of $dRe = 1$ after every 20000 time-steps, corresponding to a ramp-rate of $dRe/dt \sim 0.45$, where t is the dimensionless time based on visous time scale. Figure 6.5 shows the grid independence study $Re_i = 150$ and $Re_o = -100$ where the surface Line Integral Convolution (LIC) plots (Ahrens *et al.*, 2005) in (r,z) plane (a) 41×41 grid (b) 61×61 grid and the contour-maps of azimuthal (v) velocity (c) 41×41 grid (d) 61×61 grid. It is clear that 41×41 grid is good enough to

choose as grid size for the present simulations, as per the present computational power, however a grid clustering at the four walls would be important to resolve the boundary layers at large enough rotation rates.

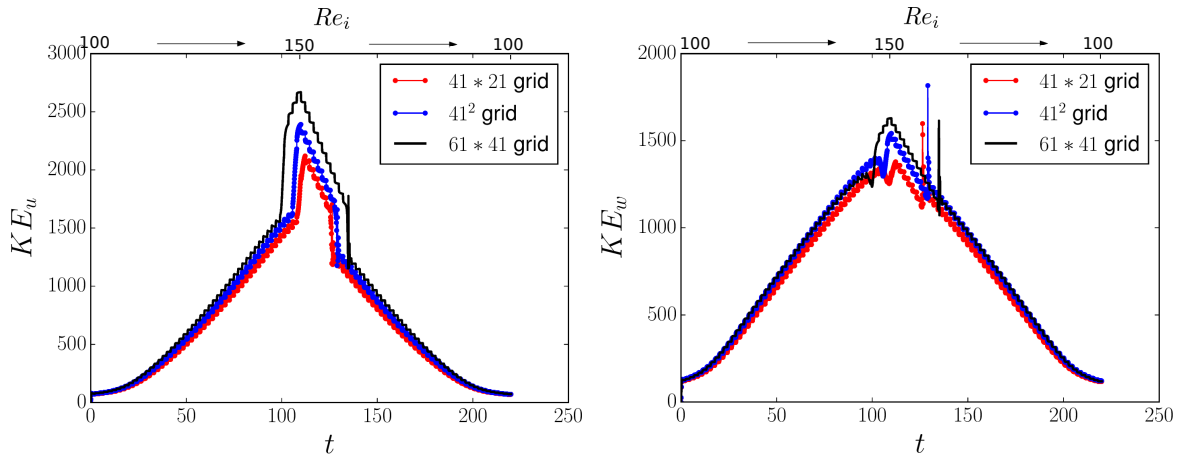

(a) (b)

Fig. 6.5 Time evolution for (a) KE_u, equation 6.9, and (b) KE_w, equation 6.10, during quasi-static upsweep/downsweep in Reynolds number of the inner cylinder (Re_i) for $Re_o = 100$, $Ma = 1$ and $Pr = 1$; grid-points along axial and radial directions $(N_z \times N_r)$ are as follows: 41×21 (red), 41×41 (blue) and 61×41 (black); during each run the Reynolds number of the inner cylinder (Re_i) is increased from 100 to 150 from $t = 0$ to $t = 110$ and then decreased back to 100 from $t = 110$ to $t = 220$; Re_i was changed in steps of $\Delta Re = 1$ after every 20000 time-steps, corresponding to a ramp-rate of $dRe/dt \sim 0.45$, where t is the dimensionless time based on visous time scale.

6.4 Phase Diagram of Patterns

Figure 6.6 shows the phase diagram of different patterns in (Re_i, Re_o) plane; grossly identified as the stationary and non-stationary patterns. In the Taylor-Couette flow (TCF) with stationary endwalls, we observe the formation of Ekman cells adjacent to top and bottom walls. However, we observe a flow state with 4 roll state with two large rolls located at the two corners of the domain, resulting in inward flow (towards inner wall) at each end and two small rolls situated symmetrically about the mid-height of the computational domain. This novel state corresponds to setting up of saddle in the flow (previously reported in incompressible literature by Abshagen *et al.* (2010) for the same parameter regime with axisymmetric compuatation and experiments).

Figure 6.7 shows the streamlines drawn using Surface-LIC module of paraview software (Ahrens *et al.*, 2005) for $Re_i = 50$ and (a) $Re_o = -300$, (b) $Re_o = -100$, (c) $Re_o = 100$, and (d) $Re_o = 300$ for $Ma = 1$, $Pr = 1$, $\eta = 0.5$, $\Gamma = 4$. These streamlines show the Ekman vortices.

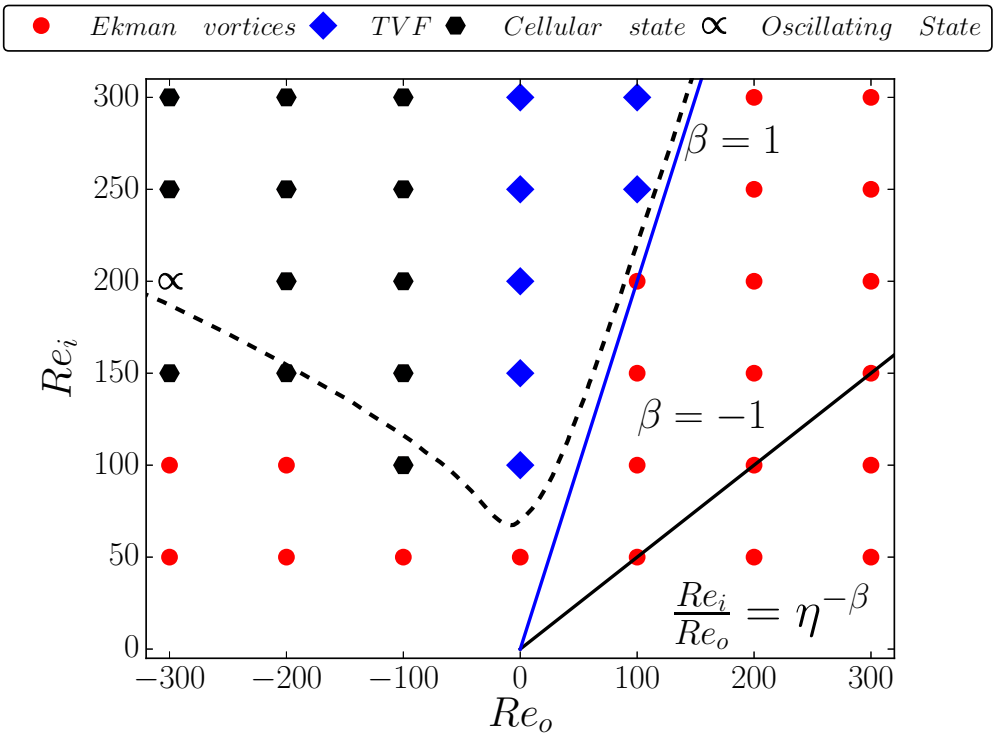

Fig. 6.6 Phase diagram illustrating the dependence of Re_i on Re_o for $Ma = 1$ and $Pr = 1$ for independently rotating inner-cylinder ($0 < Re_i < 300$) and outer cylinder ($-300 \leq Re_o \leq 300$); $\beta = 1$ corresponds to inviscid Rayleigh line and $\beta = -1$ corresponds to solid-body rotation; the dotted line shows the stability boundary $f(Re_i, Re_o)$ for $\eta = 0.5$ (Replotted from Esser & Grossmann (1996)).

It is noted that a pair of vortices are formed at the corner near the outer cylinder, which is different from the Taylor vortices, formed near the mid-height (see 6.8 (a)).

The emergence of localized cellular Taylor vortex state (Abshagen *et al.*, 2010) is found in the counter-rotation regime ($Re_i \in [150, 300]$ and $Re_o \in [-100, -300]$). We also report axisymmetric propagating vortices (previously observed by Hoffmann *et al.* (2013) in incompressible fluid systems), which travel from fixed end plates towards mid-height, where they get annihilated and the cycle continues. The phase diagram consisting of plethora of stationary and travelling patterns are constructed in the (Re_i, Re_o) plane.

Streamlines (see figure 6.8 $(a-d)$) drawn using Surface-Line Integral Convolution (LIC) module of paraview software (Ahrens *et al.*, 2005) are displayed. Panels $(e-h)$ in the figure 6.8 shows the azimuthal velocity contours for fixed rotation of inner cylinder, $Re_i = 150$, $Ma = 1$, $Pr = 1$, $\eta = 0.5$, $\Gamma = 4$ and different rotation rates for outer cylinder, (a) $Re_o = 0$, (b) $Re_o = -100$, (c) $Re_o = -200$, (d) $Re_o = -300$. Interestingly, the meridional $(r-z)$ flow pattern for the aspect ratio of $\Gamma = 4$, shown in figure 6.8 (a), contains only a pair of

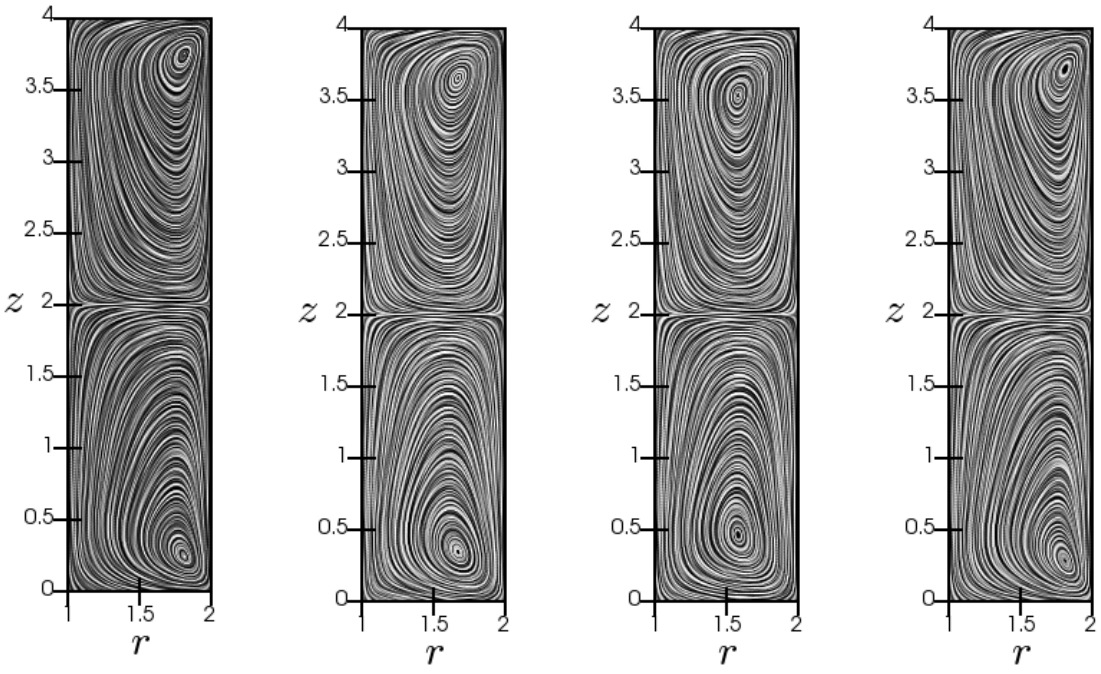

Fig. 6.7 Streamlines drawn using Surface-LIC module of paraview software (Ahrens *et al.*, 2005) for $Re_i = 50$ and (a) $Re_o = -300$, (b) $Re_o = -100$, (c) $Re_o = 100$, and (d) $Re_o = 300$ for $Ma = 1$, $Pr = 1$, $\eta = 0.5$, $\Gamma = 4$.

vortices stacked along its axial extent. The flow pattern in meridional plane at $Re_i = 150$ and $Re_o = -100$ six symmetric large vortices (end wall vortices are slightly larger) near the inner-cylinder coexisting with an array of four smaller vortices near the rotating outer cylinder. The vortices near the outer cylinder is somewhat irregular in orientation and corresponding velocity vector plots (see panel (f) of figure 6.9) confirm that the array of smaller vortices near the outer cylinder are of much weaker strength compared to domainant vortices in proximity to the inner cylinder, which has been previously reported in flow patterns pertaining to short cylinders ($\Gamma \sim O(1)$) in axially periodic boundary conditions (see Chapter 4 of the current thesis). Flow patterns illustrating azimuthal vorticity ($\Omega_\theta = \partial_z u - \partial_r w$) $(a-d)$ and temperature (T) contours with the arrows showing the flow in meridional plane with magnitude of $\sqrt{u^2+w^2}$ denoted in the length of arrow $(e-h)$ for $Re_i = 150$, $Ma = 1$, $Pr = 1$, $\eta = 0.5$, $\Gamma = 4$ for different $(a,e)Re_o = 0$, $(b,f)Re_o = -100$, $(c,g)Re_o = -200$, $(d,h)Re_o = -300$ are enumerated. It is noted from panel (e) of figure 6.9 ($Re_i = 150$ and $Re_o = 0$) that there is an "outward" jet at the mid-height of the cylinder and two "inward" jets near two end-walls. We find that the radially outward jet at the mid-height is accompanied by lower density (higher temperature)

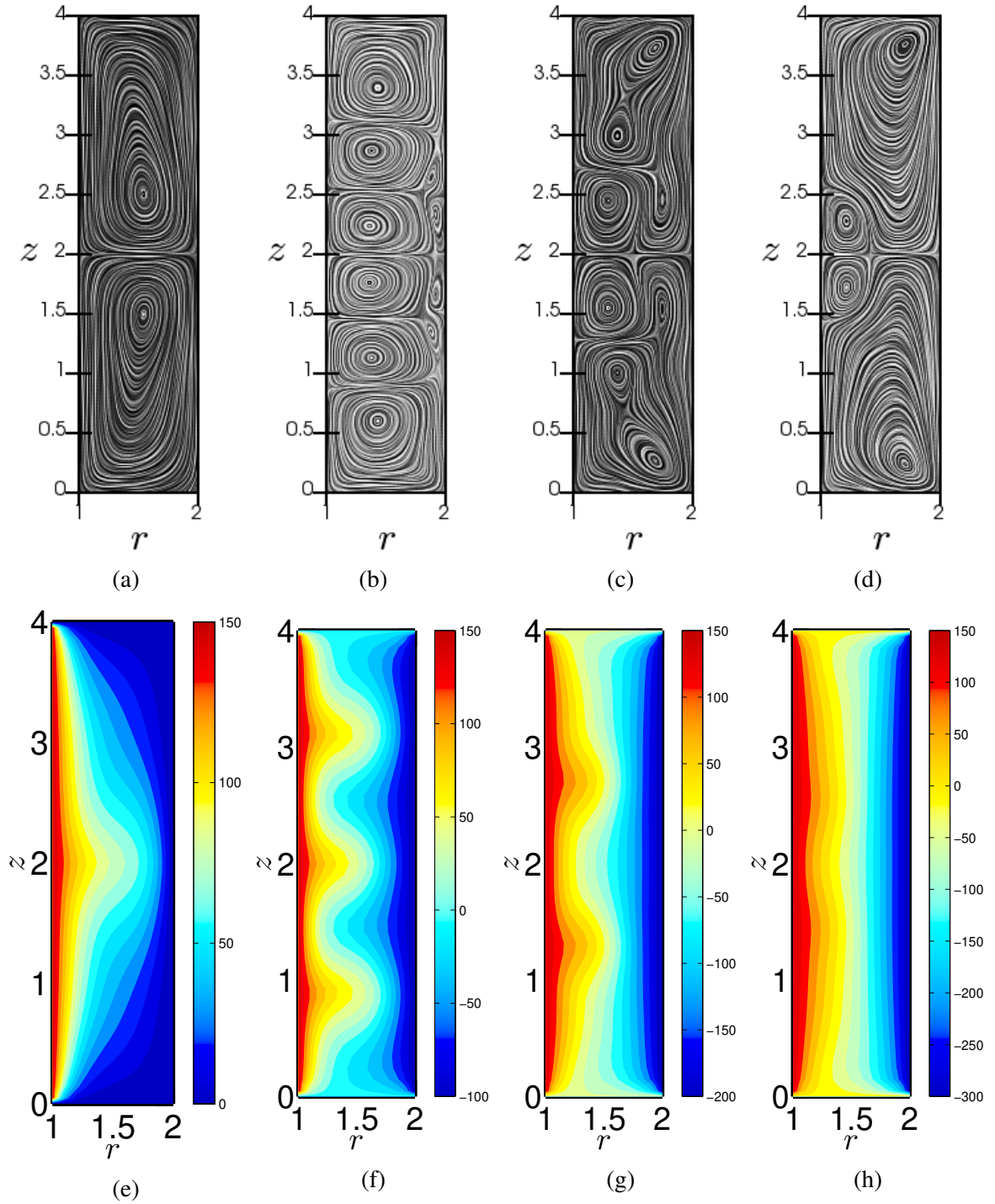

Fig. 6.8 $(a-d)$ Streamlines drawn using Surface-LIC module of paraview software (Ahrens *et al.*, 2005). $(e-h)$ Azimuthal velocity contours for $Re_i = 150$, $Ma = 1$, $Pr = 1$, $\eta = 0.5$, $\Gamma = 4$ for different; (a,e) $Re_o = 0$, (b,f) $Re_o = -100$, (c,g) $Re_o = -200$, (d,h) $Re_o = -300$.

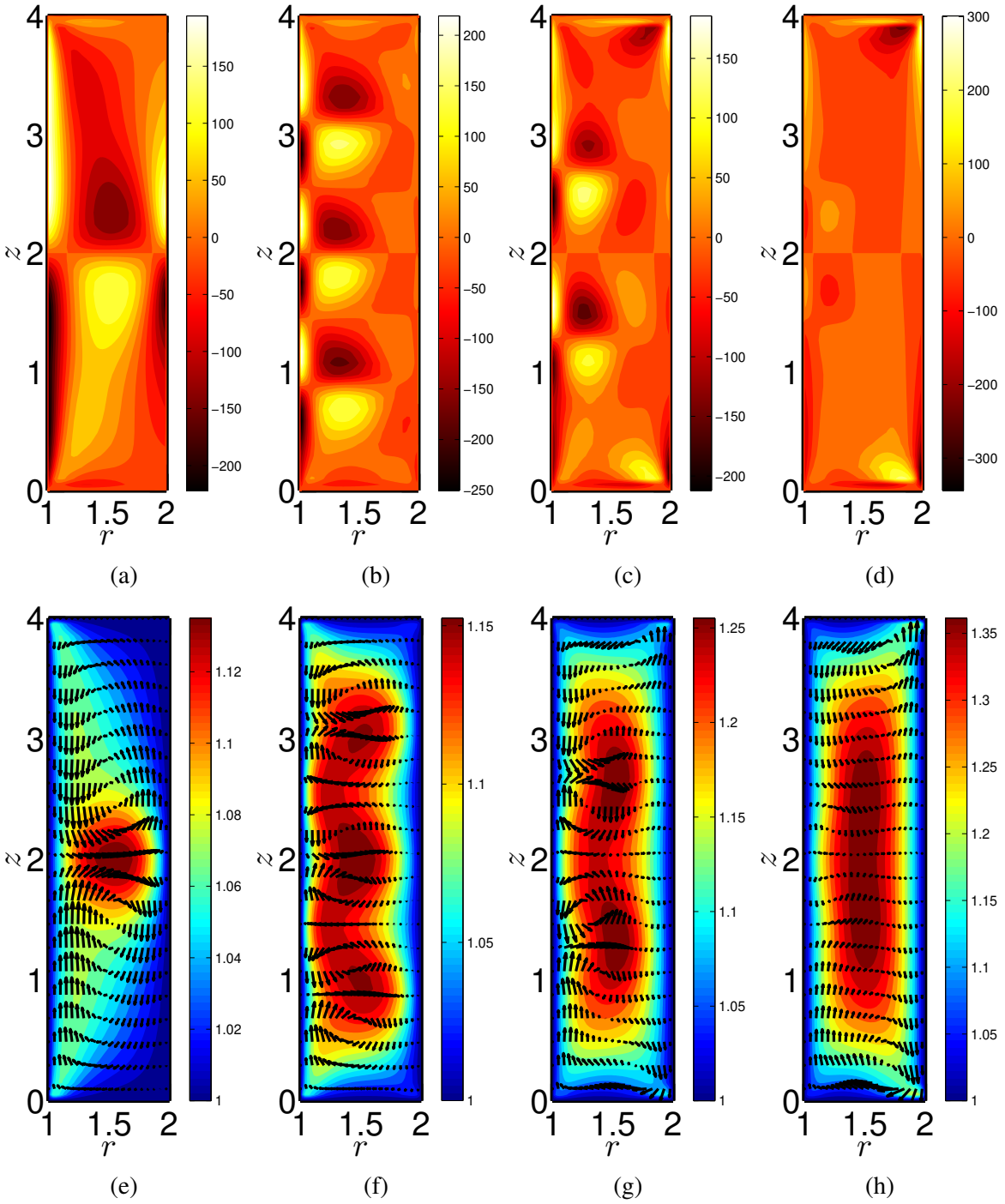

Fig. 6.9 Flow patterns illustrating azimuthal vorticity $(\Omega_\theta = \partial_z u - \partial_r w)$ $(a-d)$ and temperature (T) contours with the arrows showing the flow in meridional $(r-z)$ plane with magnitude of $\sqrt{u^2+w^2}$ denoted in the length of arrow $(e-h)$ for $Re_i = 150$, $Ma = 1$, $Pr = 1$, $\eta = 0.5$, $\Gamma = 4$ for different; $(a,e)Re_o = 0$, $(b,f)Re_o = -100$, $(c,g)Re_o = -200$, $(d,h)Re_o = -300$.

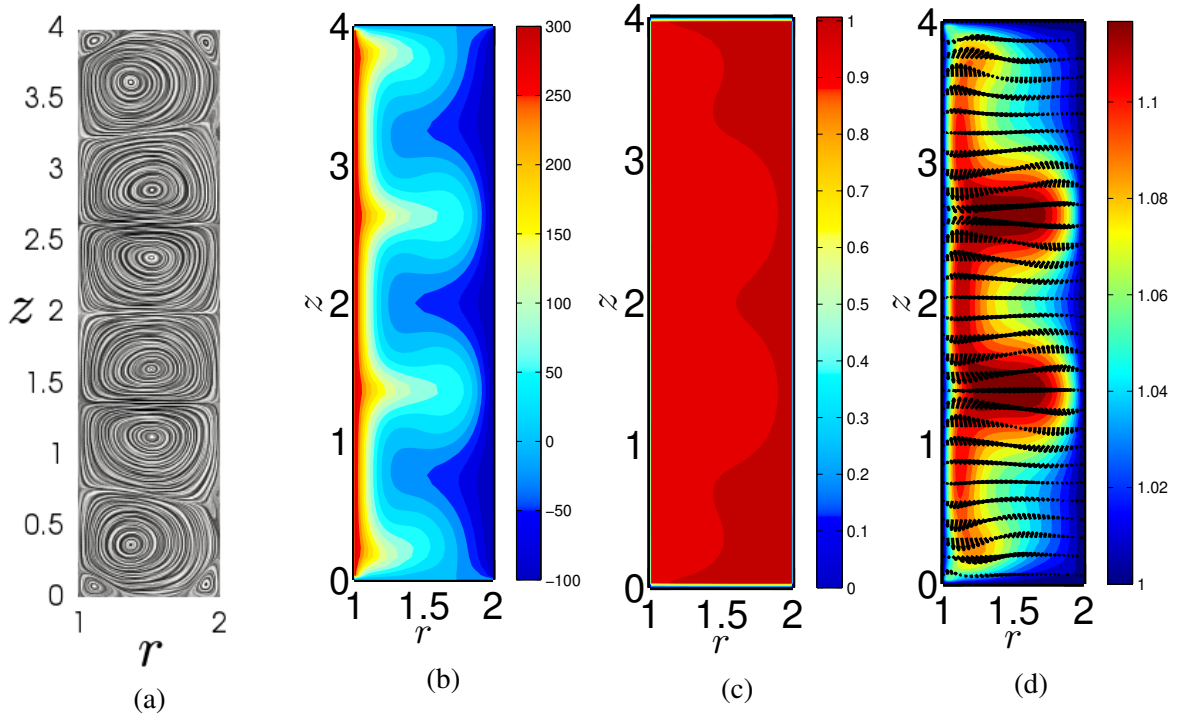

Fig. 6.10 (a) Streamlines drawn using Surface-LIC module of paraview software (Ahrens *et al.*, 2005) for $Re_i = 300$ and $Re_o = -100$, $Ma = 1$, $Pr = 1$, $\eta = 0.5$, $\Gamma = 4$. Central panels shows the color-maps in the (r,z) plane of (b) azimuthal velocity (v) contours; (c) density (ρ) contours and (d) radial-axial velocity vectors are superimposed on the background color-map of the temperature (T) fields.

and the radially inward jets are accompanied by higher density (lower temperature), which can be safely inferred from panels $(e-f)$ of figure 6.9. For a given Reynolds number of inner cylinder $(Re_i = 150)$, with increasing strength of counter-rotation $(-200 \leq Re_o \leq -300)$, a saddle point is formed at the mid-height near the outer cylinder and propagates towards the inner cylinder (see panels (g) and (h) of figure 6.9).

Figure 6.10 shows the (a) streamlines drawn using Surface-LIC module of paraview software (Ahrens *et al.*, 2005) for $Re_i = 300$ and $Re_o = -100$, $Ma = 1$, $Pr = 1$, $\eta = 0.5$, $\Gamma = 4$. Central panels shows the color-maps in the (r,z) plane of (b) azimuthal velocity (v) contours and (c) density (ρ) contours and the (d) radial-axial velocity vectors are superimposed on the background color-map of the temperature (T) fields. It is seen from the panel (a) of figure 6.10, there are four corner vortices in the domain apart from the three pair of Taylor-rolls.

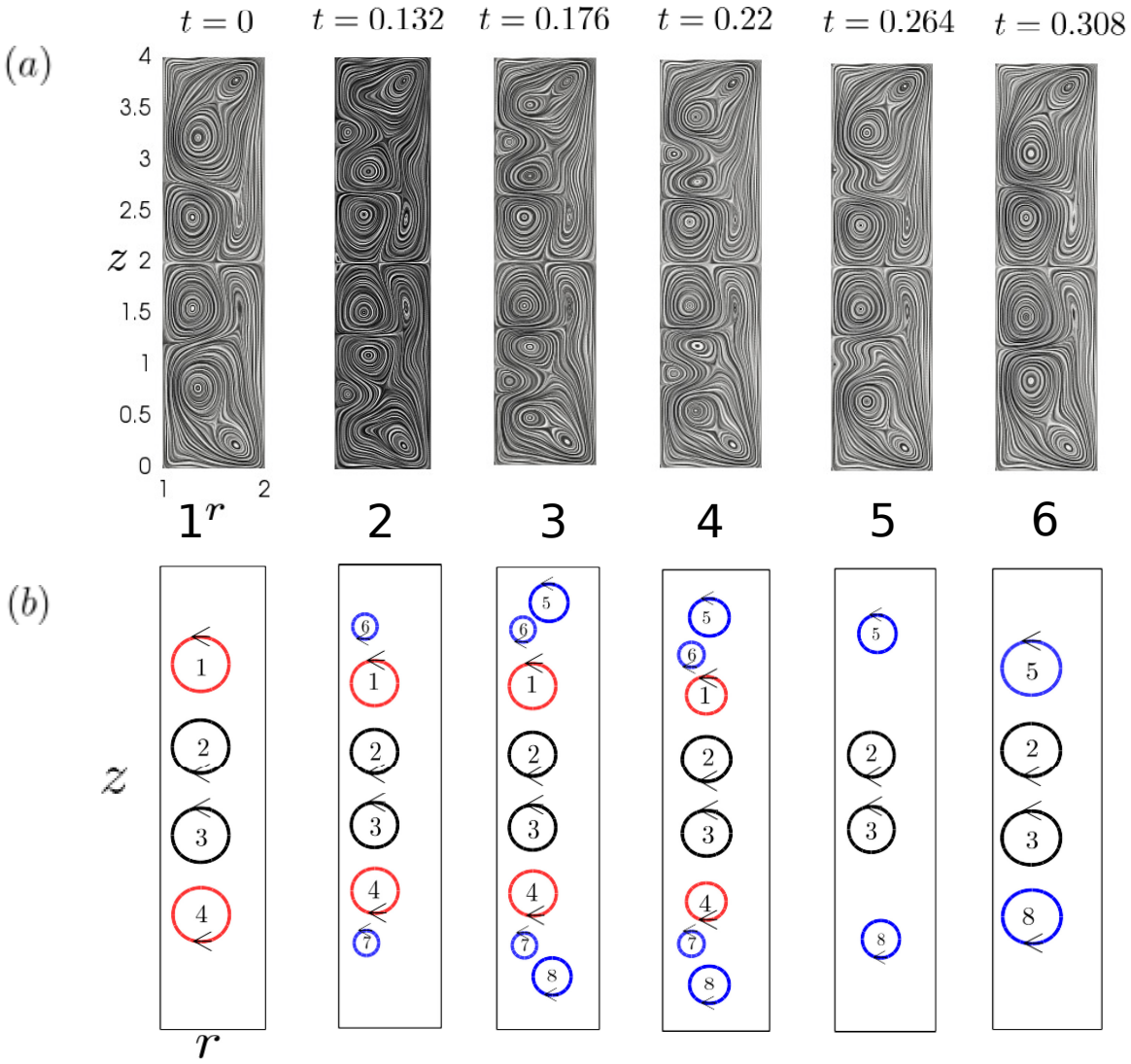

Fig. 6.11 (a) Surface Line Integral Convolution (Ahrens *et al.*, 2005) illustrating the creation and annihilation of vortices in the gap between two cylinders for $Re_i = 200$, $Re_o = -300$, $\Gamma = 4$, $Ma = 1$ and $Pr = 1$. These LIC contours cover one period of oscillation $(1-6)$ of the propagating vortices (pV) with time interval between snapshot (1) and (2) corresponding to 0.132 dimensionless times units and between (2)-(6) is 0.044 dimensionless times units, as per the viscous time scale. (b) Schematic diagram for the creation and annihilation of vortices in the gap between the inner and the outer cylinder; Ekman rolls have been not shown in the schematic to ensure clarity.

6.4.1 Propagating vortices

We report novel flow pattern, consisting of propagating vortices, being generated near both end walls and travelling towards the mid-height of the cylinder ultimately annihilated. This was previously reported by Hoffmann *et al.* (2013) where they argued that the propagating and

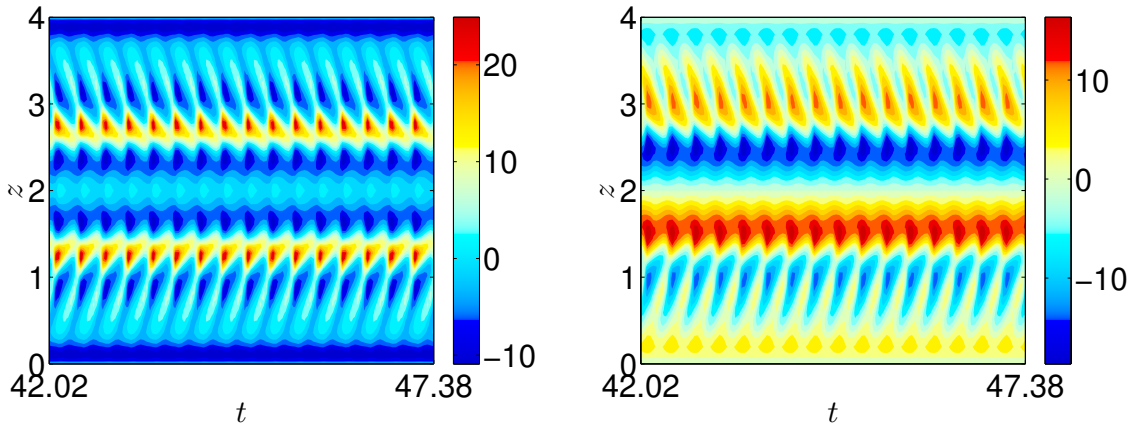

Fig. 6.12 Space time plots illustrating (a) radial velocity (u) and (b) axial velocity (w) at the mid-gap along the mid-height $(r = r_1 + \delta/2)$ of numerically simulated propagating vortex state (pV). The control parameters are $Re_i = 200$, $Re_o = -300$, $Ma = 1$, $Pr = 1$, $\eta = 0.5$ and $\Gamma = 4$.

the stationary vortices are generated by shear driven transport from Ekman circulation near both end walls. Figure 6.11 (a) shows the Surface Line Integral Convolution (Ahrens *et al.*, 2005) illustrating the creation and annihilation of vortices in the gap between two cylinders for $Re_i = 200$, $Re_o = -300$, $\Gamma = 4$, $Ma = 1$ and $Pr = 1$. These LIC contours cover one period of oscillation $(1-6)$ of the propagating vortices (pV) with time interval between snapshot (1) and (2) corresponding to 0.132 dimensionless times units and between (2)-(6) is 0.044 dimensionless times units, as per the viscous time scale. These axisymmetric propagating vortices travel towards mid-height generated from stationary end walls, where they get annihilated and the cycle continues (see panels numbered $(1-6)$ of figure 6.11). Figure 6.11 (b) presents schematic diagrams for the creation and annihilation of vortices in the gap between the inner and the outer cylinder; corresponding to every surface LIC contours placed vertically above it. The Ekman rolls presented in the corner of the LIC contours have been not shown in the schematic to ensure clarity. We start our description of vortex generation and propagation mechanism at $t_1 = 0$; panel numbered (1) in figure 6.11(b), when the cellular state portrays six vortices, i.e. four vortices symmetrically placed about the mid-height as well as two Ekman rolls (shown in panel (1) LIC plot but not shown in schematic diagram corresponding to panel (1)) near the finite endwalls. In snapshot (2), two new vortices appear close to the inner cylinder wall, namely 6/7. In snapshot (3), two more new vortices (namely 5/8), appear from the finite endwalls near the inner cylinder wall. In snapshot (4), the inner pair of vortices (6/1 and 7/4) start come closer to one another and finally disappear in (5). Finally, in (5) the vortices namely 5 and 8 come closer to 2 and 3, respectively, as shown in figure (6). The final state (6), after one cycle of oscillation

exhibits six vortices, which is the initial state (1). The time period of vortex generation from finite lids on the top and bottom of the computational domain and annihilation at the mid-height is $\tau_v \sim 0.308$, corresponding to the frequency, based on viscous time scale is $f_v \sim 3$.

Figure 6.12 shows the space-time plots for $Re_i = 200$, $Re_o = -300$ $Ma = 1$, $Pr = 1$, $\eta = 0.5$, $\Gamma = 4$ for (a) radial velocity (u) and (b) axial velocity (w) at the mid-gap along the mid-height $(r = r_1 + \delta/2)$ of numerically simulated propagating vortex state (pV). These plots indicates that the innermost vortices (2/3) lie between both vortex annihilating defects.

6.5 Summary

We have analysed the flow patterns of Taylor-Couette flow (TCF) of an molecular gas in finite cylinders obtained from independently rotating inner-cylinder ($0 < Re_i < 300$) and outer cylinder ($-300 \leq Re_o \leq 300$) by numerically integrating compressible Navier-Stokes equations (NSE) and energy equations, accompanied by ideal gas equation of state. The Mach number (Ma) of the flow and the Prandtl number (Pr) of the the fluid is set to unity. The geometrical parameters: (a) radius ratio $(\eta = r_1/r_2)$ is 1/2 (wide-gap limit) and (b) the aspect ratio $(\Gamma = h/\delta)$ is four. The emergence of localized cellular Taylor vortex state (Abshagen *et al.*, 2010) is found in the counter-rotation regime ($Re_i \in [150, 300]$ and $Re_o \in [-100, -300]$) in the compressible TCF. These axisymmetric vortices are located near the inner cylinder. We also report axisymmetric propagating vortices (previously observed by Hoffmann *et al.* (2013) in incompressible TCF), which travel towards mid-height generated from stationary end walls, where they get annihilated and the cycle continues. The phase diagram consisting of stationary and travelling patterns is constructed in the (Re_i, Re_o) plane.

Chapter 7

Summary and Outlook

The focus of the present dissertation was to study the spatio-temporal pattern formation and transport in Compressible Taylor-Couette flow. Using the Direct Numerical Simulations (DNS) to study the axisymmetric Taylor-Couette flow (TCF) of an ideal gas with inner cylinder rotating, the solutions were presented as functions of (i) Reynolds number (Re) based on the rotation rate of the inner cylinder, (ii) peripheral Mach number (Ma) of the flow and (iii) the radius ratio $(\eta = r_1/r_2)$, where r_1 and r_2 corresponds to the radii of inner and outer cylinders, respectively. The primary bifurcation from the pure azimuthal circular Couette flow (CCF) leads to the well known Taylor Vortex flow (TVF), and the phase diagrams consisting of new patterns were enumerated in the (Re, Ma) and (Re, η) plane.

A detailed introduction about Taylor-Couette Flow, and its compressible counterpart, which is essentially the flow between two differentially rotating concentric cylinders, along with its historical development and the role of using Direct Numerical Simulations to unravel the underlying flow physics was given in **Chapter 1**. **Chapter 2** presented the time-dependent axisymmetric compressible Navier-Stokes equations along with the continuity and energy equations for a mono-atomic perfect gas and the finite difference method. We employed no-slip and Dirichlet boundary conditions for velocity fields (u, v, w) and temperature field (T), respectively. Axially periodic boundary conditions were used in all simulations. The present DNS code was validated via comparisons with (i) the base state results presented in Welsh *et al.* (2014) for (a) the compressible TCF $1 \leq Ma \leq 3$ and $1 \leq Pr \leq 15$, where Pr denotes the Prandtl number of the fluid, and (b) its incompressible limit for the primary transition ($CCF \longrightarrow TVF$) using $Ma = 0.01$, (ii) the base state results for low prandtl number $Pr \leq 1$ for various $Ma \in [1,3]$ obtained from the analytical results of azimuthal velocity (v) and temperature (T) and numerical result for the density (ρ), (iii) the global response, or, the pseudo Nusselt number (Nu_ω) for the incompressible case using $Ma = 0.1$, presented in Ostilla *et al.* (2013) were summarized in **Chapter 2**.

7.1 Present Results

In **Chapter 3**, the effect of compressibility (Ma) on TCF of molecular gases was investigated and the effect of Ma on the onset of primary instability, which is the transition from purely azimuthal circular Couette flow (CCF) to Taylor vortex flow (TVF) for $\eta = 0.5$ and $\Gamma = h/\delta = \pi/2$, where Γ is the aspect ratio, h is the height of the computational domain and δ $(= r_2 - r_1)$ is gap width between two cylinders, was analyzed. It was found that at constant Re, with increasing Ma, a strong density stratification occurs along the radial direction which affects the specific angular momentum, $(\mathscr{L} = \rho v r)$, locally causing $\frac{d\mathscr{L}}{dr} > 0$ for $Ma \geq 1.5$. Interestingly, for a given Re, the radial profiles of $\mathscr{L}$ for different Ma crossed each other at a fixed radial location $(r_{\mathscr{L}})$ from the inner cylinder; $r_{\mathscr{L}}$ was found to be invariant in CCF regime and decreased in TVF regime with increasing Re. It was shown that the compressibility primarily affects the density distribution within the gap between two rotating cylinders by causing an accumulation of mass near the stationary outer cylinder and played a pivotal role in restraining the onset of instability. A new time-dependent, axially propagating, axisymmetric flow state, called the Travelling wave solution (TWS), was identified in TC cells at higher Re. Time series was analysed for the axial velocity (w) and radial velocity (u) measured at the mid-gap between the inner and outer cylinders at the mid-height of the computational domain. Low frequency axially propagating waves were found and a comprehensive phase diagram in (Re,Ma) plane was plotted that summarized these findings. Alternate regions of rarified and dense layers were identified from the axial density (ρ) profile at the mid-gap and the extent of axial stratification $[\Delta\rho = \rho(z)(\max) - \rho(z)(\min)]$ was found to increase with Re and the effect becomes more pronounced with increase in the Ma. An outward jet at the mid-height of computational domain was manifested which was accompanied by a lower density and two inward jets of relatively higher density were formed at the top and bottom of the computational domain. Transport in compressible Taylor vortices was calculated and the analyses of density (ρ) fields and axial-radial velocity (u,v,w) fields revealed that the compressibility diminished the radial (Q_r), azimuthal (Q_θ) and axial (Q_z) transports.

Chapter 4 highlighted the effects of radius ratio (η) and compressibility (Ma) on the onset of Taylor vortices from the base state of circular Couette flow (CCF). It was seen that the compressiblity (Ma) effects are less significant in smaller gap-width, TC-cell as the diffusive effects become dominant at $\eta \longrightarrow 1$. This later observation was similar to the linear stability results of Manela & Frankel (2007). We found a new state called Localized Vortex Oscillations (LVO) in the Taylor vortex pair for $\eta \sim 0.6$ for $300 \leq Re \leq 400$. We verified that the periodic boundary conditions in axial direction admits supercritical pitchfork bifurcation at the onset of TVF from CCF, and the order parameter, Δu (radial velocity at the mid-height and mid-gap of the computational domain) showed a square-root scaling $(\Delta u \propto \sqrt{\varepsilon})$, with the driving parameter

(ε) being the distance from the critical point, where $\varepsilon = (Re - Re^{cr})/Re^{cr}$. The axial velocity (w) at mid-height and mid-gap acts as an effective order parameter to quantify the "degree of asymmetry" in asymmetric stationary flow patterns. We also found the existence of side by side two rolls in short - cylinders with aspect ratios $\Gamma \leq O(1)$ at high Re in the parameter regime of the Travelling wave (TWS) flow state. The Taylor rolls near the inner cylinder were stronger compared to the rolls formed near the outer cylinder, which was ascertained from the velocity vector maps over the meridional plane in the present system. The scaling $u = \alpha\left(\frac{Re-Re_{cr}}{Re_{cr}}\right)^{\beta}$ close to the bifurcation from $CCF \longrightarrow TVF$ comes out to be $\beta \sim 0.5$, which shows that the present system follows the amplitude scaling of cubic-Landau equation. The scaling of effective-Nusselt number (Nu_{ω}) with Taylor number (Ta) were presented for different radius ratios (η). Increase in fluid compressibility decreases the effective-Nusselt number (Nu_{ω}) near the inner cylinder, at a given Re for $\eta = 0.5$.

Chapter 5 portrayed the results on Proper Orthogonal Decomposition (POD) on the flow fields obtained from Taylor-Couette flow. POD is a technique that takes a set of input data and creates an orthogonal basis constituted by functions which are the solutions of an integral eigenvalue problem. Using the "method of snapshots" on the radial-axial velocity (u,w) spectra combined with density (ρ) and temperature (T) perturbations, scaled with a weight matrix corresponding to Mack norm (Mack, 1984), over the (r,z) plane for various Re in the the wide-gap regime $(\eta = 0.5)$, it was found that the first three POD modes (for $Re = 210$) and first five POD modes $(Re = 500)$ were sufficient to capture more than 95% of the total energy content of the present system. The temporal dynamics was shown by projecting the fields onto the POD basis modes in order to calculate the associated POD coefficients and, were plotted in phase diagrams.

Chapter 6 presented the results from numerical investigations of Taylor-Couette flow (TCF) of an ideal gas in "finite" cylinders obtained with independently rotating inner-cylinder ($0 < Re_i < 300$) and outer cylinder ($-300 \leq Re_o \leq 300$), where $Re_i = \omega_1 r_1 \delta/\nu$ and $Re_o = \omega_2 r_2 \delta/\nu$ are the Reynolds number of inner and outer cylinder, respectively, and ω_1 and ω_2 are inner and outer cylinder angular velocities, $\delta = r_2 - r_1$ is the gap-width, and ν is the kinematic viscosity at inner cylinder. All these simulations were done by assuming axisymmetric flow. The emergence of localized cellular Taylor vortex state (Abshagen *et al.*, 2010) was found in the counter-rotation regime ($Re_i \in [150, 300]$ and $Re_o \in [-100, -300]$). We also reported axisymmetric propagating vortices (previously observed by Hoffmann *et al.* (2013) in incompressible TCF), which travel from end walls towards mid-height, where they get annihilated and the cycle continues. The phase diagram consisting of stationary and travelling patterns was constructed in the (Re_o, Re_i) plane for $Ma = 1$ and $Pr = 1$.

7.2 Future Work

Compressible Taylor-Couette flow (TCF) is extremely diverse in its complexity and the present work can be extended in multiple directions. Some of the future directions for this work are listed as follows.

1. Towards the non-axisymmetric compressible Taylor-Couette flow, code development (ongoing work), parallelization and pattern formation.

2. The Taylor-Couette (TC) geometry serves as a canonical test bed for probing the rheological responses of shear-driven flow of granular material. Instabilities and pattern formation scenario for dilute granular fluid would be an interesting avenue of research (ongoing work).

3. Towards Taylor-Couette flow with rotating endwalls (ongoing work).

4. Towards development of POD based low-dimensional using Galerkin projection on compressible Navier-Stokes equations.

References

ABCHA, N., CRUMEYROLLE, O., EZERSKY, A. B. & MUTABAZI, I. 2013 Velocity field of the spiral vortex flow in the couette-taylor system. *The European Physical Journal E* **36** (3), 1–7.

ABNEY, M. & EPSTEIN, R. I. 1996 Ekman pumping in compact astrophysical bodies. *Journal of Fluid Mechanics* **312**, 327–340.

ABSHAGEN, J., HEISE, M., PFISTER, G. & MULLIN, T. 2010 Multiple localized states in centrifugally stable rotating flow. *Physics of Fluids* **22** (2), 021702.

AGHOR, P. 2018 Pattern formation and anomalous modes in axisymmetic, compressible taylor-couette flow,. *M.S.(Engg.) Thesis* .

AHRENS, J., GEVECI, B. & LAW, C. 2005 Paraview: An end-user tool for large data visualization. *The visualization handbook* **717**.

ANDERECK, C. D., LIU, S. & SWINNEY, H. L. 1986 Flow regimes in a circular couette system with independently rotating cylinders. *Journal of Fluid Mechanics* **164**, 155–183.

BAKEWELL JR, H. P. & LUMLEY, J. L. 1967 Viscous sublayer and adjacent wall region in turbulent pipe flow. *The Physics of Fluids* **10** (9), 1880–1889.

BALBUS, S. A. & HAWLEY, J. F. 1998 Instability, turbulence, and enhanced transport in accretion disks. *Reviews of modern physics* **70** (1), 1.

BARCILON, A., BRINDLEY, J., LESSEN, M. & MOBBS, F. 1979 Marginal instability in taylor–couette flows at a very high taylor number. *Journal of Fluid Mechanics* **94** (3), 453–463.

BATCHELOR, G. 2000 *An introduction to fluid dynamics*. Cambridge university press.

BENJAMIN, T. & MULLIN, T. 1981 Anomalous modes in the taylor experiment. *Proceedings of the Royal Society of London. Series A, Mathematical and Physical Sciences* pp. 221–249.

BENJAMIN, T. B. 1978 Bifurcation phenomena in steady flows of a viscous fluid. i. theory. In *Proceedings of the Royal Society of London A: Mathematical, Physical and Engineering Sciences*, , vol. 359, pp. 1–26. The Royal Society.

BERKOOZ, G., HOLMES, P. & LUMLEY, J. L. 1993 The proper orthogonal decomposition in the analysis of turbulent flows. *Annual review of fluid mechanics* **25** (1), 539–575.

CHANDRASEKHAR, S. 1960 The stability of non-dissipative couette flow in hydromagnetics. *Proceedings of the National Academy of Sciences* **46** (2), 253–257.

CHANDRASEKHAR, S. 1961 Hydrodynamic and hydromagnetic stability, 652 pp., clarendon.

CHOSSAT, P. & IOOSS, G. 2012 *The Couette-Taylor Problem*, , vol. 102. Springer Science & Business Media.

COLES, D. 1965 Transition in circular couette flow. *Journal of Fluid Mechanics* **21** (3), 385–425.

COUETTE, M. 1890 Etudes sur le frottement des liquides. PhD thesis.

CROSS, M. & GREENSIDE, H. 2009 *Pattern formation and dynamics in nonequilibrium systems*. Cambridge University Press.

CURRY, J. H., HERRING, J. R., LONCARIC, J. & ORSZAG, S. A. 1984 Order and disorder in two-and three-dimensional bénard convection. *Journal of Fluid Mechanics* **147**, 1–38.

CZARNY, O., SERRE, E., BONTOUX, P. & LUEPTOW, R. M. 2003 Interaction between ekman pumping and the centrifugal instability in taylor–couette flow. *Physics of fluids* **15** (2), 467–477.

DI PRIMA, R. & SWINNEY, H. L. 1981 Instabilities and transition in flow between concentric rotating cylinders. In *Hydrodynamic instabilities and the transition to turbulence*, pp. 139–180. Springer.

DIPRIMA, R. & SWINNEY, H. 1981 Hydrodynamic instabilities and the transition to turbulence, vol. 45 of topics in applied physics .

DONNELLY, R. J. 1991 Taylor–couette flow: the early days. *Phys. Today* **44** (11), 32–39.

DRAZIN, P. G. & REID, W. H. 2004 *Hydrodynamic stability*. Cambridge university press.

DUCK, P. W., ERLEBACHER, G. & HUSSAINI, M. Y. 1994 On the linear stability of compressible plane couette flow. *Journal of Fluid Mechanics* **258**, 131–165.

ECKHARDT, B., GROSSMANN, S. & LOHSE, D. 2007 Torque scaling in turbulent taylor–couette flow between independently rotating cylinders. *Journal of fluid mechanics* **581**, 221–250.

ESSER, A. & GROSSMANN, S. 1996 Analytic expression for taylor–couette stability boundary. *Physics of Fluids* **8** (7), 1814–1819.

FASEL, H. & BOOZ, O. 1984 Numerical investigation of supercritical taylor-vortex flow for a wide gap. *Journal of Fluid Mechanics* **138**, 21–52.

GARAUD, P. 2018 Double-diffusive convection at low prandtl number. *Annual Review of Fluid Mechanics* **50**, 275–298.

GERDTS, U., VON STAMM, J., BUZUG, T. & PFISTER, G. 1994 Axisymmetric time-dependent flow in the taylor-couette system. *Physical Review E* **49** (5), 4019.

GLAUSER, M. N., LEIB, S. J. & GEORGE, W. K. 1987 Coherent structures in the axisymmetric turbulent jet mixing layer. In *Turbulent Shear Flows 5*, pp. 134–145. Springer.

GOLUB, G. & VAN LOAN, C. 1990 Matrix computations, 2nd edn. the johns hopkins.

GOLUBITSKY, M., STEWART, I. *et al.* 2012 *Singularities and groups in bifurcation theory*, , vol. 2. Springer Science & Business Media.

GORMAN, M., REITH, L. A. & SWINNEY, H. L. 1980 Modulation patterns, multiple frequencies, and other phenomena in circular couette flow. *Annals of the New York Academy of Sciences* **357** (1), 10–21.

GROSSMANN, S., LOHSE, D. & SUN, C. 2016 High–reynolds number taylor-couette turbulence. *Annual review of fluid mechanics* **48**.

GUL, M., ELSINGA, G. & WESTERWEEL, J. 2018 Experimental investigation of torque hysteresis behaviour of taylor–couette flow. *Journal of Fluid Mechanics* **836**, 635–648.

HANIFI, A., SCHMID, P. J. & HENNINGSON, D. S. 1996 Transient growth in compressible boundary layer flow. *Physics of Fluids* **8** (3), 826–837.

HARADA, I. 1980*a* Computation of strongly compressible rotating flows. *Journal of Computational Physics* **38** (3), 335–356.

HARADA, I. 1980*b* A numerical study of weakly compressible rotating flows in a gas centrifuge. *Nuclear Science and Engineering* **73** (3), 225–241.

HATAY, F. F., BIRINGEN, S., ERLEBACHER, G. & ZORUMSKI, W. 1993 Stability of high-speed compressible rotating couette flow. *Physics of Fluids A: Fluid Dynamics* **5** (2), 393–404.

HEISE, M., ABSHAGEN, J., KÜTER, D., HOCHSTRATE, K., PFISTER, G. & HOFFMANN, C. 2008 Localized spirals in taylor-couette flow. *Physical Review E* **77** (2), 026202.

HEISE, M., HOFFMANN, C., WILL, C., ALTMEYER, S., ABSHAGEN, J. & PFISTER, G. 2013 Co-rotating taylor–couette flow enclosed by stationary disks. *Journal of Fluid Mechanics* **716**.

HELLEVIK, L. R. 2018 Numerical methods for engineers. *Kompendium. NTNU* .

HOFFMANN, C., ALTMEYER, S., HEISE, M., ABSHAGEN, J. & PFISTER, G. 2013 Axisymmetric propagating vortices in centrifugally stable taylor–couette flow. *Journal of Fluid Mechanics* **728**, 458–470.

HOFFMANN, C., LÜCKE, M. & PINTER, A. 2004 Spiral vortices and taylor vortices in the annulus between rotating cylinders and the effect of an axial flow. *Physical Review E* **69** (5), 056309.

HOLMES, P., LUMLEY, J. L., BERKOOZ, G. & ROWLEY, C. W. 2012 *Turbulence, coherent structures, dynamical systems and symmetry*. Cambridge university press.

HOWARTH, L. 1951 Some aspects of rayleigh's problem for a compressible fluid. *The Quarterly Journal of Mechanics and Applied Mathematics* **4** (2), 157–169.

HU, S. & ZHONG, X. 1998 Linear stability of viscous supersonic plane couette flow. *Physics of Fluids* **10** (3), 709–729.

HYUN, J. M. & PARK, J. S. 1992 Spin-up from rest of a compressible fluid in a rapidly rotating cylinder. *Journal of Fluid Mechanics* **237**, 413–434.

IMOMOH, E., DUSTING, J. & BALABANI, S. 2010 On the quasiperiodic state in a moderate aspect ratio taylor–couette flow. *Physics of Fluids* **22** (4), 044103.

JOLLIFFE, I. 1986 Principal component analysis .

JONES, C. 1982 On flow between counter-rotating cylinders. *Journal of Fluid Mechanics* **120**, 433–450.

JONES, C. 1985 The transition to wavy taylor vortices. *Journal of Fluid Mechanics* **157**, 135–162.

JONES, C. A. 1981 Nonlinear taylor vortices and their stability. *Journal of Fluid Mechanics* **102**, 249–261.

KAO, K.-H. & CHOW, C.-Y. 1992 Linear stability of compressible taylor–couette flow. *Physics of Fluids A: Fluid Dynamics* **4** (5), 984–996.

KARHUNEN, K. 1946 Zur spektraltheorie stochastischer prozesse. *Ann. Acad. Sci. Fennicae, AI* **34**.

KIM, J., MOIN, P. & MOSER, R. 1987 Turbulence statistics in fully developed channel flow at low reynolds number. *Journal of fluid mechanics* **177**, 133–166.

KIRBY, M. & ARMBRUSTER, D. 1992 Reconstructing phase space from pde simulations. *Zeitschrift für angewandte Mathematik und Physik ZAMP* **43** (6), 999–1022.

KOSAMBI, D. D. 1943 Statistics in function space. *Journal of the Indian Mathematical Society* **7**, 76–88.

KOSCHMIEDER, E. L. 1993 *Bénard cells and Taylor vortices*. Cambridge University Press.

KUHLTHAU, A. 1960 Recent low-density experiments using rotating cylinder techniques. In *Rarefied Gas Dynamics*, p. 192.

LATHROP, D. P., FINEBERG, J. & SWINNEY, H. L. 1992 Transition to shear-driven turbulence in couette-taylor flow. *Physical Review A* **46** (10), 6390.

LOEVE, M. 1955 Probability theory: foundations, random sequences .

LOPEZ, J., MARQUES, F. & SHEN, J. 2004 Complex dynamics in a short taylor-couette annulus with the top endwall stationary and the bottom rotating. *J. Fluid Mech* **501**, 327–354.

LUMLEY, J. L. 1967 The structure of inhomogeneous turbulent flows. *Atmospheric turbulence and radio wave propagation* .

MACK, L. M. 1976 A numerical study of the temporal eigenvalue spectrum of the blasius boundary layer. *Journal of Fluid Mechanics* **73** (3), 497–520.

MACK, L. M. 1984 Boundary-layer linear stability theory. *Tech. Rep.*. CALIFORNIA INST OF TECH PASADENA JET PROPULSION LAB.

MALIK, M., ALAM, M. & DEY, J. 2006 Nonmodal energy growth and optimal perturbations in compressible plane couette flow. *Physics of Fluids* **18** (3), 034103.

MALIK, M., DEY, J. & ALAM, M. 2008 Linear stability, transient energy growth, and the role of viscosity stratification in compressible plane couette flow. *Physical Review E* **77** (3), 036322.

MALLOCK, A. 1889 Iv. determination of the viscosity of water. *Proceedings of the Royal Society of London* **45** (273-279), 126–132.

MANELA, A. & FRANKEL, I. 2007 On the compressible taylor–couette problem. *Journal of Fluid Mechanics* **588**, 59–74.

MANELA, A. & ZHANG, J. 2012 The effect of compressibility on the stability of wall-bounded kolmogorov flow. *Journal of Fluid Mechanics* **694**, 29–49.

MARCUS, P. S. 1984*a* Simulation of taylor-couette flow. part 1. numerical methods and comparison with experiment. *Journal of Fluid Mechanics* **146**, 45–64.

MARCUS, P. S. 1984*b* Simulation of taylor-couette flow. part 2. numerical results for wavy-vortex flow with one travelling wave. *Journal of Fluid Mechanics* **146**, 65–113.

MEYER, K. A. 1967 Time-dependent numerical study of taylor vortex flow. *The Physics of Fluids* **10** (9), 1874–1879.

MEYER, K. A. 1969 Three-dimensional study of flow between concentric rotating cylinders. *The Physics of Fluids* **12** (12), II–165.

MEYER-SPASCHE, R. & KELLER, H. B. 1980 Computations of the axisymmetric flow between rotating cylinders. *Journal of Computational Physics* **35** (1), 100–109.

MOIN, P. & MOSER, R. D. 1989 Characteristic-eddy decomposition of turbulence in a channel. *Journal of Fluid Mechanics* **200**, 471–509.

MOSER, R., MOIN, P. & LEONARD, A. 1983 A spectral numerical method for the navier-stokes equations with applications to taylor-couette flow. *Journal of Computational Physics* **52** (3), 524–544.

ORSZAG, S. A. & KELLS, L. C. 1980 Transition to turbulence in plane poiseuille and plane couette flow. *Journal of Fluid Mechanics* **96** (1), 159–205.

OSTILLA, R., STEVENS, R. J., GROSSMANN, S., VERZICCO, R. & LOHSE, D. 2013 Optimal taylor–couette flow: direct numerical simulations. *Journal of fluid mechanics* **719**, 14–46.

PARK, H. & SIROVICH, L. 1990 Turbulent thermal convection in a finite domain: Part ii. numerical results. *Physics of Fluids A: Fluid Dynamics* **2** (9), 1659–1668.

PARK, J. S. & HYUN, J. M. 1989 Transient adjustment of a gas contained in a rapidly-rotating infinite cylinder. *Journal of the Physical Society of Japan* **58** (11), 3949–3959.

PIRRO, D. & QUADRIO, M. 2008 Direct numerical simulation of turbulent taylor–couette flow. *European Journal of Mechanics-B/Fluids* **27** (5), 552–566.

RAYLEIGH, L. 1917 On the dynamics of revolving fluids. *Proceedings of the Royal Society of London. Series A, Containing Papers of a Mathematical and Physical Character* **93** (648), 148–154.

RODRIGUEZ, J. & SIROVICH, L. 1990 Low-dimensional dynamics for the complex ginzburg-landau equation. *Physica D: Nonlinear Phenomena* **43** (1), 77–86.

ROWLEY, C. W., COLONIUS, T. & MURRAY, R. M. 2004 Model reduction for compressible flows using pod and galerkin projection. *Physica D: Nonlinear Phenomena* **189** (1-2), 115–129.

ROWLEY, C. W. & WILLIAMS, D. R. 2006 Dynamics and control of high-reynolds-number flow over open cavities. *Annu. Rev. Fluid Mech.* **38**, 251–276.

SIROVICH, L. 1987 Turbulence and the dynamics of coherent structures. i. coherent structures. *Quarterly of applied mathematics* **45** (3), 561–571.

SIROVICH, L. & PARK, H. 1990 Turbulent thermal convection in a finite domain: Part i. theory. *Physics of Fluids A: Fluid Dynamics* **2** (9), 1649–1658.

STROGATZ, S. 2001 Nonlinear dynamics and chaos: with applications to physics, biology, chemistry, and engineering (studies in nonlinearity) .

SYNGE, J. L. 1938 On the stability of a viscous liquid between rotating coaxial cylinders. *Proceedings of the Royal Society of London. Series A. Mathematical and Physical Sciences* **167** (929), 250–256.

TAYLOR, G. I. 1923 Stability of a viscous liquid contained between two rotating cylinders. *Philosophical Transactions of the Royal Society of London. Series A, Containing Papers of a Mathematical or Physical Character* **223**, 289–343.

TAYLOR, G. I. 1936*a* Fluid friction between rotating cylinders ii—distribution of velocity between concentric cylinders when outer one is rotating and inner one is at rest. *Proceedings of the Royal Society of London. Series A-Mathematical and Physical Sciences* **157** (892), 565–578.

TAYLOR, G. I. 1936*b* Fluid friction between rotating cylinders i—torque measurements. *Proceedings of the Royal Society of London. Series A-Mathematical and Physical Sciences* **157** (892), 546–564.

TREVE, Y. & MANLEY, O. 1982 Energy conserving galerkin approximations for 2-d hydrodynamic and mhd bénard convection. *Physica D: Nonlinear Phenomena* **4** (3), 319–342.

TROPEA, C. & YARIN, A. L. 2007 *Springer handbook of experimental fluid mechanics*. Springer Science & Business Media.

VON STAMM, J., BUZUG, T. & PFISTER, G. 1994 Frequency locking in axisymmetric taylor-couette flow. *Physics Letters A* **194** (3), 173–178.

WELSH, S., KERSALÉ, E. & JONES, C. A. 2014 Compressible taylor–couette flow–instability mechanism and codimension 3 points. *Journal of Fluid Mechanics* **750**, 555–577.

Appendix A

Time series and power spectral density

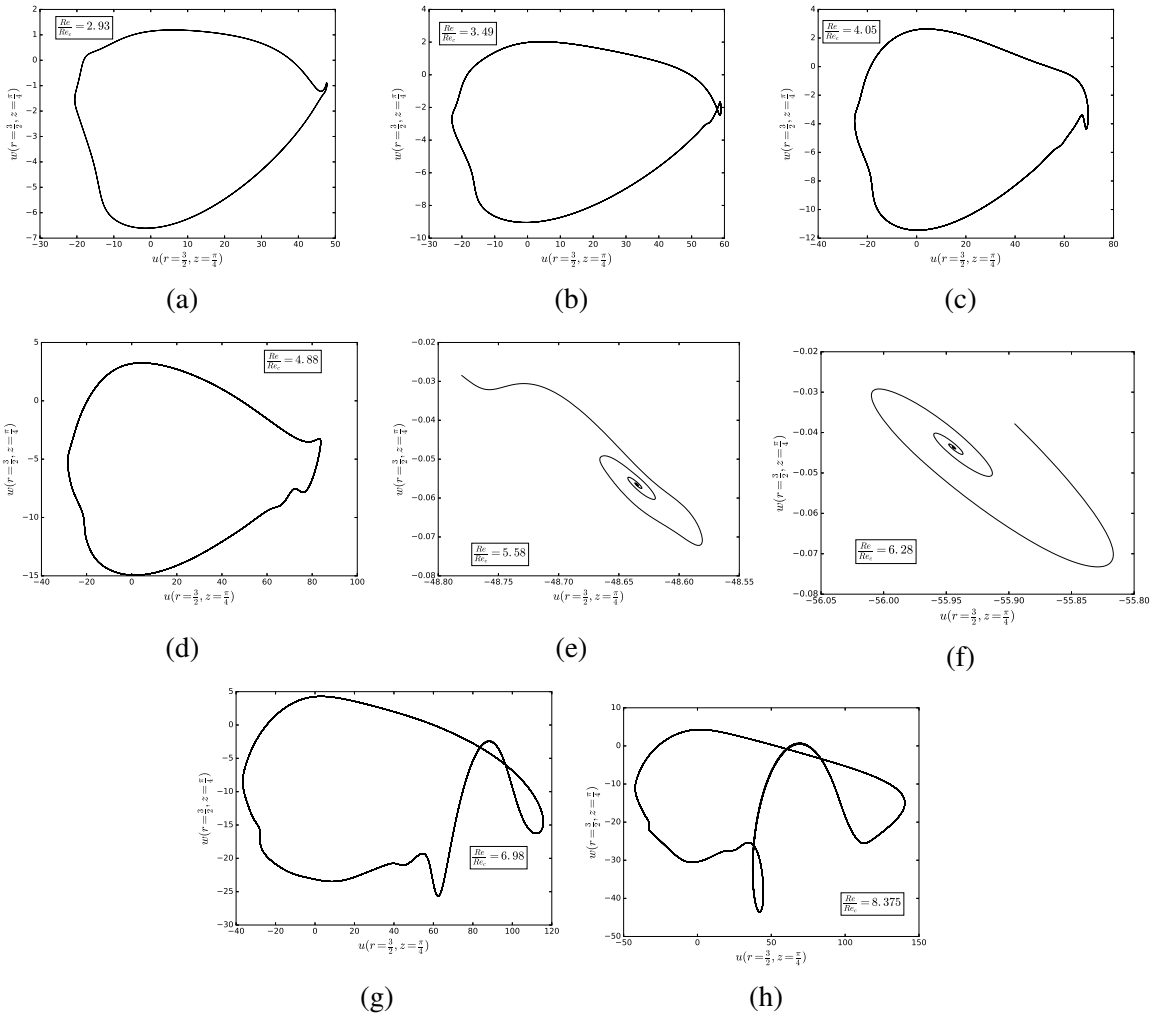

Fig. A.1 Phase plots for $(u(x,t),w(x,t))$ for grid-points along axial and radial directions $(N_z \times N_r)$ are 61×61; $Re_c (= Re^{cr})$ corresponds to the critical Reynolds number for purely azimuthal *CCF* to Taylor vortex flow (TVF) for $\eta = 1/2$, $Ma = 1$ and $Pr = 1$, for Reynolds numbers (a) $Re = 210$, (b) $Re = 250$, (c) $Re = 290$, (d) $Re = 350$, (e) $Re = 400$, (f) $Re = 450$, (g) $Re = 500$ and (h) $Re = 600$.

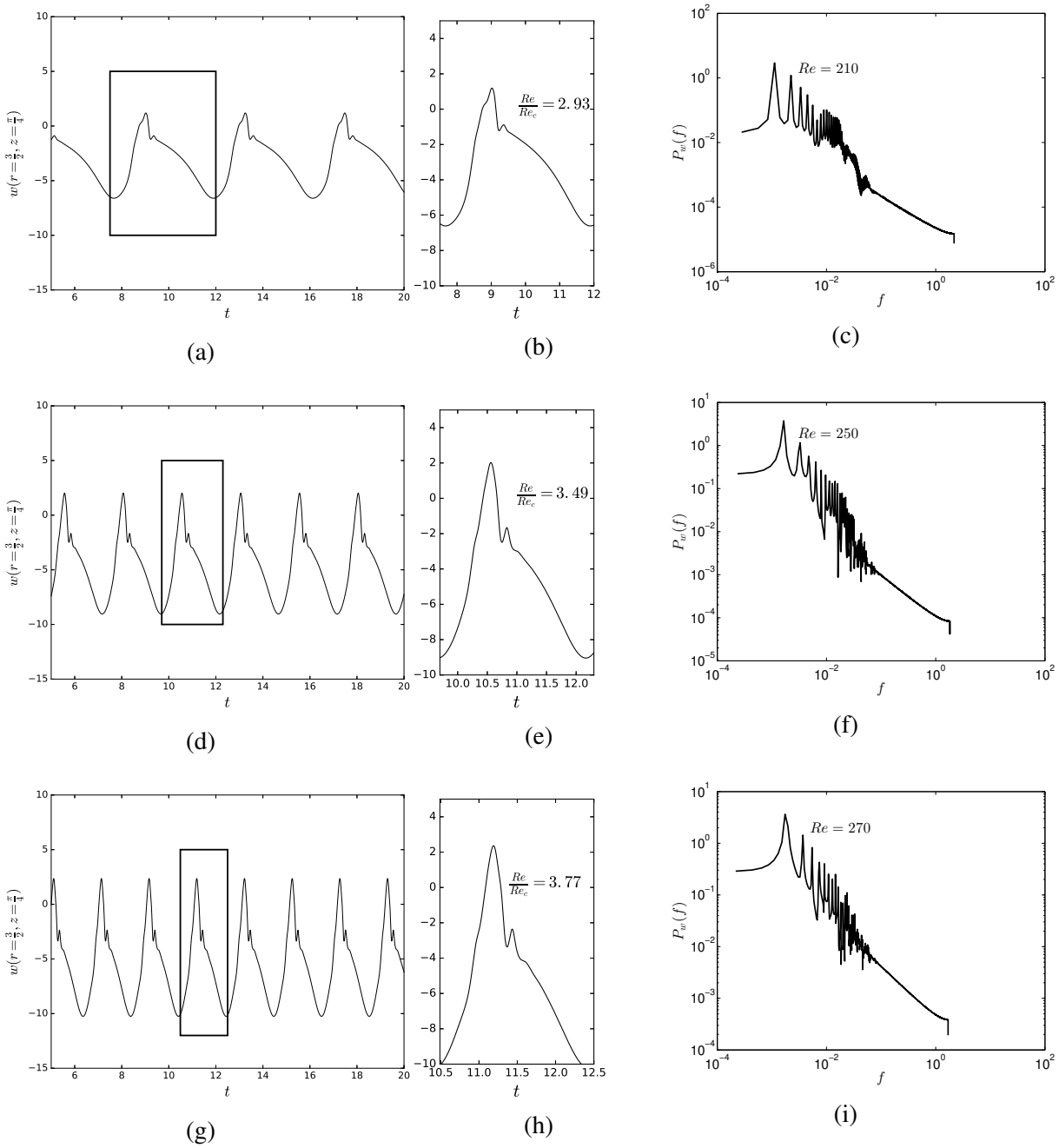

Fig. A.2 Time dependence of local axial velocity at mid-height and mid-plane of the computational domain; An enlargement of the figure showing a single wave; Single-sided axial velocity fluctuation power spectra. Only the last $\frac{3}{4}$ of the time series is used for fast Fourier transform in order to suppress initial transients.

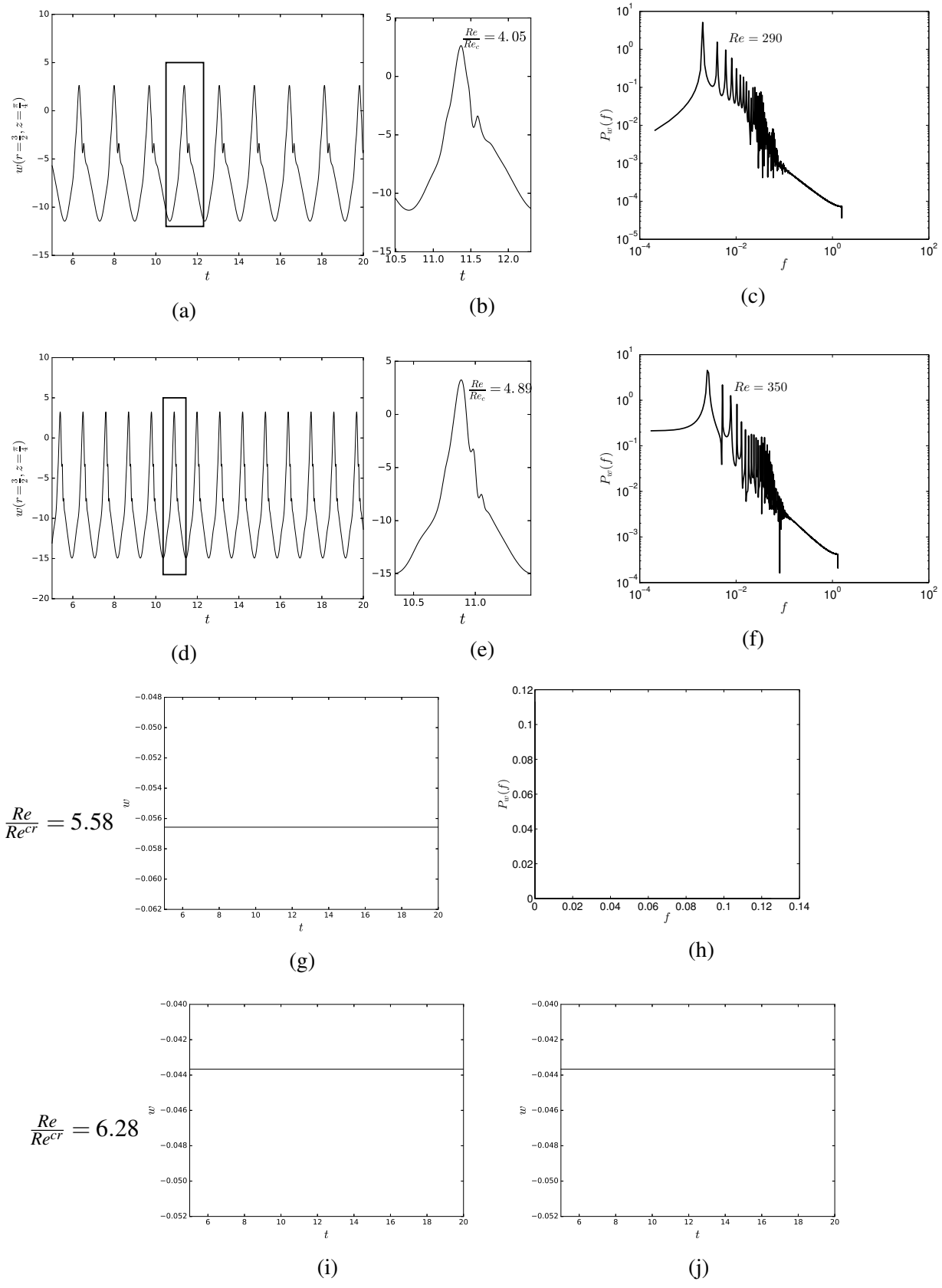

Fig. A.3 Time dependence of local axial velocity at mid-height and mid-plane of the computational domain; An enlargement of the figure showing a single wave; Single-sided axial velocity fluctuation power spectra. Only the last $\frac{3}{4}$ of the time series is used for fast Fourier transform in order to suppress initial transients.

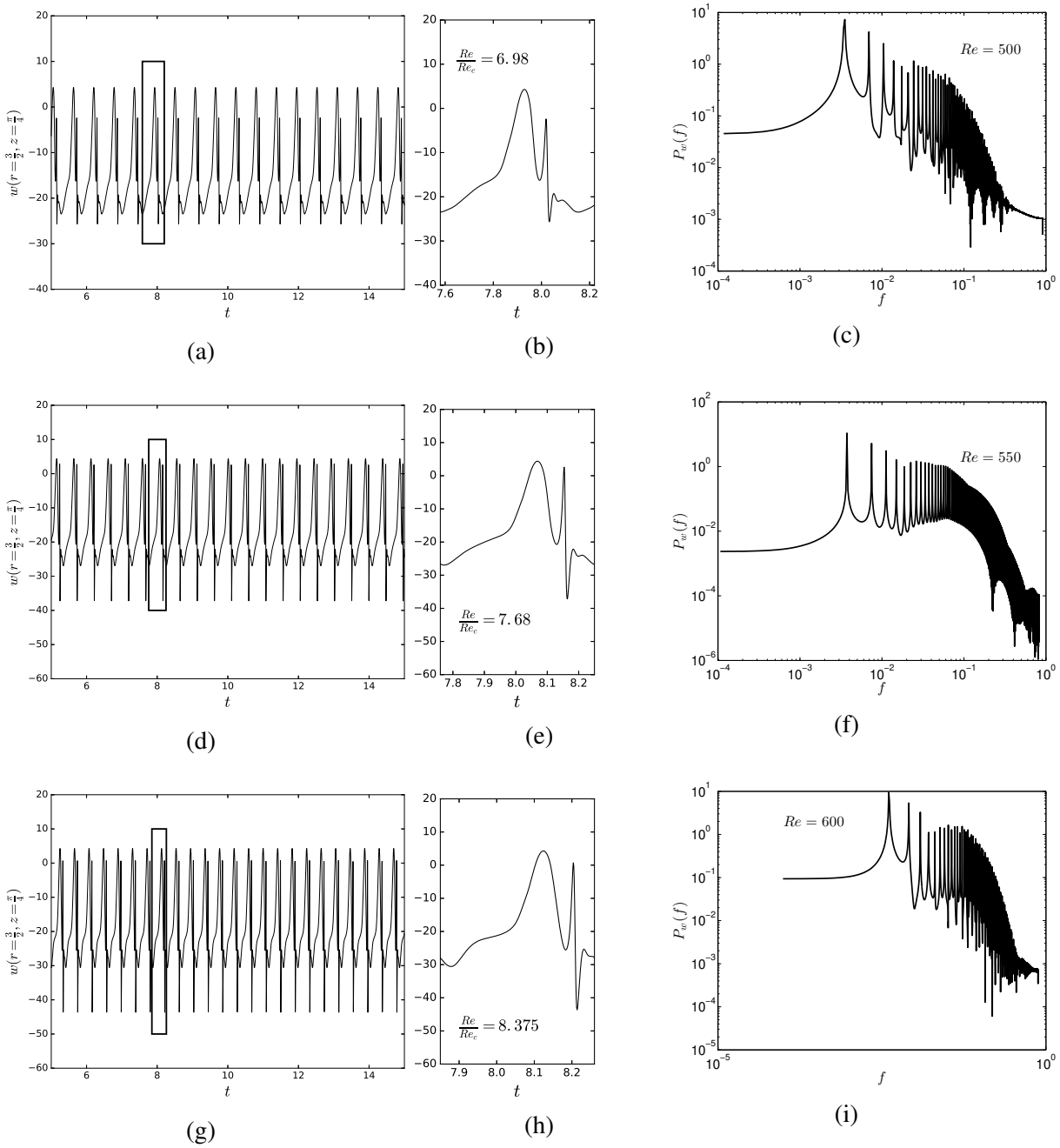

Fig. A.4 Time dependence of local axial velocity at mid-height and mid-plane of the computational domain; An enlargement of the figure showing a single wave; Single-sided axial velocity fluctuation power spectra. Only the last $\frac{3}{4}$ of the time series is used for fast Fourier transform in order to suppress initial transients.

Appendix B

Resolution Tests

Re_{r_1}	Re	$N_z \times N_r$	$\Delta z \times \Delta r$	Δt	Analysis
50	116.67	41×41	0.038×0.057	1×10^{-6}	CCF
55	128.33	41×41	0.038×0.057	1×10^{-6}	CCF
60	140	41×41	0.038×0.057	1×10^{-6}	CCF
65	151.67	41×41	0.038×0.057	1×10^{-6}	CCF
70	163.33	41×41	0.038×0.057	1×10^{-6}	CCF
75	175	61×61	0.026×0.038	1×10^{-6}	TVF - 2roll
80	186.67	41×41	0.038×0.057	1×10^{-6}	TVF - 2roll
83	193.67	41×41	0.038×0.057	1×10^{-6}	TVF - 2roll
85	198.33	41×41	0.038×0.057	1×10^{-6}	TVF - 2roll
95	221.67	101×101	0.016×0.023	5×10^{-7}	TVF - 2 roll
105	245	101×101	0.016×0.023	5×10^{-7}	TVF - 2 roll
200	466.67	101×101	0.016×0.023	5×10^{-7}	TWS
300	700	101×101	0.016×0.023	5×10^{-7}	TWS

Table B.1 Computational details for $\eta = 0.3$, $Ma = 1.0$ and $Pr = 1.0$. The columns illustrate the inner cylinder Reynolds number (Re), number of grids, grid spacing; $\Delta z = \frac{\pi}{2N_z}$ and $\Delta r = \frac{1-\eta}{\eta N_r}$, the time step size, analysis of the states. $Re = ((1/\eta) - 1) * Re_{r_1}$, where Re_{r_1} corresponds to the computational Reynolds number based on chosen length scale as inner cylinder radius.

Re_{r_1}	Re	$N_z \times N_r$	$\Delta z \times \Delta r$	Δt	Analysis
50	75	41×41	0.038×0.037	1×10^{-6}	CCF
51	76.5	41×41	0.038×0.037	1×10^{-6}	CCF
53	79.5	41×41	0.038×0.037	1×10^{-6}	CCF
55	82.5	41×41	0.038×0.037	1×10^{-6}	CCF
57	85.5	41×41	0.038×0.037	1×10^{-6}	CCF
60	90	41×41	0.038×0.037	1×10^{-6}	CCF
65	97.5	41×41	0.038×0.037	1×10^{-6}	CCF
66	99	41×41	0.038×0.037	1×10^{-6}	TVF - 2roll
67	100.5	41×41	0.038×0.037	1×10^{-6}	TVF - 2roll
70	105	61×61	0.026×0.0245	1×10^{-6}	TVF - 2roll
80	120	61×61	0.026×0.0245	1×10^{-6}	TVF - 2roll
90	135	61×61	0.026×0.0245	1×10^{-6}	TVF - 2roll
100	150	61×61	0.026×0.0245	1×10^{-6}	TVF - 2roll
200	300	61×61	0.026×0.0245	1×10^{-6}	TWS
300	450	101×101	0.016×0.015	5×10^{-7}	TWS
500	750	101×101	0.016×0.015	5×10^{-7}	TWS

Table B.2 Computational details for $\eta = 0.4$, $Ma = 1.0$ and $Pr = 1.0$. The columns illustrate the inner cylinder Reynolds number (Re), number of grids, grid spacing; $\Delta z = \frac{\pi}{2N_z}$ and $\Delta r = \frac{1-\eta}{\eta N_r}$, the time step size, analysis of the states. $Re = ((1/\eta) - 1) * Re_{r_1}$, where Re_{r_1} corresponds to the computational Reynolds number based on chosen length scale as inner cylinder radius.

$Re(=Re_{r_1})$	$N_z \times N_r$	$\Delta z \times \Delta r$	Δt	Analysis
80	41×41	0.038×0.024	5×10^{-6}	TVF - 2roll
120	41×41	0.038×0.024	5×10^{-6}	TVF - 2roll
150	41×41	0.038×0.024	5×10^{-6}	TVF - 2roll
180	41×41	0.038×0.024	5×10^{-6}	TVF - 2roll
182	41×41	0.038×0.024	5×10^{-6}	TVF - 2roll
183	41×41	0.038×0.024	1×10^{-6}	TWS
183	61×61	0.025×0.016	1×10^{-6}	TWS
185	61×61	0.025×0.016	1×10^{-6}	TWS
185	81×81	0.025×0.016	5×10^{-7}	TWS
188	61×61	0.025×0.016	1×10^{-6}	TWS
190	61×61	0.025×0.016	1×10^{-6}	TWS
230	61×61	0.025×0.016	1×10^{-6}	TWS
250	61×61	0.025×0.016	1×10^{-6}	TWS
270	61×61	0.025×0.016	1×10^{-6}	TWS
290	61×61	0.025×0.016	1×10^{-6}	TWS
300	61×61	0.025×0.016	1×10^{-6}	TWS
360	61×61	0.025×0.016	1×10^{-6}	TWS
370	61×61	0.025×0.016	1×10^{-6}	TWS
380	61×61	0.025×0.016	1×10^{-6}	TWS
382	61×61	0.025×0.016	1×10^{-6}	TWS
383	61×61	0.025×0.016	1×10^{-6}	TVF - 2roll
384	61×61	0.025×0.016	1×10^{-6}	TVF - 2roll
385	61×61	0.025×0.016	1×10^{-6}	TVF - 2roll
388	61×61	0.025×0.016	1×10^{-6}	TVF - 2roll
400	61×61	0.025×0.016	1×10^{-6}	TVF - 2roll
410	61×61	0.025×0.016	1×10^{-6}	TVF - 2roll
450	61×61	0.025×0.016	1×10^{-6}	TVF - 2roll
475	61×61	0.025×0.016	1×10^{-6}	TVF - 2roll
476	61×61	0.025×0.016	1×10^{-6}	TWS
477	61×61	0.025×0.016	1×10^{-6}	TWS
478	61×61	0.025×0.016	1×10^{-6}	TWS
500	61×61	0.025×0.016	1×10^{-6}	TWS
500	81×81	0.019×0.012	1×10^{-6}	TWS
500	101×101	0.016×0.0099	5×10^{-7}	TWS
550	61×61	0.025×0.016	1×10^{-6}	TWS
600	61×61	0.025×0.016	1×10^{-6}	TWS
600	101×101	0.016×0.0099	5×10^{-7}	TWS
650	61×61	0.025×0.016	1×10^{-6}	TWS
700	61×61	0.025×0.016	1×10^{-6}	TWS
700	101×101	0.016×0.0099	5×10^{-7}	TWS
800	61×61	0.025×0.016	1×10^{-6}	TWS
800	101×101	0.016×0.0099	5×10^{-7}	TWS

Table B.3 Computational details for $\eta = 0.5$, $Ma = 1.0$ and $Pr = 1.0$. The columns illustrate the inner cylinder Reynolds number (Re), number of grids, grid spacing; $\Delta z = \frac{\pi}{2N_z}$ and $\Delta r = \frac{1-\eta}{\eta N_r}$, the time step size, analysis of the states.

Re_{r_1}	Re	$N_z \times N_r$	$\Delta z \times \Delta r$	Δt	Analysis
77	51.33	41×41	0.038×0.016	1×10^{-5}	CCF
100	66.67	61×61	0.026×0.011	1×10^{-6}	CCF
101	67.33	61×61	0.026×0.011	1×10^{-6}	CCF
102	68	61×61	0.026×0.011	1×10^{-6}	CCF
103	68.66	61×61	0.026×0.011	1×10^{-6}	CCF
104	69.33	61×61	0.026×0.011	1×10^{-6}	CCF
105	70	61×61	0.026×0.011	1×10^{-6}	CCF
110	73.33	41×41	0.038×0.016	5×10^{-6}	CCF
110	73.33	61×61	0.026×0.011	1×10^{-6}	CCF
120	80	41×41	0.038×0.016	5×10^{-6}	TVF - 2roll
120	80	61×61	0.026×0.011	1×10^{-6}	TVF - 2roll
130	86.67	41×41	0.038×0.016	5×10^{-6}	TVF - 2roll
130	86.67	61×61	0.026×0.011	1×10^{-6}	TVF - 2roll
140	93.33	41×41	0.038×0.016	5×10^{-6}	TVF - 2roll
140	93.33	61×61	0.026×0.011	1×10^{-6}	TVF - 2roll
150	100	41×41	0.038×0.016	5×10^{-6}	TVF - 2roll
150	100	61×61	0.026×0.011	1×10^{-6}	TVF - 2roll
200	133.33	61×61	0.026×0.011	1×10^{-6}	TVF - 2roll
250	166.67	61×61	0.026×0.011	1×10^{-6}	TVF - 2roll
300	200	61×61	0.026×0.011	1×10^{-6}	TVF - 2roll
400	266.67	101×101	0.016×0.0066	5×10^{-7}	TVF - 2roll
500	333.33	101×101	0.016×0.0066	5×10^{-7}	TWS
600	400	101×101	0.016×0.0066	5×10^{-7}	LVO
700	466.67	101×101	0.016×0.0066	5×10^{-7}	TWS
800	533.33	101×101	0.016×0.0066	5×10^{-7}	TWS

Table B.4 Computational details for $\eta = 0.6$, $Ma = 1.0$ and $Pr = 1.0$. The columns illustrate the inner cylinder Reynolds number (Re), number of grids, grid spacing; $\Delta z = \frac{\pi}{2N_z}$ and $\Delta r = \frac{1-\eta}{\eta N_r}$, the time step size, analysis of the states: Localized Vortex Oscillations (LVO). $Re = ((1/\eta) - 1) * Re_{r_1}$, where Re_{r_1} corresponds to the Reynolds number based on chosen length scale as inner cylinder radius.

Re_{r_1}	Re	$N_z \times N_r$	Nu_ω	Δt	Analysis
100	48.85	41×41	0.9948	1×10^{-5}	CCF
120	51.42	41×41	0.9948	1×10^{-5}	CCF
150	64.28	41×41	0.9948	5×10^{-6}	CCF
150	64.28	61×61	0.9966	1×10^{-6}	CCF
160	68.57	61×61	0.9966	1×10^{-6}	CCF
170	72.86	61×61	0.9965	1×10^{-6}	CCF
180	77.14	61×61	0.9964	1×10^{-6}	CCF
192	82.28	61×61	1.0071	1×10^{-6}	TVF - 4roll
194	83.14	61×61	1.0204	1×10^{-6}	TVF - 4roll
196	84	61×61	1.0340	1×10^{-6}	TVF - 4roll
198	84.85	61×61	1.0475	1×10^{-6}	TVF - 4roll
200	85.71	101×101	1.0740	5×10^{-7}	TVF - 4roll
230	98.57	61×61	1.2496	1×10^{-6}	TVF - 4roll
250	107.14	61×61	1.3510	1×10^{-6}	TVF - 4roll
270	115.71	61×61	1.4443	1×10^{-6}	TVF - 4roll
300	128.57	101×101	1.5960	5×10^{-7}	TVF - 4roll
400	171.43	101×101	1.9214	5×10^{-7}	TVF - 4roll
450	192.86	101×101	2.0844	5×10^{-7}	TVF - 4roll
500	214.29	101×101	2.1754	5×10^{-7}	TVF - 4roll
500	214.29	151×101	2.1512	5×10^{-7}	TVF - 4roll
550	235.7	101×101	2.2689	5×10^{-7}	TVF - 4roll
600	257.14	101×101	2.3633	5×10^{-7}	TVF - 4roll
620	265.7	101×101	2.4009	5×10^{-7}	TVF - 4roll
640	274.28	101×101	2.4383	5×10^{-7}	TVF - 4roll
660	282.86	101×101	2.0131	5×10^{-7}	TVF - 2 roll
680	291.43	101×101	2.0511	5×10^{-7}	TVF - 2 roll
700	300	101×101	2.0874	5×10^{-7}	TVF - 2roll
700	300	151×101	2.0922	5×10^{-7}	TVF - 2roll
700	300	171×101	2.0934	5×10^{-7}	TVF - 2roll
800	342.86	101×101	2.2523	5×10^{-7}	TVF - 2roll
800	342.86	121×101	2.6027	5×10^{-7}	TVF - 2roll
800	342.86	151×101	2.6181	5×10^{-7}	TVF - 2roll

Table B.5 Computational details for $\eta = 0.7$, $Ma = 1.0$ and $Pr = 1.0$. The columns illustrate the inner cylinder Reynolds number (Re), number of grids, grid spacing; $\Delta z = \frac{\pi}{2N_z}$ and $\Delta r = \frac{1-\eta}{\eta N_r}$, the time step size, analysis of the states. $Re = ((1/\eta) - 1) * Re_{r_1}$, where Re_{r_1} corresponds to the Reynolds number based on chosen length scale as inner cylinder radius.

Re_{r_1}	Re	$N_z \times N_r$	Nu_ω	Δt	Analysis
200	50	41×41	0.9970	5×10^{-6}	CCF
200	50	61×61	0.9980	1×10^{-6}	CCF
300	75	41×41	0.9970	5×10^{-6}	CCF
300	75	61×61	0.9980	1×10^{-6}	CCF
320	80	61×61	0.9980	1×10^{-6}	CCF
330	82.5	61×61	0.9980	1×10^{-6}	CCF
340	85	61×61	0.9980	1×10^{-6}	CCF
350	87.5	61×61	0.9980	1×10^{-6}	CCF
360	90	61×61	0.9980	1×10^{-6}	CCF
370	92.5	61×61	0.9980	1×10^{-6}	CCF
380	95	61×61	0.9980	1×10^{-6}	CCF
382	95.5	61×61	0.9979	1×10^{-6}	CCF
384	96	61×61	0.9987	1×10^{-6}	TVF
386	96.5	61×61	1.0026	1×10^{-6}	TVF
388	97	61×61	1.0078	1×10^{-6}	TVF
390	97.5	61×61	1.0116	1×10^{-6}	TVF-6 roll
400	100	101×101	1.0566	5×10^{-7}	TVF-6 roll
410	102.5	101×101	1.0945	5×10^{-7}	TVF-6 roll
420	105	101×101	1.1316	5×10^{-7}	TVF-6 roll
430	107.5	101×101	1.1673	5×10^{-7}	TVF-6 roll
440	110	101×101	1.2073	5×10^{-7}	TVF-6 roll
450	112.5	101×101	1.2351	5×10^{-7}	TVF-6 roll
460	115	101×101	1.2672	5×10^{-7}	TVF-6 roll
470	117.5	101×101	1.2982	5×10^{-7}	TVF-6 roll
480	120	101×101	1.3282	5×10^{-7}	TVF-6 roll
490	122.5	101×101	1.3572	5×10^{-7}	TVF-6 roll
500	125	101×101	1.3853	5×10^{-7}	TVF-6 roll
600	150	101×101	1.6091	5×10^{-7}	TVF- 8 roll
700	175	101×101	1.8173	5×10^{-7}	TVF- 8 roll
800	200	101×101	1.9892	5×10^{-7}	TVF- 8 roll

Table B.6 Computational details for $\eta = 0.8$, $Ma = 1.0$ and $Pr = 1.0$. The columns illustrate the inner cylinder Reynolds number (Re), number of grids, grid spacing; $\Delta z = \frac{\pi}{2N_z}$ and $\Delta r = \frac{1-\eta}{\eta N_r}$, the time step size, analysis of the states. $Re = ((1/\eta) - 1) * Re_{r_1}$, where Re_{r_1} corresponds to the Reynolds number based on chosen length scale as inner cylinder radius.

Appendix C

Responses to Reviewer's Questions

1)Section 2.3: A brief discussion on the advantages of a Dufort-Frankel leapfrog type scheme would be useful. Is there any restriction on the refinement path with regard to the stability/consistency?

Some advantages of Dufort-Frankel leapfrog type scheme (see Hellevik (2018)) are:

(i) Dufort-Frankel scheme is unconditionally stable about a diffusion equation.

(ii) It is second order accurate in space and time, as well as explicit in nature. Generally, implicit methods have this accuracy, however, since there is matrix inversion involved, they are computationally expensive.

Regarding the refinement path is concerned, as described in Hellevik (2018) , the Dufort-Frankel scheme is known to pose restriction in time step sizes, arising from the consistency constraints, not from the stability point of view. However, in the present simulations the choice of time step size is generally 1/10th of the time step size, based on the viscous CFL number.

$$CFL = \frac{\nu \Delta t}{\Delta x^2} = \frac{\mu}{\rho} \frac{\Delta t}{(\Delta x)^2} \tag{C.1}$$

I restrict the CFL, to be around 1, since theoritically, Dufort-Frankel scheme is unconditionally stable for linear diffusion equation, and choose the time step size:

$$\Delta t = \frac{(\Delta x)^2 \rho_{min}}{\mu} \tag{C.2}$$

where ρ_{min} corresponds to minimum density in the domain, appearing at the inner cylinder.

2)Section 2.3: Bullet point 6 in solution procedure. I do not fully understand the meaning of computational splitting. Splitting errors if any would be present at each time time level

of advancement? Do these errors accumulate over time and then a filter is necessary to suppress them? What would happen if the filter were not applied? Typically, direct numerical simulations do not rely on filtering as they tend to resolve all the scales without invoking numerical instability at the highest wavenumbers. It would be good to expand and explain the need and the role of filtering.

To avoid computational splitting caused by leapfrog scheme, as described in **?** , filtering is performed after every m time steps is used according to the following equation-

$$\Theta^{n\pm1/2} = \frac{(\Theta^n + \Theta^{n\pm1})}{2} \tag{C.3}$$

In the present simulations, $m = 11$, and results are invariant for $m = 21$ and $m = 31$.

Yes, they are present at each time level of advancement, and, the errors accumulate over time and a filter is used to supress the computational mode. If the filter were not applied then the solution will blow up, after a certain number of time steps.

Need and Role of filtering:

Let us consider the following equation:

$$\frac{dU}{dt} = i\omega U \tag{C.4}$$

where $i = \sqrt{-1}$ and ω is a real number. Let us define G, the amplification factor, as follows:

$$U^{n+1} = GU^n \tag{C.5}$$

Now if we write a leapfrog scheme for the oscillation equation above, we will have

$$U^{n+1} - U^{n-1} = (2\Delta t)i\omega U \tag{C.6}$$

Case 1: $\omega = 0$.

The leapfrog scheme takes the following form:

$$U^{n+1} - U^{n-1} = 0 \tag{C.7}$$

which corresponds to the exact solution. It is noted that, all the values of U at the **even** time steps will be governed by the physical initial condition and the **odd** time steps, will be governed by $U(n = 1)$. We can consider the following choices (a)$U(n = 1) = U(n = 0)$, we get the exact solution without any oscillations; (b) $U(n = 1) = -U(n = 0)$, we will have oscillations $(U(n) = (-1)^n U(n = 0)$, which would give rise to entirely computational mode, for we have set $\omega = 0$). On the other hand,

Case 2: ω be some positive real number. (C.6) can be rearranged as

$$U^{n+1} - i\omega(2\Delta t)U^n - U^{n-1} = 0 \tag{C.8}$$

Putting (C.5) in (C.8),

$$G^2 - i\omega(2\Delta t)G - 1 = 0 \tag{C.9}$$

Two possible values for G are $G_{\pm} = i\omega\Delta t \pm \sqrt{1-(\omega\Delta t)^2}$

Hence,

$$U_{\pm}^{n+1} = G_{\pm}U^n \tag{C.10}$$

Comments: (i) Origin of the computational mode is purely due to the leapfrog scheme, and it is evident from Eqn. C.10, that we get two solutions for a first order equation. One of them has to be purely computational in nature.

(ii) Also for $\Delta t \longrightarrow 0$, the computational mode will remain.

Hence, in the present numerical experiments, we filter the solution after every m time steps, (details on variation of m on the solutions have been highlighted in figure 2.3 of the present thesis), and the filtering is done after using the following method, illustrated in Harada(1980a) $\Theta^{n\pm1/2} = \frac{(\Theta^n+\Theta^{n\pm1})}{2}$.

3)The candidate has considered a reasonably large data set for validation of the DNS code. The test results do indicate that the DNS code yields accurate results over the parametric space investigated. Nonetheless, a convergence check would be more convincing and conclusive (establishing convergence in terms of mesh spacing and the time step size).

Convergence checks for $Ma = 1$, $Pr = 1$ and $\eta = 0.5$ at sufficiently large enough Re, has been showed in Figure 3.1. Convergence check for $Ma = 1$, $Pr = 1$ for different radius ratios have been incorporated in the Appendix B of the present thesis.

One particular case for temporal convergence at $Re = 383$, $Ma = 1$ and $Pr = 1$ is shown below in figure C.1.

4)The phrase “For any arbitrary physical quantity....”is repeated (pages 20 and 22)

Corrected.

5)Equation 2.18: should the superscripts be (n) and not (n+1)?

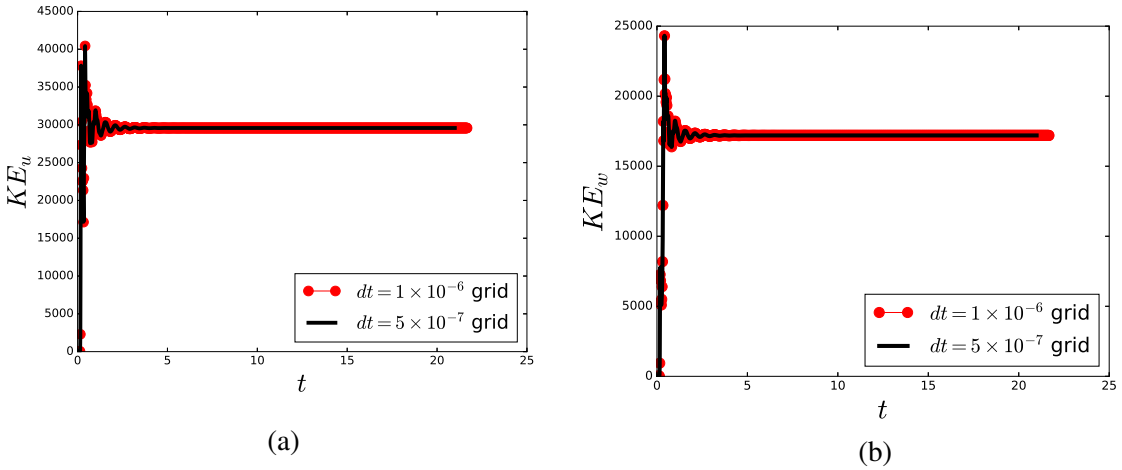

(a) (b)

Fig. C.1 Temporal evolution of the (a) radial (KE_u) and (b) axial (KE_w) kinetic energy; red solid indicates for time step, $dt = 1 \times 10^{-6}$ and the black solid line shows $dt = 5 \times 10^{-7}$.

The superscript should be (n+1) instead of (n). As discussed in Harada(1980a), in order to ensure mass conservation, two time levels (n-1) and (n+1) are allowed for the space derivatives in the right hand side of the mass conservation (viz. Equation 2.18 of the thesis). The explicit version of the equation evaluated at the backward time level (n-1) is numerically unstable and the implicit form is unconditionally stable. Hence, the mass conservation follows in the time and space using present staggered grid arrangement and this implicit form of the equation.

6)The unnumbered equation that follows Equation (3.2): Is c_{is} is a non-dimensional Reynolds number based on isentropic speed of sound?

Here, c_{is} is the dimensionless isothermal speed of sound. The correction has been implemented. Let us consider, c_{isr} as the dimensional sound speed, whose expression is given as follows:

$$c_{isr} = \sqrt{\frac{dp_r}{d\rho_r}} = \sqrt{(c_p - c_v)T_r} \tag{C.11}$$

In order to make the above quantity dimensionless, we use the velocity reference scale as per viscous time scale:

$$v_r = \frac{\mu_r}{\rho_r \delta} \tag{C.12}$$

Hence, the dimensionless sound speed (c_{is}) is

$$c_{is} = \frac{c_{isr}}{v_r} \tag{C.13}$$

$$\implies c_{is}^2 = \frac{(c_p - c_v) T_r \rho_r^2 \delta^2}{\mu_r^2} \tag{C.14}$$

and the subscript "*is*" denotes the quantity being evaluated at isothermal conditions. T_r, ρ_r and μ_r denotes the reference scale for temperature, density and shear viscosity at the inner cylinder, c_p and c_v are specific heats at constant pressure and volume, respectively. Note that, Eq.C.11 is used to calculate the peripheral/wall Mach number, $Ma = v_{in}/c_{isr}$, where v_{in} is the velocity at the inner cylinder wall, since both the cylinders have been kept at isothermal conditions.

7)If possible, it would be useful to add/discuss results from linear stability analysis in the context of DNS results shown in figure 3.4.

Our results (in the light of figure 3.4) in the context of the linear stability presented in Welsh *et al.* (2014) are as follows:

(a) As shown in figure C.2(a) the critical Re for the CCF $\longrightarrow$ TVF transition increases with increase in Ma, more prominently for $Ma > 1.5$, which explains that compressibility stabilizes.

(b) Also, from figure C.2(a), it is noted that the critical Re for the transition from CCF $\longrightarrow$ TVF is nearly same for low Mach numbers $(Ma \leq 1)$.

(c) It is also noted from figure C.2(a) that the scaling of Re vs Ma changes at higher Mach number, which enforces the point (a).

8)It would be useful to discuss (qualitatively) how three dimensionality could alter the summary given in Section 3.5. Are there additional stabilizing/destabilizing mechanisms that could influence these conclusions in three dimensional compressible flow?

Three dimensional computations will involve azimuthal variations $(\partial/\partial\theta(\cdot) \neq 0)$ in the scalar (ρ and T) and the vector fields (u, v, w). The current findings (in axisymmetric TCF) indicate that, in general, compressibility stabilises the TCF of dilute gases, in par with the linear stability data provided by Manela & Frankel (2007) and Welsh *et al.* (2014). As is well-known for the case of incompressible TCF, the axisymmetric Taylor-rolls lose stability to non-axisymmetric wavy vortices, with increasing inner cylinder rotation. In the current simulations, the observed axially-propagating wave is observed at higher Re, which need not be the case for the full 3-dimensional case. However, in the literature of incompressible TCF, people have found time dependent phenomena, both numerical and experimental, arising from purely axisymmetric flow. (see Von Stamm *et al.* (1994), Gerdts *et al.* (1994) and Heise *et al.* (2013)). Since there is little to no evidence of such axially traveling axisymmetric waves in the

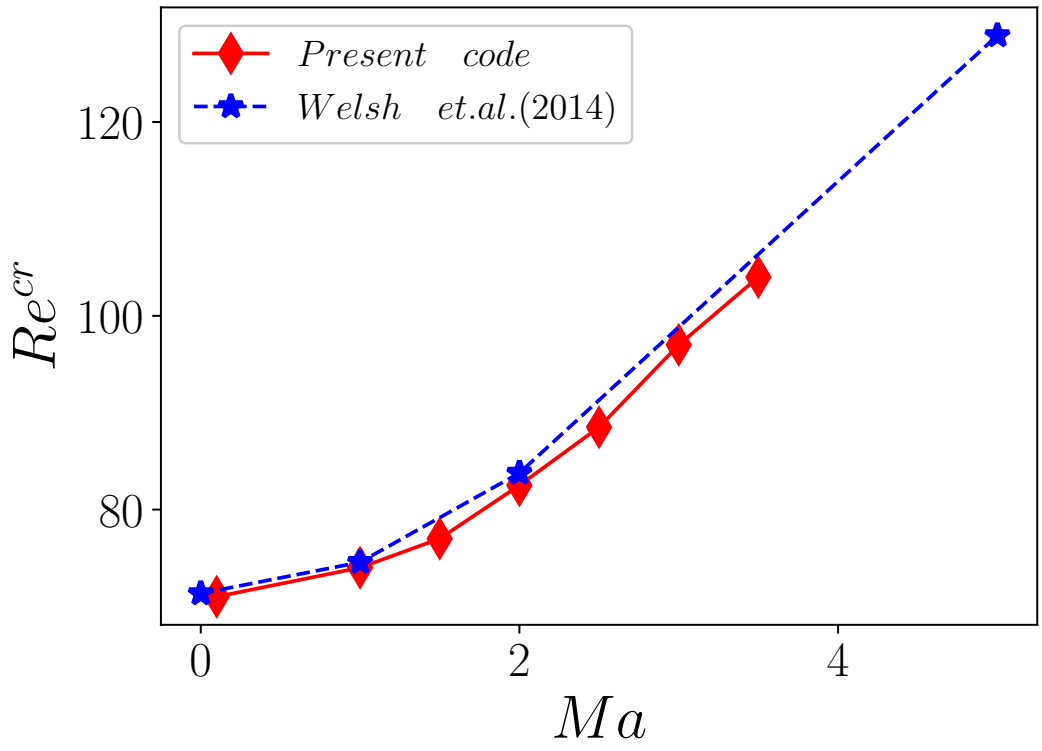

Fig. C.2 Variation of Re with Ma for $\eta = 0.5$, $Pr = 1$ and $k = 4$, where k is the axial wavenumber.

axially periodic incompressible TCF, we conjecture that this is a purely compressible effect when restricted to a particular symmetry-subspace. Since, Chapter 3 essentially considers only inner cylinder rotation, the non-axisymmetry would not change the genesis of Taylor rolls from purely azimuthal circular Couette flow (CCF). However, at large enough Reynolds number Re and Mach number Ma, the flow might develop density stratifications in azimuthal direction, which in presence of azimuthally travelling waves, can significantly alter the radial, axial and azimuthal transports.

9)Is it possible to derive the scaling law exponents for the frequency (equation 3.16 and 3.17) and effective Nusselt number through physical arguments. The adapted approach is an honest one and one would appreciate that. But the deviations in the pre-factor and exponent are quite large for the confidence bound chosen. Perhaps coming from physical arguments and then commenting on the suitability of it with respect to the data is an option worth exploring.

Scaling argument between frequency and $Re - Re_{lp}$ may not yield an exponent 1/2 for large enough Re. The canonical amplitude equation for the Hopf bifurcation is similar to pitchfork bifurcation, hence, is expected a scaling exponent of 1/2 over the variation of order parameter vs control parameter near $Re \sim Re^{cr}$.

Physical explanation of the effective Nusselt number variation with Taylor number (Ta) is in general complex, because as the gap width changes, the density near the inner cylinder (ρ_{ic}) also changes. However, a quantity $\frac{Nu_\omega}{\rho_{ic}}$ variation with Ta can be explained in the light of incompressible TCF (see Eckhardt *et al.* (2007)).

10)It might be worth considering a few simulations(time/resource permitting) with very long extended domains to ensure domain independence of the number of rolls, the characteristic roll size etc.

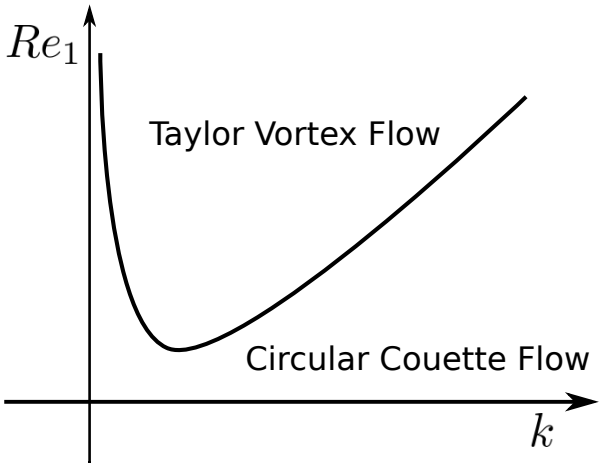

Fig. C.3 Schematic linear stability diagram depicting the variation of Reynolds number Re with axial wavenumber k for radius-ratio $\eta = 0.5$, Prandtl number, $Pr = 1$ and for a finite Mach number Ma.

A series of numerical simulations in large computational boxes (large aspect ratios, axially extended domains) has to be done in order to probe the wavelength or the characteristic roll sizes and the number of rolls for different radius ratios, apart from $\eta = 0.5$. As shown in figure C.3, long extended domains will correspond to very small values of axial wavenumber, as a result of which, one can look for the instability of highest wavelengths, if any. This will be considered in future works.

11)Since the work focuses mostly on compressibility effects, local Mach number contours could be informative, especially for high Mach number flows. This could be beyond the scope

of present work but an intriguing question that one is tempted to ask is when one can expect flow features unique to compressible flows(such as shocks, shocklets etc.)

We use the local isentropic speed of sound in ideal gases:

$$c_s = \sqrt{\gamma(c_p - c_v)T(r,z)} \tag{C.15}$$

$T(r,z)$ denotes the dimensional temperature, in K. The local "azimuthal" and "meridional" Mach numbers $[Ma_{la}$ and $M_{lm}]$ are defined as:

$$M_{lm} = \frac{(u^2 + w^2)^{1/2}}{c_s} \tag{C.16}$$

and,

$$Ma_{la} = \frac{v(r,z)}{c_s} \tag{C.17}$$

where $v(r,z)$ is the local azimuthal velocity and $u(r,z)$ and $w(r,z)$ are the radial and axial velocities, respectively. Figure C.4 displays the contours of local Ma.

It is seen that the "relative" Mach number in the azimuthal plane $(Ma_{rel} = M_{lm} * Ma_{max})$ remains subsonic for all cases; therefore the shocks/shocklets are not expected in the meridional plane over the range of Re and Ma studied.

12) In Chapter 6, the boundary conditions on the lid and rotating wall (6.5) and (6.6) seem to suggest a discontinuity in the azimuthal velocity component. Is there a singularity (in stress/pressure) and is it problematic?

There will be singularities because of the discontinuity in the azimuthal velocity (v), at the four corners of the computational domain.

However, since the present arrangement of the grids are staggered, i.e. ρ and T are defined at the center of the cell at the blue filled circles, radial, u and azimuthal, v at the side faces at the red filled circles and w at the top and bottom of the cell at the black filled circles (refer to Figure 2.2 of the thesis), the corner values never propagate inside the domain. In the problems involving mixed boundary conditions, like stress free top walls, where we need to calculate radial and axial derivatives of the scalar (ρ and T) and vector fields (u,v,w) at the boundary, we might encounter problems because of this discontinuity. In the present code, all the boundary conditions are essentially Dirichlet and henceforth, it is not problematic for the Re, we envisage.

However, we found the results to be self-consistent with increasing grid size for the parameters considered in this thesis. Grid independence of the solutions have been checked

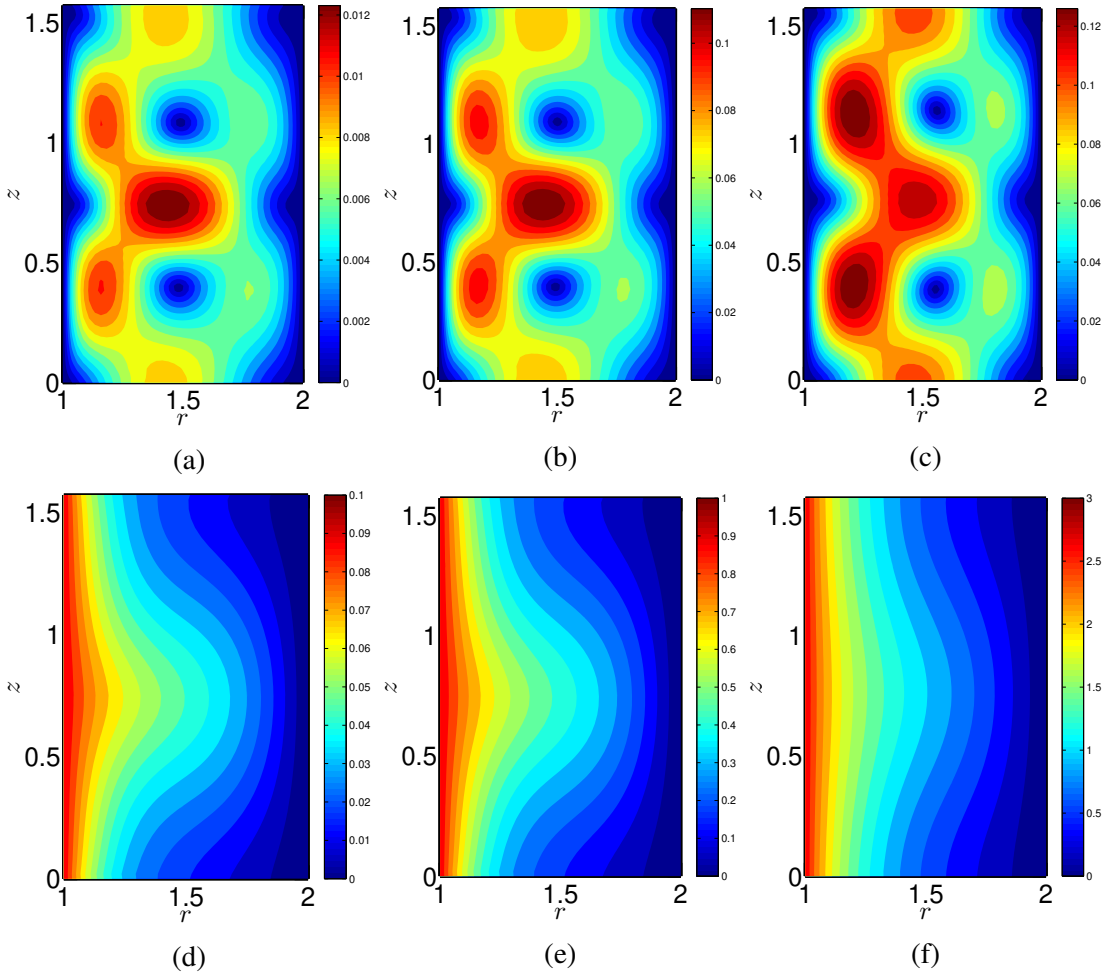

Fig. C.4 Steady state snapshot of local Mach number contours (Ma) based on (a,b,c) meridional velocity $(\sqrt{u^2+w^2})$ on (r,z) plane and (d,e,f) azimuthal velocity. The control parameters are $\eta = 0.5$, $\Gamma = \pi/2$, $Re = 100$, $Pr = 1$ for (a,d) $Ma = 0.1$, (b,e) $Ma = 1$ and (c,f) $Ma = 3$.

for $Ma = 1$, $Pr = 1$ for different Re by varying the number of grid points in the radial (N_r) and axial (N_z) for $(N_r \times N_z) \in [41 \times 21]$, $[41 \times 41]$, $[61 \times 41]$ and $[61 \times 61]$.

Also, the results presented in Chapter 6 are limited to $Ma = 1$ and $Pr = 1$. For high $Ma(\sim 3)$ and higher $Pr(\sim 10)$, we might encounter problems at large enough co and counter-rotations. This can be resolved using regularization of the discontinuities (see Lopez *et al.* (2004)), and the modified boundary condition of azimuthal velocity (v) at the stationary top and bottom endwall would be

$$v = Re_i \quad exp\left[-\left(\frac{r-r_1}{\varepsilon}\right)^2\right] \qquad r_1 \leq r \leq r_{mid} \tag{C.18}$$

$$v = Re_o \quad exp\left[-\left(\frac{r_2 - r}{\varepsilon}\right)^2\right] \qquad r_{mid} \leq r \leq r_2 \tag{C.19}$$

where, $r_{mid} = (r_1 + r_2)/2$ and ε is a very small number, say $\varepsilon = 0.001$.

13)Overall thesis has been drafted quite carefully and there are very few errors that one can find. One round of review for correction of typos would remove this.

Corrected. Thank you.